Sensing and Control for Fishlike Propulsion in Unsteady Environments

by

Amy Ruiming Gao

Submitted to the Department of Mechanical Engineering
in partial fulfillment of the requirements for the degree of

Doctor of Philosophy in Mechanical Engineering

at the

MASSACHUSETTS INSTITUTE OF TECHNOLOGY

February 2018

Signature redacted

Author .....
Department of Mechanical Engineering
October 13, 2017

Signature redacted

Certified by .....
Michael S. Triantafyllou
Professor of Mechanical and Ocean Engineering
Thesis Supervisor

Signature redacted

Accepted by .....
Rohan Abeyaratne
Professor of Mechanical Engineering
Chairman, Department Committee on Graduate Theses

Sensing and Control for Fishlike Propulsion in Unsteady Environments

by

Amy Ruiming Gao

Submitted to the Department of Mechanical Engineering
on October 13, 2017, in partial fulfillment of the
requirements for the degree of
Doctor of Philosophy in Mechanical Engineering

Abstract

Fish are equipped with a unique and elaborate flow sensing system, the lateral line, that enables them to reconstruct the near-field three-dimensional flow around their bodies, and hence effect precise control for optimal propulsion and to achieve energy recovery from vortical flows. This is a capability that is not available to engineered underwater systems today.

A paradigm example lies in the ability of fish to save energy when swimming in schools, through extracting energy from vortices generated by other fish. For a single fish modeled as an undulating, foil-shaped body at Reynolds number Re=5000, swimming directly behind another fish results in energy savings of 15-20%, compared with swimming alone. This is achieved by properly timing the interaction with vortices generated from the upstream fish, as they travel along its body and tail.

Fish that have evolved for sustained fast swimming, such as tunas and dolphins, possess a stiff tail that is morphologically separate from their body. For such fish, the phasing of tail motion is known to be important, and we demonstrate that independent and precise control of the tail is even more critical for flow control in the presence of external vortices. With an independently pitching caudal fin, small variations in phase can alter the energy savings by 15% or more, and precise timing can allow the fish to swim behind another fish with less than 50% of the energy required in quiescent water. We explore the flow mechanisms that lead to this remarkable performance and provide detailed flow visualization documenting the vorticity control effected by the independently pitching tail.

We also show that the precise feedback control required to achieve this remarkable swimming performance is feasible using the distributed flow sensing provided by the lateral line. A model-based observer is shown to be capable of extracting the positions of near-field vortices using distributed surface pressure measurements, within an error of less than 1% of the body length. With this precise feedback, we show that the fish can lock in to the frequency of an upstream wake at the correct phase, and fine-tune its tail motion to optimally exploit the wake. This demonstrates that, together, distributed flow sensing and vorticity control provide a powerful tool to control the

flow for enhanced swimming performance.

Thesis Supervisor: Michael S. Triantafyllou
Title: Professor of Mechanical and Ocean Engineering

Acknowledgments

I would like to thank my advisor, Professor Michael Triantafyllou, for his steadfast guidance throughout the years, for imparting a deeper appreciation for the beauty of fluid dynamics and the world, as well as the wonder of optimization through biological evolution. Thank you also to my committee members, Professor Harry Asada, Franz Hover and Yuming Liu for thoughtful feedback and helpful discussions. I would also like to thank Professor Gabe Weymouth for generously providing the computational code used in this project and Audrey Maertens for her work in further developing the code and for trailblazing this project that I have had the opportunity to work on.

Thank you to my wonderful labmates throughout the years - Audrey Maertens, Audren Cloitre, Dixia Fan, Fangfang Xie, Gabriel Bousquet, Heather Beem, Jacob "Izzy" Izraelevitz, James Schulmeister, Jeff Dusek, Johannes Scheller, Leah Mendelson, Stephanie Steele, Timothy Olaoye, and Zhicheng Wang. Thank you for your passion of life, science and discovery, for many good conversations and thought exercises, and for all the adventures together. It has been an honor to work with all of you, and I am truly grateful for your friendship.

I would like to say a special thank you to Professor Dave Barrett, who introduced me to the field of bio-inspired engineering and to the design of fish-like underwater vehicles. Thank you also to Maria Riefstahl, who is invaluable to our Tow Tank family in all the things that she does for us.

Thank you to our collaborators in Singapore. In particular, thank you to Ajay Kottapalli, Mohsen Asadnia, Nan Wang, Tawfiq Taher, Tony Varghese, and Vignesh Subramaniam for welcoming us in Singapore and for your friendship across the world.

Thank you to my friends and family for sustaining me - body, heart and soul. To Yukkee, Madeline and Aleida for their sistership and prayer, and the rest of SP-A for many spiritually growing discussions. To Alex, Bomy, Ina, Rohit, and Tom for the good memories in organizing GSW and Gala and traveling together. To Haritha and Akane for being like sisters to me. To Ilia for always having another adventure planned. Thank you, mom and dad, for raising me and for planting a love for science

and the pursuit of knowledge, and to my brother Allan for consistently being the happiest person I know. And last but not least, thank you, Josh, for being the person I get to come home to, and for always greeting me with a smile no matter how grumpy I am.

I would also like to acknowledge the support of the Singapore-MIT Alliance for Research and Technology (SMART), NOAA's MIT SeaGrant program, and the National Science Foundation (NSF).

Contents

List of Figures

List of Tables

Chapter 1

Introduction

1.1 Research motivation

The aquatic world is dynamic and highly energetic, containing fast currents, turbulence, and quickly-evolving flow structures. Surf zones are characterized by large spilling and plunging waves, resulting in an exceptionally complex flow field with fluctuating motions, recirculating flow, and vorticity generation. In littoral regions, strong pressure gradients exist around rocks, and Kármán vortex streets shed behind them. Animals and other objects or vehicles moving through the water similarly leave large and persevering vortex structures in their wake. The underwater environment is far from the quiescent domain it is often imagined to be, yet as scientists and engineers, we are only just beginning to imagine the possibility of capturing and exploiting the unbridled energy contained within it.

1.1.1 Exploiting unsteadiness in the underwater environment

In contrast, animals in nature are experts at exploiting their environments. Dolphins have been observed to surf in large waves, on the bow waves of ships, and even in front of larger cetaceans [15, 52, 18, 121, 174]. European eels undertake a 3500 mile migration from the coasts of Europe to their spawning grounds in the Sargasso Sea while fasting, at a rate of roughly 30 miles/day. Scientists have proposed that they are

able to make this remarkably long journey through a combination of highly efficient swimming, saving energy through schooling, and mechanisms such as selective tidal stream transport [1, 102, 163, 25].

Numerous studies have demonstrated that fish experience substantial energy savings in the presence of altered flows [90]. Fish can take advantage of the pressure gradients around rocks within a stream or extract energy from the wakes shed behind them to swim or hold position with little to no energy [138, 145, 91, 88, 10]. Research has also demonstrated that fish likely save energy when swimming in schools [65, 101, 80, 147].

These examples demonstrate that far from being just a problem to be dealt with, unsteadiness in flow presents a hidden opportunity, ready to be exploited by those who know the physics of the hydrodynamic world. However, in order to use these unsteady flows, it is critical to carefully sense and respond to the environment.

1.1.2 Flow sensing in aquatic animals

Nature has, of course, equipped animals with a number of ingeniously evolved sensors. Hydrodynamic sensors in aquatic animals include the ciliary sensor cells in flatworms and annelilds [24], sensory hairs found on many crustaceans [149, 35], scale sensilla on sea snakes [34], the epidermal lines of cephalopods [23], and the whiskers on seals [37, 173].

In nearly all fish and many amphibians, there exists a unique sensory organ known as the *lateral line*, a mechanosensory array of cells over the body which allows for the detection of local velocities and pressure gradients [31]. Researchers have shown that with the help of this distributed sensory system, fish can perform a number of tasks including object detection, prey localization, schooling, and station-holding. This sensor allows even blind fish to navigate through labyrinthine environments and hunt small crustaceans for food [137, 61, 70].

In addition, this sensory system enables fish to instinctively sense and exert precise control over their interaction with the surrounding flow in order to extract energy from waves, wakes, and even turbulence [156, 90]. By altering their kinematics in response

to the local hydrodynamic environment, fish are able to cancel or reposition vorticity or vortices to produce beneficial pressure gradients which improve the efficiency of swimming [7, 180].

1.1.3 Control of near-body flows

The concept of altering the position and strength of oncoming vortices to favorably affect the flow has been termed *vorticity control* [159, 59, 7, 184]. For a foil in the wake of a cylinder, Gopalkrishnan et al. [59] showed that increased efficiency could be achieved if annihilation occurred between vortices shed by the foil and upstream vortices, while larger forces could be generated as the result of constructive interaction between vortices. Anderson et al. [6] expanded upon these results, finding that a highly efficient gait for a flapping foil involved destructive interaction between the leading edge and trailing edge vortices shed by the foil. A number of other researchers conducted similar studies building on the idea that the control of vorticity offered a novel and powerful way to manipulate the flow to produce strong maneuvering forces, high thrust forces, or improved efficiency [143, 6, 42, 185, 81, 161].

In the majority of these studies, there is a strong emphasis on the importance of phasing of motion relative to another body or the vortex wake; relatively small changes in the timing can greatly alter the hydrodynamic load and efficiency. Through controlling the timing of a flapping foil in a regularly spaced vortex wake, the near-body flow can be manipulated in a manner that greatly alters the hydrodynamic forces on the body or the downstream wake signature.

1.1.4 Questions of fish schooling

A paradigm problem concerning the control of near-body flows is that of fish schooling. Recent research suggests that fish in schools are able to swim with 9-23% less energy than when swimming alone [65, 101, 80, 147], through drafting within the reduced velocity region close to other fish and/or exploiting the energy from vortices shed by other fish.

Fish schools are characterized by highly unsteady flows that are also periodic in nature - structured rows of vortices shed by each individual fish can be harnessed for energetic benefit. However, while there is biological evidence that fish synchronize to such structured wakes behind objects within a stream to save energy [91, 90], there is no definitive evidence for fish in the wake of other fish. There are at least two key differences between the Kármán vortex street shed behind an object in a stream and the reverse Kármán vortex street shed behind a fish: 1) the vortices in the wake of a fish are smaller, weaker, and more closely spaced, and 2) the signs of vortices within the thrust wake behind a fish are reversed, and characterized by a region of mean increased velocity, surrounded by regions of reduced velocity. These differences make it unclear if the same mechanisms that allow for energy savings when Kármán gaiting behind an object within a stream also apply to schooling fish.

For decades, researchers have acknowledged a hydrodynamic benefit to schooling, but the physical mechanisms and swimming requirements behind the energy savings remains controversial. The first theory on the hydrodynamic benefit of schooling was proposed by Weihs [170], who suggested that by swimming in a diamond configuration, fish in the back could take advantage of the reduced velocity regions within the wakes of the upstream fish and therefore save energy. However, subsequent researchers found no evidence of such schooling formations [118, 120], and recent researchers have found that it is possible for fish to save energy regardless of their specific schooling formation [63]. Maertens et al. [99] studied a fish swimming at a distance directly behind another fish, and found that despite being in a mean jet stream, energy consumption could be reduced if the fish appropriately timed its undulating motion.

This suggests that regardless of position, fish can save energy by properly exploiting individual vortices, and therefore raises a series of more fascinating questions. How can energy be captured from individual vortices, and what are the mechanisms of energy capture along the body of the fish? How much energy can be saved through proper timing? Does the fish have enough information, through sensing with its lateral line, to make the necessary control decisions to execute energy saving strategies? If so, what is the range of sensing, and how observable are near-body vortices? How

can the information captured by the lateral line be decoded into control-relevant information?

While the majority of studies on schooling fish focus on formation control [58, 56, 110], our goal is to understand how sensing and control of vortices on the scale of a single fish can affect hydrodynamic efficiency. The lateral line system of fish, being distributed in nature and extraordinarily perceptive, allows fish to respond to and exploit unsteady flows. Can this system also inform control decisions for a schooling fish?

1.2 Chapter preview

In the present work we explore the concepts of distributed sensing and vorticity control within the paradigm problem of fish schooling. The precise timing of a fish within a school can profoundly affect the hydrodynamic loads on the body as well as the wake signature. Therefore, we focus on the timing of motion of a schooling fish which is attempting to harness the energy from the wake of an upstream fish. We employ 2D numerical simulations, which allow for a systematic testing of the relationship between specific swimming parameters, the flow interactions that result, and the change in swimming efficiency. Simulations are conducted in 2D and $Re = 5000$.

In chapter 2, we describe the setup and results of the numerical simulations. The goal within this section is to identify the hydrodynamic interactions that lead to increased efficiency along the body of a fish (modeled as an undulating NACA0012) which is swimming directly behind another fish. To do so, we divide the body up into three distinct sections and identify the optimal timing for each as well as the associated hydrodynamic interactions. We discuss the physical heuristics and timing strategies that could be employed by the fish within each section to extract energy from the wake. Precedent research generally focuses on wake characteristics when quantifying the thrust or efficiency of a fish or a flapping foil [155, 43, 109]. However, a fish cannot measure its own wake, so presently we focus on vortex interactions and signals which are sensed along the lateral line of the fish. For the first time, we

highlight the role of *induced vortices* in energy capture for tandem schooling fish. As a fish swims directly within a thrust wake, secondary vortices are formed as a result of the upstream interaction with the oncoming wake. These induced vortices play an important role along the entire body of the fish, and present a novel form of energy transfer within the system.

In chapter 3, a low-order sensing model is formulated. The goal of this model is to capture information about the upstream wake, such as the size and spacing of oncoming vortices, as well as information about vortices along the body of the fish. Just as objects can be recognized from a visual picture, flow patterns can be identified from a pressure snapshot. This chapter will explore how to decode lateral line information to retrieve physical characteristics about the surrounding flow. We will describe the importance of capturing the hydrodynamic interaction between the flow and the sensing body. While it has been shown in the past that under some circumstances, a nearby wake or vortex can be characterized without modeling the sensing body [131, 165, 182, 28, 83], here we demonstrate that the instantaneous shape and motion of the fish greatly affects the signal sensed. In fact, the interaction is critical to the sensing problem, and we will show that there are key parameters that cannot be estimated without interacting with the flow.

With the model, we demonstrate that a Kalman filter estimator can be developed which allows the fish to identify all vortices in its immediate vicinity. We quantify the sensitivity and observability of the vortices in the system, and introduce an uncertainty metric which provides additional insights about the sensing abilities of the fish. Additionally, we explore the question of optimal sensor density and placement, and compare the results with available data on real fish. We demonstrate that with the optimal sensor layout, a fish can estimate the positions of oncoming vortices with an error of less than 1% of its body length, despite significant hydrodynamic noise and inconsistent interaction with the oncoming vortex street. Finally, we provide experimental results that demonstrate validity of the modeling technique in application to an artificial lateral line, and show that modeling the self-induced effect of the sensing body is critical for stable control.

In chapter 4, we consider the problem of active control for energy recovery within a wake. To decouple the tail pitching motion from the undulatory motion of the body (allowing for an additional degree of freedom), we introduce a new model of a fish that posesses a distinct caudal fin. This new model, inspired by the tuna, reproduces the morphological separation observed in 3D as well as the ability to independently pitch the caudal fin for vorticity control near the tail. With this model, we demonstrate that remarkably high efficiencies can be reached when both the body and tail are precisely coordinated with the upstream wake. We implement a phase-locked loop (PLL) controller to control the body undulation phase relative to the estimated phase of the upstream wake, and demonstrate the ability of the controller to lock in to the wake frequency at a desired phase even when the downstream fish has a different intrinsic swimming frequency. A second PLL controller is used to fine-tune the tail pitch phase to maximally extract energy from the induced vortices along the body. We demonstrate that while proper phasing of the body is certainly important, fine-tuning of the tail phase can increase the swimming efficiency by up to 30%. While the importance of independent caudal fin control is not a new idea, this is the first work that demonstrates that independent caudal fin control is even more important in the presence of vortices. Using feedback from only the lateral line, we show that model-based active control can be used to converge to the precise optimal gait, ultimately enabling a fish in the wake of another fish to swim with less than 50% of the energy that would be required to swim alone.

Chapter 2

Vorticity interactions in tandem swimming

A growing body of research suggests that fish have the remarkable ability to interact with flows around them in order to save energy [88, 90]. An interesting result is that fish tend to avoid extremely turbulent and unpredictable flows [46, 140], but prefer *predictable* unsteady flows under certain circumstances [89]. In particular, when both lateral line sensing and vision are available, Kármán gaiting trout synchronize to the frequency of vortex shedding of an upstream object, drastically changing their own swimming kinematics to hold position with almost no energy expenditure [91]. Furthermore, depending on their body size, the freestream velocity, and the characteristics of nearby objects, trout have been shown to prefer very specific station-holding positions (bow waking, entraining, or Kármán gaiting) [148]. The littoral environment is permeated with hydrodynamic microhabitats that allow fish to swim upstream or hold position with far less energy than one would expect.

In schools of fish, which similarly contains predictable rows of vortices, it has become well established that fish are able to save more energy than if they were swimming alone [65, 101, 80, 147, 117]. Several theories have arisen to explain the mechanism of energy savings. The earliest theory was put forth by Weihs [170], who suggested that schooling fish could save energy if they swam in diamond configurations. In this formation, the fish would theoretically be able to take advantage of

the regions of reduced velocity present to either side of a leader's thrust wake. However, later researchers argued that fish generally did not swim in such formations [100, 118]. More recent research has shown that in reality, fish can save energy even when swimming behind another fish and directly *within* the thrust wake [99, 63]. Liao [90] remarks that fish in schools can save energy through *flow refuging* (drafting in areas of relative reduced velocity) and *vortex capture* (exploiting individual vortices). Within a thrust wake, flow refuging obviously cannot occur, so vortex capture must be the primary mechanism of energy extraction.

How does a fish extract energy from a vortex? Past research on flapping foil wake energy extraction demonstrates that energy is extracted when the wake downstream from the foil is weakened in comparison to the wake upstream from the foil [59, 143]. Similarly, the efficiency of swimming fish has often been characterized by analyzing the characteristics of the downstream wake [43, 109]. While these studies provide useful insights, they do not translate directly to the vortex interactions and signals which are sensed along the lateral line of the fish. A fish obviously cannot measure its own wake, and therefore needs to work with a more observable signal. The lateral line provides this - a distributed sense of the flow upstream and directly to the sides of the fish.

With this in mind, the goal of this chapter is to explore the concept of vorticity control within the problem of fish schooling. The present work is restricted to a study of two fish schooling in tandem (in 2D simulations), in which we focus on the vortex-body interactions on the downstream fish. We consider interactions on a local and observable level, while also comparing significant results of the downstream wake with results from past researchers. We begin by considering how changing the timing of the downstream fish, through changing its phase of undulation, affects the overall swimming efficiency. Since multiple vortices are present along the body of the fish at any instant, we subsequently study in detail the interactions within discrete sections. Through quantifying the change to thrust and power expenditure produced in each section through interaction with the wake, we isolate important interaction mechanisms, and ultimately develop rough timing strategies that would allow the fish

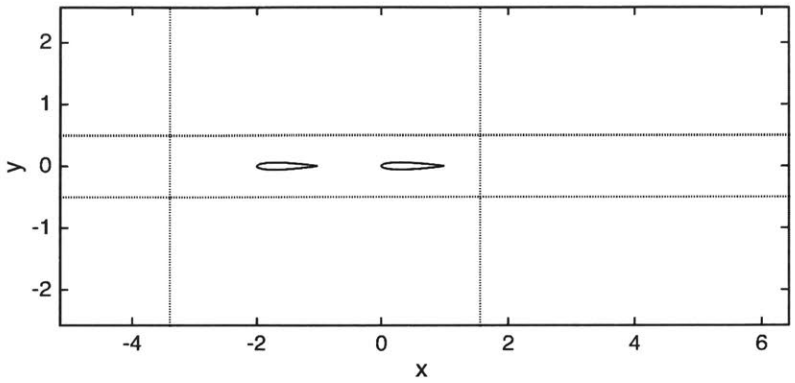

Figure 2-1: The simulation grid. The region in the center with the two fish represents the fine grid region, with $dx = dy = 1/320$.

to extract energy from vortices along each section of its body.

2.1 Problem and simulation setup

2.1.1 Numerical implementation

Simulations were conducted in 2D using the Boundary Data Immersion Method (BDIM) developed by and described in Weymouth and Yue [171] and Maertens and Weymouth [98]. The present method is adapted from the setup described in Maertens et al. [99]. The physical parameters of the simulation are nondimensionalized by the fish length L, its swimming speed $U_s = 1L/s$, and the water density ρ. To simulate a steady swimming speed for the fish, a constant velocity inlet conditions of $U_\infty = U_s$ is used on the left side of the fluid domain, and the fish maintains a position within the center of the fluid domain (figure 2-1). Two proportional-integral-derivative controllers are implemented to ensure the fish maintains its position in x and y; the details of these controllers are provided in section 2.1.4. Periodic boundary conditions are implemented on the upper and lower boundaries, and a zero gradient exit condition with global flux correction is used on the downstream (right) boundary. Simulations were conducted at $Re = 5000$.

The cartesian grid is uniform within a fine grid region near the fish (figure 2-1), with $dx = dy = 1/320$. A 2% geometric expansion ratio is used for the spacing in the

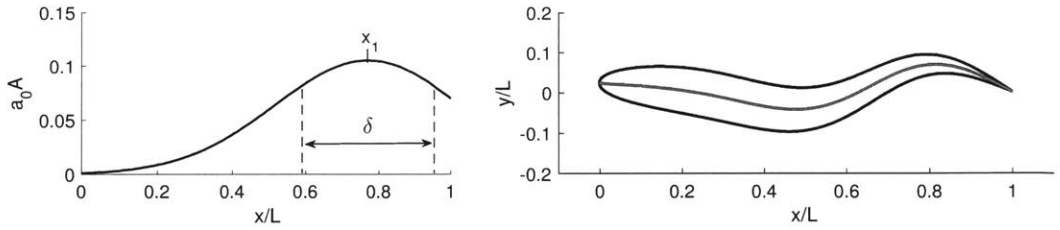

Figure 2-2: The gaussian deformation envelope for a fish with a continuous body, and a diagram of the fish at a single timestep. The black outline represents the total displacement of the fish, while the gray line represents the midline displacement.

far field. Validation for the numerical method used is published in [99].

2.1.2 Fish model

Fish swimming gaits have traditionally been classified into two groups: body and/or caudal fin (BCF) locomotion, and median and/or paired fin (MPF) locomotion [20]. The majority of fish typically use BCF locomotion for propulsion, while using their fins for maneuvering or stabilization forces. Within BCF propulsion, fish are divided into two more groups: those who propel using *undulatory* motions which involve a backward-traveling wave along the body, and those who use *oscillatory* motions which do not involve a traveling wave [136].

In this work, we focus on fish that use undulatory BCF propulsion. The first set of simulations was conducted using a fish modeled as a single, neutrally buoyant undulating NACA0012 foil (figure 2-2). The fish has a total length $L = 1$, and self-propels at an average speed of $U_s = 1L/s$.

Similar to real fish, which propel using flexural body waves that propagate from head to tail, we impose a *flexure* over the body of the fish. The flexural motion is parameterized by 5 parameters: the frequency f, phase ϕ and wavelength λ of the undulating wave, as well as two parameters (x_1 and δ) which govern the shape of the deformation envelope. This low-order parameterization allows us to capture the most prominent features of the swimming gait while keeping the parameter space

manageable. The lateral deformation of the midline is given by:

$$\begin{aligned} y_c(x,t) &= h_0(x,t) + B(x,t) + y_1(x) \\ &= a_0(t)A(x)\sin\left(2\pi(x/\lambda - ft + \phi)\right) + B(x,t) + y_1(x,t) \end{aligned} \tag{2.1}$$

The fish undulates with amplitude $a_0(t)$ within a gaussian envelope $A(x)$, defined as:

$$A(x) = \exp\left(-\left(\frac{x - x_1}{\delta}\right)^2 + \left(\frac{1 - x_1}{\delta}\right)^2\right) \tag{2.2}$$

Using the gaussian envelope, the maximum flexure for the fish occurs at a point x_1 upstream of the trailing edge, and the width of the peak around x_1 is governed by δ. With this parameterization, the flexure of the fish more accurately captures the flexing capabilities of fast fish such as the tuna and the mackerel [4] . Physically, the point of maximum flexure occurs near the peduncle of the fish, allowing the caudal fin to undergo a large displacement while retaining a low angle of attack relative to the local flow.

$B(x,t)$ is the recoil term due to hydrodynamic forces on the fish:

$$B(x,t) = (a_s + b_s x)\sin(2\pi ft) + (a_c + b_c x)\cos(2\pi ft) \tag{2.3}$$

in which a_s, b_s, a_c, and b_c are calculated to ensure that linear and angular momentum are conserved as the fish undulates.

$y_1(x,t)$ imposes a camber over the foil that can be used for steering:

$$y_1(x,t) = C(t)(x^2 + \gamma x + \beta) \tag{2.4}$$

$C(t)$ is calculated by a proportional-integral-derivative (PID) controller, and γ and β ensure that momentum is conserved through the deformation.

2.1.3 Self-propelled swimming

For a self-propelled swimmer, the exact displacement over time is governed by the coupled fluid-body dynamics. The translation and rotation of the body is governed by:

$$\frac{\mathrm{d}}{\mathrm{d}t}\left(\mathbf{M}\boldsymbol{V}\right) = \boldsymbol{F}. \tag{2.5}$$

in which:

$$\boldsymbol{X} = \begin{pmatrix} x_c \\ y_c \\ \theta \end{pmatrix}, \quad \boldsymbol{V} = \begin{pmatrix} v_c^x \\ v_c^y \\ \omega_b \end{pmatrix}, \quad \boldsymbol{F} = \begin{pmatrix} F_h^x \\ F_h^y \\ M_c^z \end{pmatrix}, \quad \mathbf{M} = \begin{pmatrix} m & 0 & 0 \\ 0 & m & 0 \\ 0 & 0 & I_c \end{pmatrix}, \tag{2.6}$$

$\vec{F}_h$ is the hydrodynamic force on the body, and $\vec{M}$ is the mass matrix, in which m is the mass of the body and I_c is its moment of inertia with respect ot the center of mass.

2.1.4 PID controllers

Two proportional-integral-derivative (PID) controllers are implemented: the first adjusts the thrust by tuning the amplitude of the swimming gait $a_0(t)$, and the second steers the fish by adjusting the camber $C(t)$. If the fish is fully self-propelled, the time-averaged linear momentum in x is used as feedback for the first controller, and the time-averaged linear momentum in y is used as feedback for the second controller. Maertens [97] showed that the streamwise oscillations were generally small, so the fish could be fixed in x to improve simulation convergence times without greatly affecting the results. In this case, the time-averaged drag is used as feedback for the first controller.

The controllers act on the time-averaged error, defined as (for the momentum):

$$\mathbf{e}_k = f\sum_{i=k_0}^{k-1} m\mathbf{v}_i(t_{i+1} - t_i) \tag{2.7}$$

where k_0 is the index corresponding to the timestep exactly one period before.

The integral of the error is:

$$\mathbf{e}_{i,k} = \sum_{i=0}^{k-1} \mathbf{e}_i (t_{i+1} - t_i) \tag{2.8}$$

And the derivative of the error is:

$$\mathbf{e}_{d,k} = \frac{\mathbf{e}_k - \mathbf{e}_{k-1}}{t_k - t_{k-1}} \tag{2.9}$$

A window smoothing filter is applied to each error term to improve stability. At the beginning of each timestep, $a_{0,k}$ and C_k are adjusted as follows:

$$a_{0,k} = \max\left(a_{0,k-1} + (t_k - t_{k-1})(K_p^x e_k^x + K_i^x e_{i,k}^x + K_d^x e_{d,k}^x), 0\right) \tag{2.10}$$

$$C_k = -\left(K_p^y e_k^y + K_i^x y e_{i,k}^y + K_d^y e_{d,k}^y\right) \tag{2.11}$$

Where e^x and e^y denote the error terms in x or y. The gain coefficients used were:

for force control in x:	$K_p^x = 5,$	$K_i^x = 5,$	$K_d^x = 0.1$
for displacement control in x:	$K_p^x = 10,$	$K_i^x = 0.1,$	$K_d^x = 1$
for displacement control in y:	$K_p^y = 30,$	$K_i^y = 30,$	$K_d^y = 10$

2.1.5 Performance metrics

To compare the performance of each fish, we use the *quasi-propulsive efficiency* defined in Maertens et al. [99]:

$$\eta_{QP} = \frac{RU_s}{\overline{P_{in}}} \tag{2.12}$$

R is the resistance of the rigid-straight towed body (i.e., the drag of a towed NACA0012), and $\overline{P_{in}}$ is the period-averaged power consumed to undulate. Note that this is distinctly different from the traditionally used Froude efficiency, which would be zero for a body moving at constant velocity [95]. The quasi-propulsive efficiency is an in-

tuitive performance metric; researchers have estimated that the drag of a swimming fish is approximately 3-5 times that of the rigid-body equivalent [136], corresponding to a quasi-propulsive efficiency of $20 - 33\%$. For simplicity, this term is used interchangeably with "efficiency" throughout this thesis.

For a fish swimming within the wake of another fish, multiple vortices are encountered over each swimming cycle, and each vortex interacts with the fish to enhance or reduce its performance. The quasi-propulsive efficiency reflects the average change to the energy consumed as a result of these interactions.

In order to resolve the effect of individual interactions better, we define a few additional metrics which reflect the change to thrust, power and efficiency over sections of the fish. For these metrics, Δ denotes a comparison between the fish swimming within the wake and a solitary fish swimming with the same kinematics. For example, the average change to thrust at a point x achieved by the fish as a result of vortex interactions is:

$$\Delta\overline{T}(x) = \overline{T}(x) - \overline{T}^*(x) \tag{2.13}$$

And the additional power consumed as a result of vortex interactions is:

$$\Delta\overline{E}(x) = \overline{E}(x) - \overline{E}^*(x) \tag{2.14}$$

$\overline{T}(x)$ and $\overline{E}(x)$ denote the period-averaged pressure thrust and power consumed at a point x along the length of the fish within the wake. $\overline{T}^*(x)$ and $\overline{E}^*(x)$ denote the period-averaged pressure thrust and power at a point x for a solitary fish swimming with the same kinematics.

The *thrust ratio* is defined as the ratio between the change to the period-averaged thrust produced in a section spanning from $x = x_1$ to $x = x_2$ and the total thrust required to overcome viscous drag in quiescent flow $\overline{T}_0$:

$$R(T) = \frac{\int_{x_1}^{x_2} \Delta\overline{T}(x)dx}{\overline{T}_0} \tag{2.15}$$

The *power ratio* is defined as the ratio between the change to the period-average

Name	Symbol	Expression
Quasi-propulsive efficiency	η_{QP}	$RU_s/\overline{P_{in}}$
Power coefficient	C_E	$2\overline{E_{in}}/(\rho U_s^3 L)$
Pressure coefficient	C_P	$2(p-p_\infty)/(\rho U^2)$
amplitude ratio	Ar	$a_{0,\text{ in wake}}/a_{0,\text{ solitary}}$
Reynolds number	Re	$U_s L/\nu$
Strouhal number	St	fa/U_s
Tail heave to chord ratio	h/c	
Nominal tail pitch angle	θ_0	
Tail pitch phase	ϕ_t	
Tail Angle of attack	α	
Tail heave-pitch phase angle	ψ	

Table 2.1: Kinematic and other dimensionless parameters.

power consumed in a section spanning from $x = x_1$ to $x = x_2$ and the total power required to self-propel in quiescent flow $\overline{E}_0$:

$$R(E) = \frac{\int_{x_1}^{x_2} \Delta\overline{E}(x)dx}{\overline{E}_0} \tag{2.16}$$

The *added quasi-propulsive efficiency* for a section spanning from $x = x_1$ to $x = x_2$ is defined as:

$$\Delta\eta_{QP} = \frac{R - D^* + \int_{x_1}^{x_2} \Delta\overline{T}(x)}{E^* + \int_{x_1}^{x_2} \Delta\overline{E}(x)} - \eta^*_{QP} \tag{2.17}$$

D^* is the drag for the solitary fish with the same kinematics (note that this is nonzero because with the same kinematics, the fish cannot swim at the same velocity in quiescent flow). E^* and η^*_{QP} are the power consumed by and the quasi-propulsive efficiency for the solitary fish with the same kinematics.

Additional useful parameters are defined in table 2.1.

2.2 Description of vorticity interaction

Fish swim by creating a propulsive wave along their bodies which acts to accelerate the surrounding water rearward while keeping it attached. The wake of the fish, a

reverse Kármán vortex street, consists of two vortices shed per swimming period, with positively-signed vortices to the right of the fish and negatively-signed vortices to the left. This is a thrust-type wake, consisting of a region of mean increased velocity (a jet) directly behind the fish, with a region of mean reduced velocity to each side.

In the present work, we consider a fish swimming directly within a reverse Kármán vortex street, at a distance $d = 1$, where energy saving mechanisms depend primarily on individual vortex capture rather than drafting (figure 2-3). Within the mean jet flow it encounters in this position, it is surprising that the fish would be able to swim with increased efficiency at all; however, it has been found that energy saving is possible with well-coordinated motions [99]. Individual interactions with vortices along the entire body can greatly influence the efficiency.

As the downstream fish encounters the oncoming wake, interaction with oncoming vorticity induces the formation of a secondary vortex. For example, in figure 2-3a, a positively-signed vortex which has just passed the nose of the fish on the right induces the formation of a negatively-signed vortex between itself and the fish. The strength of the induced vortex depends on the kinematics of the fish as well as the strength and position of the original vortex. The formation of the induced vortex is associated with a significant low pressure dip at its location of approximately $x/L = 0.2$ (figure 2-3c).

Subsequently, the vortex pair, consisting of the original vortex and the induced vortex, convects along the side of the fish. The vortex pair from the previous half cycle can be seen on the left side of the fish around $x/L = 0.5$. The dominant pressure signal (and therefore the dominant effect) is due to the induced vortex (figure 2-3b). The induced vortex loses strength over time, and due to its sign, also propagates at a reduced velocity. Meanwhile, the original vortex, which was accelerated over the nose of the fish, passes the induced vortex. While the induced vortex is shed with the trailing edge vortex, the original vortex convects downstream where it can interact with the vortices shed at the trailing edge of the downstream fish.

As can be seen in figure 2-3 , the oncoming vortices are associated with a strong pressure change at the nose (figure 2-3b) and the induced vortices create a strong

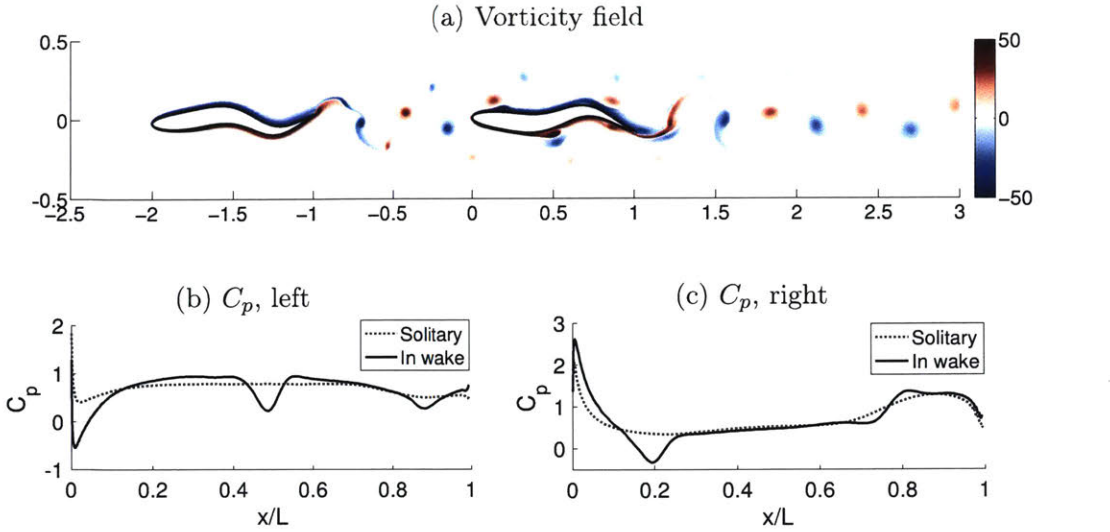

Figure 2-3: (a) A snapshot of the vorticity field which illustrates the setup of the problem studied. A fish swims at a distance of one body length directly downstream from another fish, where it interacts with the wake shed by the upstream fish. The lower plots show, for the same timestep, a snapshot of the pressure induced on the (b) left and (c) right sides of the downstream fish, compared with the pressure that would be experienced by a solitary fish swimming with the same kinematics.

pressure signature along the body (figures 2-3b and 2-3c), when compared with the pressure that would be felt by a fish swimming with the same kinematics in quiescent water. These changes in pressure can be responsible for large changes to the thrust generation and power consumption of the downstream fish.

While both 2S (two single vortices shed per cycle) and 2P (two pairs of vortices shed per cycle) wakes have been observed behind swimming fish, we focus on a fish swimming within a 2S wake in the current work.

2.2.1 Formation of secondary vortex

The formation of a secondary vortex close to the nose of the fish when it encounters the upstream wake is a phenomenon that has not been studied in great detail in the past work. However, within this study, it is shown this induced vortex can be powerful, resulting in the dominant pressure effect along the body and having the potential to interact with fins further downstream on the fish.

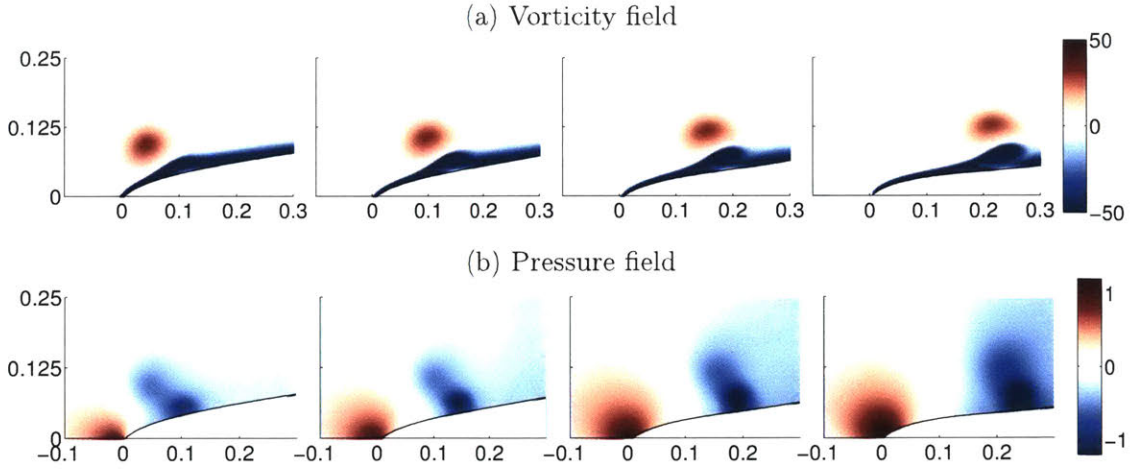

Figure 2-4: (a) Vorticity snapshots and (b) pressure snapshots at $t/T - \phi = 0, 0.08, 0.16, 0.24 \pmod 1$, showing the formation of a secondary vortex at the front of the fish as it interacts with a vortex from the upstream wake. The induced vortex begins to form just downstream of the original vortex, at the location of the adverse pressure gradient caused by the original vortex. It appears first as a thickening of the boundary layer, and subsequently rolls up into a vortex of roughly the same strength as the original vortex.

What leads to the formation of this secondary vortex? A great deal of prior research has shown that in general, a vortex convecting near a solid surface leads to a viscous response [41]. The strength of the effect can be characterized by a vortex Reynolds number $Re_v = \Gamma/(2\pi\nu)$. At sufficiently high Re_v, a buildup of vorticity occurs within the boundary layer (to satisfy the no-slip condition), culminating in the formation of a new vortex.

At the head of the fish, this effect is amplified by the curvature of the nose, which causes the original vortex to accelerate to nearly 1.5 times its original velocity. To fulfill the no-slip condition at the surface of the fish, this leads immediately to the formation of a localized and concentrated "patch" of vorticity which rolls up into a distinct vortex (figure 2-4). The secondary vortex that forms has a comparable strength to that of the original vortex, and due to its proximity to the fish, a much stronger effect.

The shedding of vorticity at any point on the fish can be considered a loss of energy.

However, it also presents an opportunity for precise and powerful control. Flying and swimming animals in nature often impart momentum to the fluid in the form of vortices [39, 123, 92]. By subsequently manipulating the vortex and positioning the body correctly, it is possible to generate large forces that can be used for a sudden change in direction or forward acceleration [57, 2].

In the case where high efficiency swimming is the goal, it is also possible to appropriately time motion of a downstream fin to recapture the energy lost from vortex shedding of an upstream fin [44, 3, 93, 142].

2.3 Timing strategies

For two fish swimming in tandem, the timing of the upstream fish is not extremely important, while the timing of the downstream fish greatly affects its swimming efficiency [99]. The timing of the downstream fish, which is modified through varying either the distance between the two fish or the phase of undulation, controls the specific interaction between the fish and the upstream wake. Numerous studies of the interaction between a foil or undulating body with an upstream wake have reinforced this finding [59, 6, 42, 75, 161].

For a fish swimming within the wake of another fish, vortex-body interactions take place at many points along its body and can all greatly affect the swimming efficiency. In this section, we aim to improve the understanding of the specific mechanisms which affect the efficiency and the timing strategies that could be used to exploit them.

2.3.1 Efficiency of schooling: whole body analysis

Simulations were conducted for fish swimming in tandem, at swimming frequencies between $f = 1.8$ and $f = 2.4$. Both fish are self-propelled, and vary their amplitude of undulation in order to maintain a steady swimming velocity. To assess the importance of timing, the phase ϕ of the downstream fish was varied while the distance d between the fish was kept constant. The timing of the downstream fish is captured by the

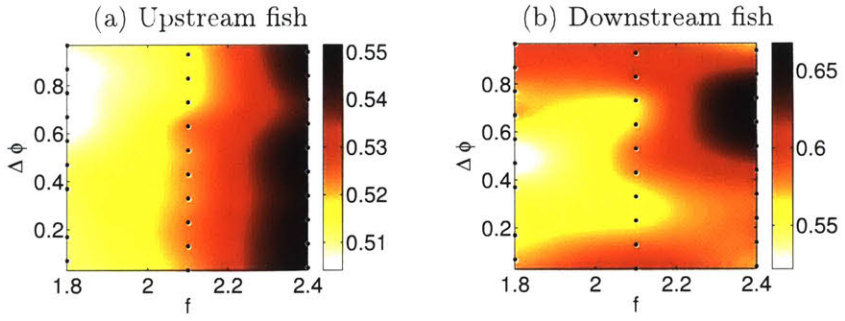

Figure 2-5: Quasi-propulsive efficiency for the tandem fish, for varying swimming frequency and body phase. The dots in each represent results from individual simulations and the contour plot is created using a thin-plate smoothing spline with smoothing parameter $p = 0.999$.

variable $\Delta\phi$, defined as:

$$\Delta\phi = \phi - \phi_1 \tag{2.18}$$

$$\phi_1 = d/\lambda_w + \phi_w \tag{2.19}$$

Physically, $\Delta\phi$ defines the phase difference between the undulating motion of the downstream fish and the wake shed by the upstream fish, which has phase ϕ_w and wavelength λ_w. ϕ_1 is the phase of the wake at the nose of the downstream fish.

Similar to previous findings, we find that the efficiency of the upstream fish is largely independent of the difference in timing between the two fish. The efficiency of the downstream fish, however, depends strongly on $\Delta\phi$, and varies by $5 - 10\%$ depending on the phasing of the fish (figure 2-5).

Notably, the value of the optimal phase difference $\Delta\phi$ varies with the frequency. Furthermore, at each swimming frequency, the efficiency of the downstream fish does not contain only one peak. Particularly at $f = 2.1$, it is clear that there are two peaks in the efficiency as the undulating phase is varied. This indicates that there is more than one significant vortex-body interaction occuring over the length of the fish. As the frequency and phase is varied, some interactions become more beneficial while others become more detrimental.

There is a noticeable correlation between the amplitude ratio of the fish and the

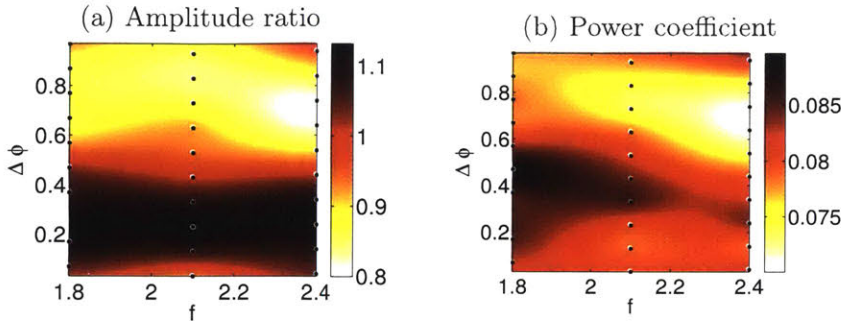

Figure 2-6: (a) Amplitude ratio and (b) power coefficient for the downstream fish, over varying frequency and phase.

power coefficient (figure 2-6). The amplitude ratio is defined as the ratio between the amplitude of undulation a_0 for the fish swimming in the wake compared with the amplitude of undulation required to self-propel in quiescent water. The PID controller increases a_0 until the fish is fully self-propelled; therefore, a less efficient fish will typically exhibit a higher amplitude of undulation. Efficency is inversely related to power consumption; as a result, a less efficient (and vigorously undulating) fish will have a higher power coefficient.

However, within a wake, a fish can save energy either by using nearby vortices to reduce the power consumed to undulate *or* by harnessing the pressure field created by the vortices for additional thrust. Using the first strategy, the power consumption can be directly reduced, though the amplitude of undulation may be high. Using the second strategy, the required amplitude of undulation for self-propulsion can be reduced, and the energy consumption is indirectly reduced as a result. Therefore, although increased efficiency can generally be achieved through using the wake to augment the thrust, this is not always the case.

2.3.2 Efficiency within sections of the body

In order to study the significance of specific vortex-body interactions over the fish better, the body of the fish was divided into three sections, and the thrust and power expenditure over each section was analyzed. The head, defined as the region $0 < x/L < 0.2$, is the region with the strongest forward-pointing normal vectors,

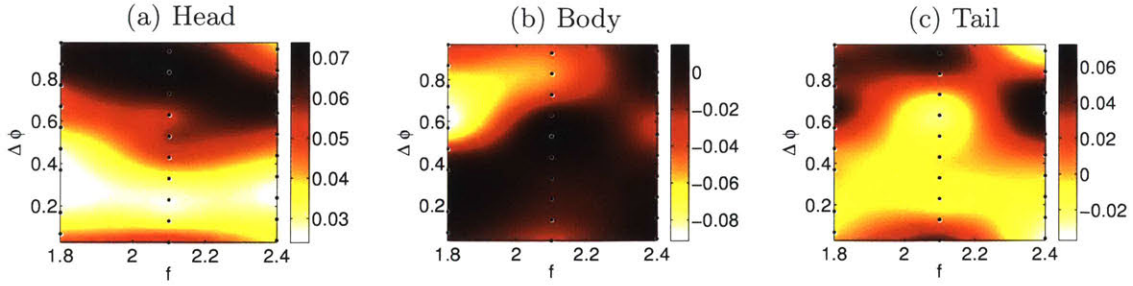

Figure 2-7: Added efficiency within each section of the downstream fish, for varying swimming frequency and phase.

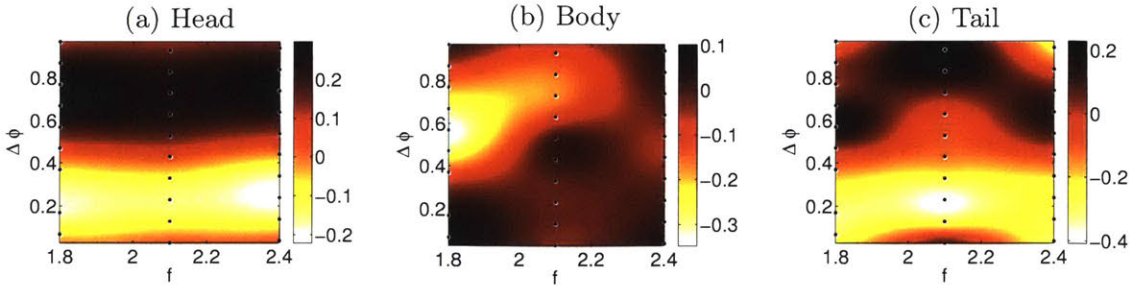

Figure 2-8: Thrust ratio for each section of the downstream fish, for varying swimming frequency and phase.

and therefore the region that is the most suitable for harnessing thrust from the low pressure cores of the approaching vortices. The body, defined as the region $0.2 < x/L < 0.6$, can extract energy from vortices to the side of the fish. The interaction mechanisms within this section also apply generally to the entire fish. The tail, defined as the region $0.6 < x/L < 1$, is the region with the largest displacement, and well-situated to gain benefits from vortex interactions downstream from the fish.

The added efficency $\Delta\eta_{QP}$ is shown in figure 2-7, for each section. The thrust ratio $R(T)$ is shown in figure 2-8. There is a strong correlation between the thrust gained in each section and the efficiency of that section, although they are not strictly comparable.

In the head region, the thrust ratio varies strongly with the phase, but not with the frequency. This indicates that in this region, a given phase difference between the motion of the nose and the oncoming wake will always yield the greatest increase to thrust attained. Interestingly, the efficiency within this section is not as straightfor-

ward. Although in general an increased thrust correlates with an increased efficiency, the phase corresponding to the greatest increase of thrust is not equivalent to the phase corresponding to the greatest increase in efficiency. However, regardless of the change in thrust, the efficiency is always improved, for the parameter space tested.

In the body region, both the thrust and efficiency vary with frequency and phase. As vortices from upstream pass the nose of the fish, they are accelerated at different rates depending on the exact motion of the fish. As a result, past the head of the fish, $\Delta\phi$ no longer corresponds to a specific phase difference between the position of the fish and the position of the relevant vortex. In this region, there is a strong correlation between $R(T)$ and $\Delta\eta_{QP}$, and for nearly all phases, the interaction with vortices results in a decreased thrust and loss of efficiency.

In the tail region, the ideal timing is similar to that at the head, and follows the opposite trend from the ideal timing in the body region. Interactions in the tail region can be beneficial or detrimental to the efficiency.

Importantly, it can be seen that the optimal phase $\Delta\phi$ is different within each section of the fish. For example, we observe local minima in the efficiency for $f = 2.1$ at $\Delta\phi = 0.28$ and $\Delta\phi = 0.73$. These dips in the efficiency correspond well with the drops in efficiency observed at $\Delta\phi = 0.23$ at the head and $\Delta\phi = 0.63$ at the tail. Similarly, the optimal phase for each fish results from balancing the effects of all vortex interactions; for fish swimming at frequencies for which a particular phase results in beneficial interactions along the entire body, the maximum attainable efficiency is higher and the minimum efficiency is lower. For example, at $f = 2.1$, the maximum efficiency is 62.1% and the minimum efficiency is only slighty lower at 56.2%. In contrast, at $f = 2.4$, the maximum efficiency is 67.6% and the minimum efficiency is 56.2%.

Furthermore, it is clear that the hydrodynamic interactions within all three sections are significant. The potential change to the efficiency and thrust is comparable within all sections. With the fish divided into sections as defined here, clear correlations could be observed between the hydrodynamic benefit to each section and specific vortex-body interactions within that section. In the next part of the paper,

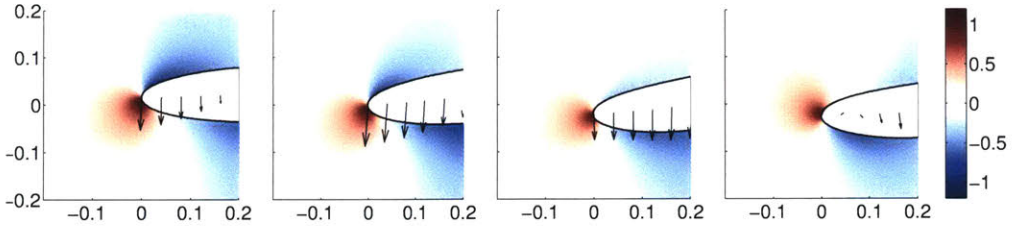

Figure 2-9: Snapshots of the pressure field around the head of a solitarily swimming fish, at $T/t - \phi_1 = 0.625, 0.75, 0.875, 1$ (left to right). The arrows represent the centerline velocity of the fish for all images.

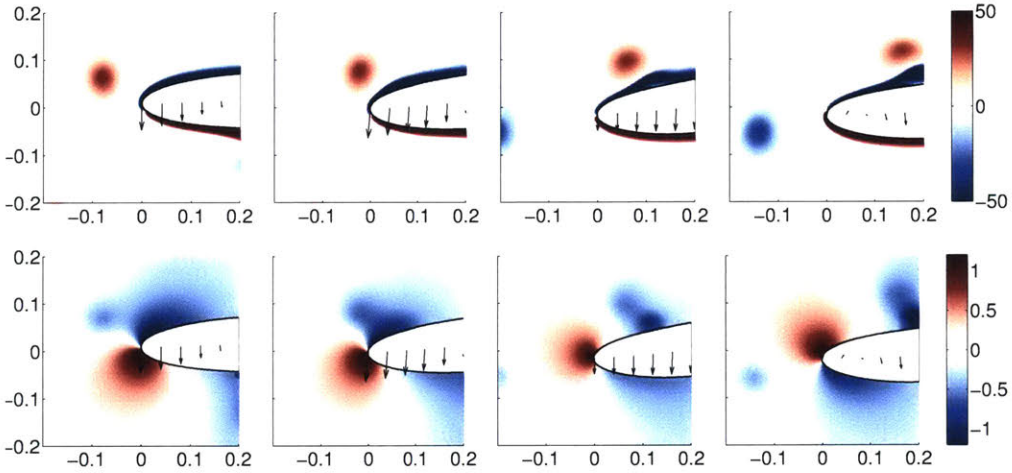

Figure 2-10: Snapshots of the vorticity and pressure fields around the head of a fish with optimal head phase $\Delta\phi = 0.87$, at $T/t - \phi_1 = 0.625, 0.75, 0.875, 1$ (left to right, mod 1). The pressure field, compared with the solitary fish in figure 2-9, is strongly amplified with a considerably deepened low pressure region.

the interactions within each section will be discussed in greater detail. Since the hydrodynamic mechanisms are similar for all swimming frequencies, we will focus on a set of fish swimming at $f = 1.8$. At this frequency, a fish swimming at the optimal phasing reaches an efficiency of 60.2%.

2.3.3 Vortex interactions: head

Fish gained the greatest efficiency at the head when slaloming between the oncoming vortices. For the optimal configuration at phase $\Delta\phi = 0.87$, the fish turns in the direction of a vortex shortly after the vortex passes the nose (figure 2-10). This results in two beneficial interactions. First, the head moves in the opposite direction

to the local transverse velocity created by the vortices; this amplifies the pressure field at the nose (compare with figure 2-9). Although the stagnation pressure close to the nose is strengthened, it is also shifted downstream from the nose. On the opposite side of the nose, a strong low pressure region forms as a result of the amplified transverse velocity, contributing to the thrust. Secondly, as the result of the interaction with the oncoming vortex and the low pressure region on the leeward side of the nose, a strong induced vortex forms which further contributes to the thrust. As the fish turns away from the approaching vortex, its head becomes angled in a manner that allows the forming vortex to contribute more strongly to the thrust. By bracing its head motion against the lateral force created by the oncoming vortices, the fish consumes more energy in turning its head from side to side ($R(E) = 0.10$), but greatly increases the thrust at the nose ($R(T) = 0.23$) for an increased partial efficiency of $\Delta\eta = 7\%$ (figure 2-12).

In contrast, for the least efficient case, the fish turns toward approaching vortices (figure 2-11). This reduces the relative transverse velocity over the nose, so that the stagnation point remains centered over the nose throughout the entire swimming cycle. Furthermore, since the vortex wake creates an increased streamwise velocity, the stagnation pressure is increased, incurring additional drag ($R(T) = -0.17$). Despite this, it is still beneficial to swim through the wake due to the energy saved ($R(E) = -0.22$)(figure 2-12). As the vortex passes the nose and induces the formation of an additional vortex, the low pressure region to the side of the head reduces the energy required for the fish to turn from side to side.

Interestingly, we observed that the induced vortex formed as the result of interaction with the fish exhibiting optimal head phasing is much stronger than the induced vortex formed from the least beneficial case, despite the closer proximity to the wake vortex in the latter case. Although separation is usually viewed as a detrimental effect, the formation of a strong induced vortex appears to be beneficial for the fish in the head region.

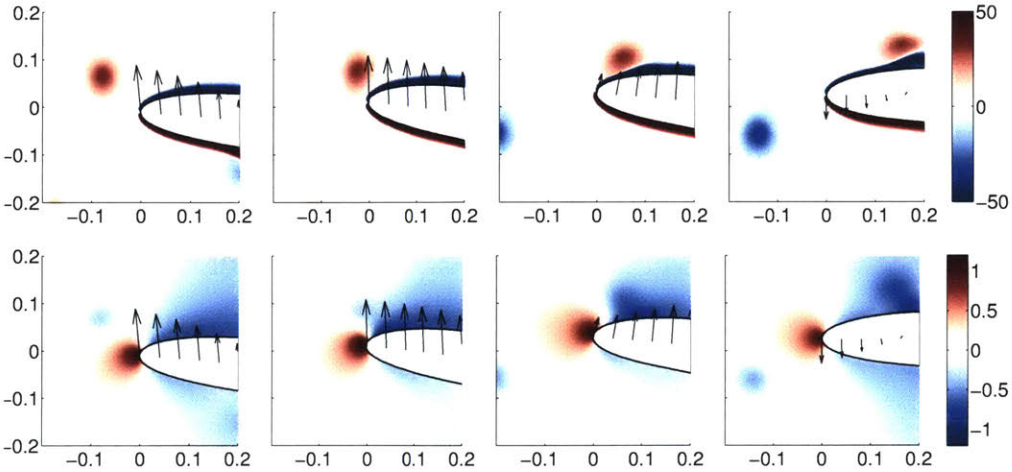

Figure 2-11: Snapshots of the vorticity and pressure fields around the head of a fish with the worst head phase $\Delta\phi = 0.27$, at $T/t - \phi_1 = 0.625, 0.75, 0.875, 1$ (left to right, mod 1). The pressure field depicts a strongly amplified stagnation point due to the mean jet stream in the wake of the upstream fish, which stays roughly centered over the nose. Although a low pressure region also forms, it is weaker than that for $\Delta\phi = 0.87$, and does not produce as much thrust due to the reduced angle of the head.

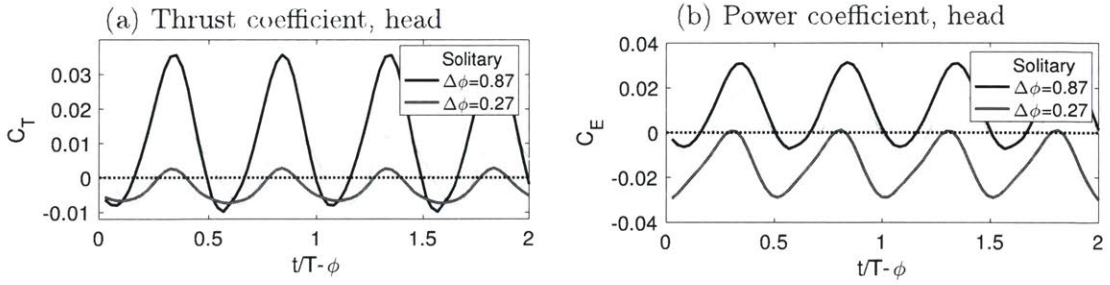

Figure 2-12: The (a) thrust coefficient and (b) power coefficient plotted over 2 swimming cycles for the fish with optimal head timing ($\Delta\phi = 0.87$) and the worst head timing ($\Delta\phi = 0.27$), compared with a solitary fish. A positive C_E indicates energy consumed.

2.3.4 Vortex interactions: body

Along the body, increased efficiency is also correlated with increased thrust. Fish which timed their undulating motion to maximize the time vortices were aligned with the forward slopes of its undulating crests also maximized their thrust (figure 2-13a). The low pressure core of the induced vortex creates a strong suction on the slope of the undulating crest, which translates to a thrust force if the vortex pair is upstream of the crest. In the optimal case, the fish achieves a thrust ratio of $R(T) = 0.07$ and an increased partial efficiency of $\Delta\eta = 1\%$. With the worst timing, the vortices consistently fall on the downstream side of undulating crests (figure 2-13b), yielding thrust ratio of $R(T) = -0.35$ and partial efficiency of $\Delta\eta = -8.8\%$.

Unfortunately, the configurations which lead to increased thrust and efficiency at the head tend to result in a loss to thrust and efficiency along the body. As the head of the fish slaloms around an approaching vortex, the vortex almost immediately falls on the downstream side of the undulating crest. Although the wave speed of the fish is faster than its swimming speed, it is not fast enough to move the crest downstream of the vortex pair, which has been accelerated around the nose. As a result, the vortex pair remains in a detrimental position along nearly the entire length of the fish.

It is important to note that while analyzing the fish in sections provides a way to draw important insights, the sections of the fish are not decoupled and therefore the comparison has limits. There are at least two mechanisms within other regions of the fish that influence the efficiency within this section. First, the overall efficiency of the fish governs its amplitude of undulation. Particularly within this section, it is evident that a reduced amplitude of undulation greatly affects the instantaneous slope along the body. Although for $\Delta\phi = 0.87$, the vortex pair also falls on the downstream side of the crest (figure 2-14), the local slope is much lower due to the greater efficiency of this fish, so this fish does not lose as much energy due to the vortices along the body.

Secondly, it is clear from figure 2-13 that the induced vortices are much weaker in the well-timed case as compared with the poorly-timed case. As previously mentioned, for a well-timed nose, a stronger induced vortex is formed. Although this appeared to

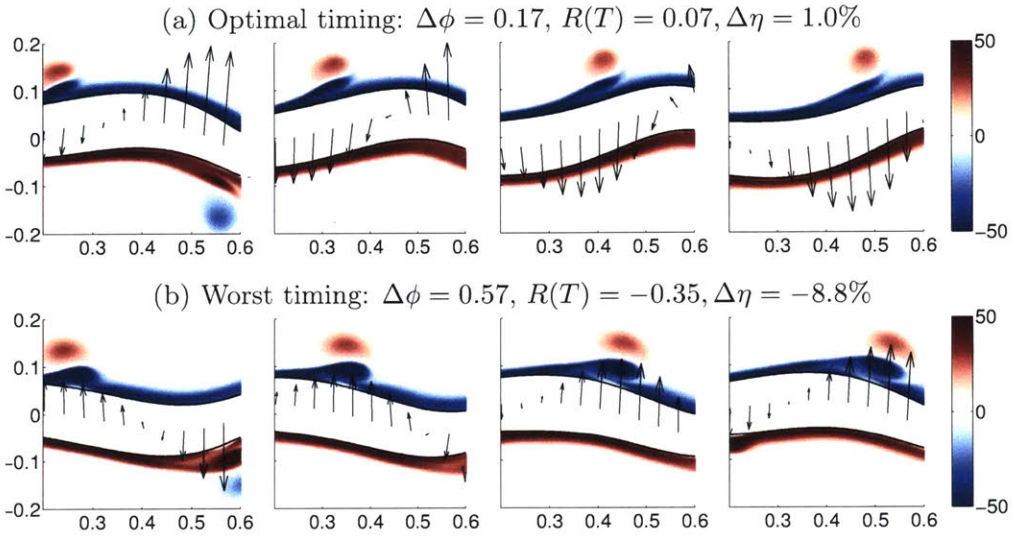

Figure 2-13: Snapshots of the vorticity field for the fish with (a) optimal body timing and (b) the worst body timing, at $T/t - \phi_1 = 0.125, 0.25, 0.375, 0.5$ (left to right, mod 1). The optimal timing keeps vortices on the upstream side of the undulating crest, while for the worst timing the vortex pair falls downstream of the crest.

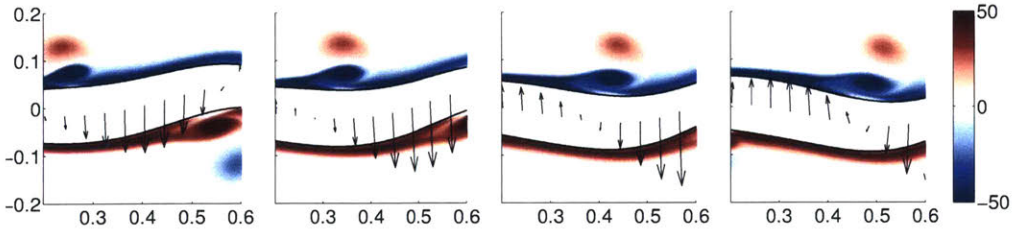

Figure 2-14: Snapshot of the vorticity field for $\Delta\phi = 0.87$, at $T/t - \phi_1 = 0.125, 0.25, 0.375, 0.5$ (left to right, mod 1). The vortex pair falls on the downstream side of the undulating crest, but due to the reduced body slope of this fish, the loss in thrust efficiency is not as large ($R(T) = -0.06$, $\Delta\eta = -4.6\%$).

be beneficial within the head region, it is harmful within the body region for the same phase. The variation in strength of the induced vortex causes a bias to the potential benefit within this section; while a maximum of $\Delta\eta = -8.8\%$ can be lost within this section, a gain of only $\Delta\eta = 1\%$ was observed for the cases tested.

Therefore, a balance of timing between the head and the body is critical.

2.3.5 Vortex interactions: tail

Downstream from the fish, a variety of wake patterns can be observed as the result of variation in the timing of vortex shedding at the tail (figure 2-15). A relatively clean wake consisting of 2 vortices per tail beat cycle is observed for $\Delta\phi = 0.57$, a wake with 4 vortices per tail beat cycle is observed for $\Delta\phi = 0.37$, and a wake consisting of 6 vortices per tail beat cycle can be seen for $\Delta\phi = 0.77$.

A large body of past research has shown that for interacting flapping foils or flexible filaments, constructive vortex interactions can result in enhanced forces, while destructive vortex interactions result in decreased drag and increased propulsive efficiency [59, 143, 6, 42, 81, 161].

This suggests that for our schooling fish, configurations that result in vorticity annihilation within the wake will tend to be more efficient. Indeed, this is roughly what is observed. The cleanest and weakest wakes (figure 2-15d) were always associated with the highest thrust ratio and a moderately high partial efficiency. With this configuration, the fish sheds a trailing edge vortex just before an oppositely-signed vortex from upstream reaches the trailing edge. In the case with the greatest thrust enhancement (figure 2-15d), a small induced vortex (on the right) of the same sign as the upstream vortex (on the left) reaches the trailing edge at almost the same time. These two negatively-signed vortices cancel the positive vorticity being shed from the trailing edge, reducing the strength of and altering the wake signature to yield a clean, narrow wake.

The tail with the highest partial efficiency is typically very close in phase to the tail with the cleanest wake. The small difference in phase of the most efficient tail is potentially due to the greater overall efficiency of the fish at $\Delta\phi = 0.67$. The

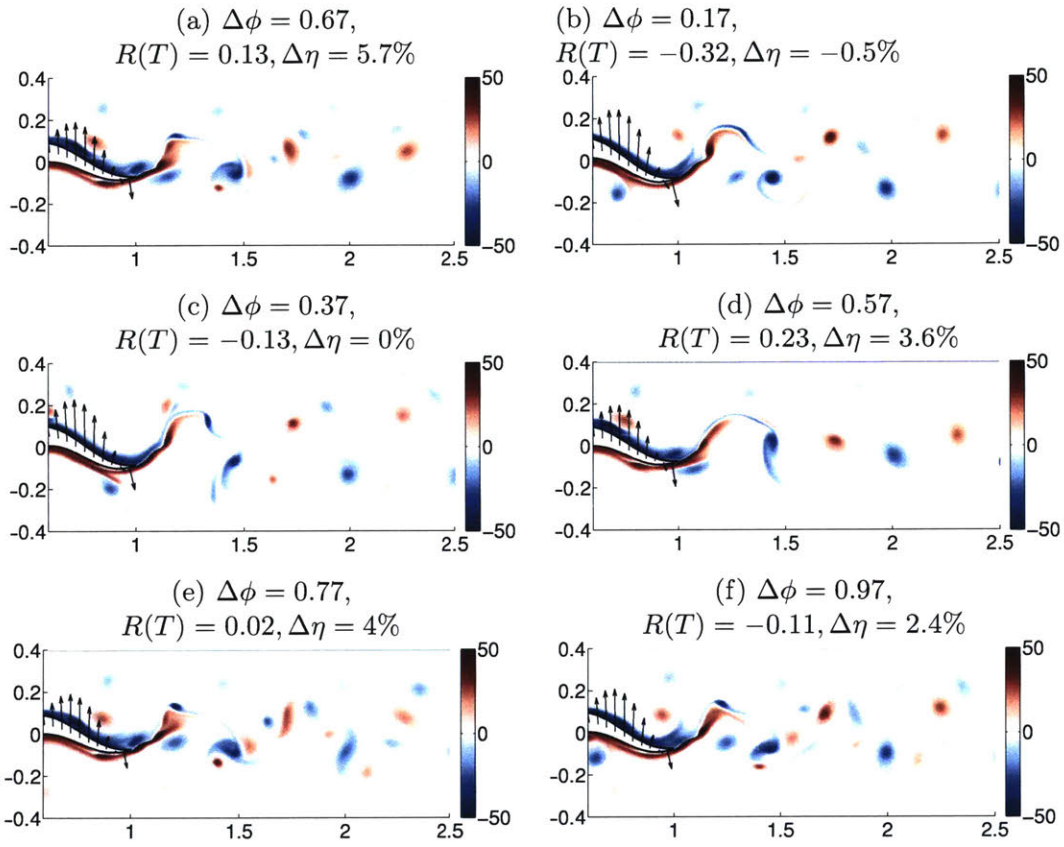

Figure 2-15: Snapshots of the vorticity field for varying undulation phases, at $t/T - \phi = 0.25 \pmod 1$. Relatively small changes in phase result in large changes to the wake topology. It can be seen that configurations which yield a high thrust ratio and efficiency are correlated with a weaker and narrower wake, in which vortices from upstream annihilate with vortices shed at the trailing edge of the fish (figure 2-15a, 2-15d). In contrast, configurations with poor performance (figure 2-15b) are associated with wider and stronger wakes, in which vortices from the trailing edge of the fish are deposited in between upstream vortices and do not annihilate as effectively.

greater efficiency results in a reduced amplitude of undulation for this fish, so that it consumes less energy in undulating its tail.

In contrast, for the configuration with the lowest thrust ratio and partial efficiency (figure 2-15b), the fish sheds a trailing edge vortex almost directly in between two vortices from upstream. Due to the distance between the vortices, they do not annihilate, so the wake vortices of the follower retain much of their original strength.

The exact timing of vortex shedding at the trailing edge of the fish is important. In the case of the two least efficient fish (figures 2-15b and 2-15c), the induced velocity field of the vortices in the wake act to push individual vortices outward, widening the wake. This acts to further reduce the efficiency of swimming in these two cases.

Similarly, for the more efficient fish, there can be a large difference between shedding a trailing edge vortex just before or just after an oppositely-signed vortex from upstream passes. When the vortex is shed just before the upstream vortex passes (e.g., figure 2-15d), the induced velocity field of the vortices act to push individual vortices inward, resulting in a more narrow wake over time. In contrast, when the trailing edge vortex is shed just after the upstream vortex passes (e.g., figure 2-15e), the induced velocity field causes the wake to widen over time.

It is also important to note that the trailing edge shedding of the fish depends on the local angle of attack. The strength and position of approaching vortices as well as vortices in the wake affect this. Although for all phases, vortices are shed at approximately the same point in the cycle, the precise distribution of vorticity shed over time depends on the angle of attack profile over time [124, 67]. As a result, for some configurations, the vorticity distribution is multimodal and rolls up into two distinct vortices. This produces the wakes with 6 vortices per tail beat which are particularly evident in figures 2-15a and 2-15e.

These results are in line with prior work reported by Koochesfahani [84], Schnipper et al. [134] and Lentink et al. [87], who demonstrated that a wide variety of wake patterns can be generated for a pitching airfoil by modifying the oscillation waveform. Waveforms which retain a harmonic angle of attack profile produce the highest efficiencies and thrust coefficients, with two vortices shed per cycle. Additional vortices

shed per cycle, caused by multiple peaks in the angle of attack profile, mix the wake and reduce thrust [67].

Researchers have observed that when maximizing efficiency, the resulting wake is a weak and narrow reverse von Kármán vortex street [108]. The formation of such a wake depends on the precise motion of the fish with respect to the surrounding flow over time.

2.3.6 Summary: vortex interactions for tandem fish

In summary, a fish swimming within the wake of another fish can exercise vorticity control methods along its entire body to save energy. Control mechanisms along the head and body can be utilized to alter the hydrodynamic load, while control of timing at the tail can cancel vortices and reduce the wake signature. Configurations that increased the thrust generated by the fish also typically increased the efficiency.

At the head, a thrust ratio of 0.3 could be reached and the partial efficiency could be increased by up to 7% when the fish phased its motion in order to slalom between oncoming vortices. Even when poorly timed, efficiency would still be increased in this region due to the suction created by the low pressure cores of the approaching vortices.

Along the body, by keeping vortices upstream of its undulating crests, the fish could reach a thrust ratio of 0.1 and increase its partial efficiency by 1%. The potential losses in this section were larger (thrust ratio of -0.35 and reduced partial efficiency by 8.8%), due to the variation in the size of the induced vortex with the interaction leading to its formation.

At the tail, by shedding trailing edge vortices at the right time to annihilate with vortices from upstream, the fish could achieve a thrust ratio of 0.23 and increase its partial efficiency by 5.7%.

Although the maximum and minimum gains within each section varied, the difference between them remained about the same in all three sections. This stresses that timing within all three regions is important, and for optimal energy savings, the timing between the regions must be balanced. In particular, the fish cannot si-

multaneously time both the head and the body optimally due to the nature of the undulating wave. With varying frequency, due to variation in the wave speed of the body, higher efficiencies could potentially be reached due to a greater fraction of beneficial interactions over the entire body.

An interesting observation is that for all of these interactions, the induced vortex plays a significant role. At the nose, the strong low pressure region created as the induced vortex is formed greatly augments the thrust. Along the body, it is the induced vortex rather than the original vortex that creates the dominant pressure signature and therefore the dominant effect. Finally, if the induced vortex has survived to reach the tail, it can combine destructively with trailing edge vorticity to reduce the wake signature and improve swimming efficiency.

2.4 Discussion

2.4.1 Physical heuristics for energy savings in a wake

Using a simple model of a fish schooling in the wake of a leader, we have been able to uncover some physical heuristics which can promote energy recovery from the upstream wake. These energy saving mechanisms can act either directly to reduce the power required to undulate, or indirectly by increasing the thrust or reducing the pressure drag incurred during swimming.

At the nose of the fish, the upstream thrust wake always increases the streamwise velocity encountered by the downstream fish, but the lateral incident velocity may be increased or reduced depending on the motion of the fish. In this study, we have found that when the fish phases its motion such that the head consistently slaloms between oncoming vortices and therefore increases the relative lateral velocity, efficiency is increased.

While slaloming between vortices is the same strategy found for Kármán gaiting trout [88], the physical mechanims behind the two slaloming behaviors are different. Most importantly, the Kármán vortex streets which trout have been demonstrated

to adopt a slaloming gait for consist of considerably stronger vortices of a longer wavelength (relative to the length of the fish). The path in between these vortices is characterized by a reduced streamwise velocity as well as a reduced relative lateral flow. Within such a wake, trout are known to activate only their anterior muscles, using the rest of the body as a self-correcting hydrofoil to passively produce the thrust required to hold position or swim upstream [88]. This configuration is stable, as evidenced by the fact that even a dead fish can take advantage of a Kármán vortex street to swim upstream [10, 45].

In contrast, in schools of fish, upstream fish which swim at high efficiencies shed a comparably weak wake, which is configured as a reverse Kármán vortex street. While Kármán gaiting fish slalom between vortices in order to "go with the flow" and reduce both the incident streamwise and lateral velocity, a fish slaloming between vortices in a reverse Kármán street increases both. Trout in a regular Kármán street minimize power input rather than maximize thrust output. Fish in a reverse Kármán street appear to maximize thrust output, which results in an immediate increase to the power consumed but overall reduction to the power required to self-propel.

Interestingly, it has been shown that when swimming within the reduced velocity region of a wake, the downstream fish prefers to time its motion such that its nose comes close to intercepting vortices rather than slaloming around them [99]. Only when swimming directly behind another fish, in a reverse Kármán street, does slaloming between vortices become the optimal gait for energy savings at the nose. The reduced velocity region of the wake is similar to a half Kármán vortex street, so this implies that the size of the oncoming vortices is an important factor for the timing chosen.

When oncoming vortices are smaller, the fish cannot use its body as a passive hydrofoil to take advantage of large regions of altered flow. Instead, the regions of altered flow are relatively small and localized, and do not induce as considerable of a change to the angle of attack over the fish. As a result, well-coordinated interaction of the fish with the localized low pressure cores of each vortex becomes the dominant mechanism of hydrodynamic exploitation. However, these localized pressure changes

can be significant (figure 2-3).

The interaction with the upstream wake and subsequent formation of a secondary vortex (which does not occur in a regular Kármán vortex street) probably plays a large role in the preference of a slaloming behavior when swimming in a thrust wake. Within a reverse Kármán street, angling away from approaching vortices exposes a larger normal surface from which the low pressure region can be translated into thrust.

Due to the presence of many more vortices along the body of the fish, timing must be balanced between numerous interactions. Along the body, it was found that the optimal timing, which kept vortices upstream of undulating crests, could not be reconciled with the optimal timing at the head. However, for fish swimming with a high efficiency overall, the lateral undulations along the body are relatively small and therefore the energy loss due to vortices in this region is also relatively small.

For energy recovery at the tail, the findings largely support previous work by Gopalkrishnan et al. [59], Streitlien et al. [143], and Zhu et al. [184]. Highly efficient gaits are associated with annihilation between the vortices shed by the fish and upstream vortices. This annihilation reduces the pressure signature of the wake and the downstream suction region, ultimately increasing the swimming efficiency.

Small changes in the swimming gait could yield large changes in the wake topology, due to changes to the interaction with the upstream wake and changes to the angle of attack profile of the trailing edge. Optimal timing resulted in a trailing edge vortex shed just before an upstream vortex of the opposite sign passed. This configuration resulted in an induced velocity field that narrowed the wake, and annihilation between vortex pairs over time which resulted in a weakened wake.

Overall, the optimal gait is influenced by many factors, including the size of the vortices, their exact configuration, as well as the interactions over the entire body of the fish. While it can be difficult to determine by intuition if a fish would choose a thrust-amplifying gait or a power-reducing gait, the present work corroborates the study by Maertens et al. [99] in that thrust-amplifying gaits are preferred when swimming in tandem with another fish. These gaits ultimately reduce the required undulation amplitude (or frequency), which reduces the overall power consumption of

the fish in a more beneficial way. While the swimming position of a fish is certainly important to the potential hydrodynamic benefit, it appears to be possible to exploit the wake in many positions. Since many vortices interact with the fish at any instant and on a very localized level, the overall benefit depends on the proper timing of individual interactions.

Chapter 3

Lateral line sensing: Extracting information from the flow

The aquatic environment is rich in information that is invisible to the eyes - information that can only be felt, heard, or perhaps somewhere in between. Since water is one thousand times as dense as air, these hydrodynamic signals can propagate quickly and powerfully. A change in pressure can be transmitted almost instantaneously from one side of a fish school to the other, alerting distant fish of imminent danger. Sound waves travel through the water over 4 times faster than they travel in air. The simple translation of an object or body is automatically communicated to nearby animals, and water motions that are left in the wake of rapidly moving organisms can remain detectable for 20 minutes or more. Nearly all underwater animals are exquisitely evolved to respond to these hydrodynamic stimuli. Their survival depends on it [158].

Indeed, underwater animals are equipped with a fascinating suite of sensors uniquely adapted to the stimuli exclusive to their environment. Many aquatic organisms possess chemosensory systems that monitor chemical signals that may signal the presence of friends or foe; the shark's acute olfactory system allows for the detection of even a single drop of blood in the water nearby. The sonar system in dolphins provides the ability to not only localize objects hundreds of meters away, but also to discriminate between objects of different composition, an ability that would be very useful for

mine-hunting underwater vehicles [66]. Sharks, rays and some fish possess electroreceptors, which detect weak electric fields that are created by other animals or the environment. To detect hydrodynamic stimuli, fish are equipped with a unique organ known as the *lateral line*, which has been the topic of intensive research in recent years. The lateral line, which contains sensory hair cells capable of detecting minute changes in water motions, allows fish to "touch at a distance", extracting information from flows to hydrodynamically image their environments even in dark or murky waters [182]. Best exemplified by the Mexican blind cavefish, which is adept at navigating through its labyrinthine environment and can even catch living prey despite its conspicuous lack of eyes, this sensor is present in nearly all fish. For many of these sensory systems, there is no analog in engineered underwater vehicles, rendering them effectively blind to the majority of underwater stimuli.

Chapter 2 demonstrated that while energy can be extracted from an upstream wake, timing is of the utmost importance. In particular, it is critical for the downstream fish to localize vortices in the flow surrounding it. Precise interactions with these vortices can give rise to remarkable swimming efficiencies. All underwater motions result in unique and characteristic signatures. What kind of information in a vortex street is available to flow sensing? What signature would a fish detect? Since research has definitively shown that fish use their lateral lines to perform a number of flow relative tasks that allow them to save energy [90, 145, 105], we will focus on exploring the abilities of this system for hydrodynamic imaging. Does the lateral line provide enough information for a fish to intelligently time its motion relative to an upstream wake? In this chapter, we will explore the lateral line sensing capabilities of the fish, and develop a strategy for deciphering the sensory input into control-relevant information.

3.1 Bio-inspiration: the lateral line system

The lateral line is a sensory organ existing in most fish and many amphibians, and is well known to provide fish with a number of unique capabilities. This sensory

system consists of tens or even hundreds of directionally sensitive hair cell sensors (neuromasts) distributed over the body of the fish, providing fish with a sense of "touch at a distance." Each neuromast consists of hair cells which are enclosed by a flexible, jellylike cupula, and acts as a mechanoreceptive organ which allows for the sensation of any movement [31]. Two types of neuromasts, canal neuromasts and superficial neuromasts, exist within the system. Superficial neuromasts are distributed over the entire surface of the fish and detect flow velocity, while canal neuromasts reside within pored subdermal canals, where they detect pressure gradients [31].

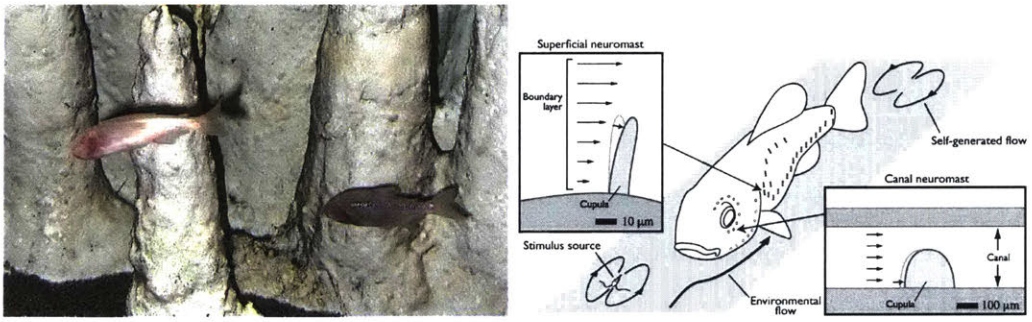

Figure 3-1: Left: blind cavefish (source: Opencage photography). right: schematic of the superficial and canal neuromast systems (source: [176]).

The lateral line provides fish with a sense that is, to date, nonexistent in engineered vehicles. The neuromasts are exceptionally sensitive, and in comparison to vision or sonar, extremely low-power and low-bandwidth. While they do not provide long-range sensing, they allow the fish to build a near-field hydrodynamic image, providing the ability to detect immediate dangers, and make control decisions for navigation or improved performance.

3.1.1 Behaviors mediated by the lateral line

Scientists have shown that the lateral line is instrumental in tasks such as obstacle avoidance [153, 177], discrimination of orientation-dependent spatial features [166] and discrimination of spacing between objects [62]. Although behaviors such as navigation and prey detection may be aided by other senses such as vision and smell, the lateral line has been shown to be critical to the speed and precision of response. For

fish with their lateral lines intact, fast-start latencies of 10-30 ms were found following a disturbance, compared with 100-120ms for the visual system response by startled fish [119]. In addition, in blind fish such as *Astyanax mexicanus*, the lateral line is solely responsible for exploration of new environments [36, 164, 154], response to dangers and prey detection [107, 178, 179]. By interacting with their environments and decoding the resulting flow signatures, fish are able to characterize their environments and make control decisions rapidly.

3.1.2 The lateral line in schooling

There is no direct evidence that the lateral line is used in schooling. Studies have shown that the lateral line is important for positional control within a school [119, 48], but no studies have established if the lateral line allows fish to use active feedback in order to swim more efficiently. However, researchers have shown that fish alter their gaits to save energy in the wakes shed behind objects within streams. In studies of fish Kármán gaiting behind such objects, gait kinematics changed substantially when the lateral line was blocked, indicating that hydrodynamic feedback is used to enhance energy savings when swimming in regular Kármán vortex streets [89]. When schooling, fish are similarly subjected to relatively predictable arrays of oncoming vortices, so there is no reason why they could not harness the energy from them in a similar way.

Swimming in unsteady flows is likely to benefit from the ability to sense small changes in the hydrodynamic environment. For example, when entraining by objects in a stream, trout lacking both visual and lateral line feedback showed a drastically reduced ability to maintain a favorable position [145].

3.2 Precedent work in distributed flow sensing

Flow sensing and control within Kármán vortex streets has been investigated by a few groups.

With underwater distributed pressure sensing platforms, researchers have demon-

strated the ability of an artificial lateral line to characterize important features of a Kármán vortex street, such as the vortex shedding frequency, vortex travelling speed, and downstream distance between vortices [165, 182]. Where the vortex street originates from an upstream cylinder, it is also possible to estimate the size and position of the cylinder [83, 28]. These studies primarily use statistical information, finding that the power spectra of the pressure measurements as well as the turbulence intensity can allow for differentiation between various scenarios.

In addition, several research groups have demonstrated the ability of an artificial lateral line to provide the feedback necessary for a robot to execute station-holding behavior within a Kármán vortex street [131, 74]. Similarly, statistical information is used for positioning.

In regard to sensing and control of the interaction between a body and individual vortices, Beal [11] demonstrated the possibility of sensing the frequency, phase and position of an oncoming Kármán vortex street with two external sensors and using a flapping foil to extract energy from it.

The signature of individual vortices has also been studied. Mathematically, it is possible to estimate the pressure field that would be created by individual vortices. The pressure resulting from the interaction between a body and a vortex can also be approximated, and used within an inverse model to estimate the strength and position of the vortex [146, 125]. However, it is still unclear to what extent these theoretical results extend to real environments, particularly those involving a deforming sensing body and strong interactions with oncoming vortices.

In general, the past work takes either a statistical approach or uses a model in which the interaction between the sensing body and the vortex wake is nonexistent or negligible. In many studies, the sensing and interaction problems are decoupled, such that the motion of the sensing body does not affect the signal it senses. However, we will demonstrate that the shape and motion of the sensing body is in fact extremely important, and greatly changes the signal sensed. Furthermore, strong interaction between the fish and the upstream wake is imperative to energy extraction. We will demonstrate that while this interaction results in the deformation of the original

vortices and the formation of new vorticity, an idealized model can still be used to capture key information about the wake.

3.3 What does the fish sense within the wake of another fish?

Within the simulation, the fish is equipped with an idealized lateral line, which consists of a total of 400 sensors configured in a cosine arrangement along each side (figure 3-2). These sensors are assumed to be capable of measuring with zero error the pressure at their location, which is interpolated from the pressure field within the simulation.

Figure 3-2: Diagram of the sensor layout in the system (in the actual system there are 400 sensors; however, only a few are plotted here to illustrate the distribution).

Within the reverse Kármán street shed by the upstream fish, the downstream fish encounters a row of oncoming vortices of alternating sign. To begin with, we simulate a "ghost" fish - that is, a fish which can sense its environment but does not interact with it. The pressure sensed by the ghost fish within a reverse Kármán vortex street is shown in figure 3-3 for a single timestep.

As can be seen, the signal consists of a pressure dip corresponding exactly with the location of each vortex. The dips are regularly spaced in the midsection of the body, as the position of the vortices is not altered by the presence of the fish. To track each vortex, the fish would only need to follow each low pressure dip. Near the head and the tail, nearby vortices cause a pressure dip on both sides. A pressure rise is never observed.

In contrast, the pressure sensed by a solid fish interacting with the upstream wake

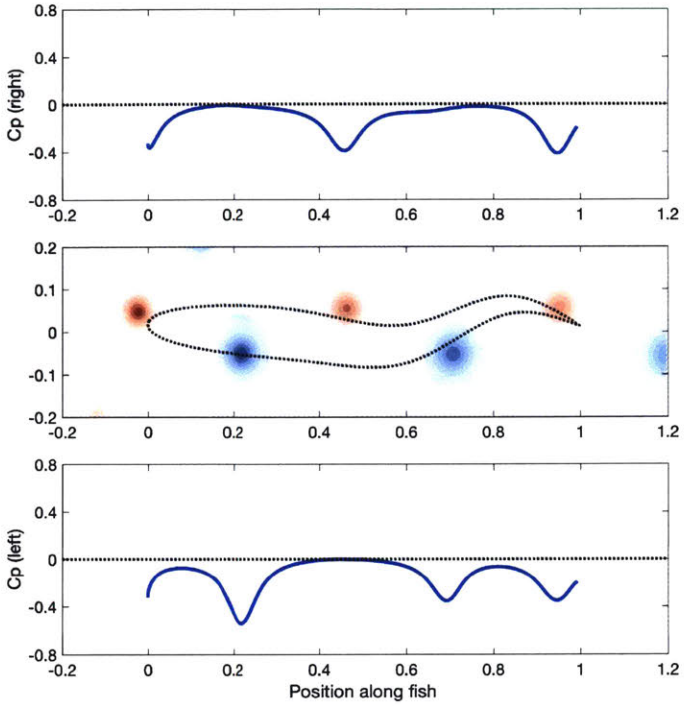

Figure 3-3: Signal sensed by a ghost fish within a reverse Kármán vortex street. Top: right lateral line signal, bottom: left lateral line signal, middle: vorticity field within wake, with outline of ghost fish.

is significantly more complex (figure 3-4). The motion of the fish causes a change in pressure along the entire body; this pressure change is of a much longer lengthscale than the pressure changes caused by near-body vortices. At the head, oncoming vortices cause a pressure rise on one side and drop on the other. As the vortices reach the fish, they are accelerated around the nose and pushed outward. Due to the interaction, an induced vortex is formed at the nose of the fish, and the dominant signal along the body corresponds with the position of this secondary vortex.

At the tail, the pressure dips created by the vortices and the pressure created by the fish motion are on the same lengthscale and therefore become difficult to differentiate.

By following the low pressure peaks, the fish can identify the induced vortex along its body, but there is not a clear way to identify where any of the other vortices are. In fact, past the nose, the original vortices from the upstream wake appear to become largely unobservable, as their presence is first masked by the induced vortices, and

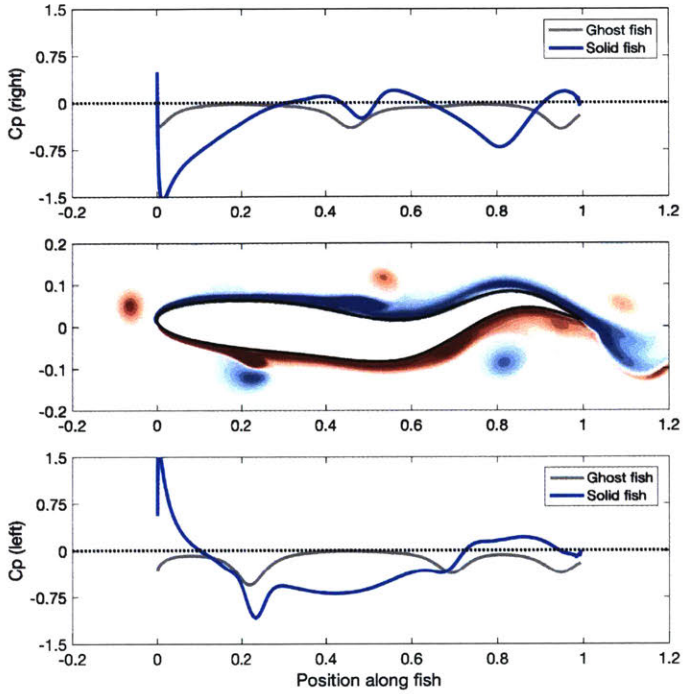

Figure 3-4: Signal that would be sensed by a solid undulating fish within a reverse Kármán vortex street (blue line), compared with that sensed by a ghost fish (gray line). Top: right lateral line signal, bottom: left lateral line signal, middle: vorticity field within wake, with outline of ghost fish.

later by the motion of the tail.

Figure 3-5 summarizes the pressure signatures captured by a rigid ghost foil, a rigid solid foil, and a rigid undulating fish within a wake, as well as a rigid undulating fish in quiescent flow. It is evident that while independent vortices in a wake yield a very simple and characteristic signature in the absence of strong hydrodynamic interactions (figure 3-5a), the signature created by the interaction between the upstream wake and a solid body is far more complex (figures 3-5b and 3-5d).

Furthermore, while the signature captured by an undulating fish within a wake (figure 3-5d) is similar to that captured by a rigid foil within a wake (figure 3-5b), there are significant differences introduced by the motion of the fish. The pressure created by these motions (figure 3-5c) can also be seen in the total signature, but the total signature is not merely a linear superposition of the signatures created by the fish motion and the external wake.

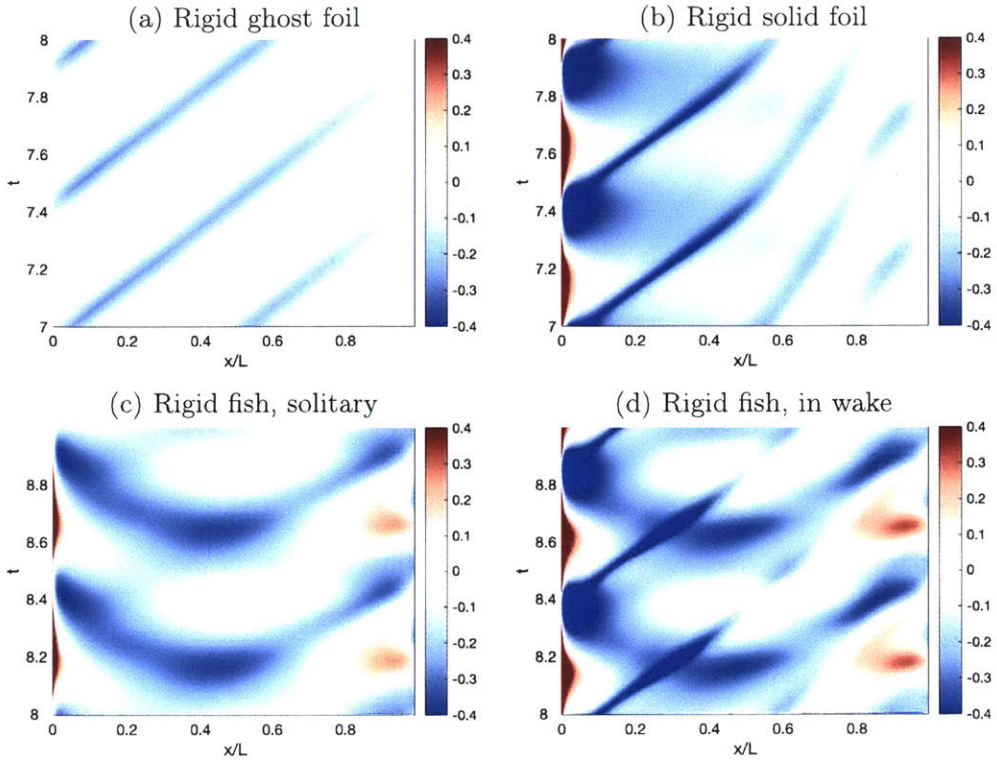

Figure 3-5: Spatiotemporal plots for the pressure signature sensed by a (a) rigid ghost foil in the wake of an upstream fish, (b) rigid solid foil in the wake of an upstream fish, (c) rigid undulating fish in quiescent flow, and (d) rigid undulating fish in the wake of an upstream fish.

Although the signature captured by a rigid fish strongly interacting with the upstream wake is complex, it is also far more rich in information. In section 3.5.1, we will demonstrate that this interaction definitely yields more information about the upstream wake. A fish which is interacting with the upstream wake can capture more information about the flow than a ghost fish, which does not.

Now that we have an idea of what the fish senses, what information is critical for control? We have established that timing along the entire body of the fish is important, and at any point in time, vortices are present along the entire body of the fish (figure 3-6).

Specifically, at the head, it is important for the fish to sense the sign and position of approaching vortices. These vortices will be referred to as the original vortices or

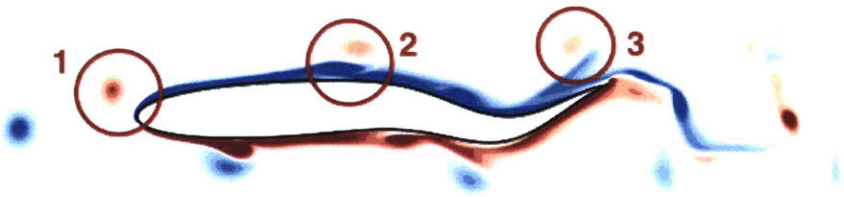

Figure 3-6: Vortices and vortex pairs along the body of the fish swimming in tandem with another fish. The vortices which are important to sense are (1) oncoming vortex from upstream wake, (2) vortex pair consisting of the original vortex and a secondary vortex induced from the interaction, and (3) the original vortex from the upstream wake, as it reaches the tail.

the upstream wake vortices throughout the chapter. Along the body, the fish must sense the strength and position of a vortex pair which consists of the original vortex as well as a vortex created from the interaction. The vortex created from the interaction will be referred to as the induced vortex throughout this chapter. At the tail, the induced vortex has largely dissipated and fallen back, but it is still important to sense the original vortex from the upstream wake.

Is this information encoded within the lateral line signal? And if so, how can it be extracted?

3.4 Modeling near-body hydrodynamics

Unsteady fluid systems are intrinsically distributed, chaotic, and noisy. Detailed computational fluid dynamics models capture these qualities, but their complexity makes them intractable for use in feedback control problems.

For example, the BDIM simulation provides a very accurate model of the system, with over 2,000,000 states (the velocity at every point within the fluid domain modeled). However, the relationship between the substantial number of states and the control action that should be taken is not intuitive. Instead, chapter 2 suggested that within this problem, control actions should be taken based on knowledge of the positions of nearby vortices. The fish also cannot directly measure the positions of nearby vortices, but it can measure the pressure along its lateral line. This signal

only captures a subset of the information within the field, so the question is: "can the fish identify near-field vortices precisely enough to make control decisions to extract energy from the upstream wake?"

In order to answer this question, we must first develop a *forward model* which can predict the pressure sensed by the fish due to the external flow. If this model performs well, it can then be used in an *inverse algorithm* to characterize the external flow using the pressure sensed by the fish.

In this section, both statistical models and physical models will be discussed. A model is developed from first principles which is capable of performing the forward problem of estimating the pressure sensed by the fish given the flow state (fish motion and swimming velocity, position and strength of vortices in the field). In section 3.6, this model will be incorporated into an estimation scheme to perform the inverse problem of estimating the unknown flow states (the near-field vortex strengths and positions).

3.4.1 Statistical models

Recent research has shown that many common flows can be characterized with a lower-order representation, for example through techniques such as dynamic mode decomposition or koopman mode analysis [129, 151, 69, 21]. These techniques have been implemented for real time flow estimation and control, for example to control vortex shedding over a cylinder [60, 14, 30].

However, the number of applications for which statistical modeling has been successfully demonstrated is extremely limited. Linear stochastic estimation (LSE), partial least-squares regression (PLSR) and principal orthogonal decomposition (POD) are linear methods. While they can occasionally be applied to nonlinear systems, they are generally only effective if one can devise a state parameterization in which the system is almost linear.

To investigate if a low-order model produced with statistical methods would work for this system, a model was developed using partial least-squares regression (PLSR) to capture the relationship between the motion of a fish (X) in quiescent flow and the

pressure captured with the lateral line (Y). For the model, a PLS regression of Y on X was calculated, using 5 PLS components, in order to estimate the pressure sensed by the fish.

While principal component analysis (PCA) decomposes a set of observations (Y) into orthogonal modes, PLSR decomposes a set of observations (Y) into orthogonal modes which are maximally correlated with an input data set (X). As a result, it is capable of finding fundamental relationships between the inputs (X) and outputs (Y); by retaining only the top PLS components, a low-order model can be generated in which the strongest relationships are retained.

For a fish swimming in quiescent flow, we hypothesized that the most relevant input was the displacement at each position along the fish. An input data set of the displacement over time was provided to the algorithm, as well as the observation data set, consisting of the pressure sensed over time. Using PLSR, a low-order model relating the lateral displacement of the fish to the pressure sensed (when swimming at constant velocity) was generated using the top 5 modes. On the training set, this model estimates the pressure reasonably well (compare figures 3-7a and 3-7b), with a mean error of 0.01 (1.7% of the maximum pressure) and a maximum error of 0.058 (10% of the maximum pressure).

However, when the model is used to estimate the pressure sensed by a fish swimming with a different motion (f=2.4 instead of f=1.8), it is no longer able to predict the pressure well (compare figures 3-7c and 3-7d). While the reconstructed pressure appears to capture the frequency and general characteristics of the true pressure signature, the magnitude is completely off. There is a mean error of 0.1 (17.3% of the maximum pressure) and maximum error of 0.325 (56.1% of the maximum pressure).

Similar results are obtained when the model is trained using the fish displacement and velocity as the input data set. This demonstrates that the relationship between the fish displacement and the pressure sensed is not close to linear, and therefore cannot be captured using a linear statistical model. Although the model performs relatively well under conditions that are close to those in the training set, it cannot capture the relationship well when the motion of the fish deviates from the training

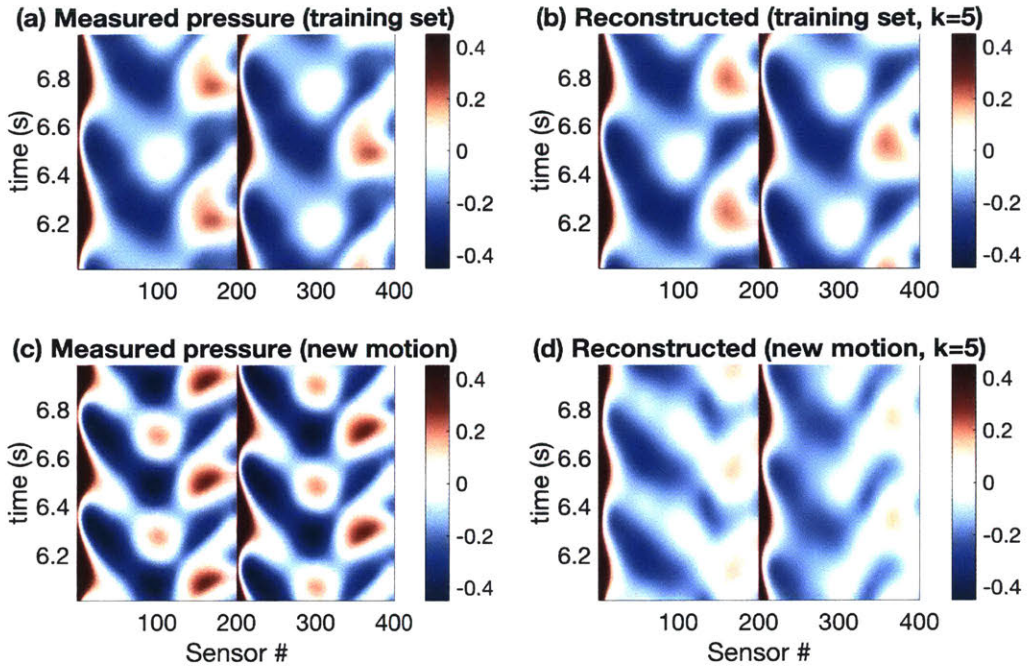

Figure 3-7: The pressure estimated by a PLSR model trained on the displacement and pressure measured by a fish swimming at f=1.8. (a) pressure observed - training data. (b) pressure reconstructed using the top 5 modes of the PLSR model, and the displacement from the training data. (c) actual pressure observed for a fish swimming at f=2.4. (d) reconstructed pressure using the model trained from the fish at f=1.8, and displacement data for the fish at f=2.4.

parameters (e.g, under sudden accelerations, changes in swimming speed, changes in swimming frequency, or the presence of disturbances). Although it may be possible to find a set of nonlinear combinations of swimming parameters, displacements, and velocities that can be used to build a more accurate model, it would require a considerable amount of time.

Furthermore, PCA, PLSR, and koopman mode analysis were investigated as techniques for decoupling the self-induced pressure from the vortex-induced pressure captured by a fish swimming through a wake. The self-induced pressure signal and the vortex-induced pressure signal were of significantly different lengthscales; as a result, it may be possible to decouple them using an input data set that captures the self-motion. In reconstructing the signal, the dominant modes would constitute the self-induced signal, while the residual would then contain information about the flow disturbances (i.e., the vortices).

The result achieved using PLSR with the top two modes is shown in figure 3-8.

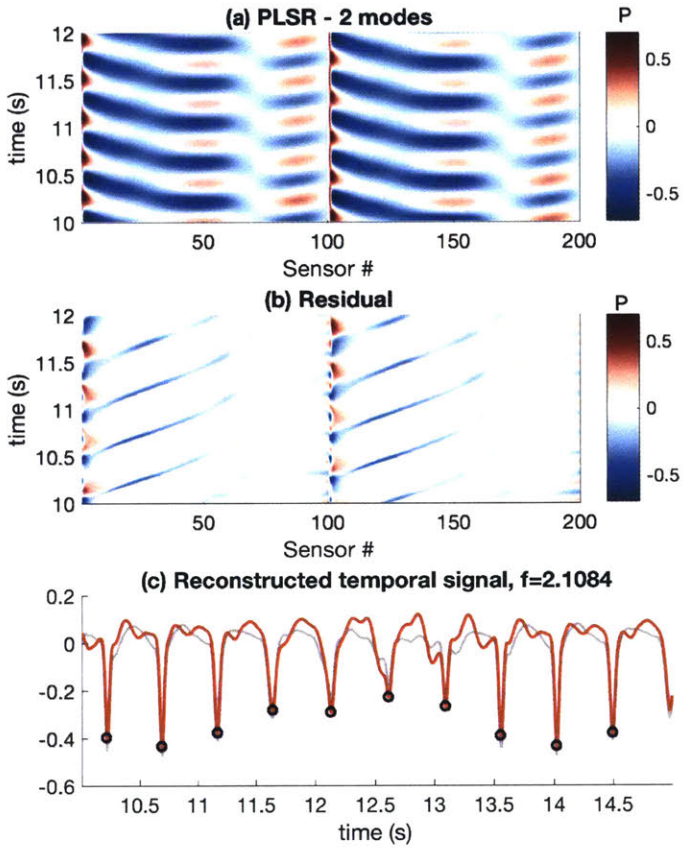

Figure 3-8: PLSR can be used to decouple a spatiotemporal pressure signal into (a) a component strongly correlated with the motion of the fish, and (b) the residual. The residual captures the pressure dips produced by near-field vortices well, which are on a different lengthscale than the pressure changes caused by the undulating motion. (c) The pressure reconstructed from the residudal matches the pressure measured by a single sensor near the head ($P_{in\ wake} - P_{solitary}$) well.

Indeed, the top two modes appear to capture the portion of the pressure signal which results from the fish motion (figure 3-8a), while the narrower low pressure bands resulting from the interaction with the near-field vortices is captured by the residual (figure 3-8b). For a sensor near the head, the temporal signal reconstructed using the residual matches quite well with the estimated vortex-induced signal (figure 3-8c), and in fact estimates the frequency of the wake with high accuracy. The estimated vortex-induced signal is calculated as the difference between the pressure measured by the fish within the wake and the pressure measured by the same fish in quiescent

flow.

However, while this algorithm works well for isolating the strong low pressure dips downstream of the nose and along the body of the fish, it fails when the vortex-induced signal is close to the lengthscale of the pressure changes caused by the fish motion. Therefore, for vortices upstream of the fish (where they cause a large-scale pressure rise on one side of the nose and pressure dip on the other), and for vortices near the tail (where the pressure changes caused by vortices are on the same lengthscale as those caused by the fish undulation), the model fails to decouple the signals.

In summary, statistical methods are capable of capturing the relationship between the motion of the fish and the pressure sensed as long as the swimming parameters remain very close to the parameters of the training set. However, in the presence of accelerations, disturbances, or changes in swimming parameters, the model breaks down due to the nonlinear relationship between these parameters and the pressure in the flow. The pressure arises in part from the requirement that no water may penetrate the surface of the fish; this requirement is affected by the external flow, the instantaneous shape of the fish, and the motion of the fish. The pressure at a single point on the fish cannot be captured by the fish kinematics at the same point, but is a nonlinear combination of many factors.

Furthermore, PLSR can be used as a technique to decouple signals on different lengthscales. For example, along the body of a fish within a wake, PLSR can decouple the self-induced pressure signal from the vortex-induced pressure signal relatively well. The estimated vortex-induced signal can be used to estimate parameters about the wake, such as the frequency. However, in the head and tail regions, where the vortex-induced signal is on the same lengthscale as the self-induced signal, the algorithm fails.

Clearly, the nonlinear relationship between the flow state and the pressure sensed by the fish is important to model correctly. In fact, the motion of the fish itself contributes to the nonlinearity; under active control, adjustments to the undulatory motion would create transient flow changes that would be completely unmodeled. A model which is trained on a steady, periodic swimming motion would fail to capture

the flow state and pressure changes that would arise from perturbations, kinematic changes, or control actions. As a result, for accurate modeling and stable control, it is critical to develop a model not from statistical or empirical methods, but fom first principles. In the following section, we will show how the nonlinear relationship between the motion of a fish, disturbances in the flow, and the pressure sensed can be captured by a physics-based model.

3.4.2 Potential flow and boundary element method

Potential flow modeling is a very old technique that models physics using harmonic functions, thereby reducing apparently complex systems to a lower order space. For example, simple flows such as the flow around a plate, a corner flow, and a vortex in uniform flow by a wall can all be represented with 3-4 states. Since potential flow modeling captures the physics of a system through first principles, it has the potential to perform better than statistical modeling.

To model the flow around a deforming body, a boundary element method (also known as a panel method) can be used. As the name implies, the deforming body is divided into a number of discretized *panels*, and each is represented as an infinitesimally thin sheet of sources, doublets, vortices, or a combination.

a. Basics of Potential Flow

In hydrodynamics, potential flow describes the velocity as the gradient of a velocity potential:

$$\mathbf{u} = \nabla\Phi \tag{3.1}$$

This is the basic equation for all potential flow, asserting both the irrotationality of the flow and its linearity. Continuity in the case of constant density provides:

$$\nabla \cdot \mathbf{u} = 0 \tag{3.2}$$

$$\nabla^2\Phi = 0 \tag{3.3}$$

This is the Laplace equation which governs flow in the fluid domain. It is a second order elliptic PDE, and all of its solutions are harmonic functions.

Two common functions which are solutions to Laplace's equation are the point source and the doublet. The point source is described by the velocity potential:

$$\Phi(\mathbf{x}) = -\frac{\sigma}{4\pi}\frac{1}{r} \tag{3.4}$$

Where σ is the source strength, and $\mathbf{x}$ represents an arbitrary point where we are evaluating the potential. A doublet is the combination of a point source and a point sink placed a small distance ϵ apart, and is described by the velocity potential:

$$\Phi(\mathbf{x}) = -\frac{\mu}{4\pi}\left(\mathbf{n}\cdot\frac{\mathbf{r}}{r^3}\right) \tag{3.5}$$

Where μ is the doublet strength, and $\mathbf{n}$ is the normal vector along the axis of the doublet.

A simple potential flow can be created by superimposing a uniform stream and a doublet. This results in a sphere, with radius defined by the strength of the doublet. Increasingly complex potential flows can be created by the addition of more sources and/or doublets.

b. Integral Representation

In order to begin moving from our full volume representation to a surface representation, let us consider two harmonic functions Φ_1 and Φ_2, which both satisfy Laplace's equation:

$$\nabla^2\Phi_1 = 0 \tag{3.6}$$

$$\nabla^2\Phi_2 = 0 \tag{3.7}$$

Then using Green's identity, we can write:

$$\int_S (\Phi_1 \nabla \Phi_2 - \Phi_2 \nabla \Phi_1) \cdot \mathbf{n} dS = \int_V (\Phi_1 \nabla^2 \Phi_2 - \Phi_2 \nabla^2 \Phi_1) dV \tag{3.8}$$

Note that the right hand side of this equation evaluates to zero, leaving us with a surface integral. To evaluate this, let us define the surface as a sum of the surface of a body, its wake, and a surface at infinity:

$$S = S_B + S_W + S_\infty \tag{3.9}$$

And consider the case where:

$$\Phi_1 = \frac{1}{r} \text{ and } \Phi_2 = \Phi$$

Where Φ is the potential of the flow of interest in the fluid volume, and $1/r$ is the potential of a point source (without the constant). In other words, $1/r$ is the Green's function for a source distribution. Then we can rewrite:

$$\int_S \left(\frac{1}{r} \nabla \Phi - \Phi \nabla \frac{1}{r} \right) \cdot \mathbf{n} dS = 0 \tag{3.10}$$

If we consider the case where our point of interest, P, is inside the fluid volume V, we must exclude it from the region of integration, putting a small sphere around it. Letting the vector $\mathbf{n}$ point out of the fluid volume and thus into the small sphere, integration over S and the small sphere yields:

$$-\int_{\text{sphere}} \left(\frac{1}{r} \frac{\partial \Phi}{\partial r} + \frac{\Phi}{r^2} \right) dS + \int_S \left(\frac{1}{r} \nabla \Phi - \Phi \nabla \frac{1}{r} \right) \cdot \mathbf{n} dS = 0 \tag{3.11}$$

For the first term, if we assume that Φ is well behaved and therefore does not vary greatly over the small sphere containing our point of interest, the first term in the

integral vanishes, and integration of the second term yields:

$$-\int_{\text{sphere}} \left(\frac{\Phi}{r^2}\right) dS = -\left(\frac{\Phi}{\epsilon^2}\right)(4\pi\epsilon^2) = -4\pi\Phi(\mathbf{x}) \tag{3.12}$$

Then equation 3.11 can be rewritten:

$$\Phi(\mathbf{x}) = \frac{1}{4\pi}\int_S \left(\frac{1}{r}\nabla\Phi - \Phi\nabla\frac{1}{r}\right)\cdot \mathbf{n}dS \tag{3.13}$$

Which gives the value of the potential $\Phi(\mathbf{x})$ at any point within the fluid volume. If the point P lies on the surface of the body, then we only need to create a half sphere around the point, so the equation would be:

$$\Phi(\mathbf{x}) = \frac{1}{2\pi}\int_S \left(\frac{1}{r}\nabla\Phi - \Phi\nabla\frac{1}{r}\right)\cdot \mathbf{n}dS \tag{3.14}$$

Inside the body, no additional sphere would need to be created, so the equation would be rewritten:

$$0 = \frac{1}{4\pi}\int_S \left(\frac{1}{r}\nabla\Phi - \Phi\nabla\frac{1}{r}\right)\cdot \mathbf{n}dS \tag{3.15}$$

Generally, we will be considering the potential within the fluid volume, governed by equation 3.13. Before, we stated that the surface S over which we are integrating is composed of three parts - the body, the wake, and a surface at infinity. Equation 3.13 is a way of describing the potential at a point as an integral of harmonic solutions to Laplace's equations which are distributed over a surface S. Where the surface is composed of these three parts, we can rewrite:

$$\Phi(\mathbf{x}) = \frac{1}{4\pi}\int_{S_B} \left(\frac{1}{r}\nabla\Phi - \Phi\nabla\frac{1}{r}\right)\cdot \mathbf{n}dS + \frac{1}{4\pi}\int_{S_W} \left(\frac{1}{r}\nabla\Phi - \Phi\nabla\frac{1}{r}\right)\cdot \mathbf{n}dS + \Phi_\infty \tag{3.16}$$

However, assuming the wake is very thin and cannot support fluid dynamic loads, the potential must be continuous across it, so the gradient of Φ in the normal direction must be zero. Thus the first term in the wake integral reduces to zero. Finally,

recognizing that a doublet represents a jump in velocity potential:

$$\mu = \Phi - \Phi_i \tag{3.17}$$

While a source represents a jump in velocity:

$$\sigma = \frac{\partial \Phi}{\partial n} - \frac{\partial \Phi_i}{\partial n} \tag{3.18}$$

We can rewrite the equation in the form:

$$\begin{aligned} \Phi(\mathbf{x}) = \; - \; & \frac{1}{4\pi} \int_{S_B} \left[\sigma \left(\frac{1}{r} \right) - \mu \frac{\partial}{\partial n} \left(\frac{1}{r} \right) \right] dS + \\ & \frac{1}{4\pi} \int_{S_W} \left[\mu \frac{\partial}{\partial n} \left(\frac{1}{r} \right) \right] dS + \Phi_\infty(\mathbf{x}) \end{aligned} \tag{3.19}$$

This is the final integral equation which governs the potential at any point $\mathbf{x}$ within a fluid volume, where the flow is defined by some distribution of sources (or single layer potentials) of strength $\sigma(\mathbf{x}')$ and doublets (or double layer potentials) of strength $\mu(\mathbf{x}')$ over a surface. The last term is a constant, and generally represents some freestream potential. That is:

$$\Phi_\infty(\mathbf{x}) = U_\infty x + V_\infty y \tag{3.20}$$

If there is no wake, the second integral in equation 3.19 can be ignored. In the first integral, the existence of both the source term and the doublet term indicates that the solution is not unique, since there are two sets of unknowns and only one equation to define them. A unique solution can be formulated if either of the terms is set equal to zero. Otherwise, there exists an infinite set of functions μ and σ that define the same $\Phi(\mathbf{x})$, and the user must specify additional conditions in order to solve for the source and doublet densities.

c. Boundary Value Problem

To solve, the no flux boundary condition is applied on the surface of the body. This condition results in a Neumann formulation, mathematically written:

$$\begin{aligned} \mathbf{v}_n &= \frac{\partial \Phi}{\partial n} = -\frac{1}{4\pi}\int_{S_B} \sigma \nabla\left(\frac{1}{r}\right)\cdot \mathbf{n} dS \\ &+ \frac{1}{4\pi}\int_{S_B+S_W} \mu \nabla\left[\frac{\partial}{\partial n}\left(\frac{1}{r}\right)\right]\cdot \mathbf{n} dS + \frac{\partial \Phi_\infty}{\partial n} \end{aligned} \tag{3.21}$$

Physically, this just states that the normal velocity on the surface of the body must be equal to the dot product of the body's velocity and the normal vector at any point on the surface.

By enforcing this condition, we can set up a matrix equation to solve for the source and/or doublet strengths at each point on the body. These strengths can then be substituted into the dirichlet formulation to solve for the velocity potential anywhere in the fluid volume.

d. Discretized Formulation

To evaluate the boundary value problem, the body is divided up into discrete panels and the integrals in equation 3.21 are evaluated on each panel.

The panels can be constructed with sources, vortices, and/or doublets. When lift must be modeled, doublet or vortex panels must be included in the formulation, because sources alone are incapable of modeling lifting flows. For this system, we begin by creating a model using only source panels, and subsequently we will demonstrate the effect of adding vortex panels for lift over the body and the development of a wake.

For a 2D source formulation, the potential at a point due to the body S_B is:

$$\Phi(\mathbf{x}) = \int_{S_B} \log||\mathbf{x}-\mathbf{x}'||\sigma(\mathbf{x}')d\S' \tag{3.22}$$

To solve for the sources strengths over the body, we derive the Neumann formu-

lation from equation 3.22, which allows us to explicitly satisfy the no-flux condition:

$$\frac{\partial \Phi(\mathbf{x})}{\partial n_{\mathbf{x}}} = -\pi\sigma(\mathbf{x}') - \int_{S_B}^{PV} \frac{(\mathbf{x}-\mathbf{x}')^T \mathbf{n}_{\mathbf{x}}}{||\mathbf{x}-\mathbf{x}'||^2}\sigma(\mathbf{x}')dS' \tag{3.23}$$

In the above, PV represents the Cauchy principal value of the integral. Although these integrals look formidable, there are well known methods for integrating singularities over panels [77], which allows for the reduction of this problem into matrix equation:

$$\mathbf{v}_n = \mathbf{A}\sigma \tag{3.24}$$

$\mathbf{A}$ is an *influence coefficient matrix* which is obtained from evaluating the integral in equation 3.23. The normal velocity $\mathbf{v}_n$ is obtained by summing the velocity contributions from all external sources. By solving equation 3.24, we can obtain the unknown source strengths σ over the body of the fish. In the event that there are multiple bodies, or multiple unknowns (e.g., wake panel strengths) which all contribute to the velocity incident on the body, equation 3.24 is augmented so that all the unknowns may be solved for simultaneously.

Similar matrix equations can be set up using equation 3.22 and its derivatives in order to solve for the velocity potential and velocity at the control points on the body.

$$\phi = \mathbf{P}\sigma \tag{3.25}$$

$$\mathbf{v}_{tx} = \mathbf{T}_{\mathbf{x}}\sigma \tag{3.26}$$

$$\mathbf{v}_{ty} = \mathbf{T}_{\mathbf{y}}\sigma \tag{3.27}$$

Model components

To model a fish within a wake, the total potential is given by a sum of the individual potentials:

$$\Phi(\mathbf{x},t) = \phi_{\text{ext}}(\mathbf{x},t) + \phi_d(\mathbf{x},t) + \phi_{\text{vort}}(\mathbf{x},t) \tag{3.28}$$

$\phi_{\text{ext}}(\mathbf{x}, t)$ is the external flow potential, and equal to $U_\infty x$ when the fish swims at constant velocity $U_s = -U_\infty$. $\phi_d(\mathbf{x}, t)$ is the disturbance potential of the fish; this potential represents the self-induced effect on the flow, and may include a wake panel if a wake is included within the model. $\phi_{\text{vort}}(\mathbf{x}, t)$ is the potential contributed by the vortices in the system, including the vortices from the upstream wake, the vortices induced from the interaction with the upstream wake, and wake vortices shed by the fish. Each velocity potential is a solution to Laplace's equation; therefore, they can be linearly superimposed to yield the total velocity potential Φ.

Similarly, the velocity field can be calculated as a sum of the contributing parts:

$$\mathbf{v}(\mathbf{x}, t) = \frac{\partial \Phi(\mathbf{x}, t)}{\partial \mathbf{x}} = \frac{\partial \phi_{\text{ext}}(\mathbf{x}, t)}{\partial \mathbf{x}} + \frac{\partial \phi_d(\mathbf{x}, t)}{\partial \mathbf{x}} + \frac{\partial \phi_{\text{vort}}(\mathbf{x}, t)}{\partial \mathbf{x}} \tag{3.29}$$

In the forward problem (estimating the pressure sensed by the fish as a result of the external flow), all potentials except for $\phi_d(\mathbf{x}, t)$ are known, and the disturbance potential of the fish must be calculated through the methodology above (satisfying the no-flux condition on the fish).

The potential contributed by the vortices in the system can be written:

$$\phi_{\text{vort}}(x, y, t) = \sum_{k=1}^{\text{nvort}} \frac{\gamma_k}{2\pi} \arctan\left(\frac{y - y_k}{x - x_k}\right) \tag{3.30}$$

Note that due to the arctan function, this formula requires careful treatment if any derivatives are taken numerically. The arctan function contains a discontinuity around $\theta = 0 \pmod{2\pi}$. Due to the unsteadiness in the problem, vortices may occasionally "jump" from one side of the line to the other, which yields a nonphysical $\partial \phi_{vort}/\partial t$, if taken numerically. Similarly, if velocities along the body are calculated by numerically taking $\partial \phi_{vort}/\partial \Gamma$, problems may be encountered if the vortex lies on one side of the discontinuity for one panel and the other side for the next panel. As a result, within this formulation, $\partial \phi_{vort}/\partial t$, and tangential velocities are calculated analytically whenever possible.

The time and spatial derivatives of ϕ_{vort} are:

$$\frac{\partial \phi_{\text{vort}}(x,y,t)}{\partial t} = \sum_{k=1}^{\text{nvort}} \left(\frac{\dot{\gamma_k}}{2\pi} \arctan\left(\frac{y-y_k}{x-x_k}\right) \right. \tag{3.31}$$

$$+ \frac{\gamma_k \dot{x_k}}{2\pi} \left(\frac{y-y_k}{(x-x_k)^2+(y-y_k)^2} \right) \tag{3.32}$$

$$\left. - \frac{\gamma_k \dot{y_k}}{2\pi} \left(\frac{x-x_k}{(x-x_k)^2+(y-y_k)^2} \right) \right) \tag{3.33}$$

$$\frac{\partial \phi_{\text{vort}}(x,y,t)}{\partial x} = -\sum_{k=1}^{\text{nvort}} \frac{\gamma_k (y-y_k)}{2\pi((x-x_k)^2+(y-y_k)^2)} \tag{3.34}$$

$$\frac{\partial \phi_{\text{vort}}(x,y,t)}{\partial y} = \sum_{k=1}^{\text{nvort}} \frac{\gamma_k (x-x_k)}{2\pi((x-x_k)^2+(y-y_k)^2)} \tag{3.35}$$

$$\tag{3.36}$$

The vortices decay slowly over time; as a result, $\dot{\gamma_k}$ is small and typically negligible. For the inverse problem (estimation), we set $\dot{\gamma_k} = 0$ to reduce the uncertainty in the problem.

The velocity of the vortices, $\dot{x_k}$ and $\dot{y_k}$, are not negligible. However, they do not represent additional states to estimate because they are prescribed by the flow. Free vortices move with the flow; therefore, once the velocity field in the flow is known, $\dot{x_k}$ and $\dot{y_k}$ can be calculated for $\partial \phi_{vort}/\partial t$ and to convect the vortex to the next position within the state transition model (for the estimator).

Point vortices are associated with a singularity at their center; this results in an infinite velocity when $(x, y) = (x_k, y_k)$. While point vortices are extremely good models for real vortices and predict the flow distribution accurately beyond a minimum distance, they become less accurate as the point of interest moves closer to the vortex core. As a result, as the vortex approaches the fish, this results in an increasingly "spiky" signal, which is not realistic. For real vortices, the flow near the core resembles a rigid body rotation. There are several ways to model this, including the Kaufmann vortex model [78], the Lamb-Oseen vortex model [115], and vortex blobs [12]. In the current project, we explored using both point vortices and vortex blobs to accurately reproduce the flow distribution created by vortices in the system. For the vortex

blob models, the velocity potential and its derivatives are multiplied by a kernel to eliminate the singularity at the core:

$$\kappa = 1 - 2\exp\left(\frac{-d(x,y)^2}{\delta^2}\right) + \exp\left(\frac{-d(x,y)^2}{2\delta^2}\right) \tag{3.37}$$

$$d(x,y) = \left((x-x_k)^2 + (y-y_k)^2\right)^{1/2} \tag{3.38}$$

However, through testing, in most cases we found no discernable improvement in using a vortex blob model over a point vortex model.

Pressure calculation

Once the evaluation of the boundary value problem is complete, the pressure anywhere in the fluid volume can be calculated using Bernoulli's unsteady pressure law:

$$P(\mathbf{x}) = -\rho\left(\frac{\partial\Phi(\mathbf{x})}{\partial t} + \frac{1}{2}|\nabla\Phi(\mathbf{x})|^2\right) \tag{3.39}$$

$$= -\rho\left(\frac{D\Phi(\mathbf{x})}{Dt} - \mathbf{v}(\mathbf{x})\cdot\nabla\Phi(\mathbf{x}) + \frac{1}{2}|\nabla\Phi(\mathbf{x})|^2\right) \tag{3.40}$$

For dynamic simulations involving multiple bodies moving over time, the matrix problem must be reformulated at each timestep, with care taken in defining the new body velocity $\mathbf{v}$. In Bernoulli's unsteady pressure law, if we are calculating the pressure on a moving body, we must take care to evaluate the material derivative of the potential instead of the normal derivative, resulting in the slight change to the usual form of Bernoulli's law.

The velocity $\nabla\Phi(\mathbf{x})$ is straightforward and defined in equation 3.29. The velocity contribution of the body is calculated using equations 3.24 and 3.25. $\partial\phi_{vort}/\partial t$ is calculated analytically using equation 3.31. $D\phi_d/Dt$, however, must be taken numerically.

On the surface of the fish, the pressure is approximately the same as the pressure just outside of the boundary layer, as pressure across a thin boundary layer is

essentially constant [172]. Therefore, this potential flow model, although only applicable where vicous effects are small, is valid for estimating the pressure that would be sensed by the lateral line on the surface of the fish.

3.4.3 Validation: source panel formulation

To test the accuracy of the source panel method developed above, a validation was run to compare the pressure estimated by the panel method against the pressure measured in the simulation, along the lateral line of the fish. Subsequently, the strengths and positions of all near-field vortices were estimated for a single simulation, and the pressure estimated using the panel method was again compared with the pressure measured in the simulation.

Figure 3-9 shows a comparison between the estimated (panel method) and actual (BDIM) pressure signals. It can be seen that the accuracy is high in the front half of the fish, and the error grows toward the back. This is expected - near the front of the fish the pressure gradient is very favorable and viscous effects are negligible. However, near the back, the boundary layer thickens and viscous effects become more prominent. Near the trailing edge, the lack of a proper wake model causes a substantial increase in error. However, for vortex sensing and control, sensing in this area is not as important.

3.4.4 Kutta condition and wake modeling

To test if the pressure estimate can be improved with the addition of a wake model, two additional models were developed. The first consists of doublet panels with a velocity Kutta condition, and the second uses panels constructed with a constant distribution of sources and vortices, and a pressure Kutta condition.

Vorticity cannot be physically generated in a potential flow; however, it is well known that vorticity develops in flows with lifting surfaces. The Kutta condition bridges this gap by mimicking the viscous effect of separation in inviscid simulations. However, despite the wide acceptance of this treatment of lifting surfaces in inviscid

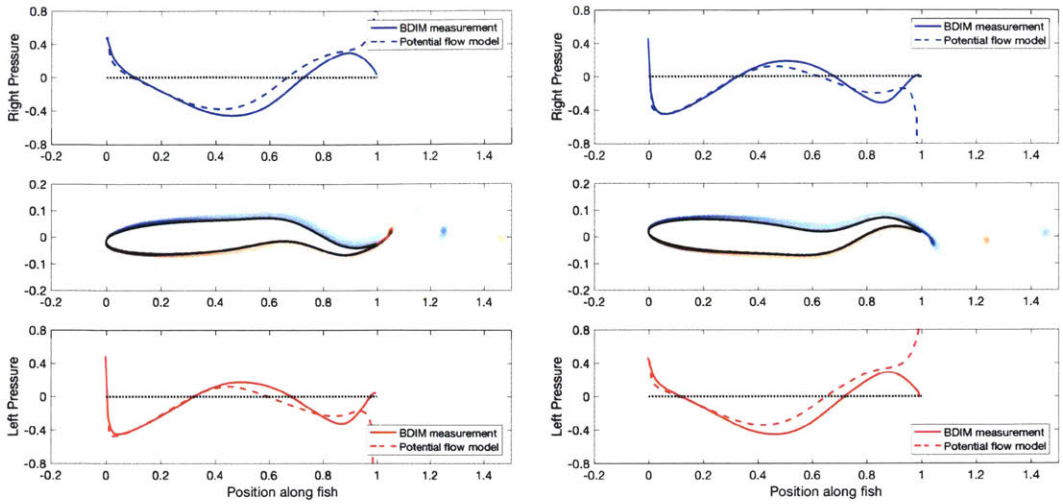

Figure 3-9: For two timesteps, a comparison between the pressure estimated with the source panel method model (dashed line) and the pressure measured within the BDIM simulation (solid line), for the left and right sides of the fish. The middle plot shows a snaphot of the vorticity field from the BDIM simulation. The two signals match very well in the front of the fish, and the error near the back is greater.

flows, the viscous origin of the lift is actually poorly understood. There remains a fair amount of controversy over the "correct" way to implement the Kutta condition. It has been defined in various ways throughout the literature: "fixing the rear stagnation point at the trailing edge", "avoiding infinite velocities at the trailing edge", and "establishing pressure continuity at the trailing edge" [103]. In steady flows, these definitions collapse to the same result, but in unsteady flows, they typically cannot be satisfied simultaneously.

Pressure continuity has been implemented in some studies [152, 82, 19], and velocity continuity has been implemented in the majority of studies [116, 9, 180]. The prevalence of the velocity Kutta condition is likely due to the fact that while enforcing a velocity condition is linear, enforcing a pressure condition is not and therefore must be solved through an iterative scheme. It remains unclear if a jump in pressure at the trailing edge is physical [133, 19].

As a result, we developed both a model with a velocity Kutta condition and a model with a pressure Kutta condition. Implementations of the models with the two different Kutta conditions are illustrated in figure 3-10.

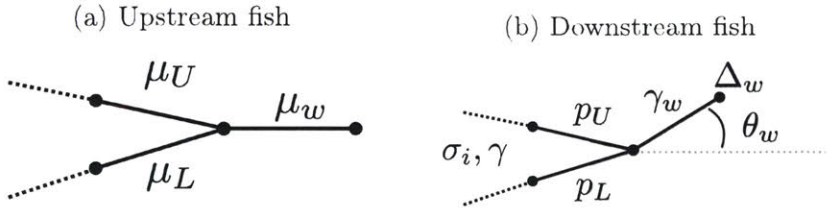

Figure 3-10: Illustration of one implementation for the (a) velocity Kutta condition and (b) pressure Kutta condition. The velocity Kutta condition can be satisfied by enforcing the shedding of a wake panel $\mu_w = \mu_U - \mu_L$ at each timestep. The pressure Kutta condition requires that there is no pressure difference across the trailing edge and the wake. A wake panel of strength γ_w, length Δ_w and angle θ_w is shed at each timestep.

A doublet panel method was used with the velocity Kutta condition. While there are other ways to implement a panel method with a velocity Kutta condition, the implementation is particularly straightforward with a doublet panel method. Doublet panels consist of a vortex on one end and a counterrotating vortex on the other, so by shedding a wake panel of strength:

$$\mu_w(t) = \mu_U(t) - \mu_L(t) \tag{3.41}$$

at each timestep, the vortex at the trailing edge has strength:

$$\gamma T.E. = 0 \tag{3.42}$$

Setting the trailing edge vorticity equal to zero is equivalent to prescribing that the velocity around the trailing edge is finite; this ensures that the flow leaves the trailing edge smoothly, which also satisfies:

$$\phi_U - \phi_L = \Delta\phi_w \tag{3.43}$$

$$|\vec{u}_U| = |\vec{U}_L| \tag{3.44}$$

For the pressure Kutta condition, a panel method using a distribution of source

and vortex elements was developed, largely based on the method described by Teng [152]. Each panel consists of a varying source strength, as well as a vortex strength that is constant over the whole body, such that there are $N + 1$ unknowns for a method with N panels. A wake panel of strength γ_w sheds at each timestep, with length Δ_w and at angle θ_w, yielding 3 additional unknowns. To solve, the no-flux boundary condition is set at each of the N control points, and the pressure on either side of the trailing edge must be equal:

$$\frac{1}{2}|\vec{u}_U|^2 + \frac{\partial \phi_U}{\partial t} = \frac{1}{2}|\vec{u}_L|^2 + \frac{\partial \phi_L}{\partial t} \tag{3.45}$$

The wake panel angle and length are calculated with its midpoint velocity:

$$\tan\theta_w = \frac{v_w}{u_w} \tag{3.46}$$

$$\Delta_w = \Delta t\sqrt{u_w^2 + v_w^2} \tag{3.47}$$

Finally, to satisfy Kelvin's theorem (the circulation in the fluid must remain constant with time):

$$(\gamma_w)_k(\Delta_w)_k = -L(\gamma_k - \gamma_{k-1}) \tag{3.48}$$

Where k represents a timestep, L is the total length of the panels on the fish, and γ_k is the vortex strength of a single panel at time k.

Since the velocity at the midpoint of the wake panel cannot be known until γ_w, θ_w and Δ_w are calculated, and the wake panel parameters also depend on the velocity at the panel midpoint, these conditions must be satisfied through an iterative scheme.

Once implemented, both methods were first validated against results published by Tuncer and Platzer [160] for a heaving airfoil with motion profile:

$$y(t) = -0.1c\cos(3t) \tag{3.49}$$

and reduced frequency $k = \omega c/(2U_\infty) = 1.5$. Tuncer and Platzer [160] present results

computed with the potential flow solver UPOT, which is a source-vortex panel method with an unsteady pressure Kutta condition, as well as results from a Navier-stokes solver.

A comparison of the drag coefficient and lift coefficient found using each method is compared with the results from Tuncer and Platzer [160] in figures 3-11 and 3-12. The source-vortex panel method (SVPM) matches the potential flow results from Tuncer and Platzer [160] exactly (as is expected), and matches the magnitudes of the Navier-Stokes results well. the doublet panel method (DPM) underpredicts the thrust generated by the foil, and slightly overpredicts the lift magnitudes.

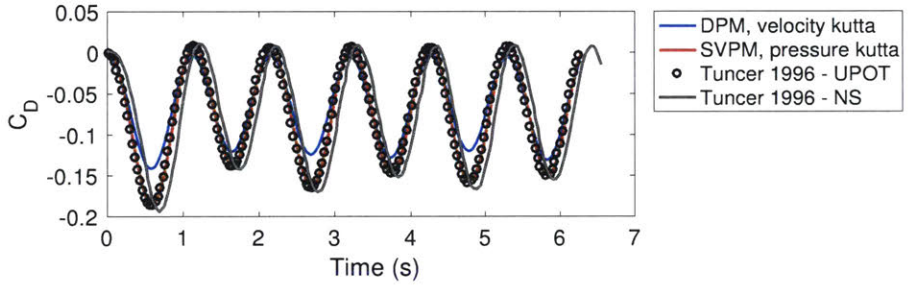

Figure 3-11: Validation of the drag coefficient computed using the presently developed doublet panel method (DPM) and source-vortex panel method (SVPM), against the potential flow (UPOT) and full Navier Stokes (NS) results from Tuncer and Platzer [160].

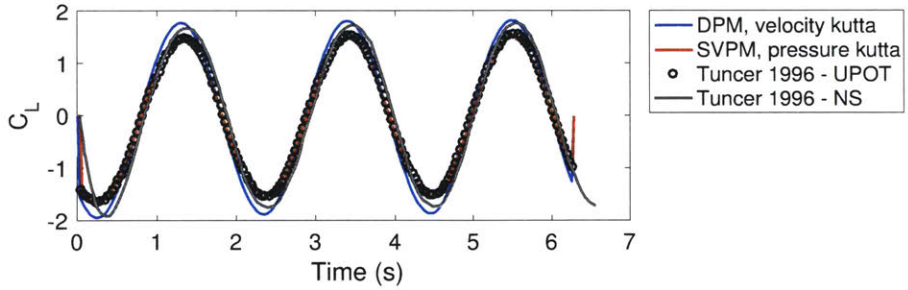

Figure 3-12: Validation of the lift coefficient computed using the presently developed doublet panel method (DPM) and source-vortex panel method (SVPM), against the potential flow (UPOT) and full Navier Stokes (NS) results from Tuncer and Platzer [160].

A comparison of the pressure at a single timestep - when the foil passes the mean position moving downward - is shown in figure 3-13. Again, the SVPM matches

the results from UPOT perfectly, and is a close match to the results from Tuncer's Navier-Stokes simulation. However, as expected, the DPM shows a pressure gap at the trailing edge, since it does not enforce pressure continuity across the trailing edge.

Overall, both methods appear to model the pressure and forces in this system reasonably well.

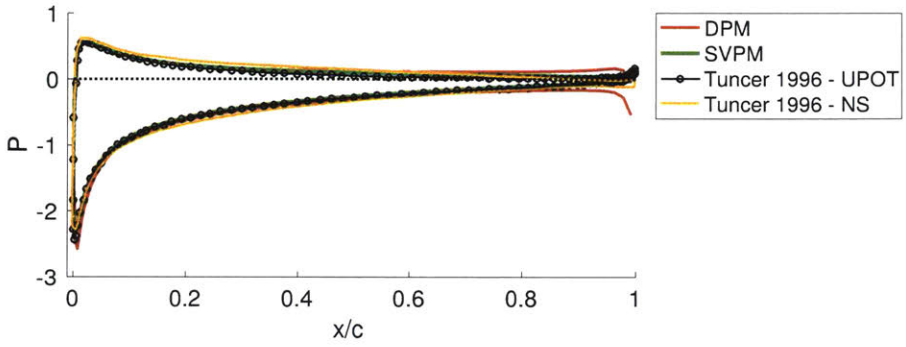

Figure 3-13: Validation of the pressure computed using the presently developed doublet panel method (DPM) and source-vortex panel method (SVPM), against the potential flow (UPOT) and full Navier Stokes (NS) results from Tuncer and Platzer [160]. The pressure is plotted at the timestep when the foil passes the mean position moving downward.

However, when applying the methods to the undulating fish, a much larger difference was observed between the doublet panel method (figure 3-14) and the source-vortex panel method (figure 3-15). While the doublet panel method captures the general trend of pressure changes, its inability to accurately capture the pressure continuity at the trailing edge results in large quantitative errors over the entire body. This is not altogether unexpected; the fish swims at a reduced frequency of 5.65 (for comparison only), indicating that the system is much more unsteady than the heaving airfoil from Tuncer and Platzer [160].

Willis [175] came to similar conclusions in his exploration of various panel method formulations and Kutta conditions. He tested a source-doublet method with a linear potential Kutta condition, a doublet lattice method with a $\gamma_{T.E.} = 0$ Kutta condition, and a source panel method with doublet wakes and a nonlinear pressure Kutta condition. He found that while for most applications, a linear Kutta condition (velocity condition) is adequate, but for highly loaded, low aspect ratio or highly swept wings

the linearization is no longer a good approximation. Although the velocity Kutta condition performs well as a first approximation for unsteady flows, highly unsteady flows will not be accurately modeled.

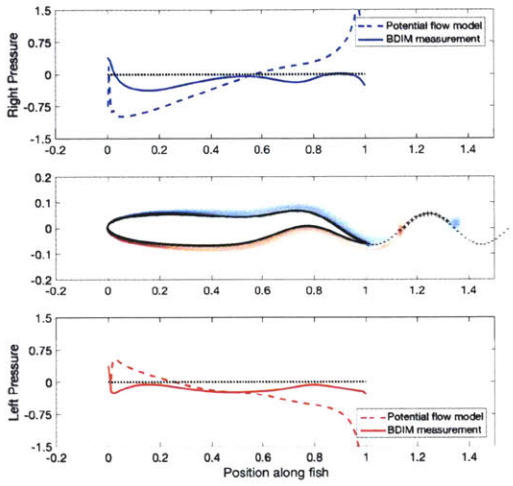

Figure 3-14: For one timestep, a comparison between the pressure estimated with the doublet panel method model (dashed line) and the pressure measured within the BDIM simulation (solid line), for the left and right sides of the fish. The middle plot shows a snaphot of the vorticity field from the BDIM simulation. The plus and minus signs in the wake represent positive and negative vortices shed by the panel method, respectively. Wake rollup is not modeled.

Interestingly, although the source-vortex panel method does perform better than the doublet panel method in estimating the pressure experienced by an undulating fish, it does not perform significantly better than a source only panel method (figure 3-15). The error appears to be slightly reduced in the midsection of the fish, but the error close to the trailing edge is still high.

As a result, we chose to use the source-only formulation within the inverse problem. The source-vortex method is considerably slower due to the nonlinear Kutta condition. Since the panel method must be formulated at every timestep and solved multiple times per timestep within the inverse problem, the computational cost of the source-vortex method would make it undesirable for a real-time controller. Furthermore, while including the wake in the model is straightforward in the forward problem, there is not an easy way to include it in the inverse problem. Since the wake results from flow interactions in the past as well as the current timestep, including it would

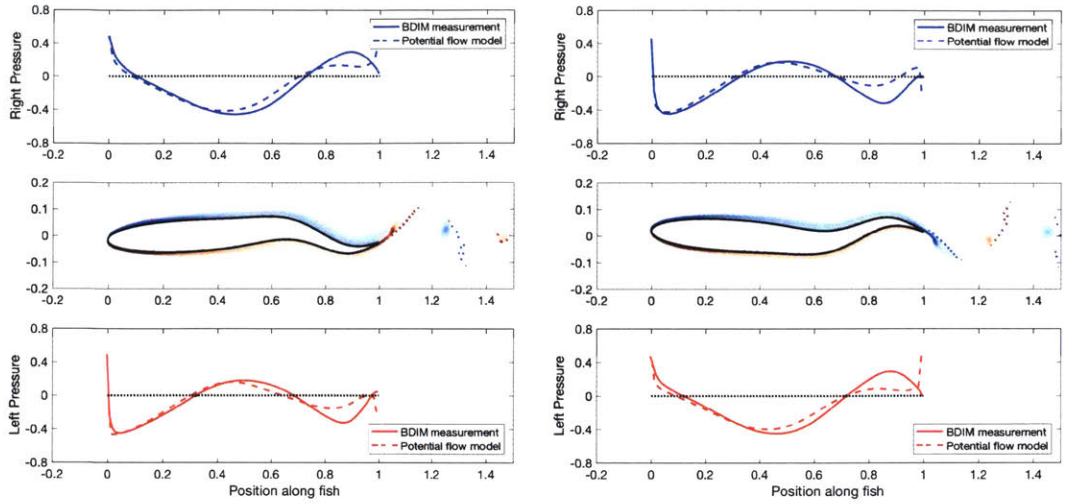

Figure 3-15: For two timesteps, a comparison between the pressure estimated with the doublet panel method model (dashed line) and the pressure measured within the BDIM simulation (solid line), for the left and right sides of the fish. The middle plot shows a snaphot of the vorticity field from the BDIM simulation. The red and blue dots in the wake represent positive and negative vortices shed by the panel method, respectively. Wake rollup is modeled.

prohibit an independent solution at each timestep.

3.4.5 Validation: within a wake

To validate the ability of the source panel method to capture the pressure sensed by a fish swimming within a wake, it is necessary to estimate the position and strength of vortices surrounding the fish.

a. Identifying vortices from the simulation data

There are several well known criteria for vortex identification, which vary in their perfomance under different circumstances [73, 27, 29]. We investigated the ability of four different criteria to identify vortices in this system, which is complicated by two things: (1) some vortices in the system are very close together, and (2) the induced vortices in the system are within the boundary layer.

In 2D, all four criteria extract require that:

$$\frac{\partial u}{\partial x}\frac{\partial v}{\partial y} - \frac{\partial u}{\partial y}\frac{\partial v}{\partial x} = \det(\nabla u) > 0 \tag{3.50}$$

$$\frac{\partial u}{\partial y}\frac{\partial v}{\partial x} < 0 \tag{3.51}$$

The Δ criterion finds areas with closed streamlines in a reference frame moving with a fluid point, which are represented by connected regions with $\Delta > 0$, where:

$$\Delta = 4\left(\frac{\partial u}{\partial y}\frac{\partial v}{\partial x} - \frac{\partial u}{\partial x}\frac{\partial v}{\partial y}\right) + \left(\frac{\partial u}{\partial x} + \frac{\partial v}{\partial y}\right)^2 \tag{3.52}$$

The λ_{ci} criterion identifies vortices by their "swirling strength", classifying vortices as connected regions where $\lambda_{ci} > 0$:

$$\lambda_{ci} = \text{real}\left(\frac{1}{2}\sqrt{-4\left(\frac{\partial u}{\partial y}\frac{\partial v}{\partial x} - \frac{\partial u}{\partial x}\frac{\partial v}{\partial y}\right) - \left(\frac{\partial u}{\partial x} + \frac{\partial v}{\partial y}\right)^2}\right) \tag{3.53}$$

The Q criterion looks for a low pressure minimum in while comparing the local vorticity magnitude with the strain rate, requiring $Q > 0$, where:

$$Q = -\left(\frac{\partial u}{\partial y}\frac{\partial v}{\partial x} - \frac{\partial u}{\partial x}\frac{\partial v}{\partial y}\right) - \frac{1}{2}\left(\frac{\partial u}{\partial x} + \frac{\partial v}{\partial y}\right)^2 \tag{3.54}$$

The λ_2 criterion does the same thing as the Q criterion, but imposes additional limitations through eliminating the terms for unsteady straining which contributes to pressure and viscous effects which can eliminate a pressure minimum. This criterion employs the eigenvalues λ of the tensor $\mathbf{S}^2 + \mathbf{\Omega}^2$, requiring that two are negative. This is equivalent to requiring $\lambda_2 < 0$, where:

$$\lambda_2 = \left(\frac{\partial u}{\partial y}\frac{\partial v}{\partial x} - \frac{\partial u}{\partial x}\frac{\partial v}{\partial y}\right) + \frac{1}{2}\left(\frac{\partial u}{\partial x} + \frac{\partial v}{\partial y}\right)^2 \tag{3.55}$$

$$+ \frac{1}{2}\left|\frac{\partial u}{\partial x} + \frac{\partial v}{\partial y}\right|\sqrt{\left(\frac{\partial u}{\partial x} - \frac{\partial v}{\partial y}\right)^2 + \left(\frac{\partial u}{\partial y} + \frac{\partial v}{\partial x}\right)^2} \tag{3.56}$$

While the Q criterion measures the excess of rotation rate over the strain rate in all

directions, the λ_2 criterion looks for the excess only along a specific plane.

In practice, the λ_2 criterion is the most restrictive and identifies the smallest number of vortices, while the Δ and λ_{ci} criteria are the least restrictive. The restrictiveness of each criteria can be adjusted somewhat through imposing restrictions on the size and circulation of areas classified as a vortex. For a single snapshot, the performance of these four criteria is shown in figure 3-16. It can be seen that while the λ_{ci} criterion misses some of the obvious vortices while misidentifying other areas as vortices, the other three criteria perform quite similarly (and well). The obvious vortices that the λ_{ci} criterion misses near the middle of the fish is due to the fact that the vortex pair is identified as a single vortex, and subsequently filtered out for having a small total circulation.

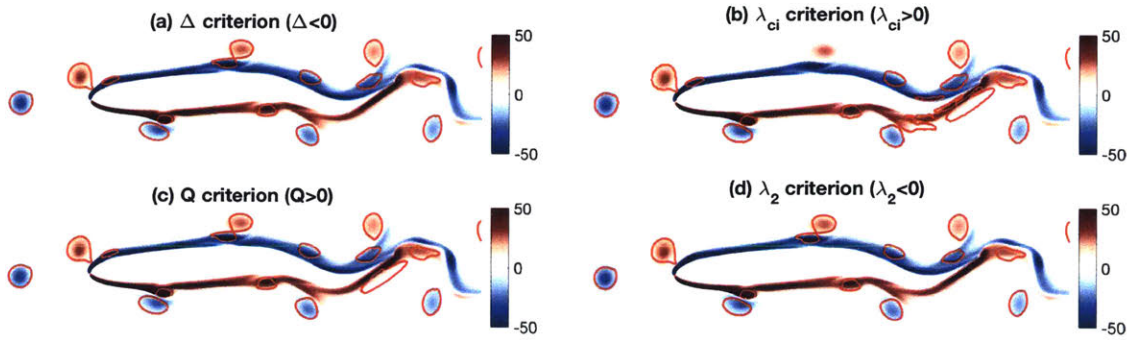

Figure 3-16: A comparison of vortices found at a single timestep using (a) the Δ criterion, (b) the λ_{ci} criterion, (c) the Q criterion, and (d) the λ_2 criterion. The contour plots show a snapshot of the vorticity field.

Using the λ_2 criterion, the vortices identified in a single snapshot are shown in figure 3-17. Following the identification of vortices, additional manual selection must be performed to isolate the actual vortices of interest, because it was not possible to find a set of conditions which would only capture true vortices and capture all true vortices. As can be seen in figure 3-17, some regions near the back of the fish are falsely identified as vortices.

More importantly, it can be seen that while the vortex pair on the right side of the fish near $x/L = 0.3$ is correctly identified, the contour outlining the positive vortex from the original wake is extremely small. As a result, while this method of vortex identification produced relatively accurate predictions for the location of each vortex,

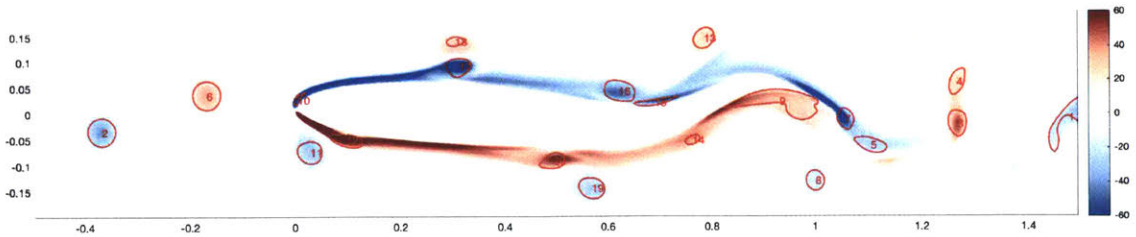

Figure 3-17: One shortcoming of the λ_2 criterion (as well as the other criterions) lies in its inability to accurately estimate the size of vortices within vortex pairs (e.g., vortex pair on the right side of the fish near $x/L = 0.3$). When close together, the size, and therefore circulation, of vortices was often underestimated.

the estimated circulation was often underestimated when vortices were close to each other.

As a result, a new methodology was developed for improved estimation of vortices from the simulation data. With this new method, a circle was drawn around a known vortex center (estimated from the λ_2 criterion), and the vorticity within the circle was integrated to yield the total circulation. Since vortices that were close together were always of opposite sign, for each vortex, only the vorticity field of the same sign is considered within the integral (figure 3-18).

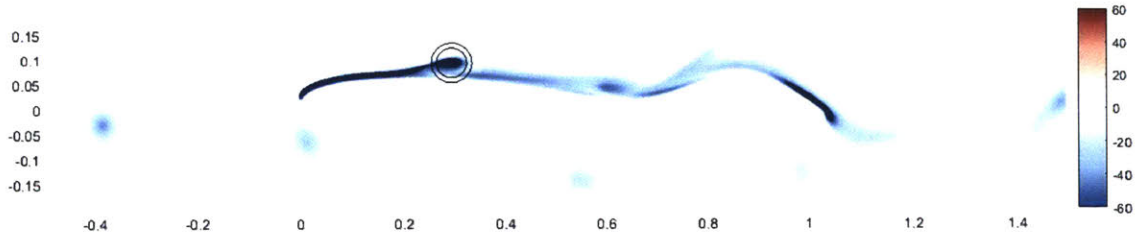

Figure 3-18: Illustration of new method used in estimating circulation of vortices in the field: the plot shows a snapshot of the negative vorticity at a timestep, and the circle represents the area over which the integration is performed.

While this method is qualitative, it provides a more accurate estimate of the circulation of vortices in the near field. Within the model, the model of near-field vortices as point vortices is already an approximation; therefore, the approximation used here is not expected to reduce the accuracy of the sensing model significantly.

b. Validation of forward model in the presence of vortices

The estimated position and strength of vortices in the BDIM simulation were used as an input to the forward model, which estimates the pressure sensed by the fish given the fish motion profile, the nearby vortex states, and the swimming speed.

Within the model, each vortex from the upstream wake is represented as a single point vortex, and the fish is represented using a source panel method (figure 3-19). Each induced vortex is represented as 3 point vortices at a small distance δ apart and tangent to the surface of the fish, which helps to model the shape of these vortices more accurately. The results are not extremely sensitive to the exact value of δ.

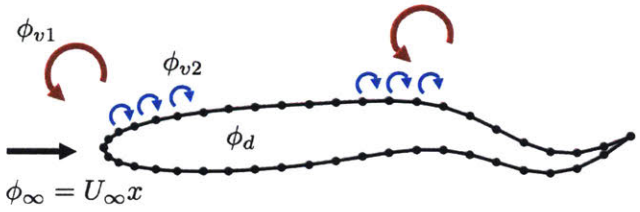

Figure 3-19: Diagram of the potential flow model, illustrating the main contributions to the velocity potential. Vortices are only shown on one side of the fish for simplicity, but they exist on both sides.

With this model, the pressure was estimated over the surface of the fish over an entire swimming period, and compared with the pressure measured within the BDIM simulation (figure 3-20).

As can be seen, the estimated pressure matches the measured pressure with remarkable accuracy, given the number of approximations used within the model. While the inclusion of a wake model may improve the accuracy near the trailing edge somewhat, its inclusion would significantly increase the computational cost of the inverse problem, and would likely have little effect over the majority of the body.

3.4.6 Discussion: panel method strengths and limitations

Potential flow makes the assumptions that the flow is irrotational and incompressible. While this is often a good assumption for systems at a high Reynolds number ($Re =$

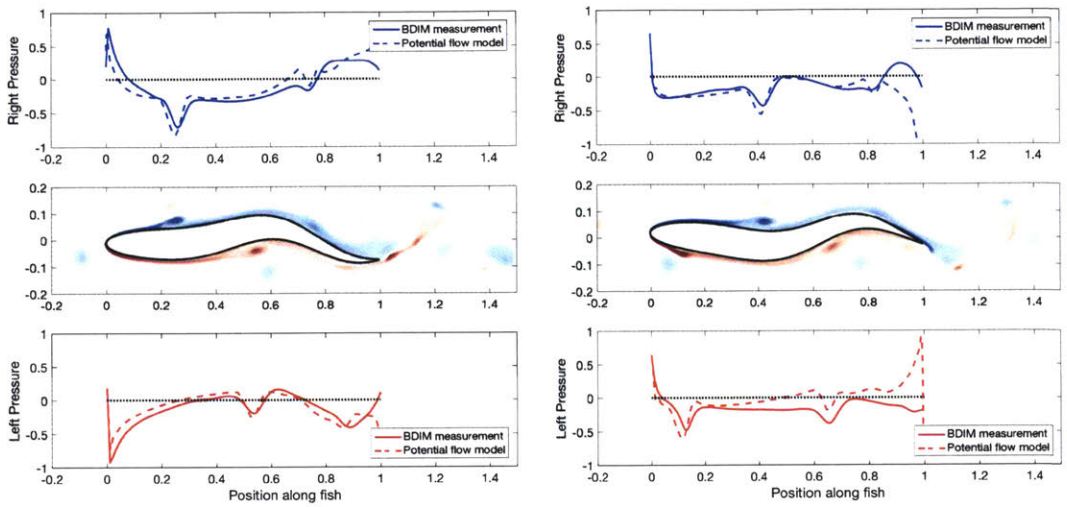

Figure 3-20: For two timesteps, a comparison between the pressure estimated with the source panel method model (dashed line) and the pressure measured within the BDIM simulation (solid line), for the left and right sides of a fish swimming within a wake. The middle plot shows a snaphot of the vorticity field from the BDIM simulation.

5000 in these simulations), it was originally unclear if the model would still work well in the event of strong interactions with external vortices. The present work has demonstrated that despite the strong interaction with upstream vortices in this problem, and the creation of new vortices, a potential flow model can still capture the flow environment with high accuracy.

Even without modeling the boundary layer of the fish, or the changes to the boundary layer that are caused by interaction with the nearby vortices, the pressure along the surface of the fish is still captured reasonably well. In this problem, where the goal is to estimate the strength and position of near-field vortices, this model is likely to be sufficient. The position of the induced vortex along the body can easily be captured by following the low pressure peak along the body. Near the head, where the model is the most accurate, it can be used to estimated both the position and strength of oncoming vortices. Due to the error near the tail, the model is likely limited in its ability to be used for estimation of vortices in this region.

A panel method is uniquely suited for this purpose, providing a good balance between computational cost and accuracy. While the compuational cost is greatly reduced from a full Navier-Stokes solver (scales with N instead of N^2 in 2D), it can

still capture the motion of the fish, and the pressure sensed by the undulating fish relatively well. Formulated as a boundary value problem, it is also uniquely suited for estimation of the pressure on the surface of the fish.

3.5 Insights from potential flow model

Experiments with the potential flow model provide unique insights into the sensing abilities of the fish within a wake. While it is difficult to test the signature created by individual vortices and the effect of changing the instantaneous fish shape or motion within the BDIM simulation, these parameters can be tested extremely quickly with the potential flow model.

In the following sections, we will discuss three insights that were drawn from analyzing the system with the potential flow model: (a) the self-induced effect improves observability, (b) the induced vortices masks the original wake vortices, and (c) the potential flow model captures the system well in the front half of the fish, but requires a modification in the posterior half.

3.5.1 Self-induced effect improves observability

In section 3.3, we demonstrated that the signal sensed by a solid fish within a wake is richer than the signature sensed by a ghost fish. It was proposed that while the signature was more complex and potentially more challenging to decode, it could actually contain more information.

In this section, we will use a simple model to demonstrate that the interaction between a solid sensing body and a nearby vortex is important, and that it definitively yields more information than the signal that would be generated with no interaction.

The simple model consists of a vortex translating by a sensing body modeled in three different ways: (1) as a flat plate, (2) as a ghost ellipse, and (3) as a solid ellipse. Both a flat plate and a ghost body have been used in prior research as models for the body of a fish, in studying the signal sensed by the lateral line. While these models have been shown to capture some qualitative aspects of the pressure signature created

by objects or vortices, we will demonstrate that they also miss some key information.

Figure 3-21 shows the instantaneous pressure signal that would be created by a positive and negative vortex at a specific position close to a wall, in a uniform current $U_\infty = 1$. As seen, there is no difference between the two signals. Given only a snapshot of the pressure, an array of sensors on a wall could not distinguish the sign of a nearby vortex.

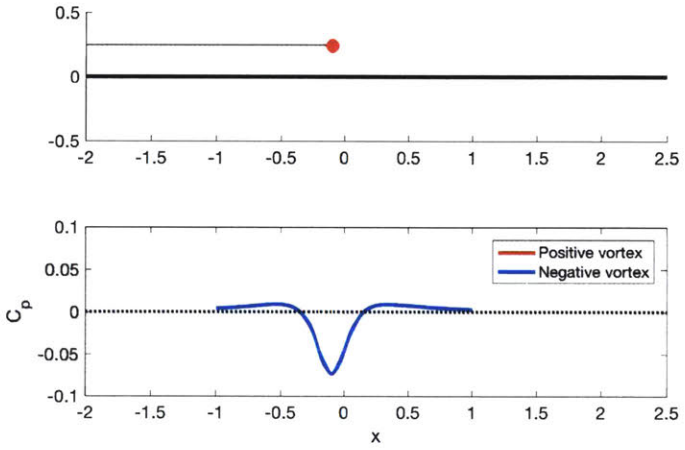

Figure 3-21: A snapshot of a positive or negative vortex by a wall (position shown at top) in uniform flow $U_\infty = 1$, and the pressure sensed by the wall. Instantaneously, the pressure signature created by a positive and negative vortex at the same position is the same.

It should be noted that physically, the interaction between the wall and the nearby vortex does create a difference in the spatiotemporal signature. Within the freestream, a positive (counterclockwise) vortex convects by a wall faster than a negative vortex. Therefore, over time, the position of the vortex yields information about its sign. However, given the same vortex position, the two signatures are instantaneously identical.

Similarly, figure 3-22 illustrates that pressure sensors on a ghost ellipse also cannot tell the difference between a positive and a negative vortex. In this case, since the ghost ellipse does not interact with the external flow at all, even the pressure signal over time would not allow for it to decode the sign of the vortex.

In contrast, the signal captured by a solid ellipse (figures 3-23 and 3-24) show that the ellipse actually interacts with its surrounding flow in a manner that allows it to distinguish between a positive and a negative vortex in oncoming flow. As the vortex

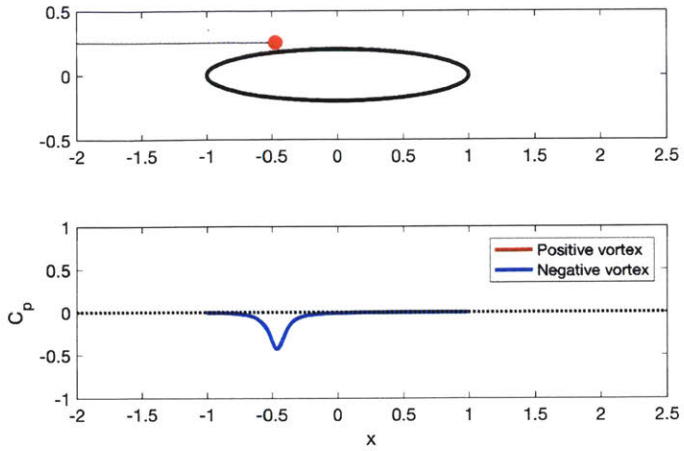

Figure 3-22: A snapshot of a positive or negative vortex by a ghost ellipse (position shown at top) in uniform flow $U_\infty = 1$, and the pressure sensed by the top side of the ellipse. Instantaneously, the pressure signature created by a positive and negative vortex at the same position is the same.

approaches the ellipse (figure 3-23), the pressure rises on one side of the nose and falls on the other. The induced velocity of the vortex causes the stagnation point to shift to the left for a positive vortex and to the right for a negative vortex.

As the vortex passes the nose of the ellipse, a pressure dip forms in both cases, which correlates with the streamwise position of the vortex (figure 3-24). However, the characteristics of the pressure signature around the dip still depends on the sign of the vortex.

This demonstrates that although a flat plate and a ghost body are sensing models that have often been used in the past, they have severe limitations. At the very least, a flat plate and ghost body are incapable of identifying the sign of a nearby vortex given a single pressure snapshot, while a solid and curved body can. Modeling the interaction between the sensing body and the flow is important, and the precise shape and curvature of the body is also important.

Blind cavefish know intrinsically that interaction is critical for sensing. Counter to intuition, scientists have observed that when when exploring unfamiliar environments, they do not slow down so as to prevent collisions, but they actually swim faster in order to strengthen their interaction with their environment and amplify the signal sensed by the lateral line [154].

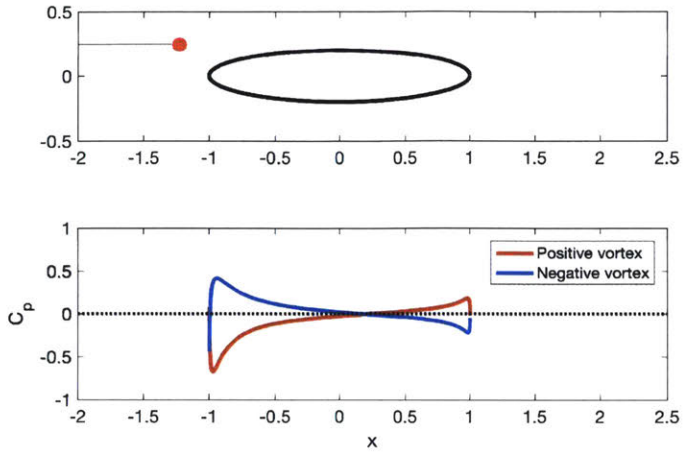

Figure 3-23: A snapshot of a positive or negative vortex by a solid ellipse (position shown at top) in uniform flow $U_\infty = 1$, and the pressure sensed by the top side of the ellipse. As the vortex approaches the ellipse, the pressure rises on one side and drops on the other. The sign of the vortex determines which side experiences a pressure rise/drop.

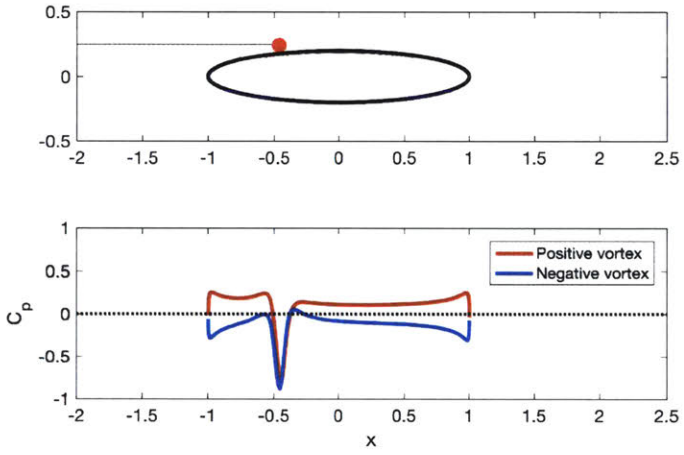

Figure 3-24: A snapshot of a positive or negative vortex by a solid ellipse (position shown at top) in uniform flow $U_\infty = 1$, and the pressure sensed by the top side of the ellipse. As the vortex passes the nose of the ellipse, a pressure dip forms correlating with the streamwise position of the ellipse. However, the characteristics of the pressure signature around the dip still depends on the sign of the vortex.

3.5.2 Induced vortex "masks" upstream vortex

Within the wake, there are numerous vortices in the near-field of the downstream fish. To the sides of the fish, a vortex pair, consisting of the original wake vortex as well as a secondary vortex induced from the interaction, must be detected. However,

prior research has shown that when tracking multiple vortices simultaneously, the accuracy based on a least squares inversion technique is substantially reduced when the vortices are close enough to affect each others' measurements [146, 50].

How observable is the the vortex pair, and specifically the original vortex from the upstream wake after it passes the nose of the fish? The potential flow model allows us to analyze the signal created by a subset of the near-field vortices. In this section, we analyze the signal created by the original vortices only, the induced vortices only, and finally all of them together.

Figure 3-25 shows the signal sensed by the fish, estimated with potential flow (dotted line), if only the original vortices are present in the surrounding flow. The solid line shows the signal actually sensed by the fish within the simulation. As described in section 3.4.5, the position and strength of vortices from the BDIM simulation are identified using a vortex tracking methodology, and used as inputs for the potential flow model.

As can be seen, while the estimated pressure near the nose of the fish matches relatively well with the pressure actually sensed, the potential flow estimate completely fails to capture the pressure dips by the side of the fish. This shows that even without the presence of the induced vortices, the original wake vortices are too weak and too far from the side of the fish to yield an obvious signal. As the induced vortex forms, it pushes the original wake vortex farther from the fish. At this distance, weakened through interaction with the fish, and with the induced vortex directly in between itself and the fish, the original vortex is effectively "masked".

Farther downstream, it is clear that the signal created by the original wake vortex only becomes weaker. Since it does not produce a discernible signal past the nose of the fish, it would be impossible for any inversion technique to estimate its position and strength past this point.

For comparison, figure 3-26 shows the signal, estimated with the potential flow model, that would be sensed by the fish if only the induced vortices were present. Each induced vortex is modeled as three point vortices a small distance δ apart, tangent to the surface of the fish. While there is naturally some error between the

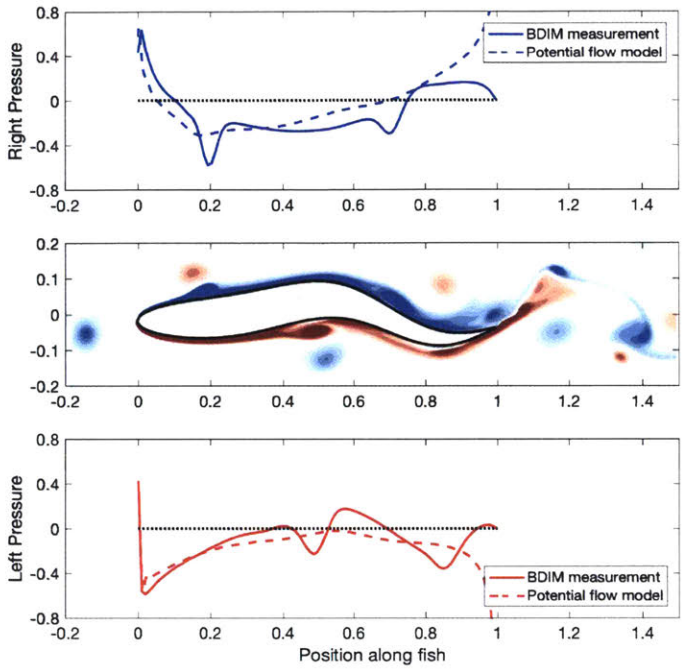

Figure 3-25: A snapshot of the vorticity field at one timestep, and the pressure measured on the left and right side of the fish. The dotted line shows the potential flow estimated pressure, if only the original vortices from the upstream wake are included in the model (and not the induced vortices). The pressure near the head is captured relatively well, but there are no pressure dips due to the vortices by the side of the fish.

flow distribution created by this model and the actual system, the model captures the pressure dips along the body remarkably well. In the head region, it is clear that including only the induced vortices is insufficient for estimating the pressure. However, along the rest of the body, the dominant signal is created by the induced vortices rather than the original vortices from the upstream wake.

Figure 3-27 shows, for the same timestep, the signal estimated by the potential flow model including all the nearby vortices. This estimate captures the pressure change at the nose due to the oncoming vortices from the upstream fish, as well as the pressure dips along the body due to the induced vortices. Interestingly, the pressure dips along the body appear to be slightly more accurate, indicating that the original wake vortices do affect the signal along the body slightly. However, in general it is evident that the signal at the nose is dominated by the vortices from the upstream fish, while the signal along the body is dominated by the induced vortices.

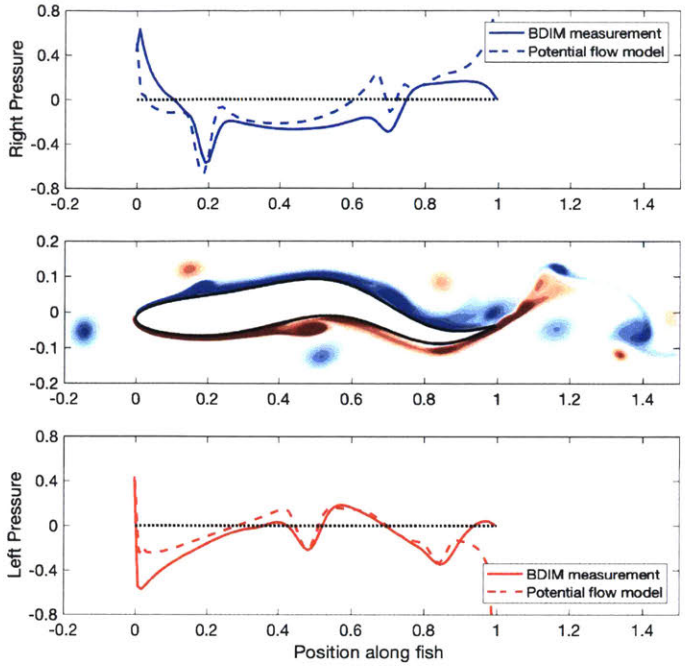

Figure 3-26: A snapshot of the vorticity field at one timestep, and the pressure measured on the left and right side of the fish. The dotted line shows the potential flow estimated pressure, if only the induced vortices are included in the model (and not the original vortices from the upstream wake).

This insight will be helpful in formulating the inverse estimation problem.

3.5.3 Comparison of measured and estimated vortex velocities

An indication of the validity of the potential flow model can be obtained through comparing the velocity of the vortices as estimated by the potential flow model against the velocity measured from the BDIM simulation (figure 3-28).

As shown, for the original wake vortex, the estimate of the streamwise velocity is reasonably good, from a point upstream of the fish to the trailing edge of the fish (figure 3-28a). Near $x/L = 0.3$, the estimated velocity is slightly lower than the actual velocity, possibly due to underestimated strength of the induced vortex. The lateral velocity estimate is also quite good for $x/L < 0.4$, but farther downstream, the estimated velocity is significantly lower than the actual velocity (figure 3-28b). In fact, along the entire length of the fish, it appears as if the vortex can be pushed away as the fish undulates toward it, but not pulled in when the fish undulates away

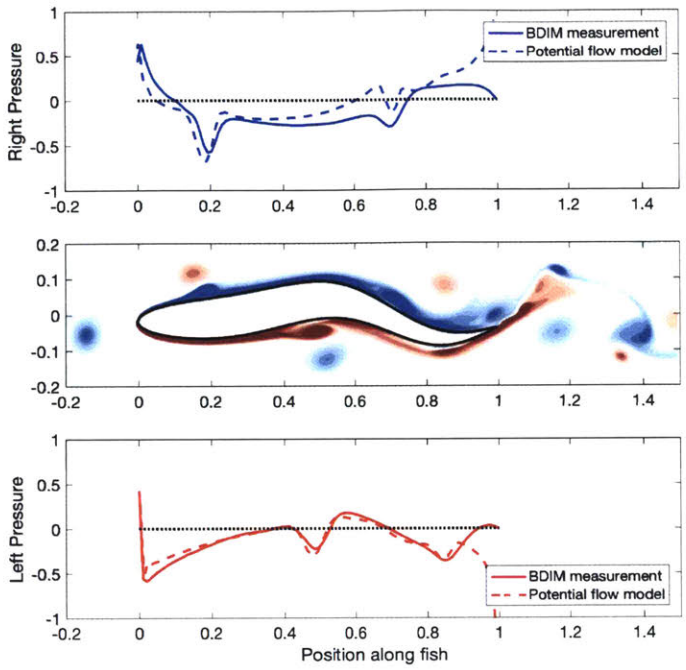

Figure 3-27: A snapshot of the vorticity field at one timestep, and the pressure measured on the left and right side of the fish. The dotted line shows the potential flow estimated pressure, with all vortices (the original vortices from upstream as well as the induced vortices) included in the model.

from it. This makes sense; in potential flow, fluid always fills in behind a withdrawing body, but this is not the case in real flows. This is a limitation of the potential flow model.

For the induced vortex, the estimated velocities match well in the lateral direction (3-28d) but not as well in the streamwise direction (3-28c). Likely, this is due to differences between the true flow distribution created by the induced vortex and the modeled distribution. In particular, as the vortex forms, the vorticity thickens in a patch before rolling up into a distinct vortex. As a result, the actual streamwise velocity for this vortex starts close to zero, but the model is unable to capture this. However, this is not essential because the induced vortex is easily tracked by following the position of the distinctive low pressure peak along the body. This peak forms even before the induced vortex clearly separates from the boundary layer, and provides a highly observable signature.

The reasonably good match between the velocity of the original vortex predicted

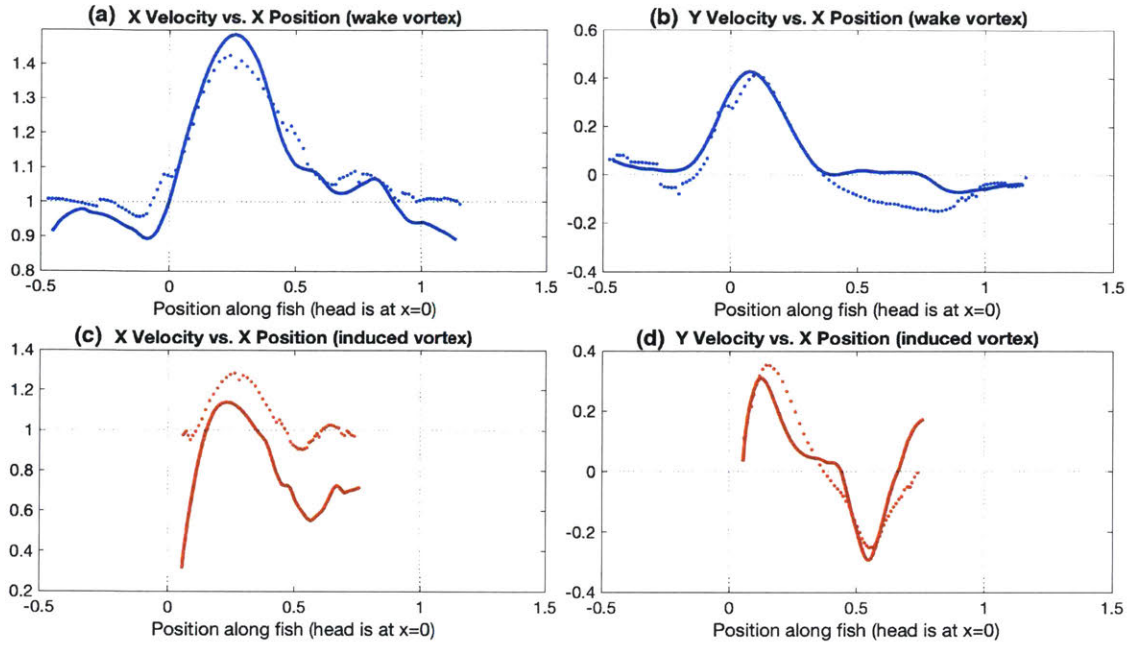

Figure 3-28: A comparison between the velocity of the vortices as measured in the BDIM simulation (solid lines) and the velocity estimated with potential flow (dots). The vortices are on the right side of the fish, such that a positive lateral (y) velocity indicates that the vortex is moving away from the fish and a negative lateral (y) velocity indicates the vortex is moving toward the fish. The top plots show the (a) streamwise and (b) lateral velocity of the original wake vortex, and the lower plots show the (c) streamwise and (d) lateral velocity of the induced vortex.

by potential flow and the actual measured velocity indicates that it may be possible to use the potential flow model to dead-reckon the position of the original vortex at the tail.

3.6 The inverse problem: vortex estimation

In section 3.4.2, a potential flow model was developed which used a panel method to model the undulating body of the fish and point vortices to model near-field vortices. This model was shown to be capable of performing the forward problem: estimating the pressure sensed by the fish when swimming within the wake of an upstream fish. This indicated that the model is capable of capturing the relationship between the fluid state and the measurement acquired by the fish.

However, the goal is not to estimate the pressure sensed by the fish, but to perform the inverse problem of decoding the pressure signal into important information about the flow. In chapter 2, it was demonstrated that vortices along the entire body greatly influence the efficiency. In section 3.3, we revealed that the vortices in the near-field consist of the upstream wake vortices at the nose, a vortex pair consisting of the original vortices and induced vortices along the body, and the original vortices at the tail. However, in section 3.5.2 we also demonstrated that the original vortex is largely unobservable after it passes the nose of the downstream fish.

As a result, the goal within this section is to develop an estimator which is capable of estimating the position and strength of vortices approaching the nose, and the strength and streamwise position of induced vortices along the body. Furthermore, the possibility of using the forward model alone to estimate the position of the original vortices will be explored. While these vortices are largely unobservable along the body, we will demonstrate that it is still possible to capture their approximate location at the trailing edge through dead-reckoning.

3.6.1 Inversion algorithms

Used in combination with an inversion technique, the forward model described in section 3.4.2 can be used to solve the inverse problem: estimating the local flow states using the pressure measured by the fish. For this problem the inversion technique must be (1) dynamic, to produce state estimates while the flow states are changing, and (2) nonlinear, since the relationship between the flow states and pressure sensed is nonlinear. In a real system, with measurement noise, the technique should also be robust to noise.

Recursive Bayesian estimation is a widely known probabilistic approach for estimating the probability distribution of unknown states recursively over time using incoming measurements and a mathematical model of the system:

$$\text{state transition model:} \qquad \mathbf{x}_{k+1} = f(\mathbf{x}_k, \mathbf{u}_k) + \mathbf{w}_k \tag{3.57}$$

$$\text{measurement model:} \qquad \mathbf{y}_k = g(\mathbf{x}_k) + \mathbf{v}_k \tag{3.58}$$

$f(\mathbf{x}_k, \mathbf{u}_k)$ represents the state transition function, given the state input $\mathbf{x}_k$ and the control input $\mathbf{u}_k$. $g(\mathbf{x}_k)$ is the measurement function. $\mathbf{w}$ and $\mathbf{v}$ are uncorrelated process and measurement noise sequences, respectively.

Bayes filters consist of two steps: prediction and innovation. If the states are linear and normally distributed, the Bayes filter becomes equivalent to the Kalman filter. When these two assumptions are true, Kalman filters provide a very simple and fast way to perform state estimation.

For nonlinear systems which are linearizable, the extended Kalman filter (EKF), which has largely the same structure as the standard Kalman filter, can be used. However, the EKF requires the computation of the Jacobian of the state transition and measurement functions: $\partial f/\partial \mathbf{x}$ and $\partial g/\partial \mathbf{x}$. For extremely nonlinear systems, these Jacobians are often costly or impossible to compute. In this problem, the state transition and measurement models require solving a panel method, which cannot be written as a closed-form equation. While it is possible to compute the Jacobians, it would be computationally expensive.

Another option for nonlinear systems is the use of sigma point filters, such as the divided difference filter and the unscented Kalman filter (UKF). Rather than approximating the state transition and measurement functions through linearization, these filters propagate a set of *sigma points*, which approximate the probability distribution of the state, through the exact nonlinear state transition and measurement functions. Typically, the UKF propagates $2n + 1$ sigma points, where n is the number of unknown states. By propagating the a set of points capturing the probability distributions rather than a single point, this filter has been shown to more accurately estimate the true mean and covariance for extremely nonlinear systems [76].

Particle filters are similar to sigma point filters. However, instead of propagating a small number of well-chosen points, particle filters often use hundreds or even throusands of points. While this can be a good approach when the state transition and measurement functions are simple, the computational cost associated with so many points becomes prohibitive when the models are more complex.

Overall, the UKF is the best-suited algorithm for estimation of states within this

nonlinear system. It provides a good balance between minimal computation and accuracy. While it is more accurate (and less costly) than the EKF, it is also much less costly than a particle filter.

A simple diagram illustrating how the relationship between the foward and inverse model is shown in figure 3-29. Within the estimator, the forward model is used to produce an estimated measurement from the estimated states. The error between this estimated measurement and the true measurement is used to correct the state estimates.

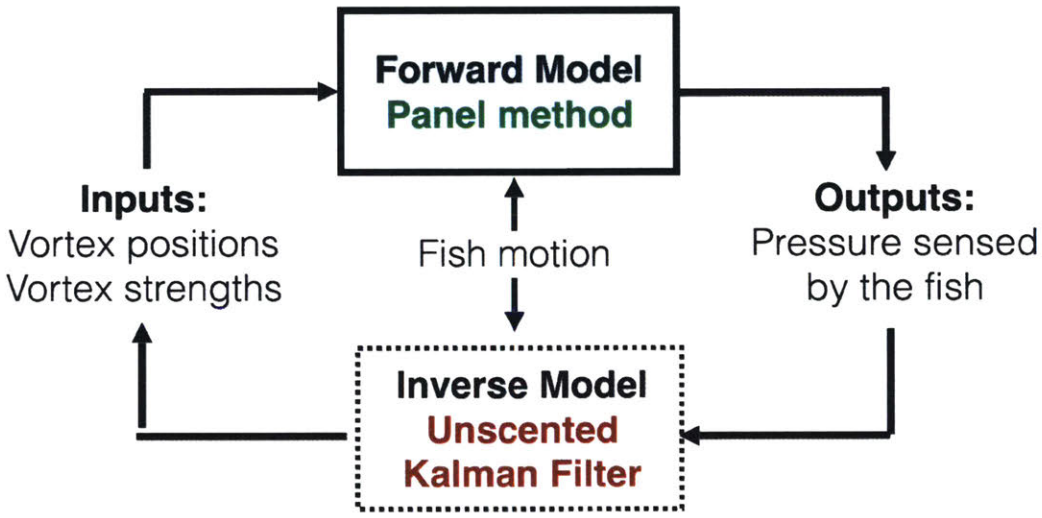

Figure 3-29: A diagram illustrating the relationship between the system inputs, measurements, and models.

3.6.2 The unscented Kalman filter

As introduced above, the UKF performs state estimation in two steps: (1) prediction, in which an *a priori* state estimate and covariance matrix are esimated, and (2) innovation, in which the actual and predicted measurement are compared to yield an updated, or *a posteriori* state estimate and covariance. In the process, the following steps are followed at each timestep:

A set $\mathcal{X}$ of $2n + 1$ sigma points are generated for n unknown states around the

previous state estimate $\mathbf{x}_{k-1}$:

$$\mathcal{X}^0 = \mathbf{x}_{k-1} \tag{3.59}$$

$$\mathcal{X}^i = \mathbf{x}_{k-1} + \left(\sqrt{(n+\lambda)\mathbf{P}_{k-1}}\right)^i, i = 0..., n \tag{3.60}$$

$$\mathcal{X}^{i+n} = \mathbf{x}_{k-1} - \left(\sqrt{(n+\lambda)\mathbf{P}_{k-1}}\right)^i, i = 0..., n \tag{3.61}$$

$\lambda = \alpha^2(n+\kappa) - n$ is a scaling parameter, where α determines the spread of the sigma points and is usually set to a small value ($10^{-4} \leq \alpha \leq 1$). κ is not critical and is often set to zero or $3 - n$.

In the prediction step, the sigma points are propagated through the nonlinear state transition function:

$$\mathcal{X}^i_{k|k-1} = f\left(\mathcal{X}^i_{k-1}, \mathbf{u}_{k-1}\right), i = 0, ..., 2n \tag{3.62}$$

The mean and covariance for the updated sigma points are:

$$\hat{\mathbf{x}}_{k|k-1} = \sum_{i=0}^{2n} W_s^i \mathcal{X}^i_{k|k-1} \tag{3.63}$$

$$\mathbf{P}_{x,k|k-1} = \sum_{i=0}^{2n} W_c^i (\mathcal{X}^i_{k|k-1} - \hat{\mathbf{x}}_{k|k-1})(\mathcal{X}^i_{k|k-1} - \hat{\mathbf{x}}_{k|k-1})^T + \mathbf{Q} \tag{3.64}$$

$\mathbf{Q}$ is the process noise covariance matrix, and W_s and W_c are the state and covariance weight matrices given by:

$$W_s^0 = \frac{\lambda}{n+\lambda} \tag{3.65}$$

$$W_c^0 = \frac{\lambda}{n+\lambda} + (1 - \alpha^2 + \beta) \tag{3.66}$$

$$W_s^i = W_c^i = \frac{1}{2(n+\lambda)}, i = 0..., 2n \tag{3.67}$$

The updated sigma points are propagated through the nonlinear measurement

function:

$$\mathcal{Y}^i_{k|k-1} = g\left(\mathcal{X}^i_{k-1}\right), i = 0, ..., 2n \tag{3.68}$$

The mean and covariance for the predicted measurement $\mathbf{y}$ are given by:

$$\hat{\mathbf{y}}_{k|k-1} = \sum_{i=0}^{2n} W^i_s \mathcal{Y}^i_{k|k-1} \tag{3.69}$$

$$\mathbf{P}_{y,k|k-1} = \sum_{i=0}^{2n} W^i_c (\mathcal{Y}^i_{k|k-1} - \hat{\mathbf{y}}_{k|k-1})(\mathcal{Y}^i_{k|k-1} - \hat{\mathbf{y}}_{k|k-1})^T + \mathbf{R} \tag{3.70}$$

$\mathbf{R}$ is the measurement noise covariance matrix.

β is an extra parameter that allows for the incorporation of prior knowledge about the distribution of $\mathbf{x}$. For Gaussian noise distributions, $\beta = 2$ has been shown to be optimal [23].

In the innovation (update) step, the transformed cross-covariance is calculated as follows:

$$\mathbf{P}_{xy,k} = \sum_{i=0}^{2n} W^i_c (\mathcal{X}^i_{k|k-1} - \hat{\mathbf{x}}_{k|k-1})(\mathcal{Y}^i_{k|k-1} - \hat{\mathbf{y}}_{k|k-1})^T \tag{3.71}$$

This is used in the calculation of the Kalman gain matrix:

$$\mathbf{K}_k = \mathbf{P}_{xy,k}\mathbf{P}^{-1}_{y,k} \tag{3.72}$$

Which is used to update the state estimate and covariance matrix:

$$\hat{\mathbf{x}}_k = \hat{\mathbf{x}}_{k|k-1} + \mathbf{K}_k(\mathbf{y}_k - \hat{\mathbf{y}}_k) \tag{3.73}$$

$$\mathbf{P}_k = \mathbf{P}_{x,k|k-1} - \mathbf{K}_k\mathbf{P}^{-1}_{xy,k} \tag{3.74}$$

Presently, a small modification is included to ensure the symmetry and condition-

ing of the covariance matrix:

$$\mathbf{P}_k^* = 0.5(\mathbf{P}_k + \mathbf{P}_k^T) \tag{3.75}$$

$$\mathbf{P}_k^{**} = \mathbf{P}_k^* + 1e^{-5}\mathbf{I}_n \tag{3.76}$$

These steps are repeated continuously to generate continuously updated estimates of the near-field vortices.

Variations of the UKF have been developed which use a different distribution of sigma points or weights. In the present application, a few different distributions of sigma points and weights were tested, but variations do not have a significant effect on the ability of the UKF to produce accurate estimates over time. However, as a general rule, it was found that when sigma points were distributed closer together, the estimated was more robust to disturbances but converged to new states slightly slower.

Furthermore, in practice, it is difficult to estimate the process noise covariance. As a result, the process and measurement noise covariance matrices $\mathbf{Q}$ and $\mathbf{R}$ can be treated as tuning parameters. $\mathbf{R}$ is a diagonal matrix with the value of the diagonal (r^2) representing the estimated measurement noise. The diagonal of $\mathbf{Q}$ represents the estimated magnitude of process noise. Therefore, by adjusting the relative values of each, we can adjust the amount of "trust" placed in each state compared with the measurements. When the value of r is large compared with $q_{i=1,\ldots,n}$, the state transition model is followed more closely in producing the updated state estimate. On the other hand, if the value of r is small compared with $q_{i=1,\ldots,n}$, the updated state estimate is produced through a near-inversion of the measurement model.

In the current problem, the following process and measurement noise covariance

matrices were found to produce a good result:

$$\mathbf{Q} = \begin{bmatrix} 1e^{-5} & 0 & 0 & 0 \\ 0 & 5e^{-6} & 0 & 0 \\ 0 & 0 & 1e^{-5} & 0 \\ 0 & 0 & 0 & 1e^{-5} \end{bmatrix}, \quad \mathbf{R} = \begin{bmatrix} 0.01 & 0 & \dots & 0 \\ 0 & 0.01 & & \\ \vdots & & \ddots & \\ 0 & & & 0.01 \end{bmatrix} \tag{3.77}$$

Overall, the performance of the estimator is not extremely sensitive the precise values of $q_{i=1,\dots,n}$ and r.

3.6.3 Estimation of near-field vortices

The vortex estimation is divided up into three distinct parts, for each vortex approaching from the upstream wake: (1) estimation of the approaching vortex street, (2) identification and tracking of the induced vortex, and (3) dead-reckoning for estimation of the original vortex at the tail. Each estimation task uses only a subset of the sensors available on the body.

The UKF described in section 3.6.2 is used to estimate the states of the approaching vortices. Since these vortices cause only a minimal change to the pressure along the majority of the body, it would be undesirable for changes in pressure along the majority of the body to affect the estimate of the vortex near the head. As a result, a subset of sensors is chosen near the nose for the estimation of oncoming vortices (figure 3-30). The choice of these sensors is discussed in section 3.6.5.

(a) Approaching vortex (b) Sensors at nose

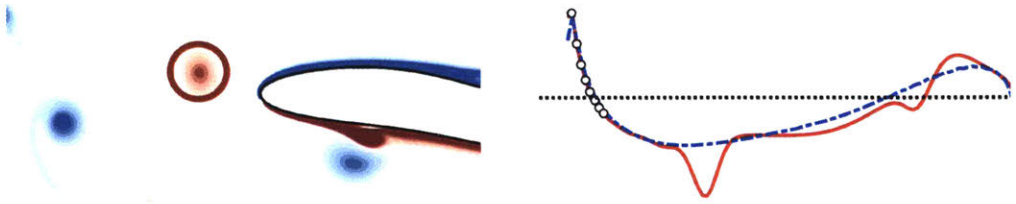

Figure 3-30: For estimating (a) approaching vortices, (b) a subset of sensors at the nose of the fish are used to produce the measurements used within the UKF.

The UKF at the head estimates four states to characterize the oncoming vortex

street: $\mathbf{x}_1 = [x; y; \gamma; \lambda]$. (x, y) is the position of the closest approaching vortex upstream of the nose, Γ is the circulation of the vortex, and λ is the estimated wavelength of the upstream vortex street. With the state estimate, three vortices are generated:

$$\mathbf{x}_{1a} = [x; y; \Gamma] \tag{3.78}$$

$$\mathbf{x}_{1b} = [x + \lambda/2; -y; -\Gamma] \tag{3.79}$$

$$\mathbf{x}_{1c} = [x - \lambda/2; -y; -\Gamma] \tag{3.80}$$

As soon as vortex a passes the nose of the fish ($x/L = 0$), the algorithm adjusts $\mathbf{x}_1$ to focus on the next oncoming vortex.

The estimator at the head must simultaneously estimate the states of several vortices, because the pressure at the nose is sensitive to multiple vortices. However, similar to the results of Suzuki and Colonius [146], we found that the accuracy of vortex estimation was significantly reduced when vortices were close enough to affect each others' measurements. In this problem, vortices are only close to the nose of the fish for a short time, and the system is highly dynamic with at least 3 vortices near the nose that significantly affect the pressure measured. This makes it impossible to estimate the 9 states associated with 3 vortices independently.

However, by incorporating the physical information that the upstream wake is not random, but consists of a regular array of oncoming vortices, the signature of all 3 vortices can be captured while keeping the number of unknown states small ($n = 4$). With this parameterization, the state estimate is still capable of adapting to small perturbations in the wake over time, for example a change in the frequency or a short pause in the upstream fish's swimming motion. An extra state can be included for the estimation of the lateral displacement from the wake centerline.

As each vortex from the upstream wake passes the nose of the downstream fish, an induced vortex forms (figure 3-31). An algorithm captures the pressure dip associated with the induced vortex as it forms, and initializes a second estimator associated with the vortex pair.

The pressure dip along the fish is well correlated with the longitudinal position of

(a) Induced vortex forms

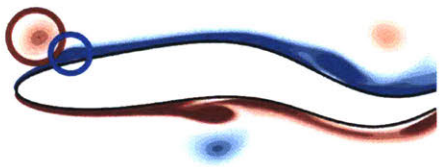

(b) Sensors around pressure dip

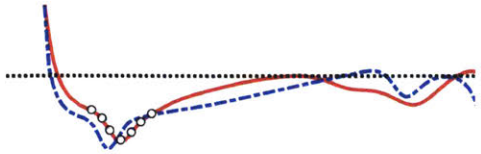

Figure 3-31: For estimating (a) the induced vortex after it forms from the interaction with the original vortex, (b) a subset of sensors surrounding the pressure dip is used.

the induced vortex. Therefore, the estimator assigns the position of the pressure dip to the x position of the induced vortex, and chooses y to be a small distance $\Delta y(x)$ from the surface of the fish. A UKF is used to estimated the strength of the induced vortex. While the position of the induced vortex can be included within the states to be estimated, it is easy to estimate without doing so and the increased number of states in the estimator reduces its accuracy.

(a) Vortex at tail

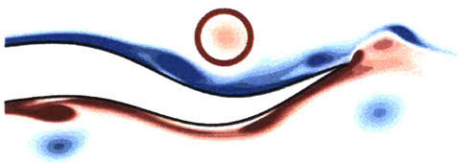

(b) Forward model

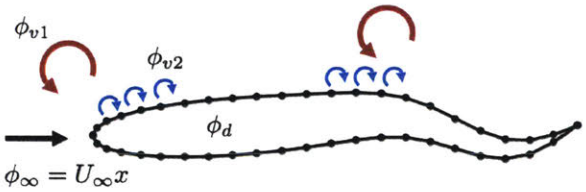

Figure 3-32: For estimating (a) the position of the original vortex at the tail, (b) the potential flow model is used to propagate the position of the vortex forward from its last known position (at the nose).

Within this second estimator, an additional algorithm propagates the position of the second vortex in the vortex pair (the original vortex from the upstream wake) forward (figure 3-32). After its position is captured as the induced vortex is first detected, the original vortex becomes largely unobservable (section 3.5.2). Presently, it was verified that an estimator performed poorly in attempting to estimate the position and strength of the original vortex along with the induced vortex. However, with a potential flow model including the fish, the current vortex pair, and the freestream, dead-reckoning can be used to estimate the position of the original vortex as it reaches

the tail.

Estimator performance

A snapshot of the final vortex estimation algorithm, which puts together the independent estimation algorithms along the body, is shown in figure 3-33. In this snapshot, taken after the estimator has converged, it can be seen that the estimator captures the sign and positions of all near-field vortices remarkably accurately. Capturing the strength accurately is only important in how it affects the model's estimate of the vortex positions, so we can infer that the strength of each vortex is captured accurately enough as well.

The blue lines, which depict the pressure estimated by the model given the estimated states, also matches the true pressure measured within the simulation remarkably well.

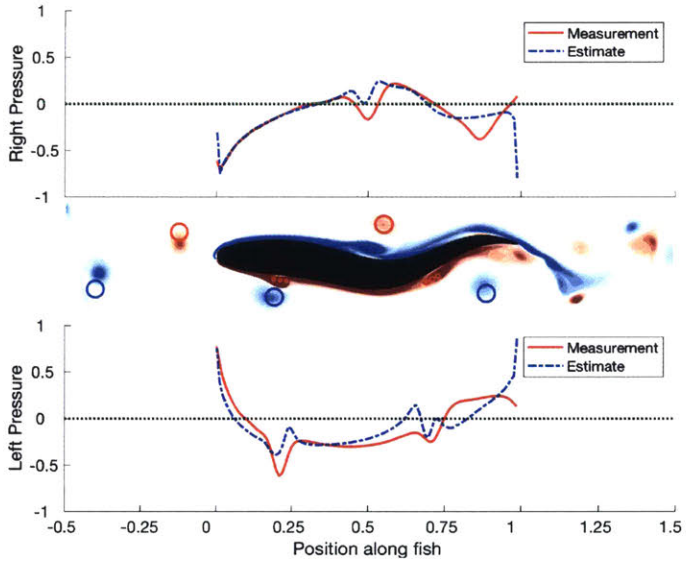

Figure 3-33: Vorticity snapshot of the fish at a single timestep (middle), with the measured (red lines) and estimated (blue lines) pressure plotted for the left and right. The circles in the middle plot show the estimated positions of near-field vortices. The two vortices upstream of the fish are estimated with the head UKF, and the three vortex pairs along the body are estimated with independent estimators.

Figure 3-34 show snapshots of the estimator performance when the forward model used for dead-reckoning of the original vortex position at the tail is varied. In figure

3-34a, only the freestream is used - this model assumes that once past the nose of the fish, the original vortex propagates with $U_\infty = 1$. We can clearly see that this model is inaccurate; the estimated original vortex position is far upstream from the true position by the time it reaches the tail. In figure 3-34b, the freestream and influence of the fish body are used to propagate the position of the original vortex forward. This model is a slight improvement, but again it is evident that something is missing.

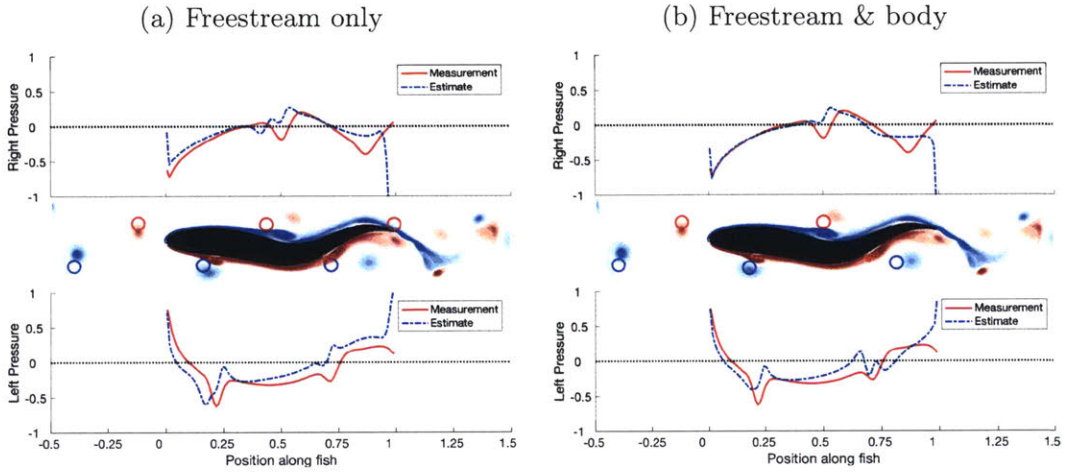

Figure 3-34: Snapshots of the estimator performance when (a) only the freestream and (b) the freestream and influence of the fish are included within the forward model used to dead-reckon the position of the original vortex after it passes the nose. These demonstrate that it is important to include the freestream, the effect of the fish, *and* the effect of the closest induced vortex in this estimator.

This shows that while dead-reckoning can be used to provide a reasonably accurate estimate of the original wake vortices at the tail of the downstream fish, a good model must be used. Despite the fact that the original vortices are nearly unobservable along the body of the fish, the fish and the induced vortices still have a significant effect on the vortices, which do not propagate with just the freestream.

Various parameters can be tuned within the estimation algorithm to improve the accuracy or convergence time. In particular, the process and noise covariance matrices can be adjusted. In general, when $\mathbf{Q}$ is increased ($\mathbf{R}$ is reduced), the vortex estimates respond more quickly to changes, but are less accurate overall. When $\mathbf{Q}$ is reduced ($\mathbf{R}$ is increased), the estimator converges more slowly, but is more accurate once it has converged.

3.6.4 Discussion: estimator limitations

In developing the estimation algorithm, a few limitations unique to this system were discovered. These limitations and their treatment will be discussed in this section.

a. Observability of vortices at the nose

Vortices approaching the fish cause a change to the pressure sensed at the nose, but changes in the streamwise position are much more observable than changes in the lateral position (figures 3-35 and 3-36), and the changes in x and y position can result in similar changes to the pressure sensed.

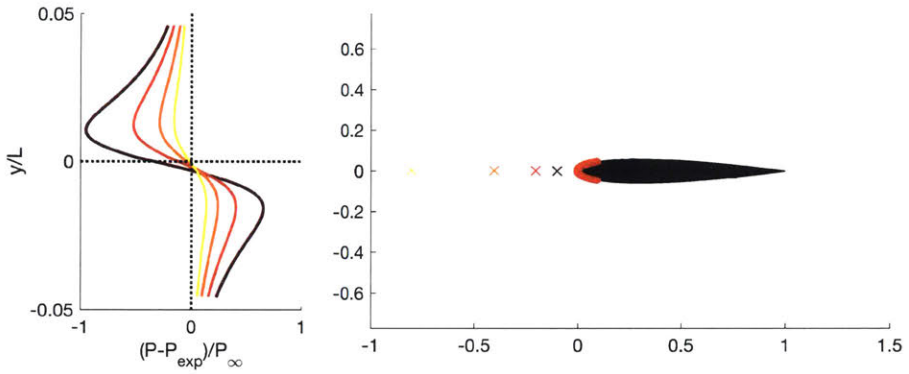

Figure 3-35: Difference between the measured pressure (P) and the self-induced pressure (P_{exp}) of the foil in a uniform stream, with a vortex ($\Gamma = 0.1$) at varying upstream position. The colors of the pressure traces on the left correspond with the vortex positions shown at the right. Calculations are performed with a potential flow model.

For a vortex approaching in the streamwise direction, the pressure at each point along the nose changes in the same direction with decreasing distance. However, this is not the case for a vortex moving laterally in front of the fish.

These characteristics make it difficult for the observer to identify the exact position of a single approaching vortex. When the estimated vortex position is within a sizeable region in front of the fish, the estimated pressure matches the measured pressure very well. As shown in figure 3-37a, although the estimated vortex (blue asterisk) is not at the true vortex position, the estimated pressure at the head (dots on the pressure traces) match the measured pressure extremely well.

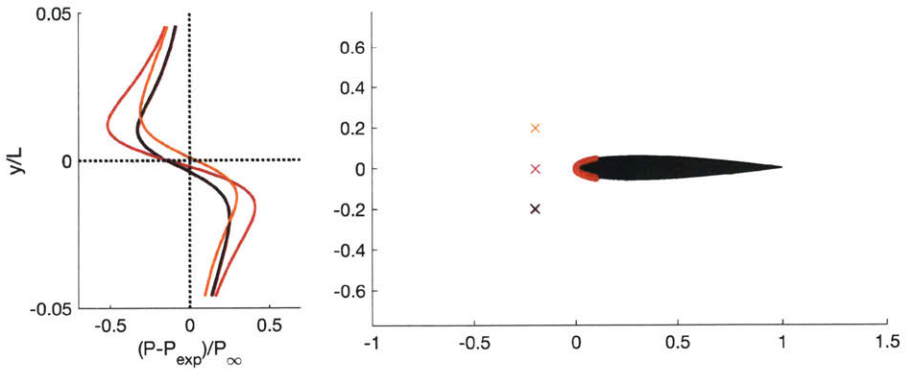

Figure 3-36: Difference between the measured pressure (P) and the self-induced pressure (P_{exp}) of the foil in a uniform stream, with a vortex ($\Gamma = 0.1$) at varying upstream lateral position. The colors of the pressure traces on the left correspond with the vortex positions shown at the right. Calculations are performed with a potential flow model.

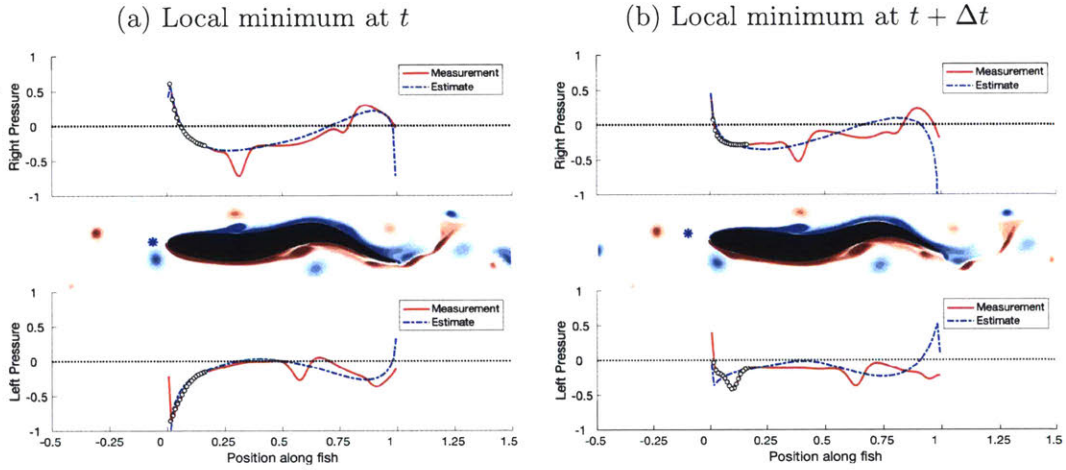

Figure 3-37: Local minimum within the estimator: two vorticity snapshots of the fish (middle), with the measured (red lines) and estimated (blue lines) pressure plotted for the left and right. The asterisk in front of the fish shows the estimated position of the approaching vortex, and the dots on the pressure traces show the sensors used within the UKF.

In this position, the estimated vortex is within the stagnation pressure field of the fish. As the UKF attempts to update the state estimate through balancing the state transition model and the measurement model, the vortex estimate gets "stuck" within this region. As can be seen in a subsequent timestep (figure 3-37b), although the negative vortex from the upstream fish has passed the nose, the vortex estimate is still stuck in front of the nose. In this position, the stagnation pressure field keeps the

vortex nearly fixed in x, and the measurement model does not correct the erroneous position because the state estimate would have to pass through a value that increases the measurement error on its way to the actual position of the vortex.

This failure mode arises partly from the nonlinearity of the system, which yields a non-convex cost function for the estimator. The estimator gets stuck within a local minimum that is not associated with the correct state estimate, and cannot recover from that position without being re-initialized. Additionally, model inaccuracies may also contribute to this failure mode. In particular, the pressure near the head may not be captured well enough by including only one vortex near the nose.

The Kalman filter is an optimal observer that attempts to balance two sources of error: the error in the state estimate (as predicted by the state transition function), and the error in the measurement (as predicted by the measurement function). When both of these functions are linear, the cost function is convex and the Kalman filter will always converge to the true state over time. However, when the system is nonlinear and the cost function is non-convex, there may be several local minima and it is challenging to ensure that the estimator does not converge to the wrong one.

A particle filter presents one solution to this problem; by estimating the pressure resulting from many different "particles", or states, scattered over the state space at each timestep, multiple local minima can be identified, and the best state estimate can be chosen as the one that minimizes the cost function. However, while the UKF requires only $2n + 1$ sigma points (for $n = 4$, 9 sigma points), particle filters require hundreds of particles or more. Since the panel method must be solved once for every point/particle, the computational cost required for using a particle filter would be prohibitive.

Instead, to resolve this failure mode, the model accuracy was improved by extending the model at the head to include three approaching vortices rather than one (figure 3-38).

Only one additional state is required for modeling three approaching vortices, as described in section 3.6.3. However, this small change improves the ability of the model to capture the pressure resulting from a stream of oncoming vortices better.

Figure 3-38: Snapshot of the vorticity field around the fish at one timestep, with the three asterisks near the head depicting the estimate of the approaching vortices. Note that while three vortices are estimated at the head, the one which is furthest downstream is inaccurate; as soon as it passes the nose, it is replaced by an estimate generated by the second algorithm, which produces the nearby vortex circled in blue.

The model also succeeds in capturing the physical nature of the oncoming wake in a manner that prevents the vortex estimate from getting trapped within a small region just upstream of the nose as previously described.

b. A second local minimum

However, this is not the only local minimum in the system. As shown in figure 3-39, the estimate for the oncoming vortices can converge to another local minimum within this framework that is also associated with an inaccurate estimated position. Again, although the state estimate is wrong, the estimated pressure near the nose matches the measured pressure reasonably well. To move toward the true state, the state estimate would have to either move in a direction against the predicted state transition $f(\hat{\mathbf{x}}_k, \mathbf{u}_k)$, or in a direction that temporarily increases the measurement residual $\mathbf{y}_k - g(\hat{\mathbf{x}}_k)$ (see section 3.8.5 and figure 3-66).

Of course, the estimator cannot do that. The precise local minimum that the estimator converges to depends on the initial conditions. Therefore, one way to increase the likelihood that the estimator will not converge to an inaccurate estimate is to initialize the estimator closer to the actual state. For example, we can initialize the state estimate for the oncoming vortices by minimizing the initial measurement residual:

$$\hat{\mathbf{x}}_0^* = \arg\min \left(\mathbf{y}_0 - g(\hat{\mathbf{x}}_0)\right) \tag{3.81}$$

This does guarantee that the state estimate is close to the true state to begin

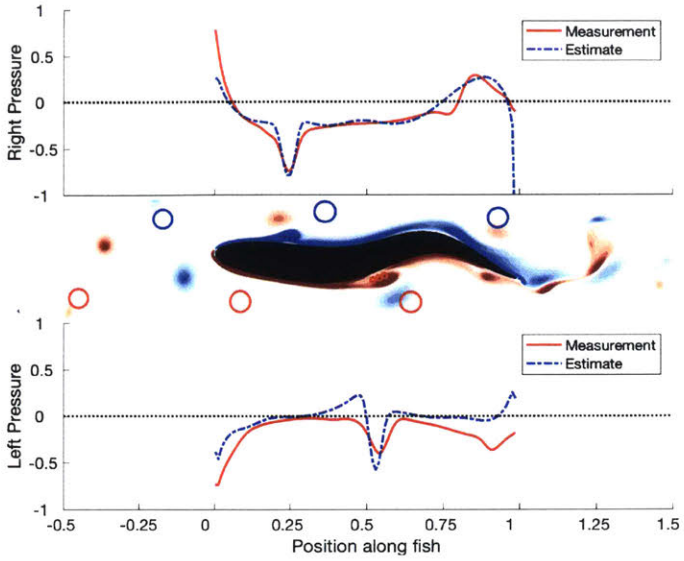

Figure 3-39: Vorticity snapshot of the fish at a single timestep (middle), with the measured (red lines) and estimated (blue lines) pressure plotted for the left and right. The circles in the middle plot show the inaccurate estimated positions of near-field vortices, as they have converged to a local minimum.

with, and therefore increases the likelihood of converging to the correct state estimate. However, under noisy conditions or sudden changes in the state, there is still a chance that the estimator can converge to the wrong state estimate.

In these circumstances, we can take advantage of physical information in order to reinitialize the estimator properly. The fish gains a key piece of information about the oncoming wake each time an induced vortex forms by the nose. Since these vortices were not observed to form as a result of the fish's own swimming motion in quiescent flow, we can infer that they are a direct result of a disturbance from the flow. Indeed, these vortices only form when a positive vortex contacts the negative vorticity in the right side of the boundary layer of the fish, or when a negative vortex contacts the positive vorticity on the left side (see sec. 2.2.1).

Using this physical information, we can implement a re-initialization law: if the fish senses a pressure dip at the nose corresponding with the formation of an induced vortex, and the estimate of oncoming vortices suggests that the closest vortex is on the other side of the head, then switch the signs of the y and Γ state estimates (figure 3-40). This state re-initialization places the state estimate in a position where it is

more likely to converge to the true state over time.

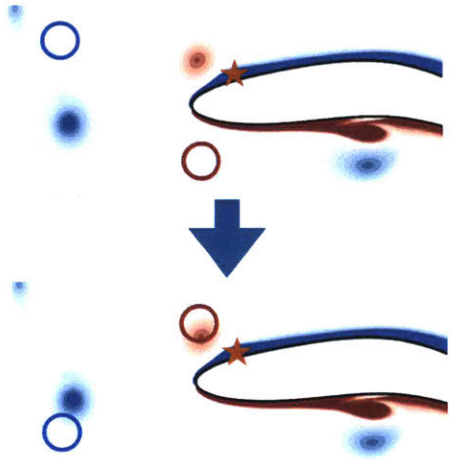

Figure 3-40: An illustration depicting a physical solution which reinitializes the incorrect vortex estimates to a more accurate location: if the fish senses a pressure dip at the nose corresponding with the formation of an induced vortex (yellow star), and the estimate of oncoming vortices suggests that the closest vortex is on the other side of the head, switch the signs of the y and Γ state estimates.

c. Viscous effects in the posterior half

In section 3.5.3, we demonstrated that while the potential flow model performs remarkably well in estimating the true velocity of the vortices in the system, there is some estimation error. In particular, in the posterior half of the fish, where viscous effects are stronger, the model failed to accurately capture the lateral velocity of the induced vortices. In a real flow, while a moving body can "push" vortices away laterally, it cannot "pull" them back.

Within the tests conducted with the estimation algorithm, this model shortcoming manifested itself as an incorrectly estimated position for the original vortex at the tail (figure 3-41a). As can be seen, the estimate of the positive vortex close to the tail is closer to the fish are farther downstream than the actual position.

By implementing a physical correction - that the original vortices from the upstream wake can only be pushed laterally away from the fish, and cannot be pulled in by the undulating motion - the estimator performs much better (figure 3-41b).

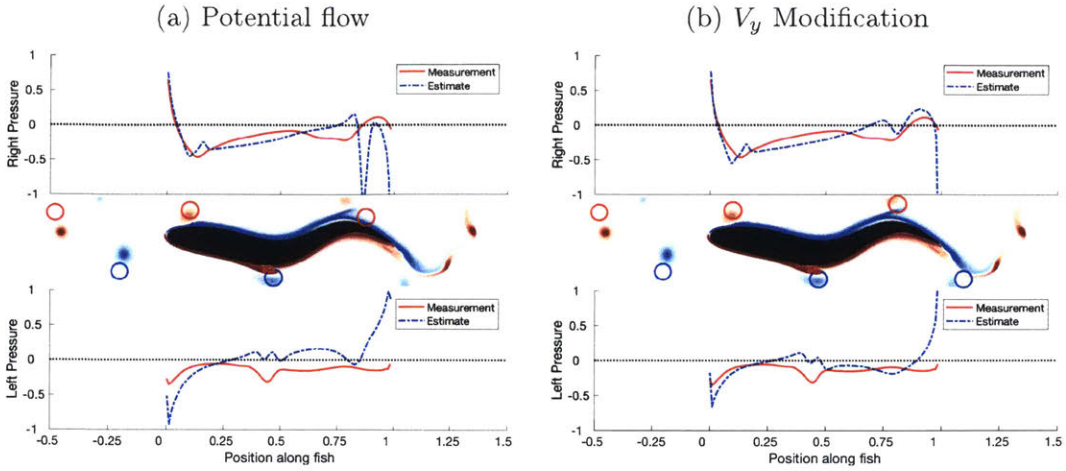

Figure 3-41: Snapshots of the estimator performance with (a) the original potential flow model and (b) a modified potential flow model that only allows the fish to push away (and not pull in) vortices from the original wake.

d. Summary: estimator modifications

In summary, a number of physical heuristics were used in improving the estimator performance. Physical heuristics provide intelligent constraints for the system, allowing for the performance of the estimator to extend beyond the reaches of its natural capability. Although the observability of the vortices in the system is highly limited by increasing distance and proximity to each other, the fish can use some very simple information about its environment and interaction in order to improve observability. Ultimately, this allows it to estimate the phase, wavelength and width of the oncoming vortex street with high accuracy and to estimate the position of both the original vortices and induced vortices along its body quite well.

While these modifications do not cover the full range of circumstances the fish may be exposed to, they do show that physical information can be used to provide very simple augmentations to the model for greatly improved estimation capability. With this framework, small additional modifications can be made to allow for additional parameters, such as deviation from the wake centerline.

3.6.5 Does the number and placement of sensors matter?

Animals which possess a distributed sensory array often exhibit a specific sensor density and/or a precise arrangement of sensors. For example, the campaniform sensilla on the wings of the moth *Manduca sexta* are distributed in a unique pattern on the dorsal surface of the wing [38]. The campaniform sensilla, which act as strain sensors, are believed to be located in a precise pattern to optimally encode information about the flow field and wing loading during flight.

Fish primarily swim within a 2D plane, providing a good explanation for the two-dimensionality of the canal lateral line system along the trunk of the majority of fish (figure 3-42). The sensors over the head, in contrast, are extremely three-dimensional, indicating the presence and importance of 3D information at the nose. Ristroph et al. [127] suggest that the canal concentration over the body is highly correlated with the expected pressure fluctuations over the body of the fish. In the nose region, where pressure fluctuations due to angled incident flow or flow disturbances is the greatest; in this region the canal concentation is also highest.

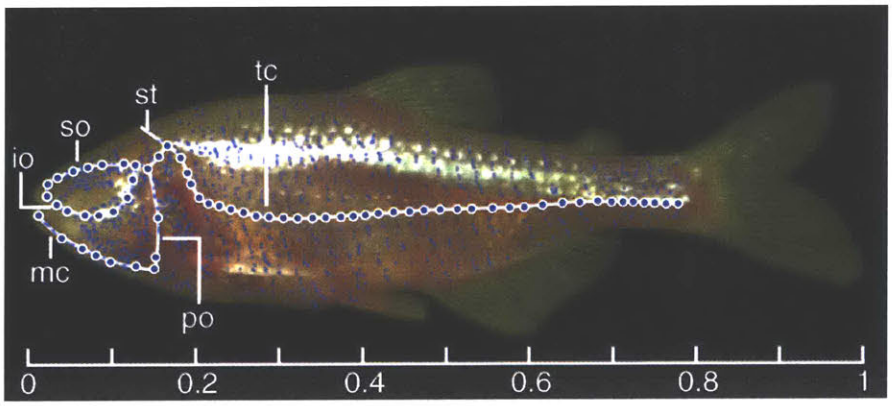

Figure 3-42: Diagram of the lateral line of a blind cave fish (*Astyanax fasciatus*). The blue dots outlined in white represent the canal pores in the canal lateral line system. Typically, one canal neuromast is located in between every two pores. The small blue dots over the body show the approximate locations of superficial neuromasts. The labels point to specific portions of the canal lateral line system: io, infraorbital; mc, mandibular; po, preopercular; so, supraorbital; st, supratemproal; tc, trunk. Figure is reproduced from Windsor et al. [178].

In this section, we will explore how the number and distribution of sensors over

the body of the fish (in 2D) affect the estimation task.

a. Optimization of m_1 and α

First, we consider how the accuracy of estimation of the oncoming vortices varies with the number of sensors used for the estimation task at the head and their distribution. According to the finding by Ristroph et al. [127] that the sensor density at the head is higher, correlating with the increased pressure fluctuations, we introduce a parameter α which varies the density of sensors at the head compared with the rest of the body. The N sensor positions, on the initial unflexed fish, are defined as:

$$x_j = \alpha\left(1-\cos\left(\frac{\pi}{2N}\left(j-\frac{1}{2}\right)\right)\right)+(1-\alpha)\frac{j}{N}, \qquad j=1,2,...N \tag{3.82}$$

$$y_j = \text{NACA}(x_j) \tag{3.83}$$

$$= 0.6\left(0.2969\sqrt{x_j}-0.1260x_j-0.3516x_j^2+0.2843x_j^3-0.1036x_j^4\right) \tag{3.84}$$

Figure 3-43 shows the effect of varying α from 0 to 1 on an arrangement of sensors over the body of the fish. For $\alpha = 0$, the sensors are linearly spaced in x, and for $\alpha = 1$, the sensors exhibit a cosine spacing over the body. For intermediate values, the sensors at the head are somewhat denser than the sensors along the body.

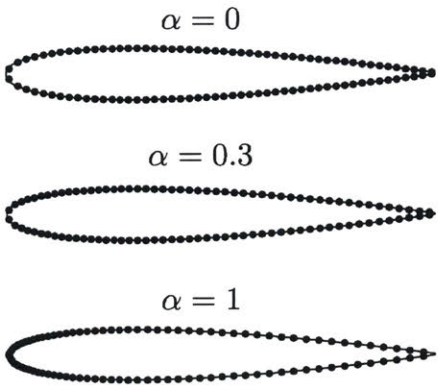

Figure 3-43: Diagram of the sensor distribution, where $\alpha = 0$ indicates a linear (in x) distribution, and $\alpha = 1$ indicates a cosine distribution near the nose.

Figure 3-44 shows the variation in estimation error with variations in the sensor distribution α and the number of sensors m_1 used for the estimation task. The

error is defined as the difference between the estimated streamwise position of the nearest vortex upstream of the nose and the actual measured position (the details of measuring the actual position are given in section 3.4.5). The error is calculated for a simulation in which the upstream fish swims at a frequency of $f = 1.8$, while the downstream fish swims at $f = 1.7$. Over a period of 10 s., the downstream fish encounters the approaching vortices at every possible phase difference ϕ_1; the error is averaged over this 10 s. period. A white gaussian noise of $\mathbf{w}_k \sim \mathcal{N}(0, 0.05)$ is added to the pressure measured at each timestep k.

Figure 3-44a shows the mean error calculated, while 3-44b shows the average of the error calculated each time the approaching vortex passes $x/L = 0$, the nose of the fish. Both error metrics look qualitatively similar, but the second error metric generally results in slightly lower errors because the estimation accuracy tends to improve as the vortex approaches the fish.

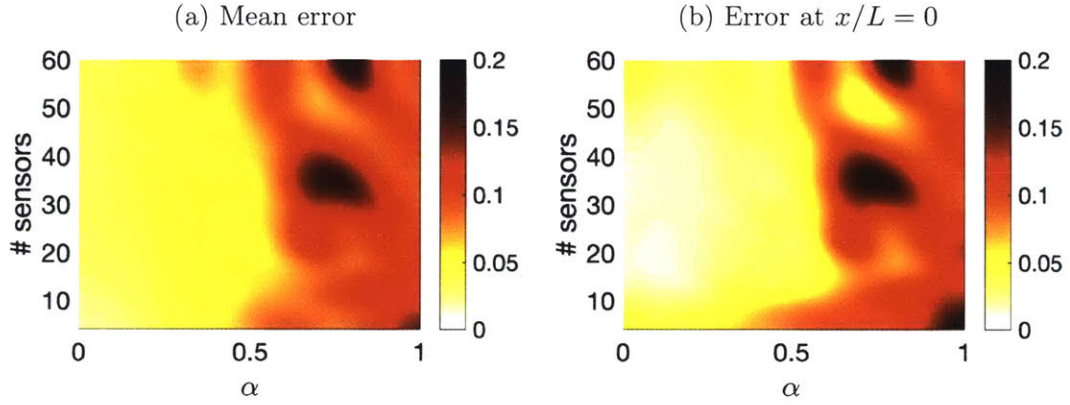

Figure 3-44: Estimation error of the streamwise position of the approaching vortex with variation of the number of sensors (m_1) and their distribution (α). (a) Mean error, (b) error at $x/L = 0$, where the vortex is closest to the nose of the fish.

Interestingly, the estimation error varies strongly with α. In particular, when $\alpha > 0.5$, the error increases dramatically for nearly all values of m_1. For $\alpha > 0.5$, the number of sensors used in the estimation greatly affects the estimation error, while for $\alpha < 0.5$, the estimation error remains very low regardless of the specific number of sensors used. The error at $x/L = 0$ is minimized for $\alpha = 0.1$ and $m_1 = 16$ ($e_x = 0.009$, $e_\phi = 0.016$).

Why is the estimation error particularly sensitive to α? For $\alpha = 1$, the first 20 sensors are contained within approximately 1% of the total length, the first 40 sensors are within 5% of the total length, and the first 60 sensors are within 11% of the total length. Within this range of values tested, the spatial features of the pressure sensed at the nose (figure 3-4) can clearly be captured regardless of the sensor density at the nose. Therefore, a higher α does not result in the ability to capture more detail (or more pressure fluctuations) near the nose, but it does result in an effectively heavier weight applied to measurements closer to the nose. However, the measurements taken at the nose are not necessarily more accurate, and the model of the interaction at the nose is not necessarily better. In fact, due to the greater pressure fluctuations at the nose, a given error in the estimated position of a vortex will often result in a greater measurement error at the nose than at a point further downstream. Therefore, a higher weight for the sensors close to the nose will often result in increased estimation error.

This is counterintuitive to the notion that fish typically possess a greater sensor density near the nose. However, while the density of canal neuromasts is higher near the nose, it is often a result of a splitting of the single trunk canal along the body into 3-4 separate canals at the head (figures 3-42, 3-49, 3-48). Each individual canal along the head does not appear to be significantly denser in pore/sensor count than the canal along the body. This suggests that the canal branching, and resultant increase in canal sensor density within the head region has evolved for the detection of 3-dimensional flow patterns rather than increased fluctuations in pressure.

b. Optimization of N and m_1

Since α effectively acts as a weight rather than a good metric for sensor distribution, we now attempt to find an optimal sensor configuration of N total sensors and m_1 sensors used for the estimation task at the head, with $\alpha = 0.1$. In this manner, N controls the density of sensors over the body, while m_1 governs the number and region of sensors at the head which are used for the estimation (figure 3-45). In addition, the robustness of the estimator was tested through adding a gaussian white noise of

$\mathbf{w}_k \sim \mathcal{N}(0, 0.1)$, $\mathcal{N}(0, 0.5)$ and $\mathcal{N}(0, 1)$.

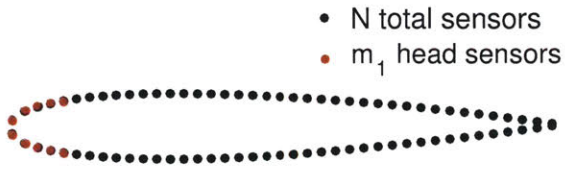

Figure 3-45: Diagram of the sensor distribution for $\alpha = 0.1$, with N total sensors over the body and m_1 sensors at the nose used for detection of oncoming vortices.

The mean error and error at $x/L = 0$ for the streamwise position of the closest upstream vortex are shown in figures 3-46a,b, given $\mathbf{w}_k \sim \mathcal{N}(0, 0.1)$. If the position of the upstream vortex is captured each time it passes $x/L = 0$ for the estimate of the wake phase, figure 3-46b shows that it is optimal to use over 150 sensors total, and 10-22 sensors at the nose for the estimator. With $N = 150$ and $m_1 = 10-22$, the error at $x/L = 0$ is under 0.02, corresponding with a phase estimate error of $e_\phi < 0.036$. It is clear that with too few sensors over the body ($N < 50$), the estimator cannot capture the pressure signature in sufficient spatial detail for a good estimate.

For $N > 150$, the estimation error is generally low ($e_x \sim 0.02$ for $10 < m_1 < 34$), and varies with both N and m_1. For low m_1, the estimate is corrupted partly by the measurement noise, and partly by reduced model accuracy very close to the nose (as was already demonstrated in the study of α). For high m_1, the sensors further downstream on the fish are corrupted by the signal induced by the formation of the induced vortex, which is not included in the immediate model. As can be seen in figure 2-4a, the induced vortex begins to form around $x/L = 0.1$, and rolls up into a distinct vortex with a very prominent signal as it passes $x/L = 0.2$.

Therefore, an optimal number of sensors at the nose is between $m1 = 10$ and 20. In general, increasing the total number of sensors N reduces the estimation error at $x/L = 0$. For $N = 200$ and $m1 = 16$, the error is minimized, at $e_x = 0.0069$, corresponding with a phase estimate error of $e_\phi = 0.0124$.

The error can be further reduced with a greater number of total sensors, but the computational cost increases as $\mathcal{O}(N^2)$. $N = 200$ total sensors, with $m_1 = 16$ sensors used for estimation of upstream vortices provides a good balance between

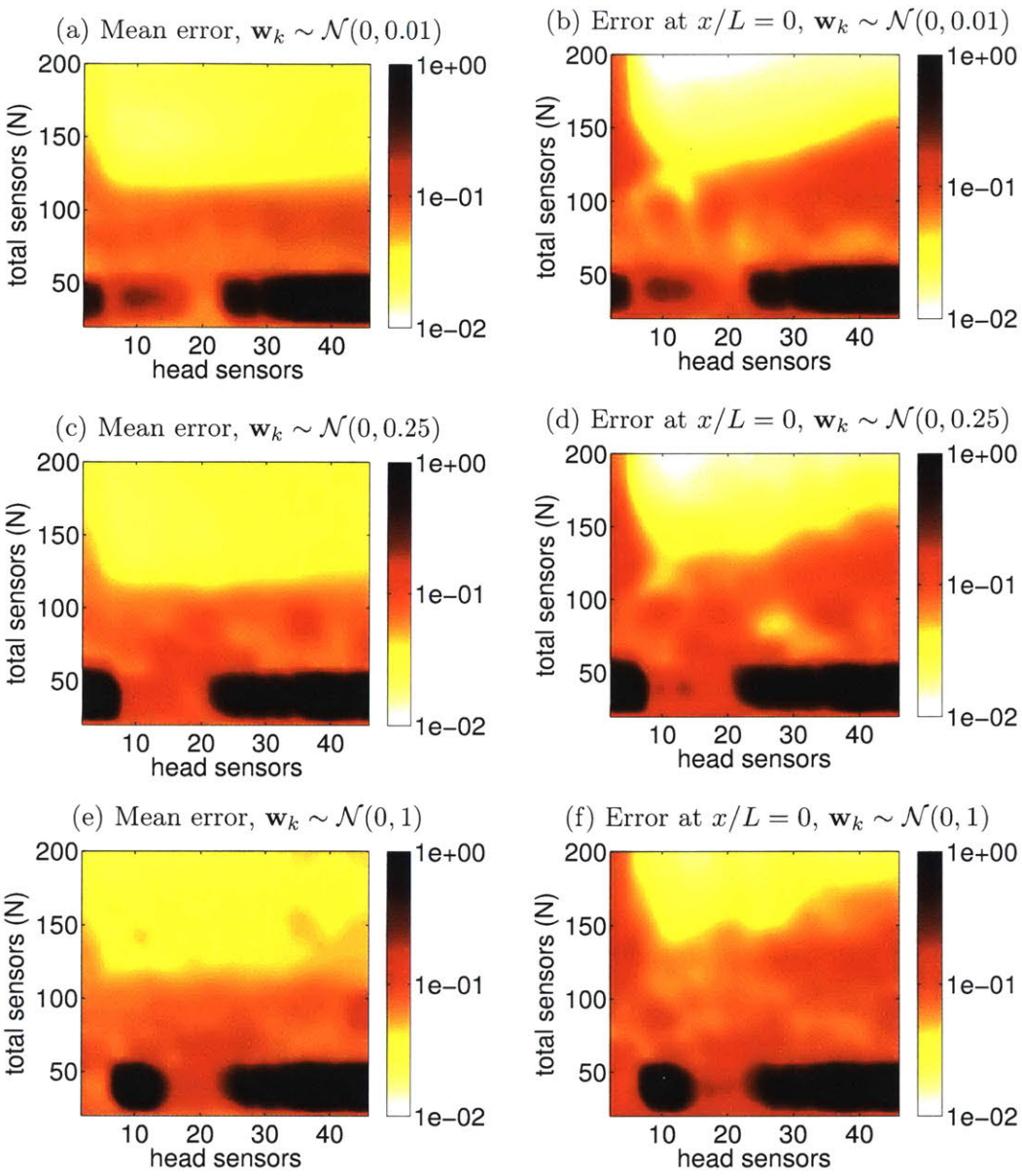

Figure 3-46: Estimation error of the streamwise position of the approaching vortex with variation of the total number of sensors on the fish (density) and the number of head sensors. (a, c, e) Mean error in the estimate of the x position of oncoming vortices for additive gaussian measurement noise with variance 0.01, 0.25 and 1, respectively. (b, d, f) error in the estimate of the x position of oncoming vortices at $x/L = 0$, where the vortex is closest to the nose of the fish, for additive gaussian measurement noise with variance 0.01, 0.25 and 1, respectively.

accuracy and computational cost. Therefore, these are the parameters used within the estimation experiments described throughout this thesis.

The estimator is extremely robust to measurement noise. As the variance of additive gaussian white noise is increased from 0.01 to 1, the estimation error decreases only slightly.

For reference, the mean variance of pressure measurements over the body of the fish is $\sigma^2 = 0.073$. The mean variance of pressure measurements over the nose of the fish is $\sigma^2 = 0.22$. For gaussian noise of the same variance as the pressure measurements themselves (figures 3-46c,d), the accuracy is only slightly reduced. For measurement noise that surpasses the variance of the pressure measurements significantly, (figures 3-46e,f), the accuracy of estimation is visibly reduced, but an error of roughly $e_x \approx 0.02$ can still be achieved with $N = 200$ total sensors and $10 < m_1 < 25$. $e_x \approx 0.02$ corresponds to a phase estimate error of approximately $e_\phi \approx 0.036$.

c. Trunk canal sensors

Within the framework presently developed, the estimation of vortices along the body of the fish is a significantly easier task than the estimation of upstream vortices. The induced vortices along the body of the fish create very characteristic pressure dips that are well correlated with their streamwise position. The estimator captures and follows these low pressure dips to infer the position of the induced vortices by the fish.

Therefore, the minimum density of sensors along the body of the fish is governed by the spatial scale of the vortices to be detected. In this case, the vortices from the wake of the upstream fish create pressure signatures with a lengthscale of roughly 0.1. With at least 10 sensors over one side of the body, the system will not completely miss any pressure changes caused by nearby vortices, but at least 20 sensors over one side ensures that the signal from each nearby vortex will be of moderate prominence. With an increasing number of sensors, the accuracy and robustness of the estimated vortex location increases (figure 3-47). 40 sensors per side appears to provide roughly 4 measurements per vortex, resulting in good peak prominence and robustness to noise.

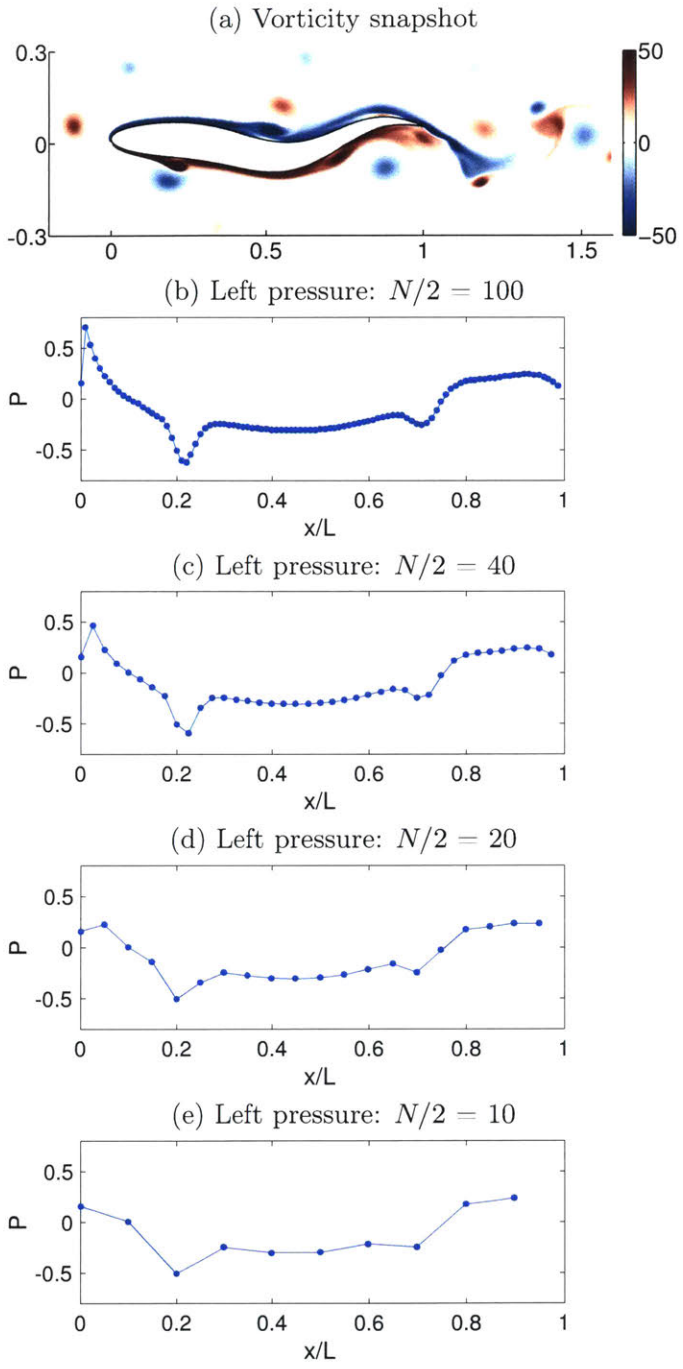

Figure 3-47: Resolution of the lateral line signal within the wake of another fish, for varying number of sensors N.

d. How do these results compare with real fish?

Our results so far suggest that along a 2D plane, fish should possess a roughly linear arrangement of sensors from head to tail. To estimate the phase of an oncoming

wake with positional error $e_x < 0.02$ and phase error $e_\phi < 0.036$, the sensor density should be such that there are at least $N = 150$ sensors over the entire body, with $10 < m_1 < 22$ sensors used for estimation at the head. Furthermore, a simple analysis of the sensor resolution along the body show that the sensor density should be capable of capturing the signature of vortices close to the body; for 4 sensors capturing each pressure dip, there should be at least $N = 80$ sensors on the whole body. How does this compare with the number of canal neuromasts found in real fish?

Figure 3-42 illustrates the lateral line system of a blind cave fish, *Astyanax mexicanus* [178]. The blue dots outlined in white represent the canal pores in the canal lateral line system, and there is typically one canal neuromast between every two pores. From the diagram, we can count roughly $N = 130$ canal pores on the entire fish, with $m_1 = 54$ pores on the head. Considering that the canal system on the head convers a three-dimensional space; on a 2D plane there would exist roughly $m_1^{2/3}$ of the sensors, for $m_{1,2D} \approx 14$ and $N_{2D} \approx 94$.

Figure 3-48 illustrates the cranial lateral line system for a rainbow trout, *Oncorhynchus mykiss* [105]. The trout possesses $m_1 = 90$ pores on the head, which translates to roughly $m_{1,2D} \approx 20$ sensors on a 2D plane. Siregar [139] found a similar number of canal pores on the head of the rainbow trout, and a total of $N = 173$ canal pores over the whole fish. On a 2D plane, this translates to roughly $N_{2D} \approx 105$ sensors.

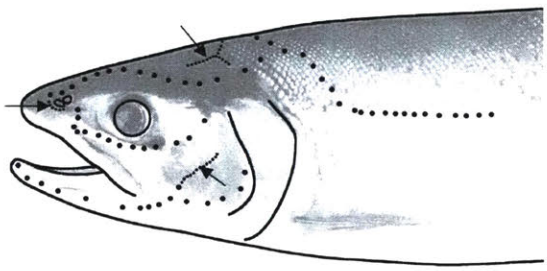

Figure 3-48: Diagram of the lateral line system for a rainbow trout, *Oncorhynchus mykiss*, reproduced from Montgomery et al. [105]. The black dots illustrate the locations of canal pores on the head and anterior trunk of the fish. The arrows point to the locations of arrays of superficial neuromasts on the head.

Figure 3-49 illustrates the lateral line system of a european carp, *Cyprinus carpio*. The red dots represent the canal pores in the canal lateral line system, and the green dots represent the superficial neuromasts on the fish. In total, the european carp has $m_1 = 116$ canal pores on its head, and $N = 190$ total canal pores over its body. This translates to roughly $m_{1,2D} \approx 24$ sensors on a 2D plane for the head, and $N_{2D} \approx 98$ total sensors over the body.

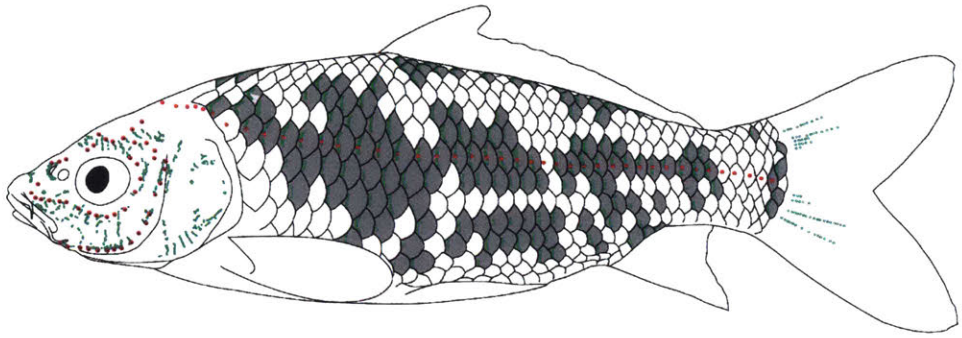

Figure 3-49: Diagram of the lateral line system for a european carp, *Cyprinus carpio*, reproduced from Watanabe et al. [168]. The red dots represent the canal pores in the canal lateral line system, and the green dots represent the superficial neuromasts on the fish.

A summary of the literature on number of canal pores/neuormasts found on the heads of some common fish is provided in table 3.1. The number of canal pores found on the bodies of these fish are also included when available. While information on the number of canal pores and neuromasts found within the cranial lateral line system is limited, the number of pored lateral line scales found on a variety of fish is widely available. The latter is summarized, for some common fish found in Wisconsin, in figure 3-50, compiled from the fish identification tool put together by the University of Wisconsin Center for Limnology, the Wisconsin Department of Natural Resources, and the University of Wisconsin Sea Grant Institute [113].

Interestingly, there is not a very strong correlation between the size of a fish and the number of canal pores/neuromasts it possesses. In fact, within a species, the number of canal pores within each canal subsystem remains roughly constant regardless of the fish size [139]. Across species, there does exist a wide range in the total canal

	Fish name	Reference	$L(mm)$	m_1	N	$m_{1,2D}$	N_{2D}
(a)	*A.mexicanus*	Windsor et al. [178]	50	54	130	14	94
(b)	*O. mykiss*	Montgomery et al. [105]	107	90		20	
(c)	*O. mykiss*	Siregar [139]	200	88	173	20	105
(d)	*E. buccata*	Reno [126]	380	64		16	
(e)	*C. carpio*	Watanabe et al. [168]	149	116	190	24	98
(f)	*Z. temminckii*	Watanabe et al. [168]	56	82	176	19	113
(g)	*A. burtoni*	Butler and Maruska [26]	72	48	121	13	86
(h)	*S. niloticus*	Peters [122]	180	64	134	16	86

Table 3.1: A summary of the literature on number of canal pores found on the heads of common fish.

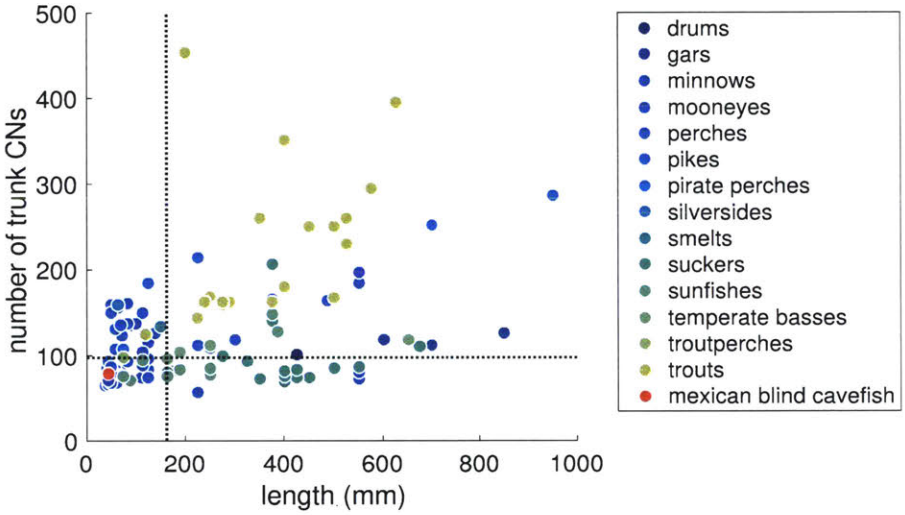

Figure 3-50: Summary of the number of pored lateral line scales found in 126 different species of fish found in Wisconsin, from a database by the University of Wisconsin Center for Limnology, the Wisconsin Department of Natural Resources, and the University of Wisconsin Sea Grant Institute [113]. The dotted represent the median values: median fish length = 162.5mm, and median number of trunk lateral line pores = 98 (counted on both sides of body).

neuromast (CN) count - between 48 and 116 in the cranial system and between 27 and 244 within the trunk canal system (for the present dataset). Fish live in a variety of environments, exposed to objects, flow structures, and prey/predator signals of varying lengthscales. Therefore, the large range in CN count is not unexpected. From table 3.1, the median value of cranial CNs is $\widetilde{m}_1 = 64$, and $\widetilde{m}_{1,2D} \approx 16$. The

median value of total CNs is $\widetilde{N} = 154$, and $\widetilde{N}_{2D} \approx 96$. From figure 3-50, the median value of trunk CNs is $\widetilde{N}_{\text{trunk}} = 98$.

These values compare very well with the ideal sensor numbers found presently ($10 < m_{1,2D} < 22$ and $80 < N < 150$).

e. Optimization of sensor layout

In contrast to the single lateral line canal along the trunk of the body, most fish are equipped with a cranial lateral line system that contains several branches, covering a three-dimensional space (figures 3-42, 3-49 and 3-48). Several hypothesis have been proposed to explain the proliferance of the lateral line system on the head. The pressure gradients and fluctuations are greatest at the head, leading to the theory that a greater density of canal sensors (as well as superficial neuromasts) are desired to adequately characterize the variations [127]. In addition, during forward swimming and when exploring new environments, fish will encounter signals first with the head. Logically, the prevalence of a branched cranial canal system is preferable because it provides the ability to gather three-dimensional information at the head to inform control decisions.

Strikingly, while there exists some diversity in the exact morphology of the cranial lateral line system among fish, the pattern of canal arrangement in most fish is very similar. The significance of the dominant canal layout remains an open question.

While the scope of the present study is limited to two dimensions, we can also ask: what sensor layout at the head results in optimal estimation of oncoming vortices? In the previous sections, we have explored the importance of sensor density and the number of sensors used for estimation at the nose. In this section, we will consider if there are regions of the head for which sensors will yield more accurate estimates.

With a base configuration of $N = 150$ possible sensor locations over the entire body, and $m_1 = 20$ possible sensor locations at the head, 1023 possible combinations of sensors at the head were tested. We assume that the sensor layout is left-right symmetric, and between 2 and 20 of the sensors at the head can be chosen for the estimation task.

Figure 3-51 shows the estimation error for each of the 1023 sensor combinations, organized by the number of head sensors (m_1) used within the configuration. There is not enough space to list each individual configuration, but generally speaking the entries closer to the beginning of each section consist of sensors closer to the nose, while later entries consist of sensors further downstream on the head. A white gaussian noise of $\mathbf{v}_k \sim \mathcal{N}(0, 0.01)$ was added to the measurements to simulate noise within the system.

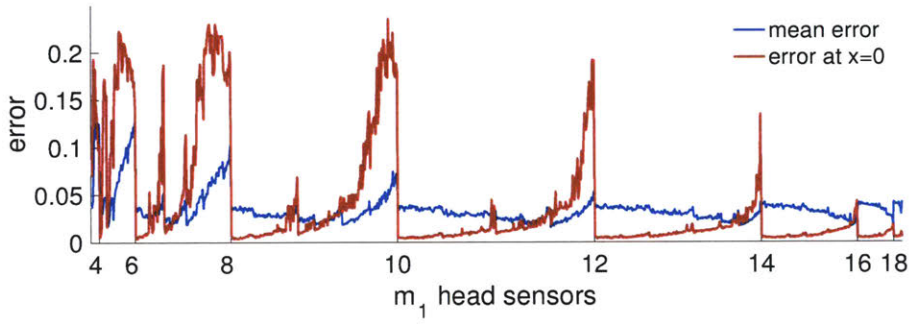

Figure 3-51: The error in the estimated streamwise position for the closest approaching vortex, averaged over the entire swimming period (blue line) and averaged over the points for which the vortex is at $x/L = 0$ (red line). Each point represents the error calculated for a specific combination of head sensors (not shown), with the total number of sensors in that configuration labeled on the x-axis.

This plot shows that the estimation error for vortices at $x/L = 0$ (closest to the nose) is minimized when sensors are closer to the nose. For the average estimation error over the entire swimming cycle, there is less variation in the estimation error, but the minimal error is reached at a slightly different point. For both, a relatively low error can be obtained regardless of m_1. Figures 3-52 - 3-55 show the configurations that minimize and maximize the average error, and configurations that minimize and maximize the error measured for vortices at $x/L = 0$, respectively.

Figure 3-52 depicts the sensor configurations which minimize the estimated vortex position error averaged over the entire swimming cycle. Each of these configurations, though they contain a varying number of sensors, result in a similar error of $e_x \approx 0.0185$, corresponding with an average phase estimate error of $e_\phi \approx 0.03$. The most prominent similarity between these configurations is that none of them include the

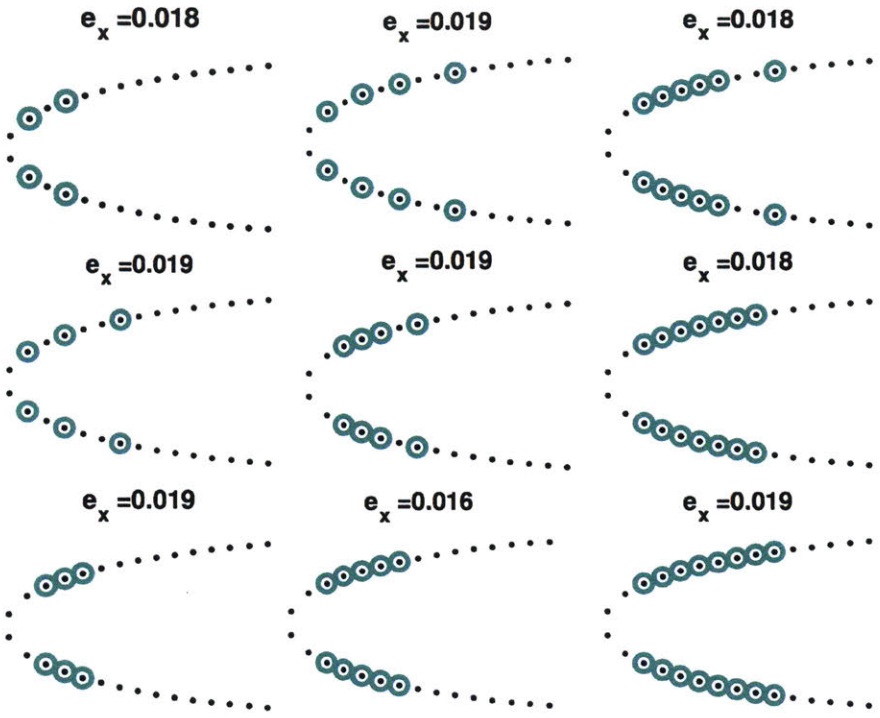

Figure 3-52: Configurations of head sensors which minimize the error in the estimated streamwise position of approaching vortices, averaged over the entire swimming cycle.

two sensors closest to the nose, and most do not include the front four sensors.

Figure 3-53 depicts the sensor configurations which maximize the estimated vortex position error averaged over the entire swimming cycle. In most of these, the sensors used are away from the nose. It follows that the error is maximized for these configurations; the sensors further downstream on the fish are corrupted by the signal created by the induced vortex, which is not included in the model for estimation of upstream vortices. When the estimate is created using the measurements from these sensors (and particularly when the total number of sensors is low), it results in high estimation error.

Interestingly, for the last two configurations on the right, the estimation error is more than doubled when the first four sensors are included (compare with figure 3-52). This enforces the idea that the sensors near the nose are harmful to the accuracy of vortex state estimation, when the state estimate is averaged over the entire swimming cycle. However, using sensors on the nose along with sensors further back yields a

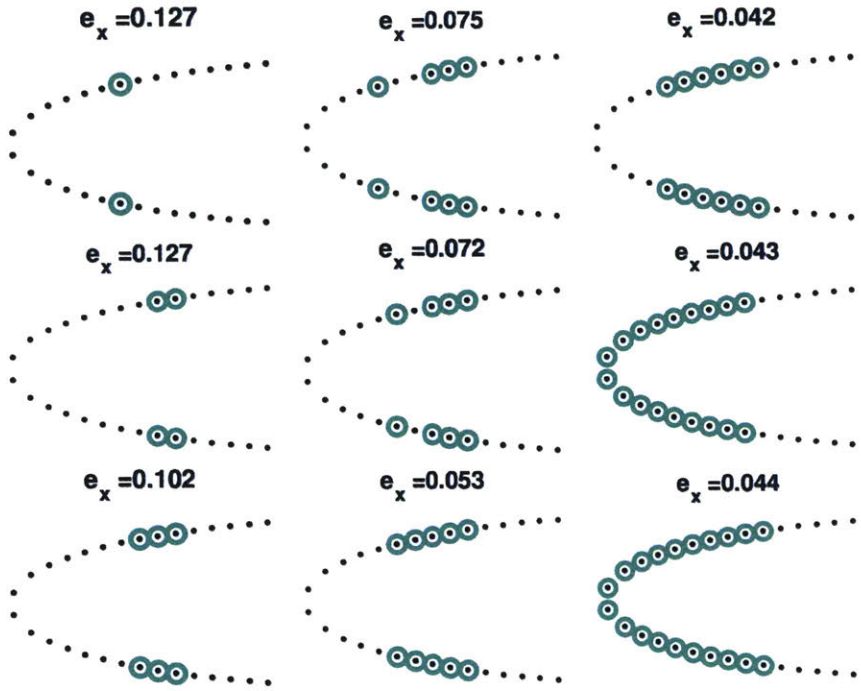

Figure 3-53: Configurations of head sensors which maximize the error in the estimated streamwise position of approaching vortices, averaged over the entire swimming cycle.

better estimate than using the far back sensors only.

Figures 3-54 and 3-55 depict the sensor configurations which minimize and maximize the estimated vortex position error averaged over the points at which the vortex is closest to the nose. Notably, all of the configurations that minimize the error at $x/L = 0$ do contain the front four sensors, in contrast with the configurations that minimized the period-averaged error. The configurations which maximize the estimation error at $x/L = 0$ are similar to those that maximize the period-averaged estimation error, focusing on the sensors further back. Clearly, to minimize the estimation error for vortices closest to the nose, it is desirable to use information collected close to the nose.

Interestingly, if only the front four sensors are used, the error is 30% higher than the error for the first case shown in figure 3-54. If only the front two sensors are used, the error is 14 times greater. This shows that while information collected at the nose is important for estimating the positions of nearby vortices, the information should

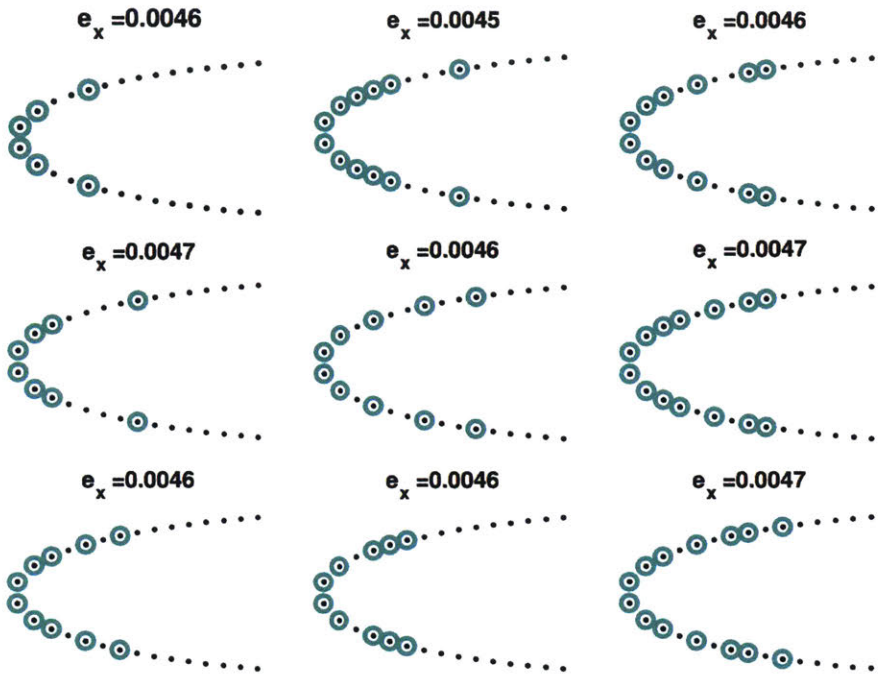

Figure 3-54: Configurations of head sensors which minimize the error in the estimated streamwise position of approaching vortices, averaged over the instances at which the closest vortex is lateral to the nose, at $x/L = 0$.

be in conjunction with additional measurements collected slightly further back for the best results. In particular, for characterizing vortices close to the nose, it appears to be best to use the front four sensors, and a scattering of sensors further downstream (the exact choice of which is not too important).

In summary, when estimating the position of vortices as they reach the nose (at $x/L = 0$), it is best to use sensors on the nose, in conjunction with a few sensors slightly further downstream. For estimating the positions of vortices within an oncoming vortex street continuously, the error is minimized when vortices close to the nose but excluding the sensors exactly on the nose are used.

These optimal sensor configurations are governed in part by the accuracy of the model; the preferred location for sensors is within areas for which the model matches the true system well. This is true for fish as well - the lateral line of fish is visibly positioned around fins and other disturbances that result in model uncertainty or measurement error [40, 32, 169]. On the head, flow disturbances can arise from the

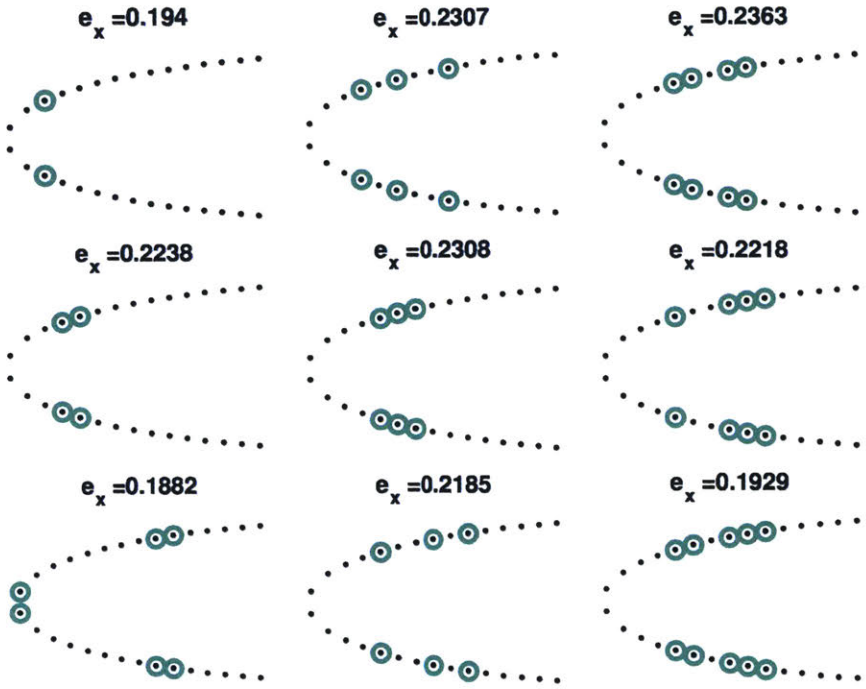

Figure 3-55: Configurations of head sensors which maximize the error in the estimated streamwise position of approaching vortices, averaged over the instances at which the closest vortex is lateral to the nose, at $x/L = 0$.

bulge of the eyes, the gills, and other features. While the source of model uncertainty is different within this system, the idea is the same - it is undesirable to place sensors in areas where the potential flow model does not perform well.

Another compelling idea in sensor placement is the concept of placing sensors in locations to capture maximally independent information (sensor B provides information that cannot be captured at sensor A), with the least number of sensors. However, at the nose of the fish, an approaching vortex will cause a unique pressure change over the entire surface. Detection and characterization of the vortex is not limited by the sensor resolution at the nose. Therefore, the more important concept within this estimation problem lies in placing sensors in locations best captured by the model.

3.7 Frequency detection

An important task in tandem schooling is the detection of and synchronization to the frequency of the upstream fish. A fish which does not swim at the same frequency as its leader will swim with an inconsistent phase relative to the upstream wake. As a result, due to a combination of beneficial and detrimental interactions over time, it will gain little to no efficiency enhancement.

Is it possible to detect the frequency of the upstream swimmer? For a ghost fish or a stationary rigid foil in the wake of a fish, the frequency would be easy to detect - the pressure changes sensed would be exactly the frequency of the upstream wake. However, when the fish swims at its own (different) frequency, the dominant signal sensed along its body is that of its own motion. Figure 3-56a shows the power spectral density of the pressure signal for a fish swimming at tail beat frequency $f = 2.4$ behind a fish swimming at $f = 2.1$. Interestingly, while there is a small peak near the nose at $f = 2.1$, the frequency of the upstream wake cannot be sensed along the rest of the body, despite the strong pressure dips associated with the vortices along the body.

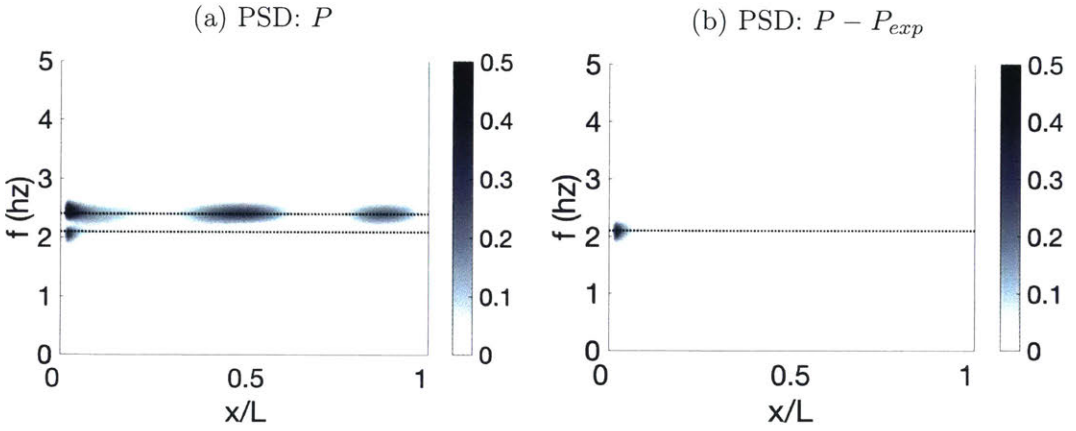

Figure 3-56: Power spectral density for a fish swimming with tail beat frequency $f = 2.4$ behind a fish swimming at $f = 2.1$, for (a) the pressure sensed by the lateral line, and (b) the pressure with the expected pressure due to its own motion subtracted.

Clearly, the signal of the upstream wake is strongest at the nose. Further downstream on the fish, the pressure changes due to vortices are weaker, and the positions of the vortices have been altered through interaction with the fish. Therefore, al-

though the weaker pressure changes along the body could likely be captured (due to the characteristic pressure dips that form), the frequency associated with them would be corrupted through interaction with the fish and would not be equal to the frequency of the upstream wake.

By subtracting the pressure expected P_{exp} from the total pressure sensed P along the fish, we can clearly can isolate the frequency of the upstream wake (figure 3-56b). Fish are presumed to be capable of doing precisely this, by using a "negative image" corresponding to the pressure expected due to their own motion to cancel out self-generated signals [106, 13]. The expected pressure signal P_{exp} in figure 3-56b is generated by measuring the pressure sensed by the fish in a separate simulation, with the fish swimming with the exact same kinematics in quiescent flow. Although pressure is nonlinear (equation 3.39), simply subtracting the expected pressure results in a markedly improved ability to extract the characteristics of the external flow field.

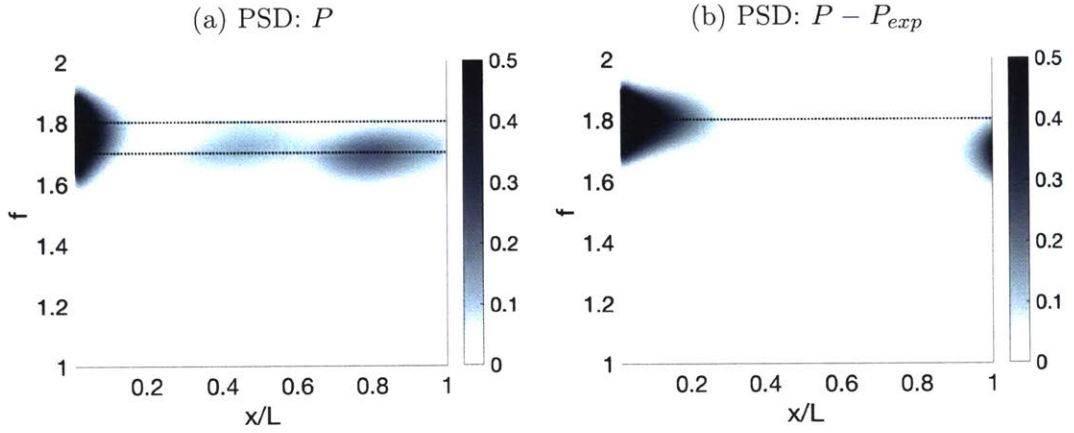

Figure 3-57: Power spectral density for a fish swimming with tail beat frequency $f = 1.7$ behind a fish swimming at $f = 1.8$, for (a) the pressure sensed by the lateral line, and (b) the pressure with the expected pressure due to its own motion subtracted.

How well does this algorithm work when the downstream fish swims at a frequency very close to the frequency of the upstream fish? In figure 3-57a, the PSD is shown for the pressure measured by a fish swimming at $f = 1.7$ behind a fish swimming at $f = 1.8$. In this case, the importance of filtering out the self-generated signal becomes much more evident. When the swimming frequencies are close together, the

frequency spectrum at the nose does not appear as two distinct peaks, but rather a single, wide-band peak.

Figure 3-57b shows the PSD for the pressure signal, with the expected pressure signal subtracted. In this case, the estimated pressure signal was generated using the potential flow model. The model captures the self-induced pressure extremely well at the head, allowing for a clear isolation of the upstream wake frequency of $f = 1.8$. Closer to the tail, there is a strong peak at the fish's own swimming frequency of $f = 1.7$; however, since only the signal at the head is used for wake frequency estimation, this is insignificant.

The potential flow model, similar to the model used by real fish, allows the fish to estimate its self-generated signal even when it is not swimming in quiescent water. From an engineering standpoint, this means that a separate (computationally costly) simulation does not need to be run in parallel for the estimation task to be performed. The potential flow model (panel method) can be solved within a fraction of a second at each timestep, leading to easy and fast integration within real-time control systems.

Through subtracting the estimated self-generated signal from the total pressure sensed, a fish can clearly identify the frequency of the oncoming wake.

3.8 How observable is the flow?

In section 3.6.4, we demonstrated that a foil sensed very similar signals due to a vortex placed in certain locations around its nose. Particularly in the lateral direction, relative large changes in the position of the vortex yielded pressure signatures that were very similar. Is there a way to quantify just how observable vortices in the near field around a fish or a foil is? In which positions is a vortex more observable and less observable? What is the range at which a fish can decipher the presence and position of a vortex with reasonable accuracy?

In this section, we will explore the sensitivity and observability of the fish lateral line in order to try to answer these questions. We use a potential flow model, consisting of a single point vortex with circulation $\Gamma = 0.1$ at position (x_1, y_1) within

a uniform stream of velocity U_∞, near a foil with N pressure sensors (figure 3-58). We begin by considering a fish moded as a rigid foil, and subsequently explore the sensitivity and observability of an undulating fish at a single timestep.

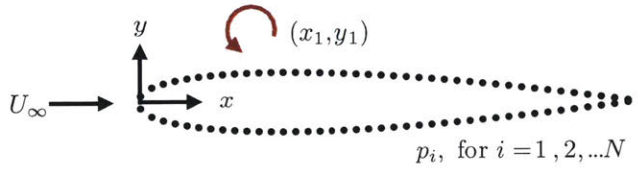

Figure 3-58: Diagram of the potential flow foil + vortex system used in the following studies on system sensitivity and observability.

3.8.1 System sensitivity

Sensitivity measures the change in the output $\mathbf{p}$, due to a disturbance to the system. We consider three types of sensitivity: 1) the sensitivity S_0 to the presence of a vortex (flow disturbance) in the near field, which indicates how detectable a vortex in that position is, 2) the sensitivity S_x to the streamwise vortex position, and 3) the sensitivity S_y to the lateral vortex position:

$$S_0(\mathbf{x}) = \text{mean}\left(|\Delta \mathbf{p}|\right) = \frac{1}{N}\sum_{i=1}^{N} |p(\mathbf{x}_1) - p_{exp}| \tag{3.85}$$

$$S_x(\mathbf{x}) = \text{mean}\left(\left|\frac{\partial \mathbf{p}}{\partial x}\right|\right) = \frac{1}{N dx}\sum_{i=1}^{N} |p(\mathbf{x}) - p(\mathbf{x} + \delta x)| \tag{3.86}$$

$$S_y(\mathbf{x}) = \text{mean}\left(\left|\frac{\partial \mathbf{p}}{\partial y}\right|\right) = \frac{1}{N dy}\sum_{i=1}^{N} |p(\mathbf{x}) - p(\mathbf{x} + \delta y)| \tag{3.87}$$

The pressure vector $\mathbf{p}$ is a function of $\mathbf{x} = [x\ y\ \Gamma]$, the state of the vortex. $\mathbf{p}_{exp}$ is the expected pressure; treating the vortex as an unknown disturbace, $\mathbf{p}_{exp}$ is the pressure the fish expects to feel due to its own swimming motion only.

For each of these, we calculate the sensitivity of the pressure measured by the fish for an ideal point vortex located at an array of points in the near field; the sensitivity as a function of the vortex position is plotted in figure 3-59.

(a) S_0: Sensitivity to vortex presence

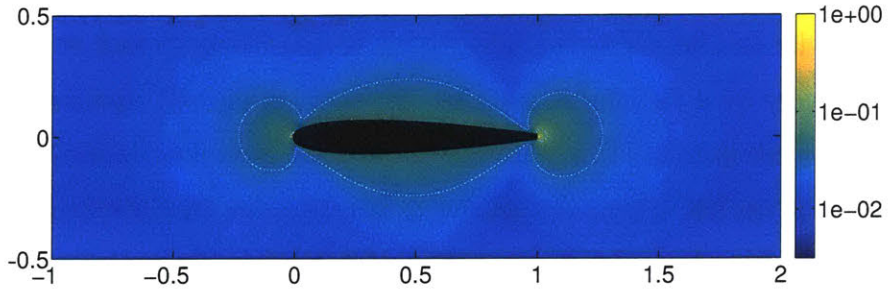

(b) S_x: Sensitivity to streamwise vortex position

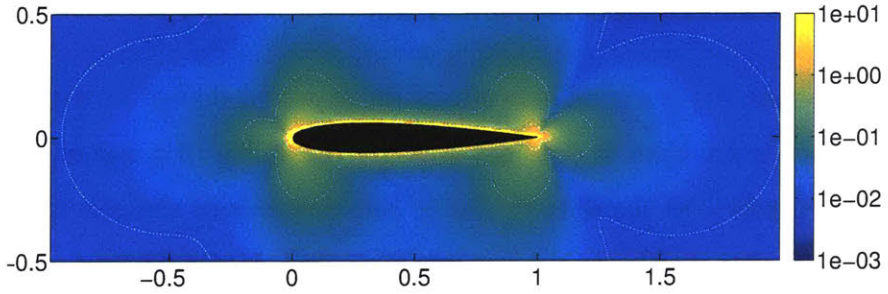

(c) S_y: Sensitivity to lateral vortex position

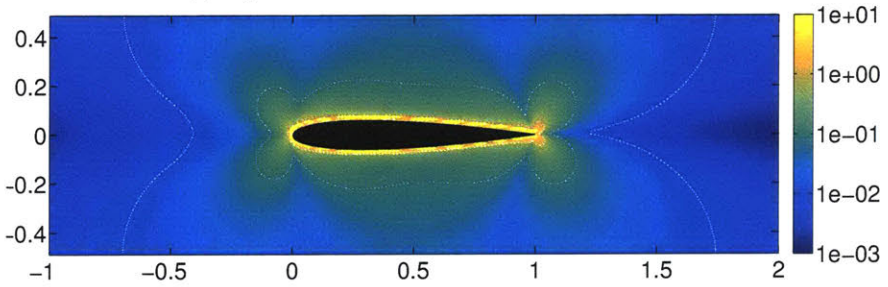

Figure 3-59: Sensitivity of the pressure measurements to (a) the presence of a vortex in the near field, (b) the streamwise position of a vortex in the near field, and (c) the lateral position of a vortex in the near field. Calculations were performed with a potential flow model (no wake), for a single positively signed point vortex ($\Gamma = 0.1$) in various positions around the foil in uniform stream $U_\infty = 1$. The color at each point in the field represents the mean change to the pressure sensed by the fish (equations 3.85-3.8.3), and a few contours are highlighted to illustrate the shape of the sensitivity regions.

Figure 3-59a shows that vortices directly in front of and to the sides of the foil will yield an average pressure change over the foil of $\bar{\Delta p} = 0.1$ within a quarter of a body length. The sensitivity drops off quickly from there. Furthermore, there is a "blind spot" laterally away from the head, in which the sensitivity is reduced.

From figures 3-59b and c, we can see that while the foil is about equally sensitive to the streamwise and lateral motion of a vortex, its sensitivity to each at a particular location may vary by a significant amount. For vortices directly upstream from the foil, the foil is more sensitive to streamwise rather than lateral deviations in location. Along the side of the foil, it is more sensitive to lateral rather than streamwise changes in position. This is in line with figures 3-35 and 3-36. Directly upstream of the foil, the signals due a variation of streamwise position are far more distinguishable than the signals due to a variation of lateral position.

While the sensitivity is a good indicator of the expected change in output provided a change in the vortex state, it does not measure the ability of a system to infer the unknown states provided the output. Some combinations of changes in the vortex state can yield similar changes to the pressure measured. If two different combinations of state changes result in the same change to the pressure, the system is unobservable. In the next section, we will consider the observability of the system.

3.8.2 System observability

In control systems theory, *observability* is a measure of the ability of a system to infer its states $\mathbf{x}$ provided the available measurements $\mathbf{y}$. A system is observable if, for any possible combination of state and input vectors, the current state can be determined in finite time using only the available measurements. For time-invariant linear systems, an observability matrix can be constructed to easily test if the system is observable. For the state space system:

$$\text{state transition model:} \qquad \dot{\mathbf{x}} = \mathbf{A}\mathbf{x} + \mathbf{B}\mathbf{u} + \mathbf{w} \tag{3.88}$$

$$\text{measurement model:} \qquad \mathbf{y} = \mathbf{C}\mathbf{x} + \mathbf{v} \tag{3.89}$$

the observability matrix $\mathcal{O}$ is defined as:

$$\mathcal{O} \equiv \begin{bmatrix} \mathbf{C} \\ \mathbf{CA} \\ \mathbf{CA}^2 \\ \vdots \\ \mathbf{CA}^{n-1} \end{bmatrix} \tag{3.90}$$

and the system is observable if $\mathcal{O}$ has rank equal to n, where n is the number of states within the system.

For a nonlinear system defined by the nonlinear state and measurement functions f and g,

$$\text{state transition model:} \qquad \dot{\mathbf{x}} = f(\mathbf{x}, \mathbf{u}) + \mathbf{w} \tag{3.91}$$

$$\text{measurement model:} \qquad \mathbf{y} = g(\mathbf{x}) + \mathbf{v} \tag{3.92}$$

the system is *locally* observable if for combinations of state and input vectors close to the current state and input vector, the current state can be determined in finite time using the available measurements. The local observability matrix can be constructed using the Lie derivatives of the system, which represent the time derivatives of g along the system trajectory $\mathbf{x}$:

$$L_f^j[g(\mathbf{x})] \equiv \frac{\partial^j h(\mathbf{x})}{\partial \mathbf{x}}^j f(\mathbf{x}) \tag{3.93}$$

The observability mapping $\mathbf{Q}(\mathbf{x})$ is then:

$$\mathbf{Q}(\mathbf{x}) \equiv \begin{bmatrix} \mathbf{y} \\ \dot{\mathbf{y}} \\ \ddot{\mathbf{y}} \\ \vdots \\ \partial^{n-1}\mathbf{y}/\partial t^2 \end{bmatrix} \begin{bmatrix} L_f^0[g(\mathbf{x})] \\ L_f^1[g(\mathbf{x})] \\ L_f^2[g(\mathbf{x})] \\ \vdots \\ L_f^{n-1}[g(\mathbf{x})] \end{bmatrix} \tag{3.94}$$

The nonlinear system is locally observable if $\partial \mathbf{Q}(\mathbf{x})/\partial \mathbf{x}$ is full rank [64].

For a potential flow foil + vortex system, in which the goal is to estimate the unknown vortex state:

$$\mathbf{x} = [x \quad y \quad \Gamma] \tag{3.95}$$

and the state transition and measurement functions (with no noise) are given as:

$$\dot{\mathbf{x}} = f(\mathbf{x}) \tag{3.96}$$

$$\mathbf{p} = g(\mathbf{x}) \tag{3.97}$$

the local observability matrix is:

$$\mathcal{O}(\mathbf{x}) \equiv \frac{\partial \mathbf{Q}(\mathbf{x})}{\partial \mathbf{x}} = \begin{bmatrix} \frac{\partial}{\partial \mathbf{x}} L_f^0[g(\mathbf{x})] \\ \frac{\partial}{\partial \mathbf{x}} L_f^1[g(\mathbf{x})] \\ \frac{\partial}{\partial \mathbf{x}} L_f^2[g(\mathbf{x})] \end{bmatrix} \tag{3.98}$$

$$= \begin{bmatrix} \begin{bmatrix} \frac{\partial \mathbf{p}}{\partial x} & \frac{\partial \mathbf{p}}{\partial y} & \frac{\partial \mathbf{p}}{\partial \Gamma} \end{bmatrix} \\ \frac{\partial}{\partial \mathbf{x}} \begin{bmatrix} \frac{\partial \mathbf{p}}{\partial x}\dot{x} & \frac{\partial \mathbf{p}}{\partial y}\dot{y} & \frac{\partial \mathbf{p}}{\partial \Gamma}\dot{\Gamma} \end{bmatrix} \\ \frac{\partial}{\partial \mathbf{x}} \left(\begin{bmatrix} \frac{\partial}{\partial \mathbf{x}} \begin{bmatrix} \frac{\partial \mathbf{p}}{\partial x}\dot{x} & \frac{\partial \mathbf{p}}{\partial y}\dot{y} & \frac{\partial \mathbf{p}}{\partial \Gamma}\dot{\Gamma} \end{bmatrix} \end{bmatrix} \begin{bmatrix} \dot{x} \\ \dot{y} \\ \dot{\Gamma} \end{bmatrix} \right) \end{bmatrix} \tag{3.99}$$

Note that while $\partial/\partial \mathbf{x} L_f^0[g(\mathbf{x}]$ simply consists of the partial derivatives of the measured pressure $\mathbf{p}$, $\partial/\partial \mathbf{x} L_f^1[g(\mathbf{x}]$ and $\partial/\partial \mathbf{x} L_f^2[g(\mathbf{x}]$ also include the dynamics of the system.

A quick calculation shows that for all vortex positions within the fluid domain, the local observability matrix is full rank. However, for a real system, which contains process and measurement noise, the rank of the observability matrix may not be the best indicator. In the presence of noise, it is generally impossible to reconstruct the exact state from the measurements. While a full rank observability matrix indicates that it is possible to reconstruct *some* state from the measurements collected, the reconstructed state may not be accurate. In this case, it is more practical to consider

an unobservability index. Some common unobservability indices are the reciprocal of the smallest singular value of $\mathcal{O}$, and the *condition number* of $\mathcal{O}$, which is the ratio between the largest and smallest singular values [85].

Presently, we use the condition number κ of $\mathcal{O}$ to quantify the observability. If this is large, it indicates that small changes in the output (i.e., noise in the pressure measurements) will cause large changes in the estimated states.

The condition numbers for $\partial \mathbf{Q}_0(\mathbf{x})/\partial \mathbf{x}$, $\partial \mathbf{Q}_1(\mathbf{x})/\partial \mathbf{x}$ and $\partial \mathbf{Q}_2(\mathbf{x})/\partial \mathbf{x}$ are plotted in figure 3-60, in which:

$$\frac{\partial \mathbf{Q}_0(\mathbf{x})}{\partial \mathbf{x}} = \left[\frac{\partial}{\partial \mathbf{x}} L_f^0[g(\mathbf{x})]\right] \tag{3.100}$$

$$\frac{\partial \mathbf{Q}_1(\mathbf{x})}{\partial \mathbf{x}} = \begin{bmatrix} \frac{\partial}{\partial \mathbf{x}} L_f^0[g(\mathbf{x})] \\ \frac{\partial}{\partial \mathbf{x}} L_f^1[g(\mathbf{x})] \end{bmatrix} \tag{3.101}$$

$$\frac{\partial \mathbf{Q}_2(\mathbf{x})}{\partial \mathbf{x}} = \begin{bmatrix} \frac{\partial}{\partial \mathbf{x}} L_f^0[g(\mathbf{x})] \\ \frac{\partial}{\partial \mathbf{x}} L_f^1[g(\mathbf{x})] \\ \frac{\partial}{\partial \mathbf{x}} L_f^2[g(\mathbf{x})] \end{bmatrix} \tag{3.102}$$

Which condition number provides the best indicator of local observability? Recall that in equation 3.99, we demonstrated that while $\partial/\partial \mathbf{x} L_f^0[g(\mathbf{x}]$ simply consists of the partial derivatives of the measured pressure $\mathbf{p}$, $\partial/\partial \mathbf{x} L_f^1[g(\mathbf{x}]$ and $\partial/\partial \mathbf{x} L_f^2[g(\mathbf{x}]$ also include the dynamics of the system. Therefore, while κ_0 reflects the observability of the system, provided only the instantaneous pressure measurements, $\kappa_1(\mathbf{x})$ and $\kappa_2(\mathbf{x})$ reflect the observability of the system provided the current and past pressure measurements. With knowledge of the state transition function, past measurements can also contribute to the current state estimate. The plots of $\kappa_1(\mathbf{x})$ and $\kappa_2(\mathbf{x})$ reflect this - the condition number is much lower across the fluid domain in these case, indicating that observability is improved with the utilization of dynamic information.

What does the use of dynamic information entail? With a recursive estimation algorithm such as the Kalman filter, a series of measurements over time are used, in conjunction with models of the state transition and measurement, to estimate the unknown states within the system (section 3.6.2). In this manner, they produce more

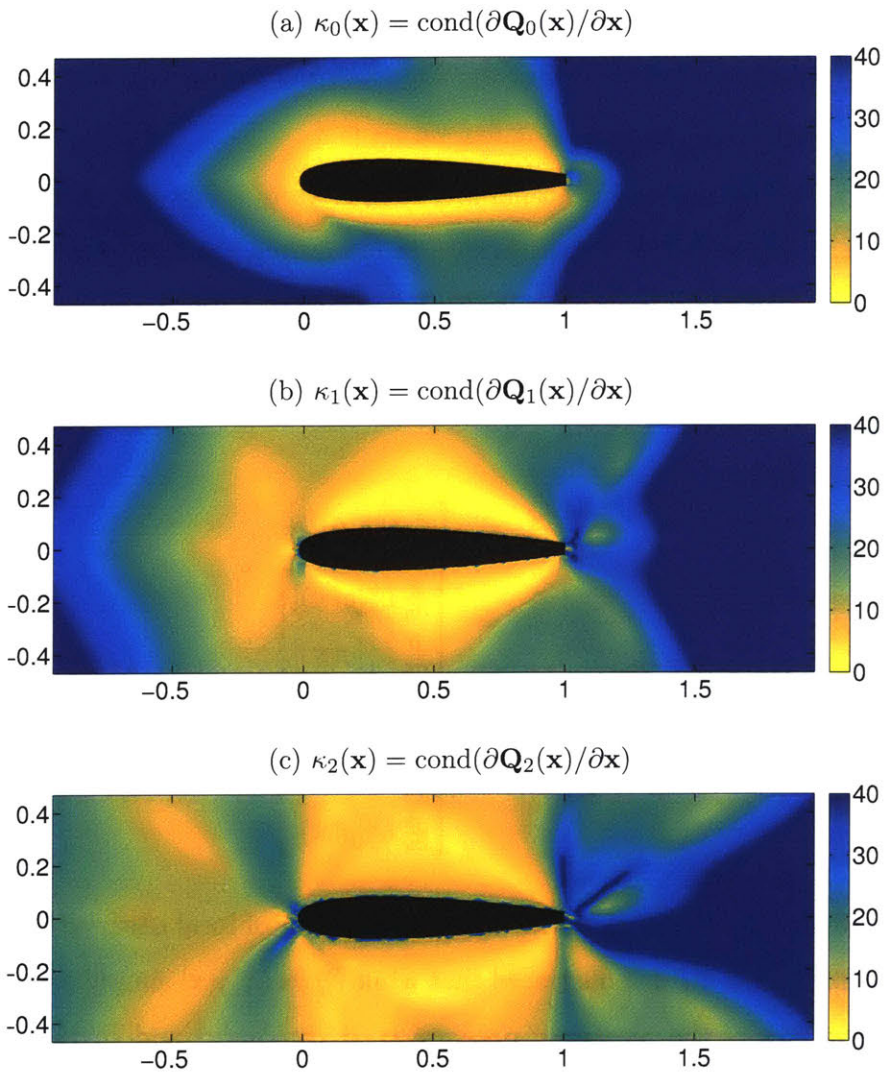

Figure 3-60: The conditioning numbers for the local observability matrices are plotted, in which the local observability matrix is defined as (a) $\partial \mathbf{Q}_0(\mathbf{x})/\partial \mathbf{x}$, (b) $\partial \mathbf{Q}_1(\mathbf{x})/\partial \mathbf{x}$, and (c) $\partial \mathbf{Q}_2(\mathbf{x})/\partial \mathbf{x}$, for vortex state $\mathbf{x} = [x\ y\ \Gamma]$. The definitions for the three matrices are provided ins equations 3.100-3.102. Calculations were performed with a potential flow model, for a stationary foil (no wake) in uniform stream $U_\infty = 1$, with a single point vortex at varying locations in the near-field (figure 3-58).

accurate estimates than could be produced using a single measurement alone. Similarly, figures 3-60b,c show that the observability is improved through use of dynamic information.

In particular, the regions to each side of the fish become significantly more observable, in comparison with the other regions around the fish. This makes sense -

vortices to the side of the fish are particularly easy to track; for a vortex which has convected to the middle of the fish, the history of pressure changes over time should allow for a very good estimate of its position.

What can we infer from $\kappa_0(\mathbf{x})$, shown in figure 3-60a? This index is more intuitive, providing a way to quantify the system observability, when provided an instantaneous pressure signal. As expected, it shows a region of high observability (low condition number) immediately surrounding the fish, which quickly decays with distance from the fish.

Can we draw any physical conclusions from the magnitude of the condition number $\kappa_0(\mathbf{x})$? What is considered a "high" condition number? Traditionally, ill-conditioned matrices are defined as those with condition numbers of 10^5 or even higher. $\kappa_1(\mathbf{x})$, however, within the region shown, only reaches a maximum of about 100 (for $x < 1$, upstream of the fish trailing edge). As previously mentioned, κ provides a measure of how much we can expect the state estimate to fluctuate, given noise in the measurements. Mathematically, for a linear system $\mathbf{Ax} = \mathbf{b}$, the condition number of $\mathbf{A}$ is the maximum ratio of the relative error in $\mathbf{x}$ divided by the relative error in $\mathbf{b}$. We can write:

$$d\mathbf{p} = \begin{bmatrix} \frac{\partial \mathbf{p}}{\partial x} & \frac{\partial \mathbf{p}}{\partial y} & \frac{\partial \mathbf{p}}{\partial \Gamma} \end{bmatrix} \begin{bmatrix} dx \\ dy \\ d\Gamma \end{bmatrix} = \frac{\partial \mathbf{Q}_0(\mathbf{x})}{\partial \mathbf{x}} \begin{bmatrix} dx \\ dy \\ d\Gamma \end{bmatrix} \tag{3.103}$$

where $d\mathbf{p}$ is a small deviation in the pressure measurement vector (i.e., the vector of measurement noise $\mathbf{v}$). Therefore, the condition number $\kappa_0(\mathbf{x}) = \text{cond}(\partial \mathbf{Q}_0(\mathbf{x})/\partial \mathbf{x})$ indicates the expected variation in the state estimate $[dx;\ dy;\ d\Gamma]$, given some amount of measurement noise. For a vortex in a position within the field with a condition number of $\kappa_0(\mathbf{x}) = 40$, a single pressure measurement with noise $v = 0.01$ could result in an estimated postion error of 0.4! Therefore, while an observability matrix with a condition number of 40 is far from singular, it does indicate that a small amount of noise within the measurements will result in significant estimation error.

3.8.3 Sensitivity and observability: undulating fish

Until this point, we have considered the sensitivity and observability of near-field vortices to a rigid foil within a uniform stream. However, the fish is not rigid but undulates within the wake. In section 3.5.1, we demonstrated that the interaction between a solid body and the flow field affects the signal sensed by the fish. In fact, the self-induced effect was shown to improve observability, allowing for the distinction between a positive and negative vortex. How does the undulating motion of the fish affect sensitivity and observability?

Humans interact with their environments to explore them and learn about them. Children are fascinated by new textures and new shapes, interacting with them by running their hands over them, banging them against other objects, and putting them in their mouths in order to learn about them. Indeed, by interacting with new objects in a variety of ways, children can gain a comprehensive understanding of the objects over time.

Fish similarly interact with their environments in order to learn about them over time. Blind fish are known to explore their environments, building a spatial map and learning to navigate solely by using information captured with the lateral line [36]. Studies have also shown that by gliding past an object a few times and analyzing the hydrodynamic interaction with the object, fish can identify the shape, size and location of the object [96]. Within a wake, Chambers et al. [28] showed that a moving robotic fish head could characterize the flow better when compared with a fish head held in place. Indeed, this is likely why dolphins swim back and forth in front of a ship before settling on a bow-riding position [53]. Hydrodynamic interaction is clearly important for sensing, but is it possible that fish also possess the ability to precisely control their interaction with the environment to gather the most information?

Furthermore, it has been shown that flapping wings can enhance stability and maneuverability at the same time, compared with rigid wings. While the downstroke is always stabilizing, the upstroke can be varied for varying levels of stability and maneuverability [150]. Can unsteady propulsion also enhance observability?

In this section, we explore the ability of unsteady propulsion to enhance sensitivity and observality to a vortex wake, through plotting the sensitivity and observability metrics previously described for a vortex around an undulating fish at a single timestep.

(a) S_0: Sensitivity to vortex presence

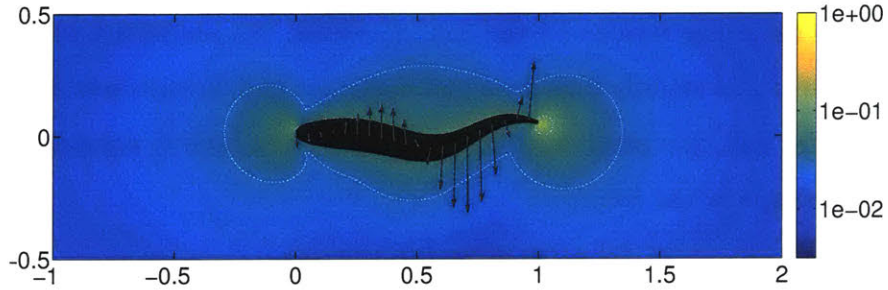

(b) S_x: Sensitivity to streamwise vortex position

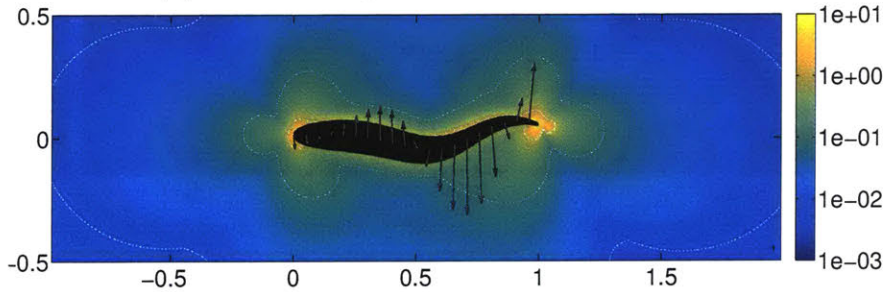

(c) S_y: Sensitivity to lateral vortex position

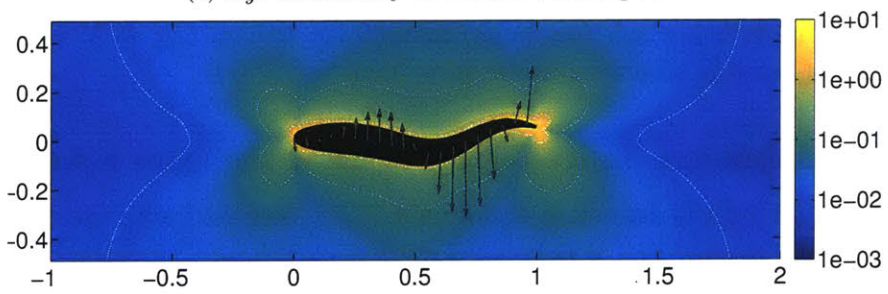

Figure 3-61: Sensitivity of the pressure measurements to (a) the presence of a vortex in the near field, (b) the streamwise position of a vortex in the near field, and (c) the lateral position of a vortex in the near field. Calculations were performed with a potential flow model (no wake), for a single positively signed point vortex ($\Gamma = 0.1$) in various positions around an undulating fish in uniform stream $U_\infty = 1$. The color at each point in the field represents the mean change to the pressure sensed by the fish (equations 3.85-3.8.3), and a few contours are highlighted to illustrate the shape of the sensitivity regions.

Figure 3-61 illustrates the sensitivity of the pressure sensed by an undulating fish to the presence and position of a vortex in the near-field. S_0, S_x, and S_y are defined in equations 3.85-. Qualitatively, the sensitivity contours around an undulating fish look very similar to those around a rigid foil (figure 3-59).

Some qualitative differences do exist. Near the undulation trough on the right side close to $x/L = 0.6$, the sensitivity to vortex streamwise position is reduced in comparison to the other regions on the fish. However, the sensitivity to streamwise position appears to be slightly improved just upstream and downstream of this point. Along the entire fish, the sensitivity contours for vortex lateral position appear to shift with the shape of the fish.

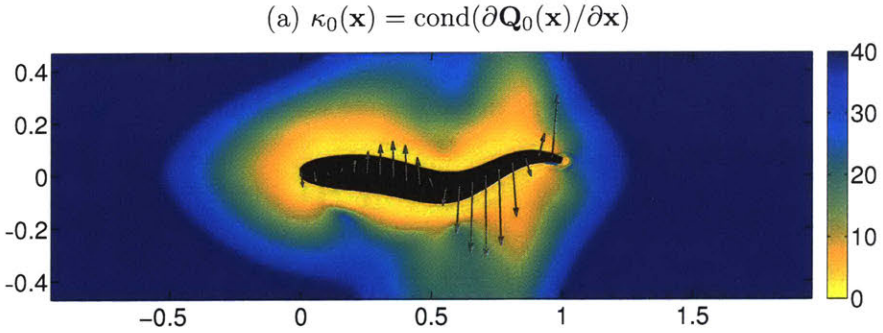

Figure 3-62: The conditioning number for the local observability matrix is plotted, in which the local observability matrix is defined as $\partial \mathbf{Q}_0(\mathbf{x})/\partial \mathbf{x}$. The definitions for the matrix is provided in the text. Calculations were performed with a potential flow model, for an undulating fish (no wake) in uniform stream $U_\infty = 1$, with a single point vortex at varying locations in the near-field.

Figure 3-62 illustrates the observability of the system (given a single pressure snapshot). $\partial \mathbf{Q}_0(\mathbf{x})/\partial \mathbf{x}$ is defined in equation 3.102. Compared with the observability of a single vortex by a rigid foil (figure 3-60), the observability appears to be slightly improved in some areas and slightly reduced in others.

These results suggest that unsteady propulsion does not generally improve the sensitivity or observability of a fish to vortices in the near field. While the flexed shape and lateral velocity of the undulating fish does result in changes to the local sensitivity and observability in some regions, the change is not significant. However, the results do suggest that vortices may be slightly more observable away from the

undulation troughs.

3.8.4 Observability: varying swimming parameters

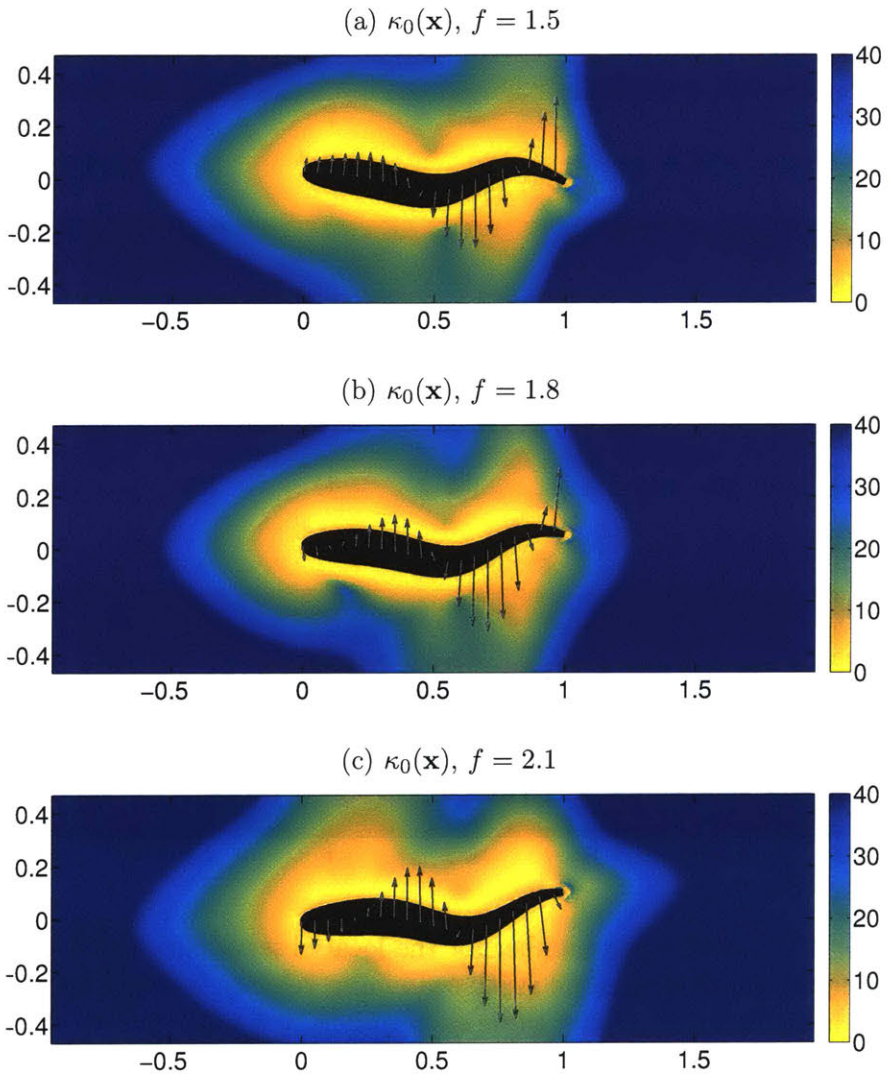

Figure 3-63: The conditioning number for the local observability matrix, for varying tail-beat frequency (with swimming velocity, tail beat amplitude, and all other swimming parameters held constant). Under these assumptions, the observability of a near-field vortex in all three cases is similar, but lateral observability appears to be increased with increasing frequency.

To ensure that the observability of a vortex near the fish does not vary significantly with its swimming parameters, an observability analysis was additionally carried out

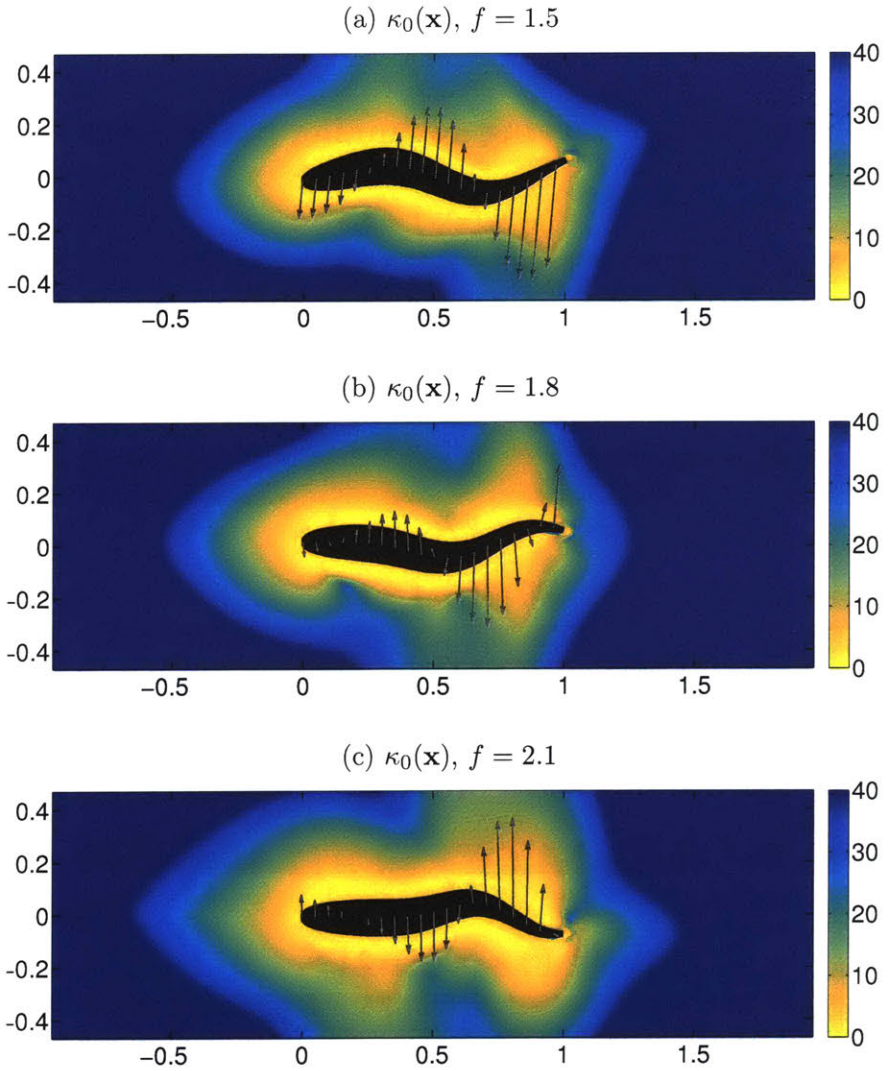

Figure 3-64: The conditioning number for the local observability matrix, for varying tail-beat frequency and amplitude (with swimming velocity, and all other swimming parameters held constant). Under these assumptions, the observability of a near-field vortex in all three cases is similar.

for fish swimming with varying frequency, and varying wavelength.

Figure 3-63 shows the conditioning number for the local observability matrix, for fish swimming at frequency $f = 1.5$, $f = 1.8$, and $f = 2.1$, with all other swimming parameters held constant.

It can be seen that while there the observability for all three systems is comparable, increasing the swimming frequency does appear to result in a slight increase

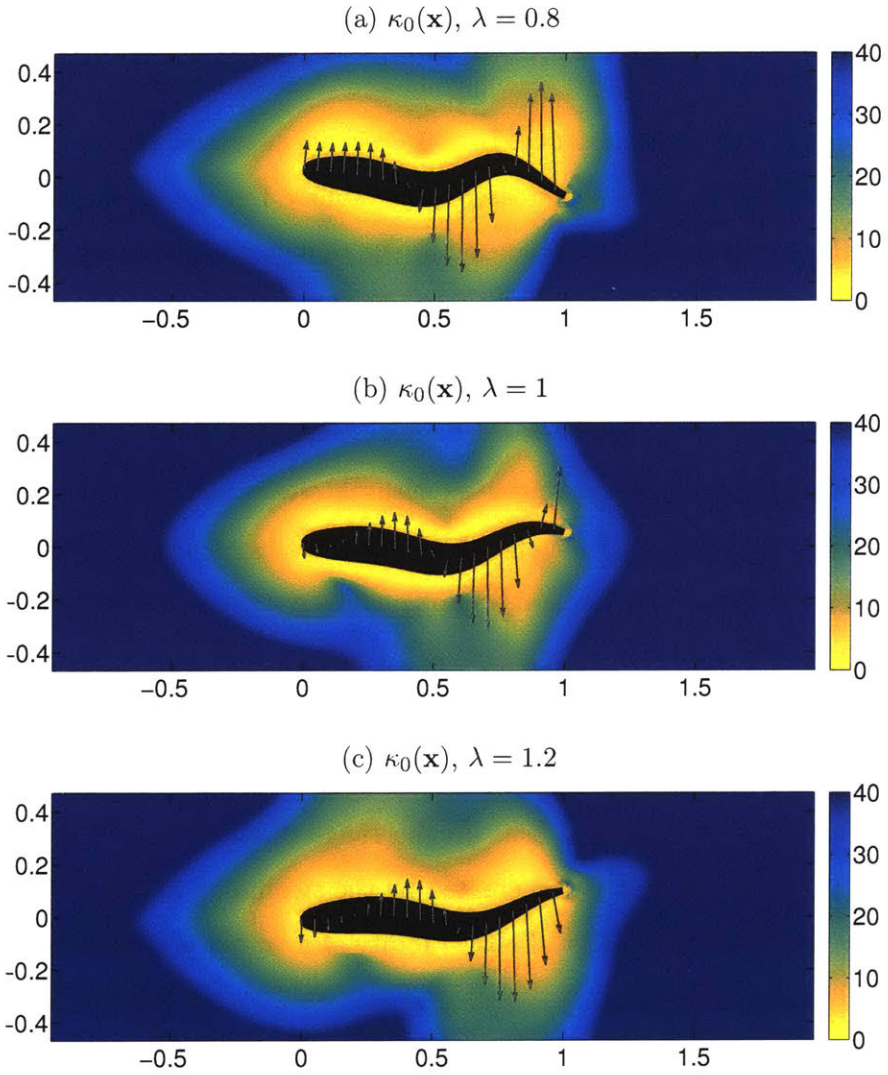

Figure 3-65: The conditioning number for the local observability matrix, for varying body wavelength (with swimming velocity, tail beat amplitude, and all other swimming parameters held constant). Under these assumptions, the observability of a near-field vortex in all three cases is similar in magnitude.

to the lateral observability. This makes sense - while the swimming velocity is held constant, an increased frequency increases the lateral velocity of the fish and therefore increases the relative lateral perturbation. Increased flow perturbation also improves the sensing ability of the fish, so this is associated with increased lateral observability.

However, in practice, increase in the swimming frequency results in increased swimming speed or decreased tail-beat amplitude. Figure 3-64 shows the condition-

ing number for the local observability matrix, for fish at $f = 1.5$, $f = 1.8$, and $f = 2.1$, in which all fish are self-propelled (varying a_0) and swimming with the optimal shape parameters (x_1, δ) for that frequency. In this case, an increased swimming frequency still appears to result in slightly increased observability, but the increased observability may be due to the increased frequency or the change in swimming kinematics.

Figure 3-65 illustrates the conditioning number for the local observability matrix, for a fish swimming with wavelength $\lambda = 0.8$, $\lambda = 1$, and $\lambda = 1.2$, with all other swimming parameters held constant.

It can be seen that variation of the wavelength affects the instantaneous geometry of the fish and therefore the shape of the observability contours around the fish. However, the magnitude of the conditioning number remains relatively the same, indicating that changes to the wavelength of the fish do no significantly affect observability.

In general, observability of a nearby vortex appears to be directly related to the flow perturbation created by the fish. In the range of effective swimming parameters tested, the lateral perturbation created by the swimming motions does not vary significantly, and therefore the local observability of a vortex also remains fairly constant.

3.8.5 Uncertainty contours

While the sensitivity and observability of a system are well-established measures for quantifying the ability of a system to determine a set of unknown states from the measurements, they are somewhat difficult to interpret intuitively. In this section, we introduce a new metric $\zeta(\mathbf{x}, \mathbf{x}^*)$, which allows for the visualization of *regions of uncertainty*, regions that the unknown vortex state can be narrowed down to given some level of noise:

$$\zeta(\mathbf{x}, \mathbf{x}^*) = \frac{2}{N} \sum_{i=1}^{N} |p_i(\mathbf{x}) - p_i(\mathbf{x}^*)| \tag{3.104}$$

With this metric, we consider a vortex at position $\mathbf{x}^*$, and for every other possible vortex location in the fluid domain, we calculate $\zeta(\mathbf{x}, \mathbf{x}^*)$, which represents the average difference in the pressure measured when the vortex is at $\mathbf{x}$ instead of $\mathbf{x}^*$. A low value represents high uncertainty - a vortex at that point yields a very similar pressure signature. A high value represents low uncertainty - a vortex at that location yields a very different pressure signature. Therefore, a contour drawn at $\zeta(\mathbf{x}, \mathbf{x}^*) = c$, where c is a constant, represents the region of uncertainty at c, the rough region in which we could narrow the position of the vortex down into, given a noise level $\mathbf{v} \sim \mathcal{N}(0, c^2)$.

These uncertainty contours are plotted for a rigid foil in uniform stream $U_\infty = 1$, with a single vortex convecting by on the right, in figure 3-66. The bolded white contour at $\zeta = 0.016$ illustrates a region of uncertainty following the vortex, which shrinks and grows as the fish glides by.

We can see that the region of uncertainty is large when the vortex is upstream of the fish. Even at a relatively close distance of $\mathbf{x}^* = -0.3x/L$, the fish can only narrow the estimated vortex position down into a relatively large region. The uncertainty in lateral position is also much greater than the uncertainty in streamwise position. However, as the vortex approaches the fish, the uncertainty rapidly decreases; by the time the vortex reaches the nose, the fish can estimate its position quite well. The low uncertainty persists until the vortex passes the point of maximum width. Then, while the uncertainty in lateral position remains low, the uncertainty in streamwise position grows.

Note, however, that this metric does not take physical information into account. While the total change in pressure might be small for a small streamwise deviation of a vortex to the side of a fish, the streamwise position is actually extremely easy to track due to its strong correlation with a characteristic pressure dip. Explicitly incorporating physical heuristics such as this can yield great improvements in estimation.

Interestingly, the region of uncertainty for a vortex upstream of the fish is distinctly kidney-shaped. This provides some additional insight into one of the estimator failure modes previously discussed in section 3.6.4. Using a Kalman filter to estimate the state of an upstream wake, we found that under certain initial conditions, the estima-

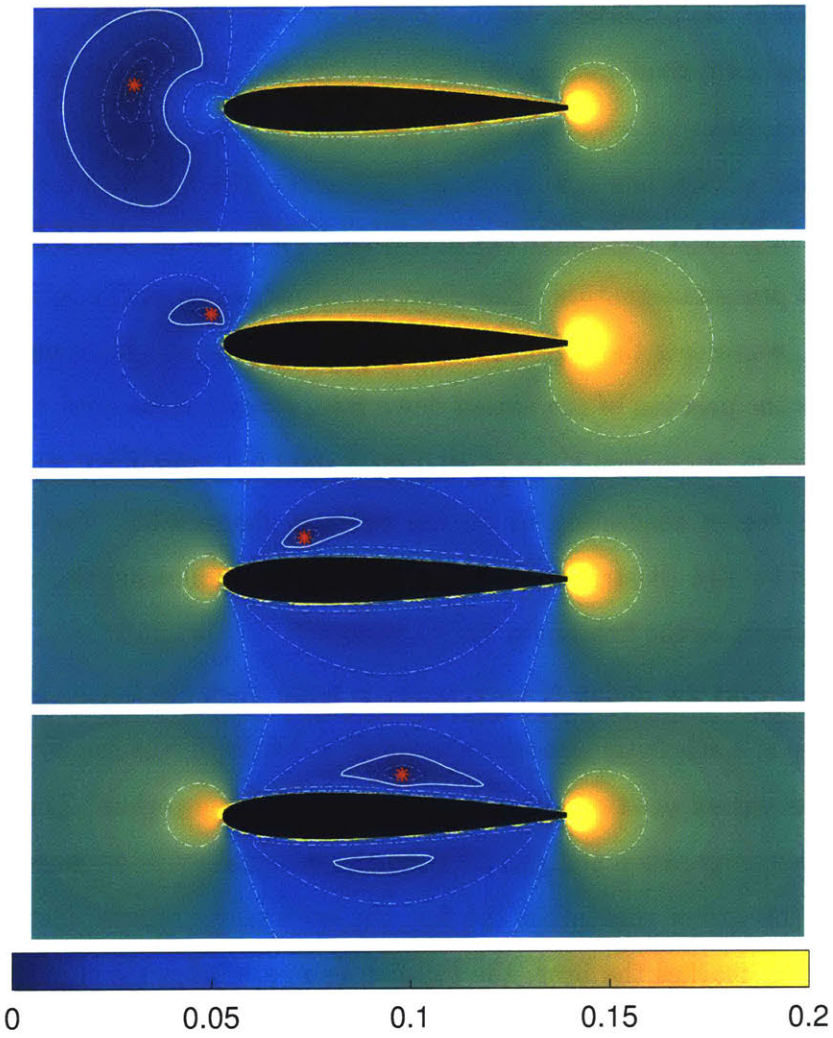

Figure 3-66: Uncertainty contours around a rigid foil in uniform stream $U_\infty = 1$, for four consecutive snapshots in which the vortex ($\Gamma = 0.1$) is located at the red asterisk in each. The contour map illustrates ζ, defined in equation 3.104. With this interpretation, the bolded contour at $\zeta = 0.016$ roughly shows the region in which we could expect to narrow the estimated vortex position into using the instantaneous pressure measurement, with noise $\mathbf{v} \sim \mathcal{N}(0, \zeta^2)$.

tor could converge to the wrong local minimum, in which the sign of the vortex street was reversed (figure 3-39). In order to move toward the true state, the state estimate would have to move in a direction against the predicted state transition $f(\hat{\mathbf{x}}_k, \mathbf{u}_k)$, or in a direction that temporarily increased the measurement residual $\mathbf{y}_k - g(\hat{\mathbf{x}}_k)$. The state transition function strongly predicts that the vortex will only move from left to right (convecting with the flow). However, this uncertainty region is kidney shaped.

If the vortex estimate is incorrectly stuck on one side of this kidney-shaped region, it cannot move to the other side (which may provide a more accurate measurement), without moving backward (within the kidney-shaped region) and without passing through a region that results in a significantly different measurement (through the kidney-shaped region). Therefore, it gets "stuck" there.

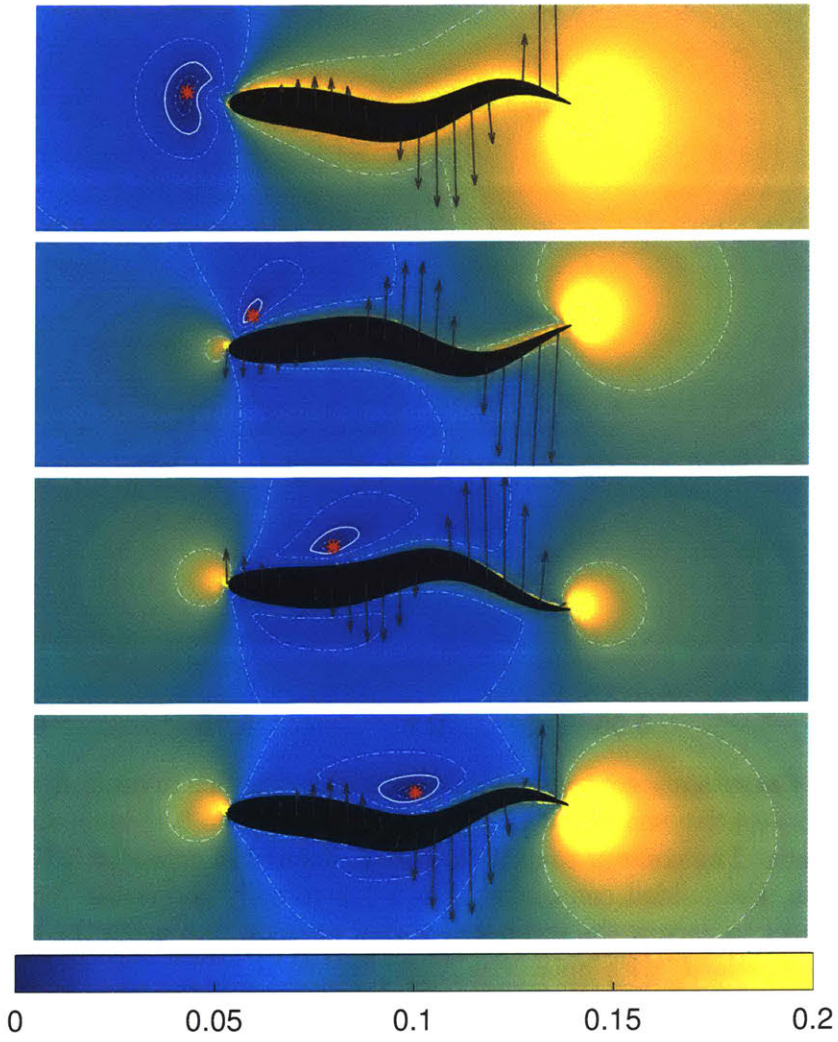

Figure 3-67: Uncertainty contours around an undulating fish in uniform stream $U_\infty = 1$, for four consecutive snapshots in which the vortex ($\Gamma = 0.1$) is located at the red asterisk in each. The contour map illustrates ζ, defined in equation 3.104. With this interpretation, the bolded contour at $\zeta = 0.016$ roughly shows the region in which we could expect to narrow the estimated vortex position into using the instantaneous pressure measurement, with noise $\mathbf{v} \sim \mathcal{N}(0, \zeta^2)$.

Figures 3-67 and 3-68 show the uncertainty contours for an undulating fish, at

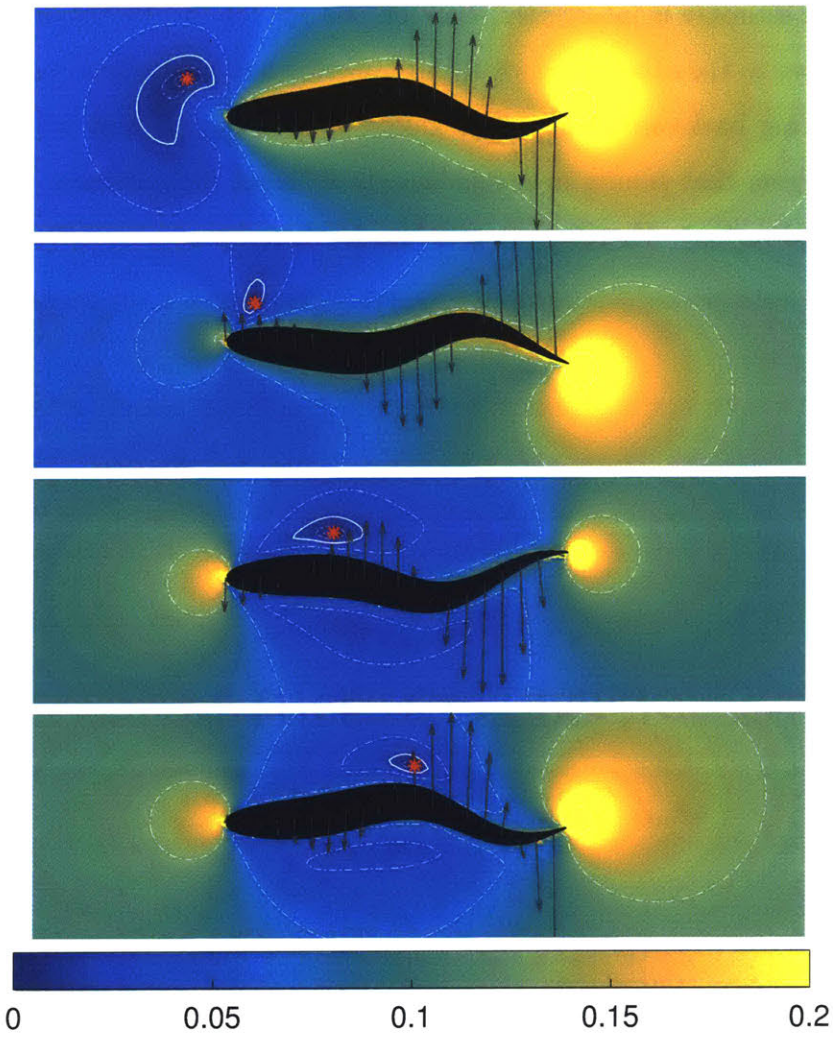

Figure 3-68: Uncertainty contours around an undulating fish in uniform stream $U_\infty = 1$, for four consecutive snapshots in which the vortex ($\Gamma = 0.1$) is located at the red asterisk in each. The contour map illustrates ζ, defined in equation 3.104. With this interpretation, the bolded contour at $\zeta = 0.016$ roughly shows the region in which we could expect to narrow the estimated vortex position into using the instantaneous pressure measurement, with noise $\mathbf{v} \sim \mathcal{N}(0, \zeta^2)$.

two different phases relative to the passing vortex. These are similar to those for the rigid foil, but the uncertainty as the vortex is on the side of the fish appears to be lower in general. In particular, the streamwise uncertainty appears to remain very low, even in the posterior half of the fish, in contrast with the rigid foil system.

One question of interest was: does undulating toward or away from the vortex affect uncertainty in its position? According to these plots, the undulating motion

does not greatly affect the uncertainty. The exact size of the uncertainty region depends the most on the distance between the vortex and the fish. As this distance is not regulated between the three cases (the vortex moves with the local velocity field), they are not strictly comparable. However, while the exact shape of the uncertainty region appears to differ between the fish undulating at different phases, the size of the regions do not vary significantly when the fish is undulating toward the vortex compared with undulating away from it.

The measurement noise is specific to the engineered system or the fish, so the true region of uncertainty varies. Furthermore, it is important to note that dynamic information (such as that used in the Kalman filter) can yield better estimates by building a good framework with which to interpret measurement information over time. The present illustrations are meant to serve as a qualitative picture. Plotting uncertainty contours provides an intuitive way to visualize the ability of the fish to characterize vortices in the near field. In particular, it serves as a good visualization of the tremendous reduction in uncertainty as the vortex approaches the fish, and the relatively low uncertainty for vortices directly next to the fish.

3.9 Experimental testing of an artificial lateral line

In order to test the ability of an artificial lateral line to collect flow-relevant information for control in an experimental setting, a towed vehicle equipped with 5 frontal pressure sensors was constructed (figure 3-69a). While being towed at a steady yaw angle through the water, a control system attempts to use the feedback from the sensors to orient the vehicle to the flow. For fish, this is a well known behavioral task known as rheotaxis.

An electronics board within the vehicle contains the pressure sensors (Honeywell MPXV7007) as well as a low pass filter and signal amplifying circuit for each. The pressure sensors are connected via PVC tubing to canals within the nose cone. The canals are open to the water on the surface of the nose cone. Pressure changes on the surface of the nose cone, at the location of each pore, are therefore transmitted

(a) Diagram of vehicle

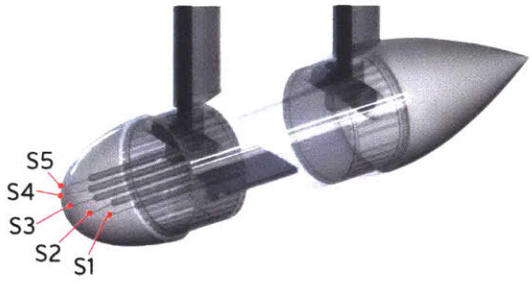

(b) Experimental setup

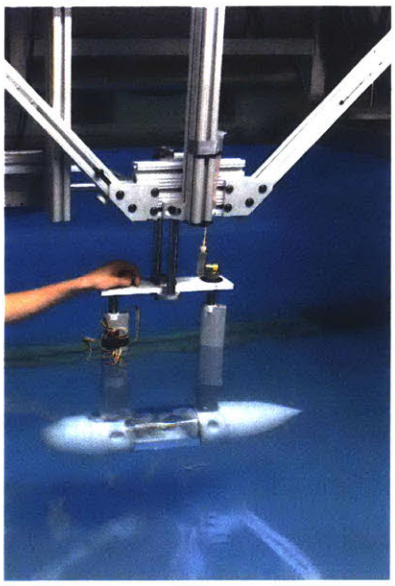

Figure 3-69: (a) Diagram of the experimental vehicle equipped with an artificial lateral line consisting of 5 frontal pressure sensors, labeled S1-S5. (b) Picture of the experimental vehicle in the tow tank, mounted to the carriage. A linear actuator mounted at the left turns the vehicle in yaw, while the vehicle is towed forward (toward the left).

to the sensors within the vehicle. The vehicle is mounted to a motion carriage, which tows it down the length of the MIT towing tank, at 1 m/s. A linear motor (pictured on the left in figure 3-69b) is capable of actuating the vehicle in the yaw direction.

Following the strategy introduced by Salumäe et al. [132], we implemented a Braitenberg controller to orient the vehicle to the flow. Salumäe et al. [132] showed that this simple controller, which uses two pressure sensors on the left and right side of the head on a robot to control the heading, allowed the robot to orient itself to the oncoming flow and maintain the orientation. Many natural organisms use simple algorithms to orient toward or away from sources of stimulation (e.g., light); by reproducing these intuitive control mechanisms in robotic vehicles, scientists have been able to simulate a variety of natural behaviors. For a left-right symmetric underwater robot within a uniform stream, the pressure difference between a mirrored point on the right and left side will be zero only when the robot is aligned with the flow. Therefore, a simple proportional controller acting on the pressure difference

between the two sensors should have a nonzero output whenever the vehicle is not aligned with the flow.

As a result, a simple controller can orient the vehicle to the flow by applying a gain K_p to the pressure difference measured between the left and right:

$$u = K_p(p_l - p_r) \tag{3.105}$$

$$\psi \sim p_l - p_r \tag{3.106}$$

Indeed, we observed that a simple proportional controller, using a low gain, could use the pressure measurements to drive the yaw angle ψ to zero over time. Using a medium gain, the controller still worked to align the vehicle to the flow, but there were some oscillations in the control response (figure 3-70a). When the gain was turned up higher, the vehicle oscillated wildly from side to side, exhibiting system instability (figure 3-70b).

(a) Medium gain control

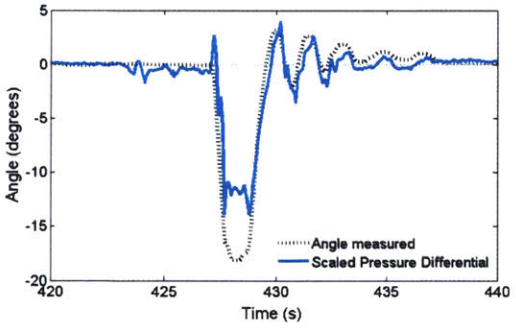

(b) High gain control

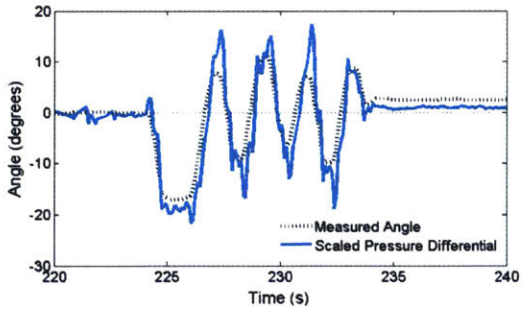

Figure 3-70: Vehicle closed-loop response with (a) medium gain, and (b) high gain. The blue line shows the measured pressure difference between the left and right sensors, and the black dotted line shows the yaw angle of the vehicle as it is first commanded (in open loop) to turn to 18 degrees, and subsequently (in closed loop) back to 0 degrees. With a medium gain, the system returns to 0 degrees with a few oscillations. With a high gain, the system becomes unstable. In the unstable case, the controller was turned off manually to stop the oscillating motion before any damage resulted.

What caused this instability? In analyzing the pressure measured during open-loop turns to a non-zero angle and back to zero, we observed a sharp pressure spike

associated with each turn (figure 3-71a). Zooming in on each of these spikes revealed a non-minimum-phase-like response - the pressure temporarily shifts in one direction before settling to the steady state value in the other direction (figure 3-71b). Clearly, pressure is not a function of the steady flow only.

(a) Nonlinear pressure response

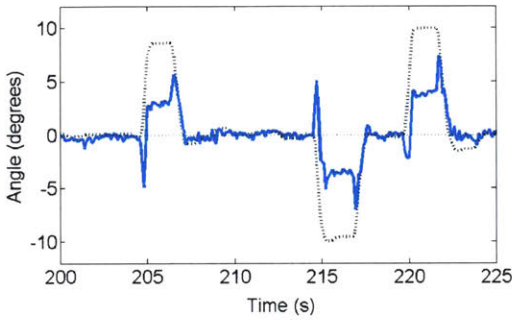

(b) Nonlinear pressure response - zoom

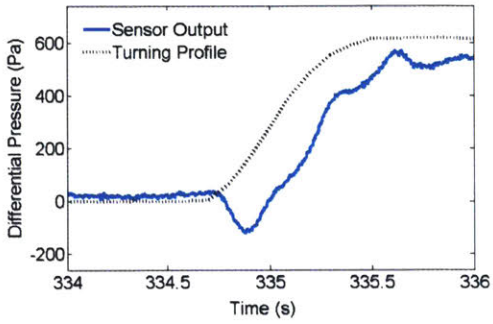

Figure 3-71: (a) The vehicle yaw angle (black dotted line) and pressure difference measured (blue line), during a series of open loop turns. Pressure spikes were observed during each turn, illustrating a nonlinear relationship between the yaw profile and the pressure response. (b) A zoomed in view of a single pressure spike, which resembles a non-minimum phase response. Although the yaw angle of the vehicle increases monotonically, the pressure difference measured first drops before rising to its new steady state value.

In order to determine the cause of this nonlinear response, we developed a model of the system that would be able to predict the pressure measured by the pressure sensors during maneuvers. The model used a 3D panel method, and Bernoulli's pressure law (equation **??**) to capture the relationship between the motion of the vehicle, the oncoming flow, and the pressure measured on the surface. The formulation of the model is similar to the panel method formulation described in section 3.4.2, with the exception that the model is in 3D. The formulas for the 3D source panel influence coefficients are given in Katz and Plotkin [77].

Using source panels with constant distributions, the model was found to capture the pressure measured at the nose during steady towing experiments remarkably well (figure 3-72). For the Reynolds number of the experiment ($Re \sim 100,000$), inertial effects greatly outweight viscous effects, so that the flow resembles a potential flow extremely well. At the nose, where the pressure gradient is favorable and the flow

is entirely laminar, the flow predicted by the potential flow model is expected to be very good.

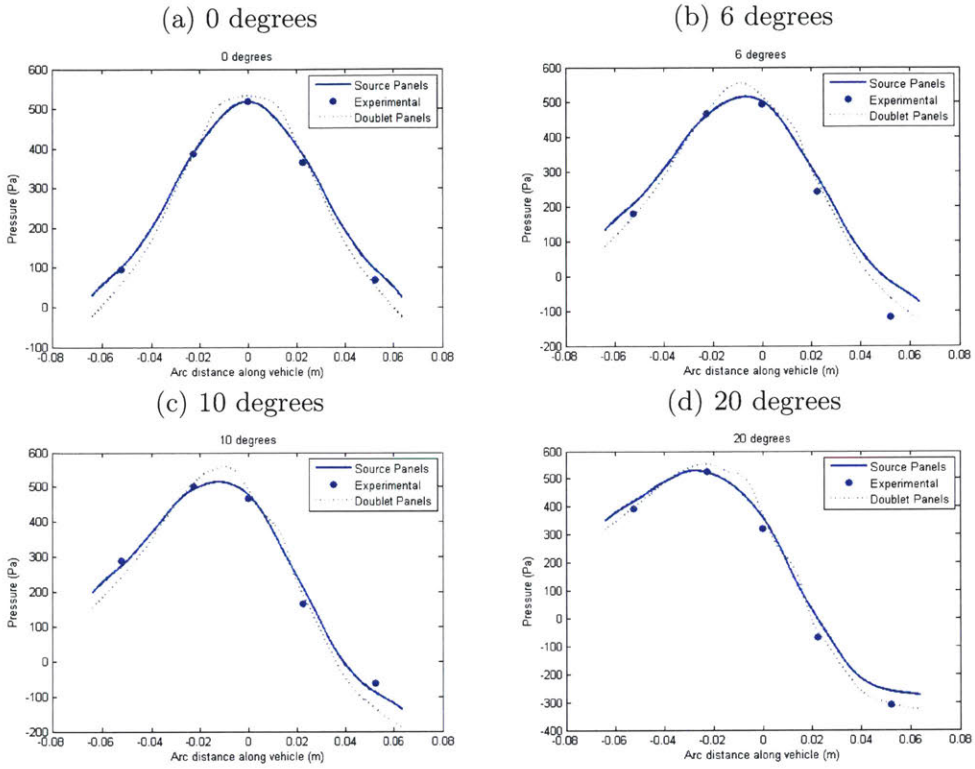

Figure 3-72: Comparison between the experimentally measured pressure (blue points) and the pressure estimated with a 3D source (solid blue line) and doublet (dotted line) panel method, for steady towing angles of 0, 6, 10 and 20 degrees.

The model was similarly capable of capturing the pressure measured during dynamic turns with remarkable accuracy (figure 3-73). As can be seen, the model reproduces the transient pressure spikes observed during each turn.

Using this model, we isolated the cause of the pressure spikes to the flow acceleration term $\partial\phi/\partial t$ within Bernoulli's equation - the same term giving rise to the added mass effect. Figure 3-74 shows the pressure on the surface of the vehicle at 5 subsequent instances during a left turn from 0 degrees to 20 degrees. We can clearly see the stagnation pressure at the front shift toward the left before finally settling on the right side. Physically, the temporarily increased pressure on the left results from the vehicle "pushing" the water out of the way during the turn. As the final angle is reached, the flow hits the vehicle on the right side of the nose, where the stagnation

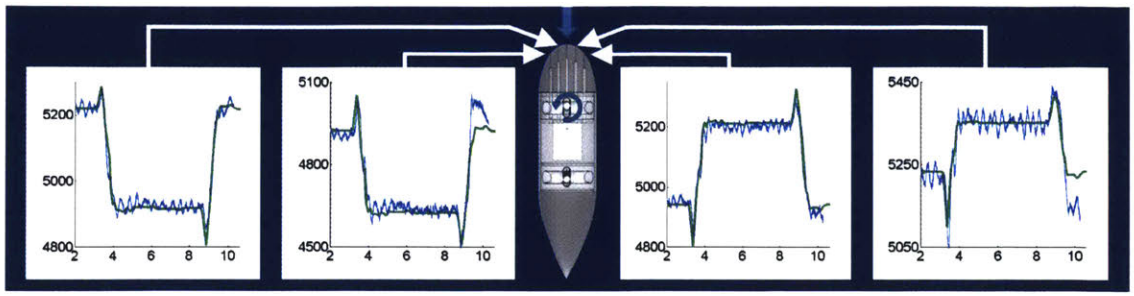

Figure 3-73: Comparison between the experimentally measured pressure (blue lines) at the four side pressure sensor locations and the pressure estimated with a 3D source panel method (green lines). The pressure is measured for an experiment in which the vehicle first turns from 0 degrees to 20 degrees (t=3), and subsequently turns back to 0 degrees (t=9) while being towed at a steady velocity. (Note: the pressure, measured in Pa, includes a hydrostatic term.)

point settles.

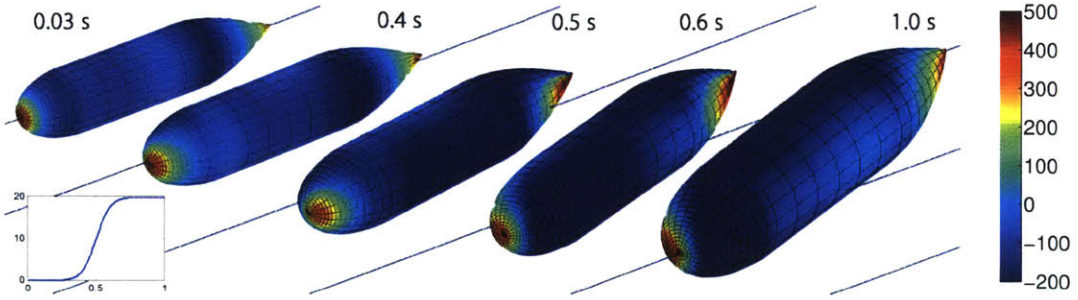

Figure 3-74: Pressure snapshots of the vehicle surface at 5 consecutive timesteps, as the vehicle turns toward the left, with the profile shown at the lower left. The black lines in the background represent the direction of the freestream (left to right). The pressure, estimated using a source panel method, shows that at the nose, the stagnation point shifts to the left before ultimately settling on the right.

Indeed, this effect arises not from the velocity-dependent term within Bernoulli's equation ($1/2|\nabla\phi|^2$), but from the acceleration-dependent term ($\partial\phi/\partial t$). While this term is often ignored in experimental and robotic studies with an artificial lateral line, the present works demonstrates that its magnitude can be significant during fast maneuvers.

3.9.1 Control deficiency without modeling self-induced effect

In fact, control is deficient without modeling this self-induced effect. The Braitenberg controller initially used to orient the vehicle to the flow resulted in system instability with high controller gains. Without accounting for the acceleration-dependent contribution to the total pressure measured, the system always runs the risk of becoming unstable. The control output, the pressure measured, exhibits a non-minimum-phase-like response. In control systems theory, non-minimum phase systems have a fundamentally limited control performance - it is as if there is a time delay in the system.

However, the performance of the system can be improved if we can develop a model that eliminates this effect. Rather than using the control output directly as an input to the proportional controller, a model can be used to estimate the actual yaw angle of the vehicle, which is then used as the control input. Using the previously developed panel method model of the system with an unscented Kalman filter, the actual yaw angle can be estimated (figure 3-75).

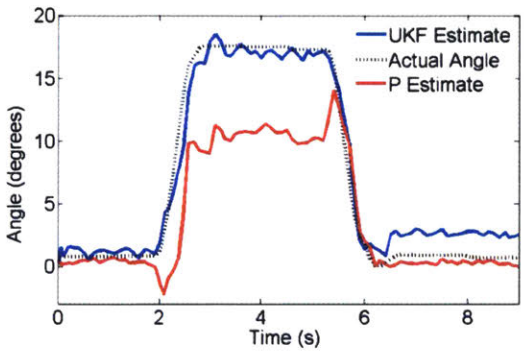

Figure 3-75: Estimation of yaw angle with an unscented Kalman filter and potential flow model (blue line) shows a close match to the the true angle (black dotted line). The red line shows the angle estimate produced by simply multiplying the left-right pressure difference by a gain.

As observed, through capturing the physics of the system, the model is able to accurately estimate the yaw angle to be used as feedback for the system, therefore eliminating the non-minimum-phase-like character of the signal fed into the controller. A controller which uses this model to estimate the actual yaw angle captures the self-induced flow acceleration effect of the vehicle's own motion, resulting in stable control.

In summary, the experimental work showed that 1) a panel method works extremely well as a model for the pressure sensed on the surface of a maneuvering underwater vehicle, even during fast turns and under noisy experimental conditions, and 2) it is critical to model the self-induced flow of the vehicle for stable fast control.

Chapter 4

Active control for energy recovery

Fish are capable not only of sensing the details of their surrounding flow, but they also respond instinctively, tuning the motion of their bodies in order to take advantage of flow disturbances and pressure gradients to save energy. While the ability of fish to take advantage of flow patterns is well accepted, what is not clear in the existing literature are the control principles that allow for this flow field exploitation to take place. If the lateral line signal is used, how do fish incorporate this sensory feedback into a control system?

The issue of control of swimming fish or even schooling fish has not been altogether unaddressed. The problem of formation control and stability of schooling formations has been studied by a few groups [112, 58], and a few groups have demonstrated the use of heuristic-based controllers that allow a foil to capture energy from upstream wakes [79, 104]. Beal [11] considers intentional vortex-relative timing, showing that appropriate synchronization to a wake could be achieved for a flapping foil by using two upstream sensors, allowing the foil to converge to the wake frequency and an optimal phase.

The present work is unique in using sensors mounted on the body (lateral line sensors) to provide feedback for a model-based controller that allows a self-propelled fish to extract energy from the wake of an upstream fish. This work contrasts from that of Beal [11] in that the sensors are mounted on a self-propelled body, for which the estimation and control problem is significantly more challenging. Additionally,

it is a fundamentally different problem to extract energy from the smaller and more closely-spaced vortices within the wake of a fish (compared with the Kármán vortex street studied by Beal [11]). As mentioned in Chapter 2, within the wake of another fish, the fish cannot save energy by using its body as a passive hydrofoil to take advantage of large regions of altered flow, but instead, it must coordinate its motion to properly interact with multiple vortices simultaneously. The model-based observer developed in Chapter 3 allows the fish to localize near-field vortices, providing the feedback required for such flow-relative control. This allows the controller to target the physically important mechanisms in the system, which is a unique contribution of this work. Rather than executing control actions in response to a change in pressure or a perceived change in distance from the leader, which do not relate directly to the state of nearby vortices, the fish can respond directly to vortices in the near-field.

However, many questions remain. For example, we have shown that while the basic physics can be boiled down to a few consistent rules along sections of the body, the optimal phase overall depends on interactions along the whole body (section 2.3.1). How can a fish control the timing along different sections of its body to take advantage of interactions at each? Furthermore, the act of adjusting the body motion to a desired phase intrinsically changes the hydrodynamic interactions with the wake. Will this result in control instability? Will the observer be capable of keeping track of the near-field vortices as the motion of the fish is adjusted? For a real fish, there will likely always exist small oscillations around control setpoints - will these small oscillations reduce the swimming efficiency?

In this chapter, our goal is to explore these questions through building simple controllers within the simulation that are based on the fluid interaction mechanisms discovered in Chapter 2, and use the vortex estimation scheme designed in Chapter 3. Our hypothesis is that in building simple controllers which are built on a physical model of the system, the system will have the potential to respond intelligently to a wide range of conditions that have not been explicitly studied *a priori*. Up to this point, the vortex-body interactions and signals sensed have been studied after the tandem swimmers reach a quasi-steady configuration. The control actions of the

downstream fish, however, will change these interactions over time. The interactions, as well as the signals sensed, will enter territory that has not previously been explored or characterized. The hydrodynamic interaction and signal sensed is a function of the motion at every point along the fish, the unknown external flow, and the history effect of past interactions with the flow. This results in an immense state space that is impossible to fully characterize through empirical information. This complexity of the interaction and the curse of dimensionality is precisely what makes the problem challenging. However, with a simple controller that acts on physical heuristics, it is possible to tackle this problem despite having gathered only a small amount of empirical data. Despite large variations in the lateral line signal as the fish adjusts its motion, the physical model should allow the fish to break down the information into control-relevant pieces that remain consistent despite the exact motion of the fish.

In this chapter, we will first introduce a new swimmer, which has a physically distinct tail. This distinct tail allows for an explicit separation between the undulatory kinematics of the body and the flapping kinematics of the tail. The tail, free to pitch independently from the body, allows for an extra degree of freedom which can be used to tune the interaction between the tail and the surrounding vortices. We will demonstrate that this new model can experience remarkable swimming efficiencies with proper timing. Fine-tuning of the tail pitch phase is shown to result in clear changes to the vorticity interaction around the tail, yielding a significant difference to the overall efficiency for relatively small changes in motion. This suggests that through vorticity control, a fish can induce powerful changes to its thrust or efficiency by executing small control efforts.

Finally, we will demonstrate active control on simulated swimmers. Within the simulation, a fish swimming in the wake of another fish actively synchronizes to the upstream wake, converges to a desired body phase, and fine-tunes its tail motion, through using only feedback from the lateral line (and knowledge of its own state). Although it does not know where the upstream fish is, it is capable of exploiting the wake in order to swim with less than 50% of the energy required to swim by itself.

4.1 Bioinspiration from tuna

Chapter 2 demonstrated the importance of timing along the entire body of the fish. In particular, it is evident that it would be beneficial for the fish to be capable of timing the motion of its body and tail indepedently. What is the best way to add this extra degree of freedom?

Fish such as the tuna, which have evolved a striking form optimized for sustained high speed swimming [54, 4], are characterized by a high-aspect ratio, lunate caudal fin. The caudal fin, which is stiff, is attached to the body by a trunk of greatly reduced width, the peduncle. These fish use the caudal fin as a *flapping foil*, a foil that undergoes an oscillatory heaving and pitching motion to generate lift-based thrust. In addition, the caudal fin can interact with vorticity shed upstream to yield highly efficient swimming. A large body of research shows that the motion profile of the caudal fin strongly affects its performance [157, 135, 67, 59]. Indeed, tuna in nature have precise control over an independently pitching caudal fin, allowing them to achieve optimal swimming configurations under many different conditions. Figure 4-1 shows snapshots of a tuna over a single tail-beat cycle, evidencing that the caudal fin is clearly not a passive extension of the body undulatory wave, but is capable of independent pitching motion.

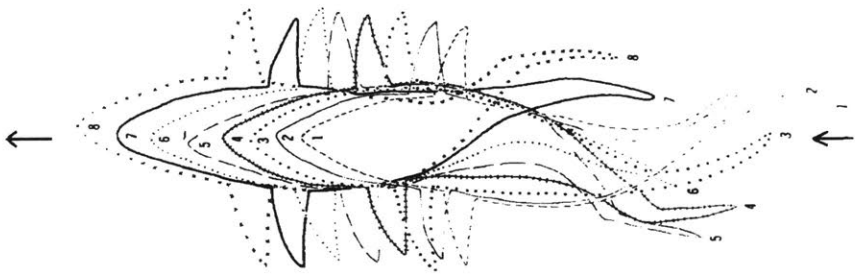

Figure 4-1: Kinematic snapshots of a tuna over a full tail-beat cycle, demonstrating that the caudal fin is not a passive extension of the body undulatory wave, but is capable of independent pitching motion. Reproduced from Fierstine and Walters [51].

To actuate the caudal fin powerfully and precisely, tuna possess a very distinctive peduncular keel, as shown in figure 4-2. The tendons which transmit force from the

muscles in the body to the rays of the caudal fin actually follow the outer contour of the bony peduncular keel, rather than staying near the center (figure 4-3). Fierstine and Walters [51] proposed that in doing so, the peduncular keel acts as a pulley for the great lateral tendons which transmit force from the muscle mass within the body to the rays of the caudal fin. The peduncular keel acts to increase the angle of pull of the tendons on the caudal fin, increasing the torque applied to the fin rays for powerful and precise control.

Figure 4-2: Photo of a school of tuna (Photo credit: Brian Skerry, National Geographic). An arrow points to the distinctive peduncular keel in the tuna.

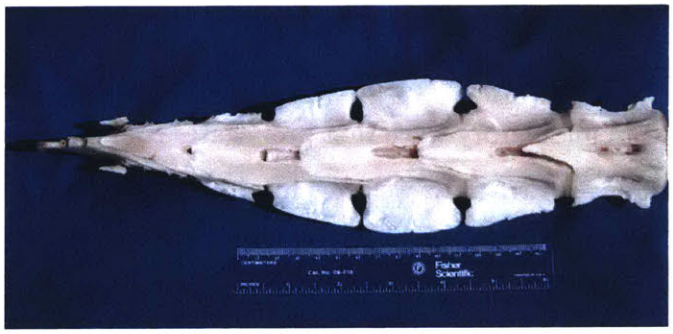

Figure 4-3: Photo of the peduncular vertebrae (Photo credit: Rob Nawojchik).

In fact, the same thing was found by researchers at MIT when designing the robotuna - they found that precise and powerful control was required to independently actuate the tail for the optimal swimming configurations, and using a large pulley at the caudal peduncle allowed for this (figure 4-4). Without an expanded keel, it was

impossible to generate the large torque required to actuate the tail along the desired motion profiles [130].

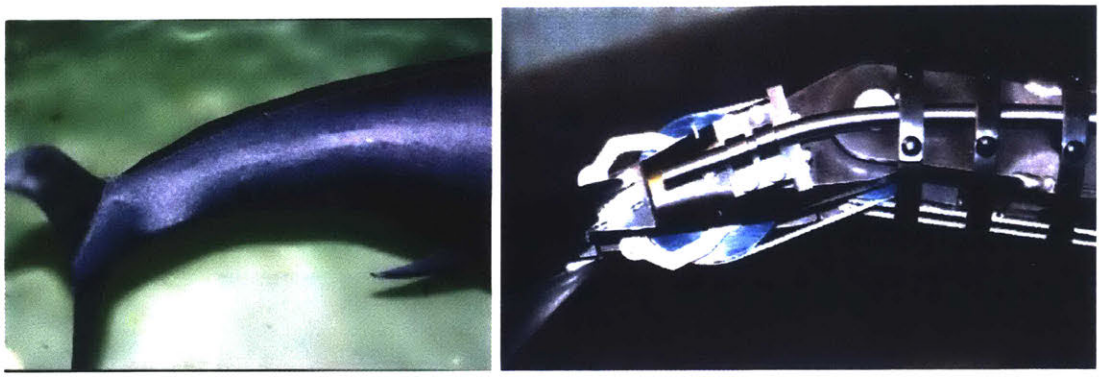

Figure 4-4: Left: photo of the posterior part of the Robotuna II, showing clearly the lateral extension at the peduncle. Right: photo under the skin of the Robotuna II peduncle, showing the pulley mechanism used to transmit torque to the caudal fin (both pictures reproduced from Sachinis [130]).

This example from nature shows us that it is very important to have an independently actuated tail fin, capable of precise control and sustaining high hydrodynamic loads.

4.2 Setup: fish with a distinct caudal fin

Up to this point, we have studied a swimmer which is modeled as a NACA0012 foil which swims using an undulatory wave that propagates continuously from the leading edge to the trailing edge. Presently, we draw inspiration from the tuna to introduce a new swimmer which has a physically distinct tail. While a physical gap is obviously not realistic in 3D, this idea is taken from the fact that a 2D cross-section of the 3D tuna shape would have a gap between the main body and the caudal fin, as shown in figure 4-5. Reproducing this gap allows us to capture the potential interaction between the independent caudal fin and upstream flow.

The tail, which is physically separate from the main body but kinematically and dynamically connected through an invisible link, is free to pitch independently from the main body. In this manner, the fish has one additional degree of freedom, in

Figure 4-5: Photo of a tuna, demonstrating that a horizontal plane taken above the mid-plane results in a 2D section with a gap between the main body and the caudal fin (photo by Tono Balaguer).

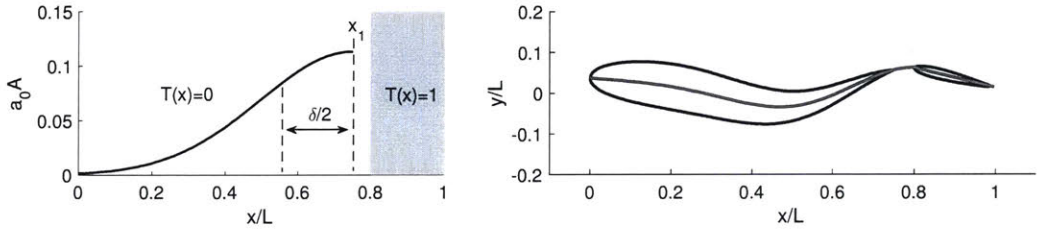

Figure 4-6: The deformation envelope for a fish with a distinct tail, and a diagram of the fish at a single timestep. The black outline represents the total displacement of the fish, while the gray line represents the midline displacement. Note that although there is a physical gap between the body and the tail, the midline displacement is continuous between the two, creating an invisible kinematic link.

addition to the body phase, with which it can use to time its motion.

The fish has a total length $L = 1$, where a NACA0015 of chord length $c_b = 0.75$ is chosen for the main body, and a NACA0012 of chord length $c_t = 0.2$ is chosen for the caudal fin. The gap between the two bodies is $l_g = 0.05$. Although the caudal fin is not physically attached to the main body, the centerline extending from the head to the trailing edge is continuous, and its flexure is given by:

$$\begin{aligned} x_c(x,t) &= T(x)(x_p + (x - x_p(t))\cos(\theta_t(t))) \\ y_c(x,t) &= a_0(t)(1 - T(x))[A(x)\sin(2\pi(x/\lambda - ft + \phi)) + B(x,t)] \\ &\quad + T(x)(y_p(t) + (x - x_p(t))\sin(\theta_t(t))) \end{aligned} \tag{4.1}$$

$T(x)$ is the tail envelope and is defined as 0 over the main body and 1 over the caudal fin. This allows for the separation of the body kinematics into two sections corresponding with the undulating main body and a rigidly-rotating caudal fin. As

with before, $a_0(t)$ is the amplitude of undulation and the fish undulates with frequency f and wavelength λ.

The caudal fin heaves following the trajectory at the peduncle $(x_p(t), y_p(t))$, and pitches with angle $\theta_t(t)$, defined as:

$$\begin{aligned}\theta_t(t) = \theta_D(t) + \theta_0(t)\sin(2\pi(x/\lambda - ft + \phi + \phi_t)) \\ + \arctan(a_0(t)(b_c(t)\cos(2\pi ft) + b_s(t)\sin(2\pi ft) + d(t)))\end{aligned} \tag{4.2}$$

$\theta_D(t)$ is a time-varying tail bias term which is calculated through a PID controller and used for steering. $\theta_0(t)$ is the nominal pitch angle, which is set to vary with the amplitude of undulation through a gain k_t, such that $\theta_0(t) = k_t a_0(t)$. ϕ_t is the tail pitch phase, which can be varied to adjust the phase lag between heave and pitch motion of the tail. The last term in the equation carries the angle from the hydrodynamic recoil on the body over to the tail pitch angle.

The envelope of motion, $A(x)$, is the same as the envelope for the fish with a continuous body (eqn 2.3), and the hydrodynamic recoil term, $B(x,t)$ contains two additional terms to ensure momentum is conserved as the caudal fin deflects.

$$B(x,t) = (a_c + xb_c)\cos(2\pi ft) + (a_s + xb_s)\sin(2\pi ft) + c(t) + xd(t) \tag{4.3}$$

Instead of adjusting the body camber in order to steer, this fish can steer by adjusting the tail bias $\theta_D(t)$. The undulation amplitude $a_0(t)$ is adjusted in order to maintain self-propulsion at constant velocity $U_s = 1$.

4.3 Hydrodynamic interactions and timing for fish with a distinct tail

When swimming in line with another fish, the interaction of the fish with the upstream wake produces prominent induced vortices which have already been shown to impose a significant effect on the thrust production and efficiency along the body. When the fish

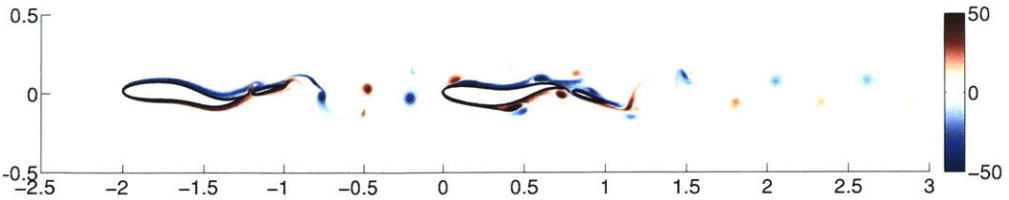

Figure 4-7: A snapshot of the vorticity field which illustrates the simulation setup for tandem swimming fish modeled with a physically separate tail. The downstream fish swims at a distance of one body length directly behind the upstream fish, where it interacts with the wake shed by the upstream fish. The resulting wake develops from numerous vortex-vortex and vortex-body interactions, and is greatly modified from the upstream wake.

is modeled with a distinct tail fin, these induced vortices have the ability to interact with the tail in a way that can yield even larger changes to the thrust or efficiency. Tuna in nature, which are capable of both fast accelerations and efficient swimming at high speeds, are believed to have fine control over the vorticity interactions that occur at the tail. By precisely timing when constructive or destructive interactions occur, high-thrust or high-efficiency swimming modes can both be achieved [184].

For a model of a fish with a distinct tail, the tail pitch phase is constrained to be within a range of about 70 degrees for thrust-producing configurations. However, we will demonstrate that small phase changes well within this range have the ability to evoke large changes in the swimming efficiency of the fish. Because it is a separate body, the caudal fin has the ability to strongly interact with the induced vortices formed upstream to create large changes in the flow around the peduncle region. Therefore, this swimming model captures the ability to effect large changes with only a small control effort - a concept frequently observed in nature.

4.3.1 Characterization of fish with distinct tail

With a rigidly rotating tail, the specific nature of the propulsion and the wake signature can be greatly altered by modifying the nominal pitch θ_0 and the tail pitch ϕ_t. As can be seen in figure 4-8, a variation in these parameters can change the wake structure from a 2S to a 2P wake.

It is well known that variation in phase lag between heave and pitch, the heave

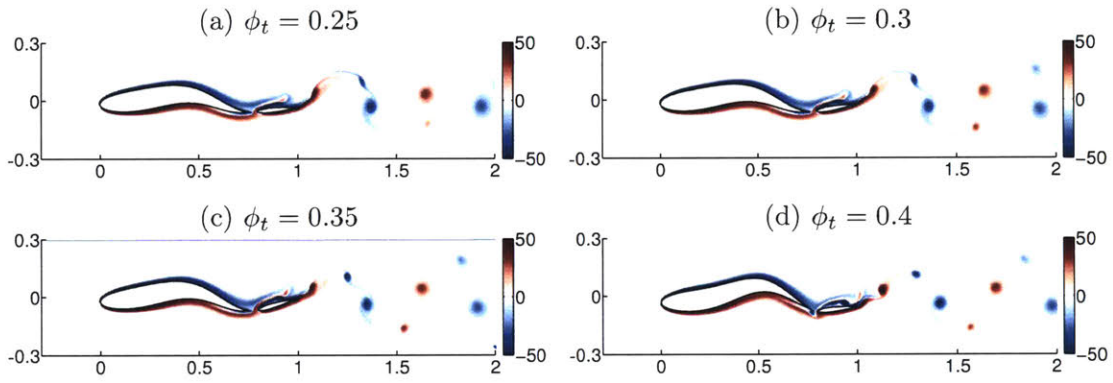

	θ_0 (deg.)	ϕ_t	η_{QP}	a_0	St	$\alpha_{\max}$ (deg.)	ψ (deg.)	h/c
(a)	16.6	0.25	0.38	0.056	0.28	27.2	87.1	0.28
(b)	19.0	0.30	0.42	0.059	0.28	16.5	92.8	0.32
(c)	22.5	0.35	0.44	0.064	0.28	21.5	113.7	0.35
(d)	28.0	0.40	0.42	0.076	0.30	26.0	112.0	0.44

Figure 4-8: Snapshot of the vorticity field for fish with distinct tail at varying tail phase ϕ_t, and a comparison of the key kinematic parameters (defined in table 2.1) and quasi-propulsive efficiency η_{QP} when swimming solitarily. The maximum angle of attack $\alpha_{\max}$ is defined at $x/c = 0.95$ (the three-quarter chord of the tail fin

to chord ratio, and the heave and pitch amplitudes can result in a wide variety of wake topologies for flapping foils [84, 134, 87, 6]. The exact angle of attack profile for the foil can also greatly affect wake topology [124, 67]. Within this study, the heave profile for the caudal fin emerges from the displacement at the peduncle $y_p(t)$, and cannot be directly controlled. This displacement is a complex function of the prescribed deformation, the amplitude of undulation, and the hydrodynamic recoil, and is in general not harmonic.

For the present study, we vary only the phase of the tail pitch in optimizing the motion of the downstream fish. The pitch magnitude is prescribed to vary linearly with the ampitude of undulation. An optimization was performed to determine the ideal factor between the pitch magnitude and amplitude of undulation.

4.3.2 Optimization of body and tail pitch phase for tandem swimming

Simulations were conducted in which two fish with distinct caudal fins swim in tandem, with the follower fish at one body length downstream from the leader. The leader fish employs a tail phase of $\phi_t = 0.25$, chosen in order to produce a clean reverse Kármán street for the follower to swim through. The body and tail phase of the follower fish were varied.

The optimization (figure 4-9) shows that the quasi-propulsive efficiency for the downstream fish varies by only about 10% over the majority of the parameter space, which is similar to the variation in efficiency shown previously for the fish without a distinct tail. However, within a very narrow parameter range, the efficiency is a remarkable $\eta_{QP} = 90\%$. At this configuration, the fish swims with less than half the energy required to swim by itself!

It is interesting to note that the region of high efficiency is incredibly narrow. In contrast to the efficiency for continuous fish as a function of frequency and body phase (figure 3-10b), the fish is not relatively efficient for half of the possible phases. Instead, it swims with an efficiency of around 50% for all phases more than 0.1 away

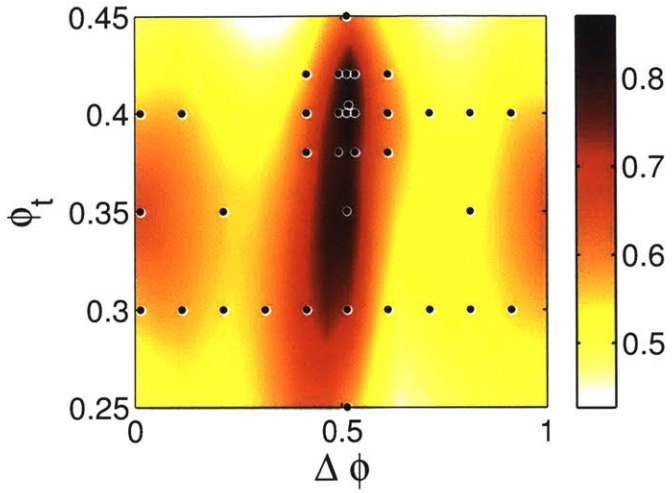

Figure 4-9: The swimming efficiency of the downstream fish, modeled with a distinct tail, as a function of the body undulation phase ϕ and the tail pitch phase ϕ_t.

from $\Delta\phi = 0.51$. While this is higher than the efficiency of swimming alone (about 40%), it is much lower than the optimal efficiency. There is another region of locally increased efficiency roughly 180 degrees from the optimal body phase, at which the fish reaches an efficiency of 67%.

Near the optimal efficiency, proper timing of the body phase and the tail pitch phase are incredibly important. Although a solitary fish swims optimally with $\phi_t \approx 0.36$, the optimal tail pitch phase within the wake in this case is $\phi_t = 0.4$. When swimming solitarily, the tail phase affects the swimming efficiency by only roughly 5%. In the wake of the upstream fish, adjusting the the tail phase across the range of reasonable values can change the efficiency by over 30%! This shows that independent control of the tail pitch is crucial in the presence of vortices; fine vorticity control around the caudal peduncle and tail can be executed to yield a dramatic rise in efficiency.

4.3.3 Energy recovery through vorticity control

For the optimal configuration of $\Delta\phi = 0.51, \phi_t = 0.4$, the fish swims with an efficiency of $\eta_{QP} = 90\%$. What interactions give rise to this remarkable efficiency?

Similar to the results found for a fish with a continuous body, the efficiency de-

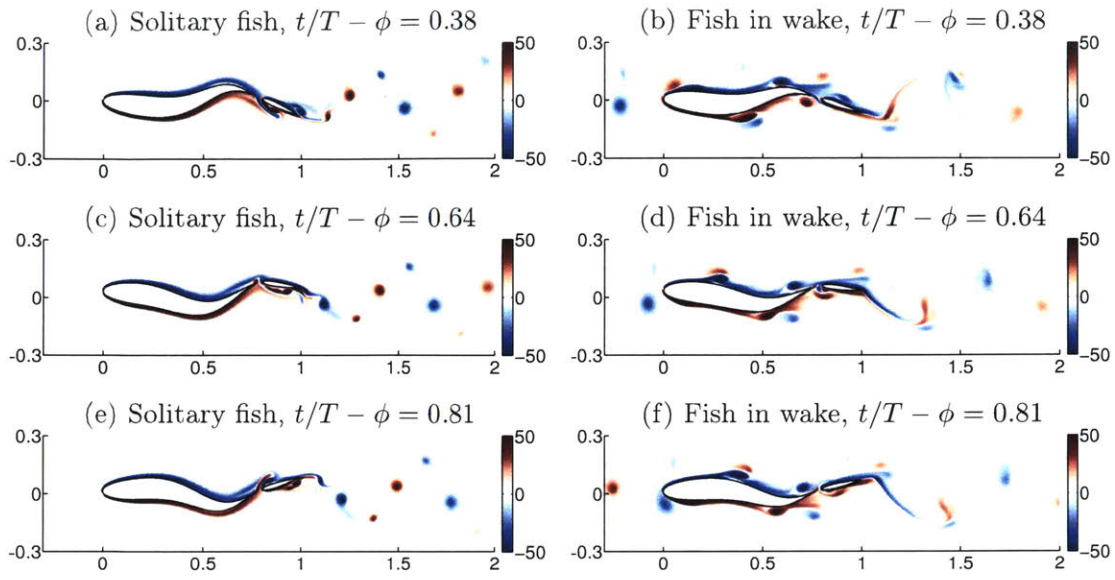

Figure 4-10: Snapshots of the vorticity field for a solitary fish (left) and a well-coordinated fish within the wake of an upstream fish (right), for consecutive timesteps (mod 1). The interaction with the upstream wake greatly modifies the downstream wake, as well as the flow around the peduncle.

pends on the control of vorticity along the entire body. Near the head, the fish significantly increases the thrust generated by generally slaloming between the oncoming vortices. Along the body, some energy is lost, but due to the phasing which keeps the induced vortices close to the peak of the undulation crests, the energy loss is relatively minimal. By balancing timing at the nose and timing along the body in this manner, the fish manages to maximize energy savings at the nose while minimizing energy loss along the body. Proper timing of interactions at the nose and along the body are important, but in this case, well-coordinated interactions at the peduncle and tail give rise to the most significant energy savings.

Figure 4-10 depicts three consecutive snaphots of the fish swimming in solitary (left) and the fish swimming with the optimal phase within the wake (right). These snapshots demonstrate the significance of the change in flow over the peduncle of the fish and within the wake.

Notably, in figure 4-10a, leading edge vortex shedding on the caudal fin is accompanied by a small jet through the peduncle region. Simultaneously, the leading edge

vortex from the previous half-cycle on the right has just reached the trailing edge of the caudal fin. In figure 4-10c, the leading edge vortex on the right has just shed. In figure 4-10e, a smaller trailing edge vortex is shed from the the right side of the caudal fin, while the leading edge vortex on the left approaches the trailing edge. A small jet forms at the penduncle, directed toward the right.

In contrast, figures 4-10b, 4-10d, and 4-10f do not depict a jet forming through the peduncle region at all. In fact, as the positively-signed induced vortex approaches from upstream (on the left), it changes the nature of the flow around the caudal fin such that leading edge vortex formation is nearly suppressed. Although a small jet forms through the gap in figure 4-10d, the negative vorticity annihilates with the passing induced vortex to weaken both. The remaining positive vortex is significantly weakened and sheds with the positive trailing edge vortex during the following half-cycle. Due to the suppressed vortex shedding and the annihilation of upstream vorticity, the wake signature of the downstream fish is significantly reduced, resulting in increased swimming efficiency. In fact, in comparing this fish (right) with its solitary counterpart (left), the row of vortices near the center of the wake has completely disappeared, leaving only the weaker set of vortices on the outside of the wake.

The pressure fields corresponding with the vorticity fields shown in figures 4-10a and 4-10b are shown in figures 4-11a and 4-11b, respectively. As the induced vortex on the left approaches the peduncle, its induced flow, along with the flow induced by the small leading edge vortex on the right side of the caudal fin, acts to oppose and reduce the relative velocity due to the transverse motion of the caudal fin. This causes a significant reduction in the pressure gradient around the caudal fin, and the instantaneous pressure difference between the left and right sides. Over a full swimming cycle, this does not significantly reduce the mean thrust force, but greatly reduces the magnitude of oscillations in the thrust and lift forces experienced by the caudal fin to reduce the overall power consumption (figures 4-11c, 4-11d, and 4-11e).

Furthermore, energy is recovered through two additional mechanisms near the tail. First, as the induced vortex approaches the caudal fin, its thrust coefficient is amplified due to its inclined slope which is exposed to the low pressure core of the vortex.

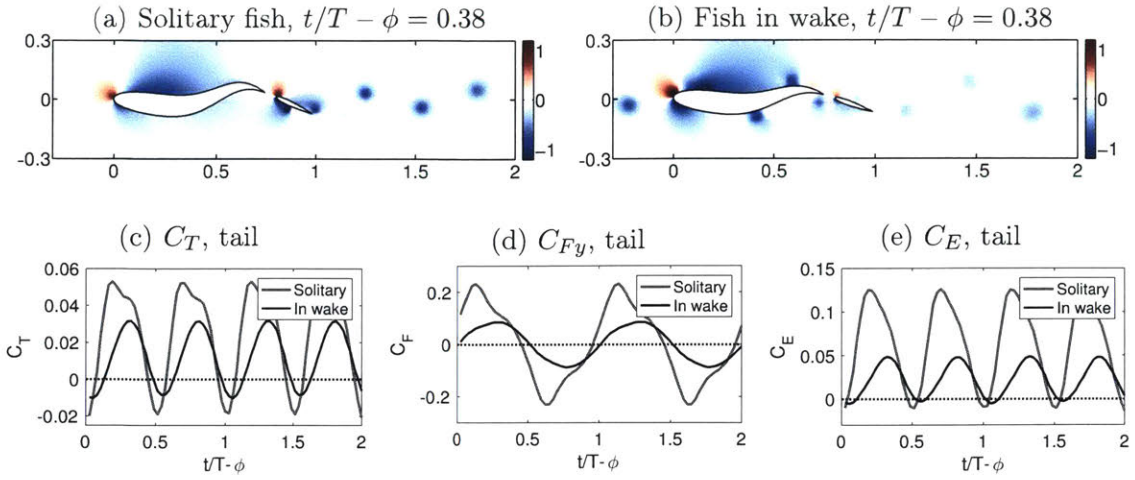

Figure 4-11: Snapshots of the pressure field for a (a) solitary fish and a (b) well-coordinated fish within the wake of an upstream fish. The high pressures around the leading edge of the caudal fin for the solitary fish have been greatly reduced for the fish within the wake, resulting in (c) nearly the same thrust generation with (d) decreased lateral force magnitudes and (e) greatly reduced power consumption.

Secondly, as the vortex from the original upstream wake passes the trailing edge of the downstream fish (figure 4-10f), it pairs up with and annihilates an oppositely-signed vortex shed by the downstream fish to further reduce the downstream wake signature.

This combination of events, from the balance of timing between the nose and the body, to the transfer of energy at the caudal peduncle and tail of the fish, all contribute to the greatly increased efficiency of this fish. Ultimately, it is clear that the wake signature for the fish within the wake (figures 4-10b, 4-10d, and 4-10f) is significantly weaker than both the wake of the upstream fish, and the wake shed by the fish swimming solitarily (figures 4-10a, 4-10c, and 4-10d). This is a clear indication that energy has been extracted from the wake in a beneficial manner, which is supported by the radically increased efficiency of the fish.

4.3.4 Sensitivity to timing

The prior results, as well as figure 4-9, show that timing is especially critical for this fish. The annihilation of vorticity at the peduncle as well as vortices in the downstream wake of the fish depends on the precise phase relationship to both the original wake vortices from upstream as well as the induced vortices on the body of the fish. Furthermore, since the velocity of the induced vortices depends on the kinematics of the fish as well as the positions and strengths of other vortices in the field, the optimal phase of the fish cannot be pre-determined but rather depends on the exact nature of the interaction.

In order to demonstrate the precise interactions that give rise to the dramatically increased efficiency at $\Delta\phi = 0.51, \phi_t = 0.4$, we will show results for fish swimming at a small deviation from the optimal body phase and tail phase.

As previously mentioned, the quasi-propulsive efficiency is around 50-60% over the majority of the parameter space spanning $\Delta\phi$ and ϕ_t. For $\Delta\phi = 0.41$, the efficiency is $\eta_{QP} = 63\%$. As shown in figure 4-12a, at this phase the induced vortex does not suppress the leading edge vortex shedding at the caudal fin but promotes it. As the induced vortex arrives slightly later, it reaches the peduncle just as the caudal fin leading edge reaches its maximum displacement to the left and begins to move toward the right. As a result, the induced vortex is pulled through the gap, causing stronger leading edge vortex shedding and a messier and stronger wake. Although this fish still swims more efficiently than a solitary fish, with $\eta_{QP} = 63.4\%$, it does not harness the energy of the induced vortex optimally.

Similarly, for $\Delta\phi = 0.61$, the induced vortex does not suppress the flow through the peduncle region. In this case, the vortex arrives slightly early, as the leading edge of the caudal fin is just beginning to move away (figure 4-12c). As a result, the vortex is already above the peduncle when the caudal fin flaps with the maximum transverse velocity in the opposite direction. In this position, the vortex is unable to negate the large pressure difference across the caudal fin, or the leading edge vortex shedding that results. However, it can be seen that the induced vortex successfully

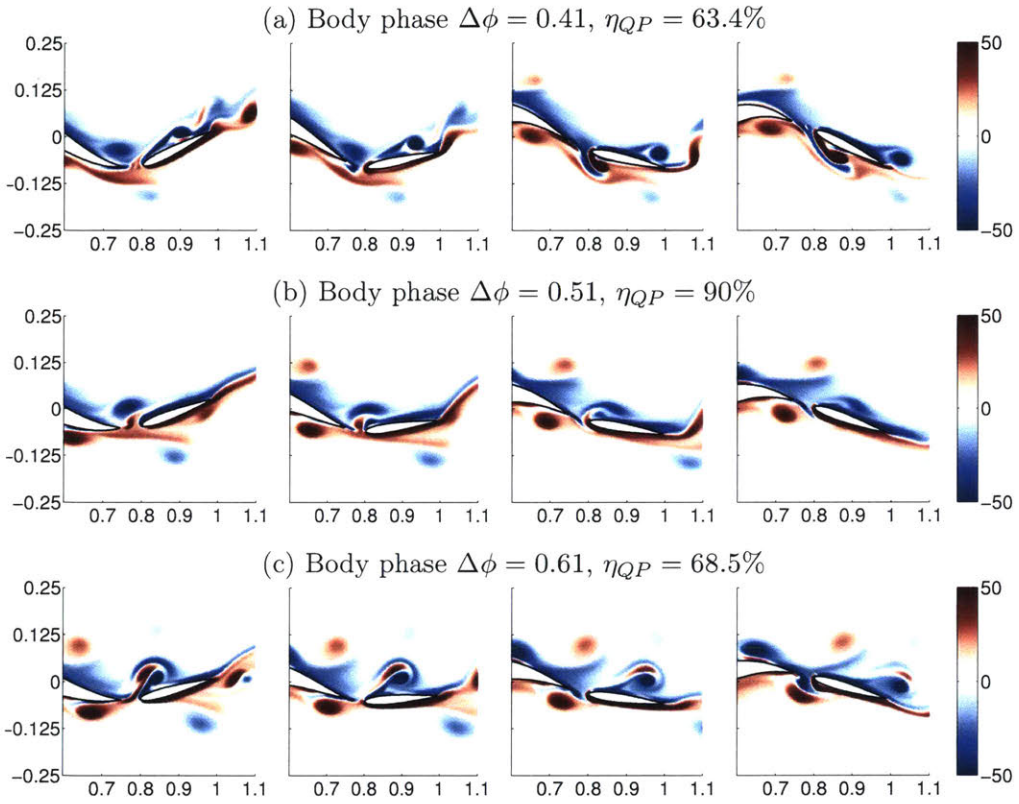

	θ_0 (deg.)	ϕ_t	η_{QP}	a_0	St	$\alpha_{\max}$ (deg.)	ψ (deg.)	h/c
(a)	30.7	0.40	0.63	0.081	0.32	33.0	117.3	0.45
(b)	22.8	0.40	0.90	0.056	0.26	20.1	119.8	0.30
(b)	18.2	0.40	0.69	0.045	0.22	18.2	108.9	0.29

Figure 4-12: Snapshots of the vorticity field at $t/T - \phi = 0, 0.125, 0.25, 0.375$ (left to right, mod 1) for fish with varying body phase. When the timing is varied from the optimal point of (b) $\Delta\phi = 0.51$, the interaction between the peduncle and the approaching negative induced vortex (on the right) is changed. As a result, the jet and leading edge vortex shedding is not suppressed when the vortex arrives (a) slightly later or (c) slightly earlier.

annihilates some of the oppositely-signed vorticity flowing through the gap, leading to some energy recovery. The efficiency, $\eta_{QP} = 68.5\%$, is slightly higher than for $\Delta\phi = 0.41$, but still much less than the optimal efficiency.

At the ideal phase of $\Delta\phi = 0.51$, as shown in figure 4-12b, the induced vortex passes over the peduncle exactly as the jet begins to form through the gap (as the peduncle moves toward the left). In this configuration, the fish captures the energy of the induced vortex optimally, exploiting it to control the flow around the peduncle region in a manner that suppresses the leading edge vortex formation on the caudal fin and greatly reduces the magnitude of force oscillation for enhanced efficiency. The induced vortex is annihilated as it interacts with the caudal fin, and the downstream wake is much weaker and cleaner as a result of the vorticity annihilation and leading edge vortex suppression. This ultimately result in a large rise in efficiency, and with the proper feedback, the fish can intentionally control its interaction with the flow to take advantage of these mechanisms.

The phasing of the tail also greatly affects the swimming efficiency. For a tail phase of $\phi_t = 0.3$, the efficiency is moderately high, at $\eta_{QP} = 74.1\%$. However, by fine-tuning the phase of the tail to $\phi_0.4$, the efficiency is increased by over 15%. Although this change in motion does not result in as significant of a change to the downstream wake as changes to the body phase (figure 4-14b), the change to swimming efficiency is still significant. The rise in efficiency is a result of two clear hydrodynamic mechanisms. First, at a tail phase of $\phi_t = 0.4$, the leftmost figure in 4-13a shows that the tail is more angled as the induced vortex approaches. This allows the tail to harness the low pressure core of the vortex more effectively for enhanced thrust. Secondly, the specific kinematics of the fish with $\phi_t = 0.4$ causes the vortex at the trailing edge to shed slightly later, and pair up with an oppositely signed vortex from the upstream wake more advantageously (rightmost image in figure 4-13a). This vortex pairing effectively cancels the induced velocity field created by the negative vortex at $x/L \sim 1.4$. Over time, vorticity annihilation occurs to yield a weaker overall wake which is also slightly narrower.

These results demonstrate that the timing of a distinct tail is critical in the pres-

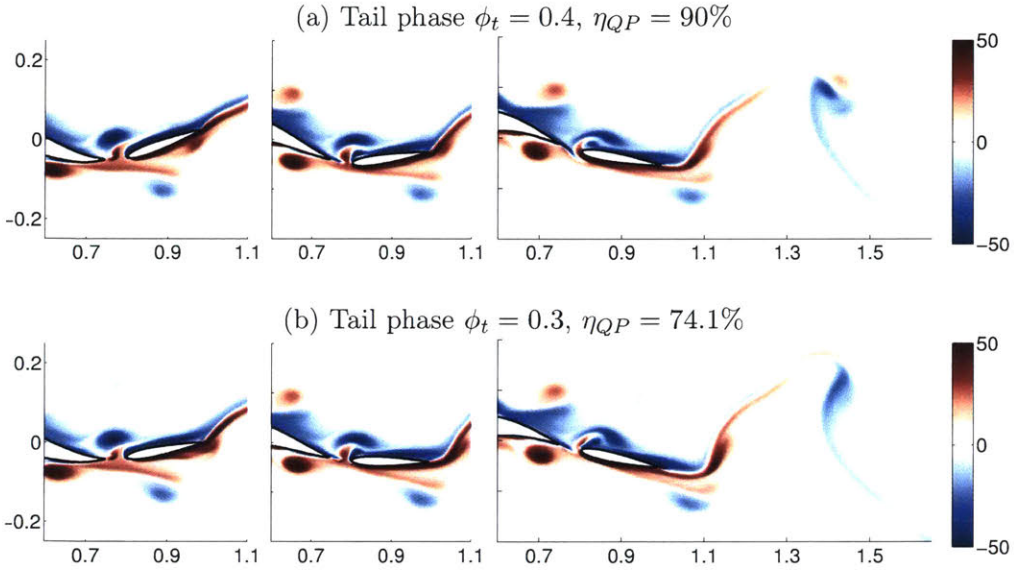

	θ_0 (deg.)	ϕ_t	η_{QP}	a_0	St	$\alpha_{\max}$ (deg.)	ψ (deg.)	h/c
(a)	22.8	0.40	0.90	0.056	0.26	20.1	119.8	0.30
(b)	16.2	0.30	0.74	0.046	0.24	24.5	102.7	0.23

Figure 4-13: Snapshots of the vorticity field, for a tail phase of (a) $\phi_t = 0.4$ and (b) $\phi_t = 0.3$. Reducing the tail phase reduces the inclination of the caudal fin as the negative induced vortex approaches on the left, reducing thrust generation. Furthermore, downstream, it can be seen that for $\phi_t = 0.4$, the positive vortex from upstream pairs up with a negative vortex shed from the trailing edge such that they annihilate each other, while reducing the width of the wake.

Figure 4-14: Illustration of the kinematic changes resulting from small variations in the (a) body phase ϕ, and (b) tail pitch phase ϕ_t. While changes to the body phase affect the timing of the entire body relative to surrounding vortices, changes to the tail phase affect only the timing at the tail.

ence of vortices, and that independent pitch control of a distinct tail can be used to fine-tune the interaction for great hydrodynamic benefit. The swimming performance is extremely sensitive to the precise timing of both the body undulation phase and the tail pitch phase; a change of even 0.1 in either can result in over a 15% change to the efficiency. While this makes sense for the body undulation phase, which affects the timing of the entire body relative to the surrounding vortices, it is more surprising that small changes in the tail pitch motion, which affects the timing of only the tail, would also result in such large efficiency changes. Figure 4-14 shows, qualitatively, the effect on the body kinematics of small variations in the body phase and the tail pitch phase.

From a grand perspective, the optimal tail phase depends on the swimming parameters of the upstream fish, the distance between them, the body undulation phase of the downstream fish, and the additional swimming parameters of the downstream fish. However, on a local level the optimal tail pitch phase depends directly on the state of the induced vortex as it approaches the tail. By learning the ideal vortex-relative phase over time and using flow feedback to maintain the optimal vortex-relative timing, the fish can consistently harness energy through the mechanisms described here.

Fish, equipped with the lateral line, have the ablity to instinctively respond to their surrounding flow in order to make the minute kinematic adjustments necessary to control their interactions with it in an advantageous manner. Although numerous interactions take place along the body of the fish, each with the ability to significantly affect the efficiency, simple heuristics can be followed to maximize the energy

recovery along the entire body. Presently, we have demonstrated that small kinematic changes can result in large changes to the swimming efficiency. However, as the positions of surrounding vortices are very detectable and directly related to energy recovery mechanisms, coordination strategies can be devised to interact with the flow in hydrodynamically favorable ways.

4.4 Active feedback control

Fish can save energy even when swimming directly within the thrust wake behind another fish, through carefully timing their motion relative to the oncoming vortices. The results from chapter 2 and this chapter demonstrate that the timing is extremely critical - to harness energy from the upstream wake, the downstream fish must lock in to the upstream wake frequency at the correct phase. In addition, the results from the present chapter suggest that the efficiency can be further improved through fine-tuning of the tail motion.

In theory, it would be possible to perform this by knowing exactly where the upstream swimmer is. Indeed, some researchers have shown that it is possible to use learning algorithms to teach a downstream swimmer to maintain an efficient schooling position using the position of the upstream swimmer as feedback. However, in practice, it is rare for the upstream wake to be perfectly regular, and impossible for the downstream fish to know the position of the upstream fish with the required precision. Our results suggest that a phase error of even 0.1 could result in an efficiency reduction of over 10%; effective control would require a downstream fish to estimate the position of the upstream fish with an error of less than 5% of its body length - a difficult feat by vision alone. However, as demonstrated in chapter 3, the lateral line is more than capable of this level of precision, even when the measurements are very noisy (figure 3-46).

This section will describe the implementation of active feedback controllers which adjust the undulation phase and tail pitch phase of the downstream fish, using only feedback from the lateral line. We assume that prior to executing control, the fish has

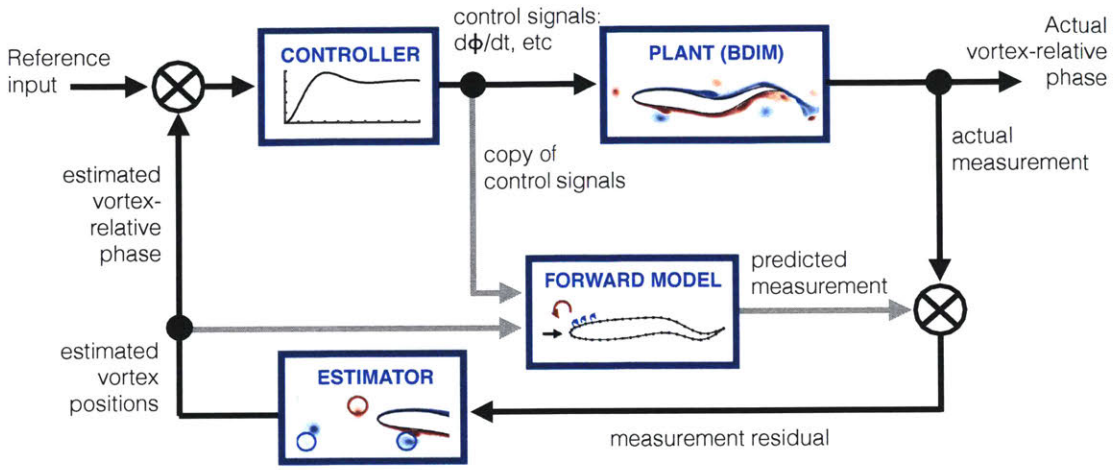

Figure 4-15: Diagram of the entire control system, in which the plant is modeled using the BDIM simulation, the forward model captures the plant using a lower-order model (potential flow model), the estimator is the unscented Kalman filter designed in Chapter 3, and the controller is presently considered.

already "learned" the optimal flow-relative phase differences to aim for. This learning process has effectively been performed by the optimization procedure. A diagram of the entire system designed so far is shown in figure 4-15. The controller is the final part of this system that we design.

We will demonstrate that despite changes to the flow interaction that arise from fast control, the observer is able to yield an accurate estimate of the upstream wake phase. Despite the marked sensitivity of the vorticity interaction at the tail to the precise timing of the fish, the downstream fish is nevertheless able to find and maintain a swimming configuration that yields the optimal efficiency previously discovered.

4.4.1 Phase-locked loop controller

In order to capture energy from the upstream wake, the downstream fish must first lock in to the frequency of the upstream wake. If the frequency of swimming is even slightly different from that of the wake, the vortex-body interactions will be inconsistent over time, leading to little to no gain in efficiency. The concept of mutual synchronization of oscillators arises in many biological sytems, for example in oscillating neurons, the synchronization of fireflies, the unified chirping of crickets,

and the human circadian rhythm [55, 144, 22, 49, 167]. In fireflies, an individual insect can entrain with no phase lag even when its natural flashing frequency differs from the stimulating frequency [47]. Fish are also known to synchronize their tail beat frequency to the frequency of an external source, even when that frequency is significantly different from their own [91, 88].

Beal [11] described the implementation of an Ermentrout controller, inspired by the synchronization of fireflies, on a flapping foil in a wake with feedback from external anemometers, in addition to a stubborn ramp follower (SRF). He found that while both controllers worked to synchronize to the upstream wake well enough to achieve the expected efficiencies, each controller had its own shortcomings. The Ermentrout controller converged to the desired phase with an error of only about 0.05 degrees, but oscillated around the desired frequency considerably ($\sigma = 0.51$ around a desired frequency of $f = 6.5Hz$). The SRF did not exhibit these oscillations in frequency, but retained a phase lag of about 5 degrees.

Therefore, in the present work, we attempt to combine the capability of the Ermentrout controller to follow a sinusoidal signal at exactly the desired phase, and the robustness of the SRF, through the implementation of a new controller. For this controller, we borrow the idea of the phase-locked loop from the field of electronics [68].

A phase-locked loop (PLL) controller regulates the phase of an output signal relative to the phase of an input signal. Such controllers are used for computer clock synchronization, to demodulate signals, or to generate frequencies at multiples of an input frequency. The PLL controller compares the phase of an input signal with that of an output signal, and adjusts the frequency or phase of the system in response. On its own, this will typically result in a noticeable phase lag when the natural frequencies of the two systems are different, but a correction term can be included to compensate for this, as will be demonstrated later.

Figure 4-16 shows a diagram of the PLL controller developed presently, which is similar to classical PLL controllers. The controller consists of three main parts: 1) the phase comparator, 2) the proportional-integral (PI) controller, and 3) the latch

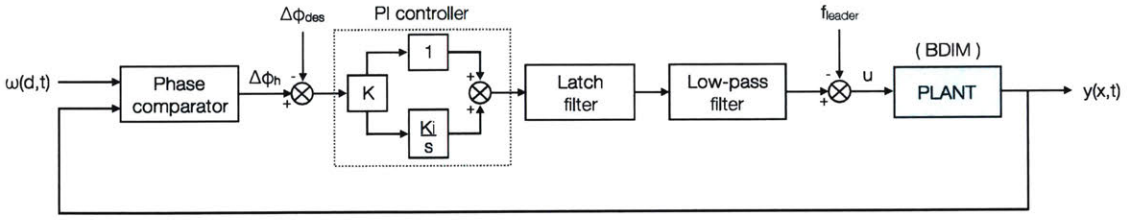

Figure 4-16: Diagram of the phase-locked loop controller for the head.

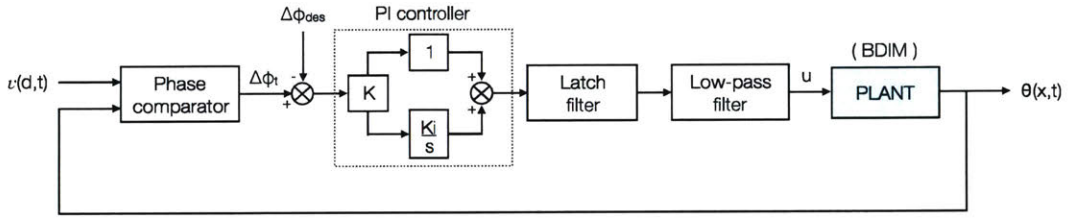

Figure 4-17: Diagram of the phase-locked loop controller for the tail.

filter and low-pass filter.

The phase comparator quantifies the difference between the phase of the output signal (head or tail pitch phase) with that of the input signal (vortex phase). For the body undulation controller, the phase of the head motion y_0 at t_n is calculated by nonlinear optimization:

$$\phi_h(t_n) = \underset{\phi_h,a,b}{\operatorname{argmin}} \sum_{k=n_0}^{n} (y_0(t_k,\phi) - (a\sin(2\pi(\phi_h - ft_k)) + b)) \tag{4.4}$$

where n_0 is the first index for which $t_{n_0} > t_n - T$, a is the amplitude of the fitted sinusoid, f is the known swimming frequency, and b is the mean value (usually close to zero).

It is important to note that the motion of the head, $y_0(t,\phi)$ is typically not perfectly sinusoidal. As the fish executes control motions and interacts with the wake, the average position of the nose may drift, and the frequency varies with the control input $\dot{\phi}$. As a result, it is not straightforward to estimate the phase precisely. A nonlinear optimization procedure can be used to find the best fit for a sinusoid, and in this case Fletcher's version of the Levenberg-Maquardt algorithm for sum of squares minimization is used [8]. Since the frequency varies, even over a single period, the

choice of which frequency to use is not obvious. Possible options are the best-fit frequency, the estimated frequency of the upstream wake, and the "natural" swimming frequency of the fish. Each of these options has a different strength and weakness, but all work as long as the frequency used remains close to the actual frequency of the nose motion. Due to the fact that the original frequency of the downstream swimmer remains constant, it tends to be the most robust choice.

Nonlinear optimization is also used to estimate the wake phase:

$$\phi_w(t_n) = \underset{\phi_w}{\operatorname{argmin}} \sum_{i=1}^{4} \left(\operatorname{mod} \left(t_i + \operatorname{sign}(\hat{y}_w(t_i)) \frac{T}{4} - \phi_w T \right), T \right) \tag{4.5}$$

While the choice of frequency to use for the estimation of ϕ_h is not important, it is important to use the same frequency in the estimation of ϕ_w. $T = 1/f$ is the estimated period, and $\hat{y}_w$ is the estimated y position of the next approaching vortex.

The phase difference between the lateral nose motion and the wake is then:

$$\Delta\phi_h(t_n) = \operatorname{mod}(\phi_h(t_n) - \phi_w(t_n), 1) \tag{4.6}$$

Note that this is distinct from $\Delta\phi = \phi - \phi_1$ (equation 2.18), which denotes the phase difference between the undulating phase of the prescribed flexure ϕ and the wake phase ϕ_1 at the nose of the fish. The phase of prescribed flexure ϕ is different from the phase of lateral nose motion ϕ_h because the latter includes additional terms resulting from the hydrodynamic forces and recoil, which are not known *a priori*. ϕ_w represents the wake phase which is calculated from the vortex state estimates given by the unscented Kalman filter.

The phase comparator for the tail controller is similar, finding the phase difference between the tail pitch motion θ_t and the phase of the induced vortex just upstream

of the caudal peduncle:

$$\phi_t(t_n) = \underset{\phi_t,a,b}{\operatorname{argmin}} \sum_{k=n_0}^{n} (\theta_t(t_k,\phi) - (a\sin(2\pi(\phi_h - ft_k)) + b)) \tag{4.7}$$

$$\phi_v(t_n) = \underset{\phi_w}{\operatorname{argmin}} \sum_{i=1}^{4} \left(\operatorname{mod}\left(t_i + \operatorname{sign}(\hat{y}_v(t_i))\frac{T}{4} - \phi_v T \right), T \right) \tag{4.8}$$

$$\Delta\phi_t(t_n) = \operatorname{mod}(\phi_t(t_n) - \phi_v(t_n), 1) \tag{4.9}$$

Note that the phase difference in both cases is modulated to 1 (recall from equations 4.1 and 4.2 that the body and tail phase are normalized by 2π). This is important in order to ensure that the control input due to a certain phase difference is always consistent. Since the desired phase difference is also constrained such that $0 \leq \Delta\phi_{des} < 1$, the error between the two will always range between -0.5 and 0.5.

The proportional-integral (PI) controller drives the error between the phase difference $\Delta\phi_h$ or $\Delta\phi_t$ and the desired phase difference to zero. The error terms are:

$$e(t_n) = \Delta\phi(t_n) - \Delta\phi_{\text{des}} \tag{4.10}$$

$$e_i(t_n) = \sum_{k=1}^{n} e(t_k)(t_k - t_{k-1}) \tag{4.11}$$

and the PI controller outputs a control signal u:

$$u(t_n) = K_p e(t_n) + K_i e_i(t_n) \tag{4.12}$$

The PI controller, in this case, is modifed in order to limit the maximum control input due to the proportional error term:

$$u(t_n) = K_p \tanh(ke(t_n)) + K_i e_i(t_n) \tag{4.13}$$

This typically results in greater stability of control and a faster convergence time.

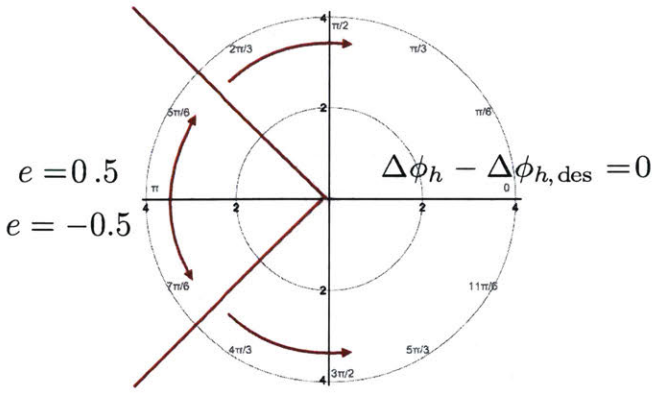

Figure 4-18: Illustration of the latch filter mechanism. When the error signal approaches the maximum ($e = \pm 0.5$), the phase of the head is 180 degrees from the desired phase. Noise around this point may cause the controller to fluctuate between pushing ϕ in one direction and and the other. To prevent these fluctuations, within a band around $e = \pm 0.5$, the latch filter commands that the control signal be of the same sign as it was during the previous timestep. This provides momentum in pushing the control input past this point and preventing it from getting stuck there.

The gains and setpoints used for the controllers are as follows:

head:	$K_p = 0.5,$	$K_i = 0.1,$	$k = 2,$	$\Delta\phi_{h,des} = 0.74$
tail:	$K_p = 0.5,$	$K_i = 0.1,$	$k = 2,$	$\Delta\phi_{t,des} = 0.92$

The desired phase differences were calculated *a priori* using the optimal swimming configuration of $\Delta\phi = 0.51, \phi_t = 0.4$.

The control input for the head, u, is passed through two filters, a latch filter and a low-pass filter. The latch filter prevents the control input from getting stuck at $e = \pm 0.5$, which is possible due to noise in the system. Figure 4-18 illustrates the filter mechanism.

When the phase difference of the nose is the farthest possible from the desired phase difference ($e = \pm 0.5$), a positive or negative control input will work to push it toward the setpoint. However, in the presence of noise, the control input will fluctuate between positive and negative values at this point. Therefore, to counteract this, the

latch filter works within a band around $e = \pm 0.5$ to regulate the sign of the control input such that it is always the same as that of the previous timestep:

$$\begin{cases} u'(t_n) = u(t_n), & \text{if: } -0.45 < e < 0.45 \\ u'(t_n) = \text{sign}(u(t_{n-1}))|u(t_n)|, & \text{if: } e < -0.45 \text{ or } e > 0.45 \end{cases} \tag{4.14}$$

Following this, a moving-average filter is used to reduce the noise in the control signal. While moving average filters are not ideal for separating frequencies, they are optimal for reducing random noise while retaining a sharp step response [141].

An additional modification is included to the PLL controller for the head in order to accurately synchronize the frequency of swimming to the oncoming wake frequency and converge to the desired phase difference. With a high enough proportional gain, the PLL controller drives the swimming frequency to the upstream wake frequency, but there always exists some error between the desired and actual phase difference (when the natural swimming frequencies of the two fish are different). This error can be eliminated through subtracting the estimated frequency difference from the filtered control input:

$$u*(t_n) = u'(t_n) - (f_{leader} - f_{follower}) \tag{4.15}$$

This is equivalent to setting the frequency of the output signal equal to the estimated frequency of the leader, as depicted in figure 4-16. The ability of the downstream fish to estimate the upstream wake frequency is described in section 3.7. For the tail controller, this is implicitly performed, since the body phase is included in the total tail pitch motion profile (equation 4.2).

4.4.2 Simulated active control setup

Figure 4-19 shows the setup of the simulation for testing the active feedback control. The BDIM simulation simulates the real fluid dynamics. Probed pressure values on the downstream fish's lateral line are passed to the estimator at regular time intervals

t_k, which uses the potential flow model and unscented Kalman filter to estimate the positions of near-field vortices. The estimated phases of the oncoming wake and induced vortices by the peduncle are passed to the PLL contoller. The controller determines a control signal, the rate at which to update the body undulation phase ($\dot{\phi}$) and the rate at which to update the tail pitch phase ($\dot{\phi}_t$), which is passed back to the BDIM simulation. This process continues until the fish has converged to both the desired phase differences.

Active control simulations were conducted with the upstream fish swimming at a constant velocity of $U_l = 1$ and frequence $f_l = 1.8$, and the following fish $U_f = 1$ and $f_f = 1.7$. In order to consistently extract energy from the upstream wake, the following fish must synchronize to the upstream wake frequency and converge to a desired phase difference, using feedback from the lateral line.

The desired phase difference for the tail controller is only valid at $\Delta\phi = 0.51$, since the development of induced vortices along the body depends directly on the interaction with the upstream wake. Therefore, the body controller works first to find and converge to the desired body undulation phase, and subsequently the tail controller drives the tail pitch phase difference to the desired value.

In the following section, we will demonstrate first the results from the body and tail controllers individually, and then the result of implementing both controllers within a single simulation.

4.4.3 Results: control implementation

The first controlled simulation was executed to adjust the phase of body undulation, driving it toward a predetermined desired phase difference from the upstream wake. In the simulation, the downstream fish swims at a slightly different natural frequency ($f = 1.7$) from that of the upstream fish ($f = 1.8$), in order to simulate realistic conditions. Figure 4-20 shows that the downstream fish successfully synchronizes the the frequency of the upstream wake, and converges to a steady phase difference relative to the wake $\Delta\phi_h$. However, it is clear that there is a steady state error between the phase difference and the desired phase difference (e=0.05).

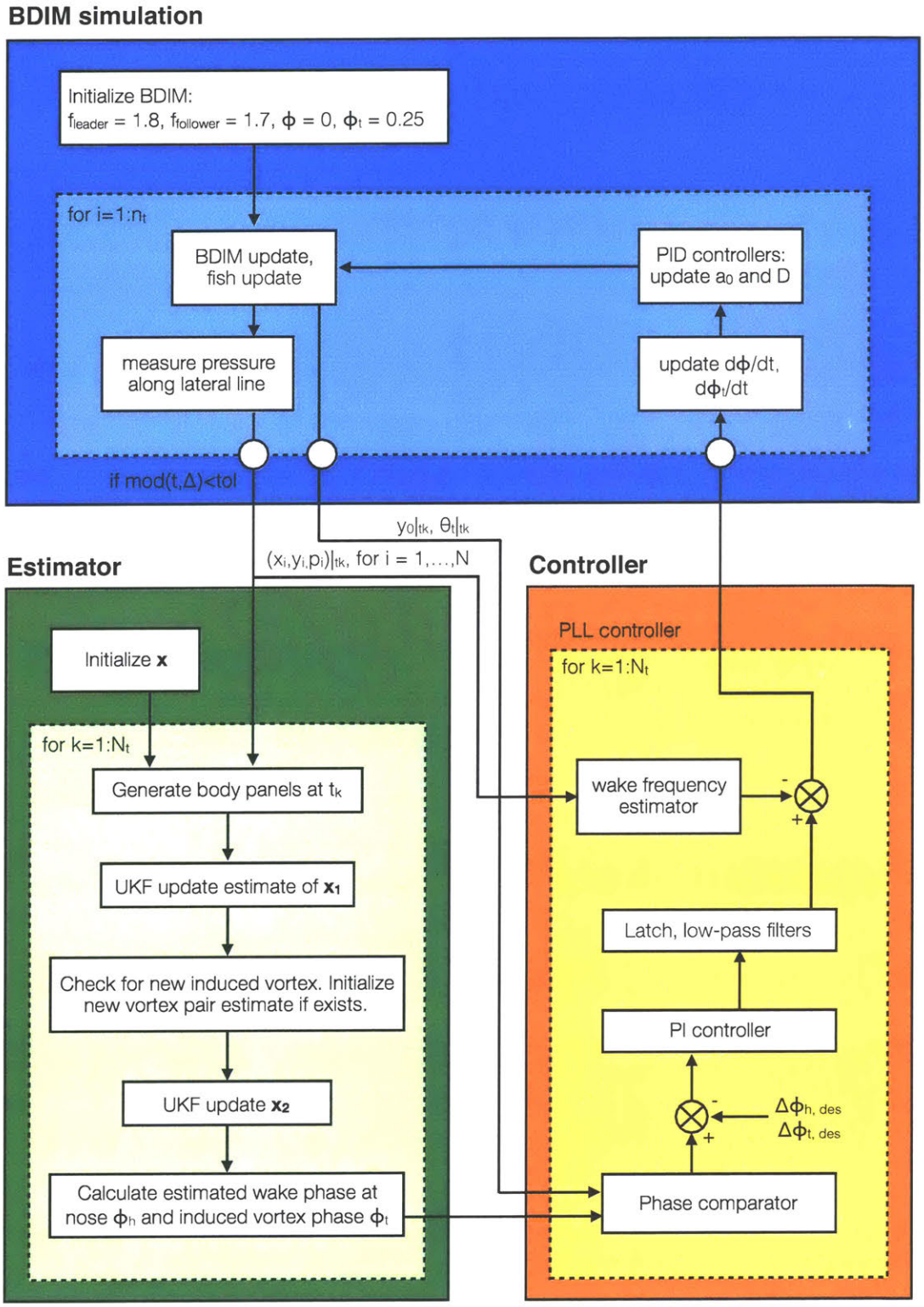

Figure 4-19: Diagram of the entire system.

(a) power spectral density: y_0 (b) head phase difference

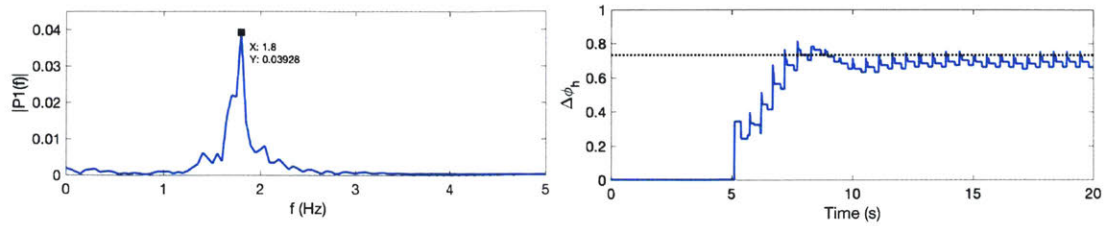

Figure 4-20: (a) power spectral density for the lateral head motion and (b) the estimated head phase difference, for a simulated fish with active body phase control implemented, without the frequency correction term. The fish converges to the frequency of the upstream wake ($f = 1.8$), but there remains some error between the actual (blue line) and desired (dotted line) phase difference.

This error in phase difference is significant, and increases if a lower control gain is used or if there is a greater difference between the natural frequency of the two swimmers. Indeed, this fish swims with an efficiency which is 13% lower than the fish executing the optimal configuration. Figure 4-21 shows two snapshots of the vorticity field for the controlled fish after the motion has converged.

These snapshots show that although the error in the phase difference is small, there are differences in the surrounding flow that lead to significantly reduced efficiency. Compared with the optimal configuration shown in figure 4-10, the negative vortex shed at the trailing edge is not as well paired with the positive vortex from the upstream wake, and the negative induced vortex over the peduncle region does not cancel the jet through the gap as effectively.

This example shows that a PLL controller that does not include a correction term for the difference between the intrinsic frequency and the tracked frequency will always lag behind the desired phase difference. An ermentrout controller is able to correct for this by slowly adapting the frequency of the internal system. However, Beal [11] showed that this controller resulted in a considerable amount of oscillation about the tracked frequency and phase in the presence of noise.

With the correction described with equation 4.15, this phase lag is eliminated, as will be demonstrated with the final controller.

Secondly, we will demonstrate the results of a simulation in which the following

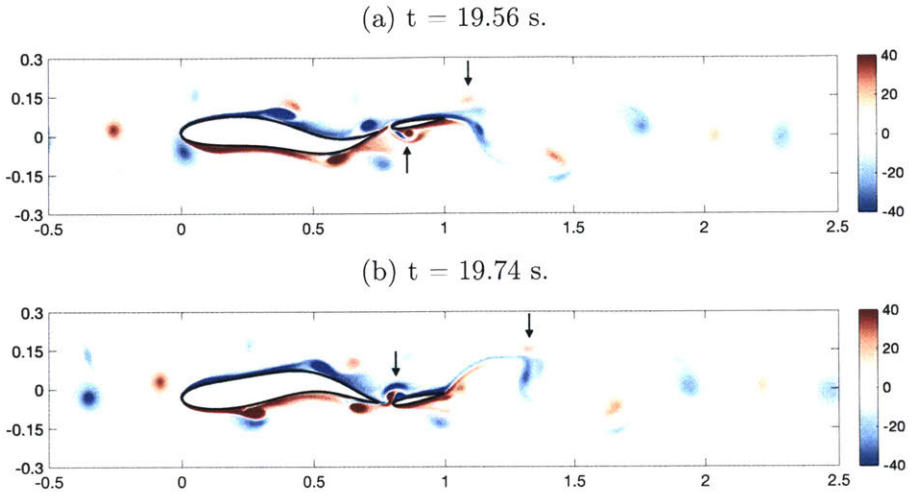

Figure 4-21: Snapshots of the vorticity field for the controlled fish after the motion has converged. These show that while the flow state is similar to that of the optimal configuration shown in figure 4-10, there are noticeable differences due to the small difference from the optimal phase, highlighted with arrows. In particular, the negative vortex shed at the trailing edge is not as well paired with the positive vortex from the upstream wake, and the negative induced vortex over the peduncle region does not cancel the jet through the gap as effectively.

fish is already phase-locked to the upstream frequency and desired phase, and the tail controller is activated to lock to the desired pitch phase difference. The results of this simulation are shown in figures 4-22 - 4-24.

Figure 4-22 shows that the fish converges to the desired tail pitch phase difference quickly - within 2.5 s after the controller is activated (roughly 5 swimming periods), the tail pitch has converged to the desired phase difference with a standard deviation

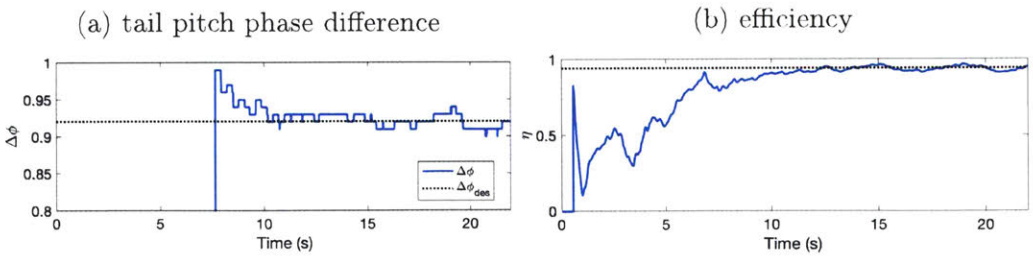

Figure 4-22: (a) the estimated tail pitch phase difference and (b) the period-averaged quasi-propulsive efficiency for a fish that begins at the optimal body phase, and uses active control to converge to the optimal tail pitch phase over time.

(a) Before control: t = 7.31 s.

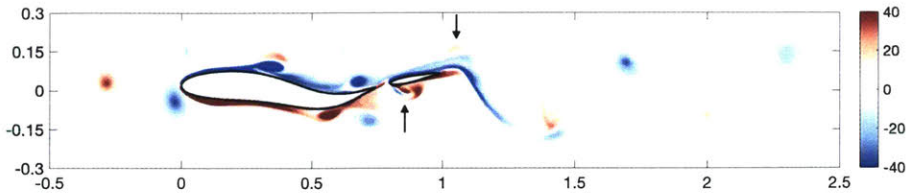

(b) After control: t = 21.75 s.

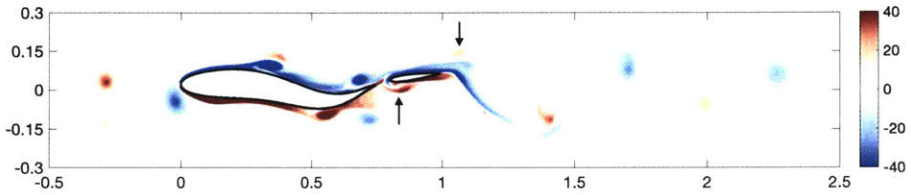

Figure 4-23: Snapshots of the vorticity field which show the swimming configuration and surround flow field (a) before the tail control is activated, and (b) after the tail controller has driven the tail phase to the desired flow-relative state. The arrows highlight the important details.

of $\sigma < 0.01$. The resulting efficiency shows that once the controller has converged, the efficiency also converges to the optimal efficiency found previously. Due to the history effect of the wake, the efficiency takes slightly longer to converge.

Figures 4-23 and 4-24 show snapshots of the vorticity field surrounding the fish (a) before control is applied and (b) after control has converged. These illustrate two characteristics of the flow that result in a large difference to the swimming efficiency. As the tail pitch phase shifts by about 0.15 (54 degrees), the flow around the peduncle region changes significantly; the induced vortex is annihilated more effectively as it passes over the peduncle region, and the caudal fin is angled in a manner that allows it to harness the low pressure core of the induced vortex for additional thrust. Furthermore, we can see that the subtle difference in the phasing of the tail pitch results in improved pairing and cancellation between the vortex shed at the trailing edge and an oppositely signed vortex from upstream. This results in a weaker and narrower wake downstream from the fish.

It is interesting to note that the efficiency of the downstream fish is relatively robust to oscillations around the desired tail pitch phase difference (figure 4-25).

In this simulation, the gain applied to the tail control was too high, leading to

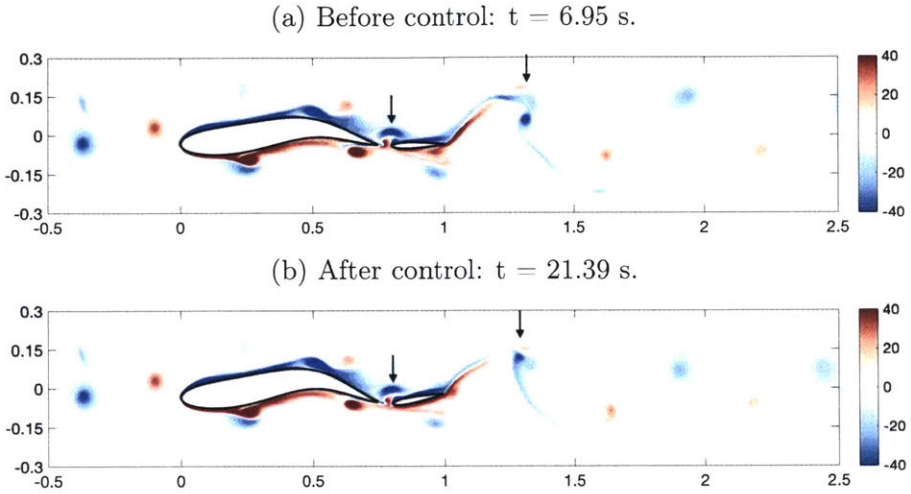

Figure 4-24: Snapshots of the vorticity field which show the swimming configuration and surround flow field (a) before the tail control is activated, and (b) after the tail controller has driven the tail phase to the desired flow-relative state. The arrows highlight the important details.

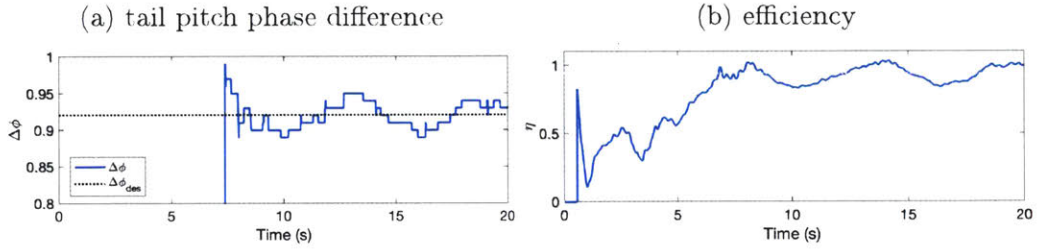

Figure 4-25: (a) the estimated tail pitch phase difference and (b) the quasi-propulsive efficiency for a fish that begins at the optimal body phase, and uses active control to converge to the optimal tail pitch phase over time. In this case, a large proportional gain causes the tail phase to fluctuate around the desired value (dotted line), but the average efficiency is still close to the desired value (dotted line).

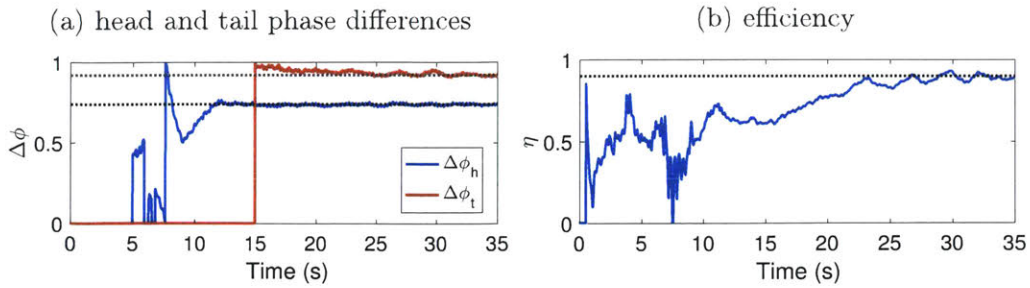

Figure 4-26: (a) the estimated head and tail phase differences and (b) the period-averaged efficiency over time, for a fish which first converges to the desired body undulation phase, and activates the tail control at t=15.

oscillations in the phase difference for an extended period of time. However, as seen in figure 4-25b, the efficiency also oscillates around the optimal efficiency, rather than begin reduced.

A final control simulation was conducted in which the fish is first driven toward the desire body phase difference, with the frequency correction described in equation 4.15, and subsequently fine-tunes the tail pitch phase. The phase differences and period-averaged efficiency over time are shown in figure 4-26.

In this final controller, the tolerance of the phase estimation algorithm has been reduced, so the phase differences shown are much more smooth over time. As shown, both the body phase and the tail phase converge to the setpoints quickly. The vortex estimator takes some time at the beginning to converge to an accurate estimate. Following convergence of the estimator ($t = 6.5$), the body phase controller converges to the desired phase within about 5 seconds, or 10 swimming periods. After the tail controller is activated at $t = 15$, the tail pitch phase converges to the desired value in about 10 seconds. Figure 4-26b shows that shortly after this, the period-averaged efficiency converges to the optimal value of $\eta_{QP} = 90\%$.

Figure 4-27 shows vorticity snapshots of the flow surrounding the fish before the body phase controller has converged, after the body phase controller has converged, and after the tail controller has converged. We can see clear changes to the flow surrounding the fish between each of these frames. While the body controller is working to drive the body phase toward the ideal phase difference, the amplitude of

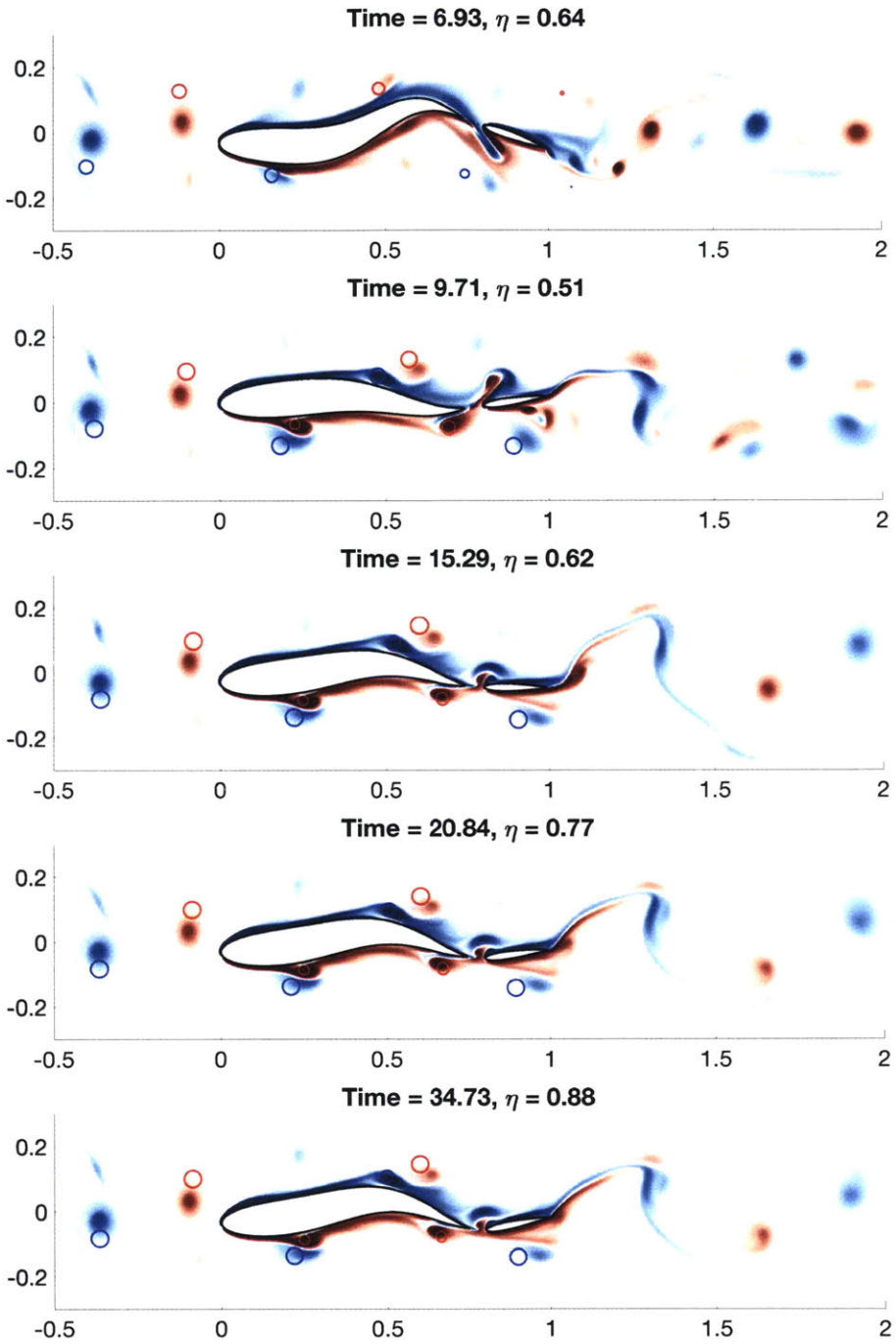

Figure 4-27: Vorticity snapshots of the fish (a-b) before the body phase controller has converged, (c-d) after the body phase controller has converged and after the tail controller is activated, and (d) after the tail controller has converged. The circles show the estimated vortex positions, as given by the model-based observer.

undulation and efficiency vary wildly, along with the downstream wake. Changes to the phase dramatically affect the interaction between the entire body of the fish and the upstream wake. The interactions vary between being beneficial and detrimental, but the overall efficiency hovers around $50 - 60\%$.

In fact, even after the body phase has converged, the efficiency is not much higher. However, this step is still necessary, as no amount of fine-tuning of the tail motion would be effective if the induced vortices were not properly positioned to be exploited by the tail. As shown in figure 4-26a, the greatest change to the efficiency occurs between $t = 15$ and $t = 25$, as the tail motion is fine-tuned. As shown in the last three snapshots of figure 4-27, although the flow field looks very similar in $t = 15.29$ and any subsequent timesteps, this fine-tuning of the tail motion results in a 30% increase to the efficiency! Flow sensing and vorticity control make this possible, as described in sections 4.3.3 and 4.3.4.

This shows that the ability to independently control the tail pitch is crucial. Small but precise changes to the tail motion have the potential to dramatically improve the swimming efficiency. As previously shown, real tuna possess a strikingly pronounced keel which provides the ability to precisely execute powerful control of the caudal fin. This precise and independent control has been known to allow tuna to execute optimal kinematic patterns to swim efficiently when alone. In the presence of vortices, we demonstrate here that independent control is even more critical - very precise interactions with the surrounding vortices can allow a fish to swim with less than half the energy required to swim by itself.

4.4.4 An example of bad control

While the final controller is very robust to the initial conditions of the simulation, many simulations were run during the development of the controller which demonstrated that control within the wake is a challenging task. One example is shown here, in which the added synchronization term (equation 4.15) is missing, and a high integral gain is used instead to attempt to drive the phase error to zero.

Figure 4-28 shows the head and tail phase differences, and the time-averaged

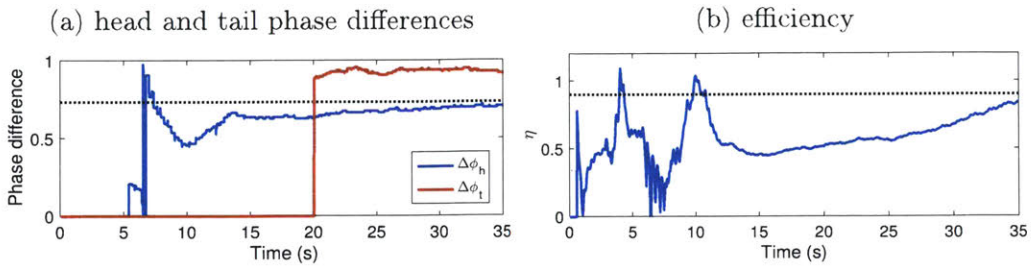

Figure 4-28: (a) the estimated head and tail phase differences and (b) the period-averaged efficiency over time, for a fish which does not execute very good control. Note: the head controller is activated at $t = 5$, and the tail controller is activated at $t = 20$.

efficiency. We can see that in contrast to figure 4-26, the efficiency does not increase shortly after the controllers are turned on, but instead it takes an extremely long time. In particular, although it is clear that the tail phase converges to the desired value shortly after $t = 20$, the fish has not converged to the optimal efficiency even by the end of the simulation at $t = 35$. Even with a much higher integral gain of $k_i = 1$, the error $\Delta\phi_h$ decreases very slowly.

As previously mentioned, fine-tuning of the tail phase is not helpful unless the fish has already positioned the peduncle relative to the induced vortices appropriately via control of the body phase. The effect of an error in this positioning can be clearly seen in figure 4-29. This figure shows a sequence of snapshots, all taken after the tail controller has been activated. Although the tail has reached the "optimal" phase by $t \approx 26$, the efficiency remains low, around $\eta_{QP} \approx 60\%$. The snapshots show that while the induced vortex on the right is positioned roughly over the peduncle, it does not appropriately suppress the jet flow.

In the last snapshot of figure 4-29, the body undulation phase has almost converged to the desired value, and the surrounding flow looks much closer to the optimal case.

In general, the model-based observer is extremely robust in its ability to converge to an accurate estimate of near-field vortices (usually converges within 10 tail-beat cycles or less), regardless of the exact UKF parameters used. Similarly, the controllers are robust in driving the fish toward a higher swimming efficiency regardless of the exact control gains used. However, as shown here, depending on the exact configu-

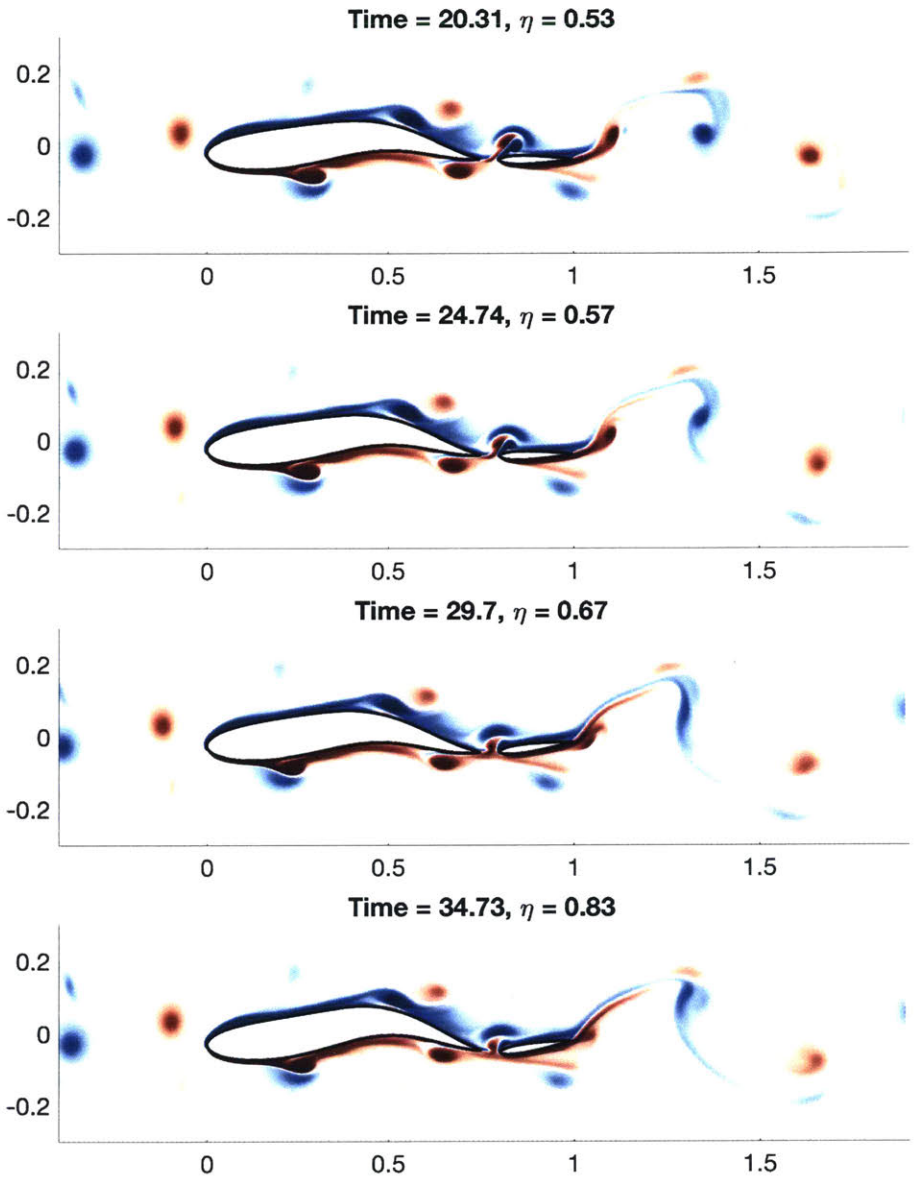

Figure 4-29: Vorticity snapshots of the fish after the tail controller has been activated. Although the tail pitch phase converges quickly to the desired value, the efficiency takes a long time to converge to the known optimum.

ration of the controller, the fish may require a long time to converge to the optimal swimming configuration. The optimal phase difference relative to the upstream wake $\Delta\phi_h$ must be achieved before the tail phase difference $\Delta\phi_t$ is relevant.

Note that the current work is still conducted under highly idealized conditions. Within a wake subject to perturbations in individual vortex strength or wake width and wavelength, or within the chaotic conditions that may exist within an actual school of fish, the ability of downstream fish to perfectly synchronize to the upstream wake would likely be greatly reduced. However, the results of the present work still serve to provide insight into the conditions and interactions which would lead to increased efficiency when schooling, and the sensing and control requirements that could be used to exploit individual vortices within a wake.

4.4.5 Summary: control

Table 4.1 summarizes the power expended C_E and swimming efficiency η_{QP} for a few cases described in this chapter. A fish swimming by itself swims with an efficiency of roughly $\eta_{QP} = 40\%$. While changes to the tail pitch phase can change the efficiency by a few percent, the effect is relatively small. For a fish which is in the wake of another fish, but swimming at a slightly different frequency and therefore interacting inconsistently with the upstream wake, it is able to swim at a slightly higher efficiency of $\eta_{QP} = 59\%$. Through consistently interacting with the upstream wake, but without fine-tuning of the tail pitch, the fish can achieve an efficiency of roughly $\eta_{QP} = 74\%$. Finally, through interacting with the upstream wake at the optimal body undulation phase and the optimal tail pitch phase, an efficiency of 90% can be reached.

Section 4.3.4 demonstrated that while an extremely high swimming efficiency can be reached in a tandem swimming configuration, the efficiency is extremely sensitive to the precise timing of the fish. For small deviations (around 0.1) from the optimal body phase or tail pitch phase, the efficiency is reduced by $10 - 20\%$. Therefore, a key question is: can a controller be developed which is capable of using lateral line feedback to converge to a desired flow-relative phase difference with the required precision?

	case	f	$\Delta\phi$	ϕ_t	C_E	η_{QP}
(a)	solitary fish	1.8	n/a	0.25	0.114	0.38
(b)	solitary fish	1.8	n/a	0.30	0.105	0.42
(c)	solitary fish	1.8	n/a	0.40	0.105	0.42
(d)	fish in wake	1.7	n/a	0.40	0.076	0.59
(e)	fish in wake	1.8	0.51	0.30	0.060	0.74
(f)	fish in wake	1.8	0.51	0.40	0.048	0.90

Table 4.1: Summary of the swimming efficiency for several solitary and tandem swimming configurations.

Section 3.6.5 demonstrated that even with a significant amount of measurement noise, a model-based observer using feedback from the lateral line on a fish could estimate the position of an oncoming vortex with a positional error of 0.0069 (with $N = 200$ sensors, $m_1 = 16$ nose sensors). This error is equivalent to a phase estimate error of 0.0124 (about 5 degrees). Presently, we demonstrated through a simulation of an actively controlled fish that this is sufficiently precise. Using only feedback from the lateral line, the downstream fish is able to lock in to the upstream wake at the appropriate phase to reach and maintain the optimal efficiency of $\eta = 90\%$. The design of the controller is important - it is important not only to synchronize to the wake frequency but also to a specific phase with zero phase lag. A phase-locked loop controller which incorporated the estimated frequency of the upstream wake provided the ability to do this.

Therefore, the answer is a resounding *yes* - the lateral line provides feedback that allows the fish to identify surrounding vortices with the required precision with which to execute flow relative control. Although the swimming efficiency is extremely sensitive to the timing of interaction with the upstream wake, the fish can control its motion precisely to extract energy from the flow and reach extremely high swimming efficiencies.

4.5 Discussion

4.5.1 Model-based flow-relative control

The benefit of model-based flow-relative control warrants further discussion. Several groups have shown that various simple control strategies can be used to accomplish flow-relative control tasks. For example, Salumäe et al. [132] and Salumäe and Kruusmaa [131] used empirically derived controllers to accomplish station-holding tasks for a robotic fish equipped with an artificial lateral line. The average pressure difference sensed by probes on the left and right over time is linearly related to the yaw angle. Through experiments, other empirical relationships can be found between the time-averaged pressure measurements and the flow velocity, presence and distance from an upstream object, and lateral deviation from an upstream wake. Similarly, Venturelli et al. [165] show that in the wake behind a cylinder, the statistical characteristics of the flow are different than those of a steady flow, allowing a fish equipped with an artificial lateral line to extract features such as the vortex shedding frequency, speed, and wavelength. In comparison, there is very little work which accomplishes the same tasks through using model-based control, due to the increased complexity of including a hydrodynamic model.

However, section 3.9 demonstrates precisely why empirically-derived control laws are dangerous. Indeed, the signal averaged over many cycles will approximate a quasi-steady system, but when fast control is of interest, the transient hydrodynamics must also be taken into account. Empirically-derived control laws often neglect these transient effects. For a fish within a wake, the upstream flow is never perfectly regular. In order for a control system to respond to perturbations quickly, the transient signals induced by them must be detected and interpreted.

Figure 4-30 shows the pressure measured over space and time along the lateral line of a fish swimming at a different frequency from the upstream wake. We will explore a few different strategies for the "seemingly" simple task of characterizing the upstream wake. This is a straightforward problem that is slightly complicated by the fact that the interaction between the downstream fish and the wake changes slowly

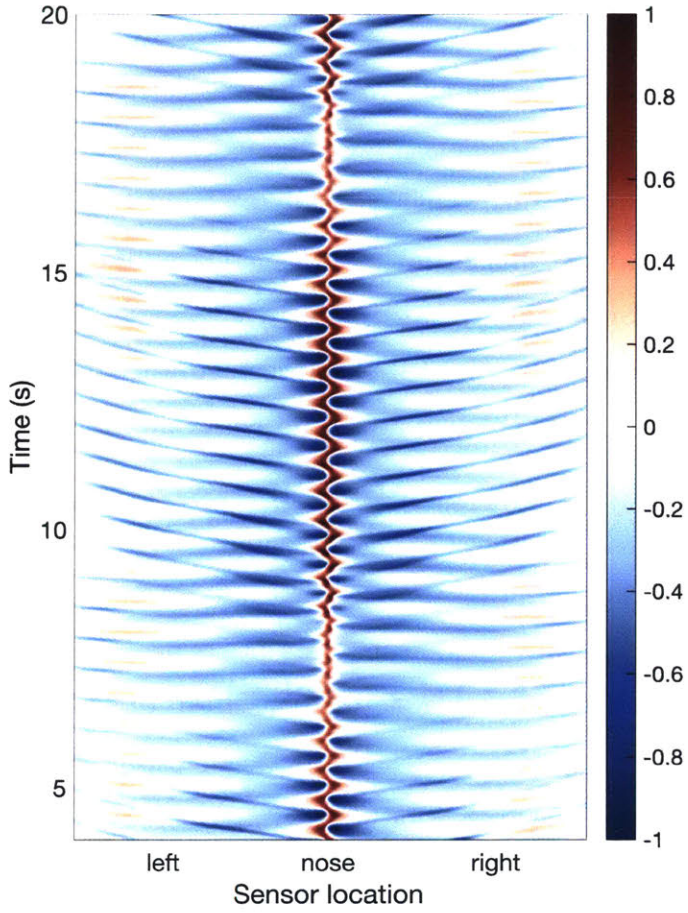

Figure 4-30: Spatiotemporal plot showing the pressure measured by the lateral line on a fish swimming with tail beat frequency $f = 1.7$ within a wake of frequency $f = 1.8$.

over time.

Assuming the upstream wake is periodic in nature, the vorticity at some distance d downstream from the trailing edge of the upstream fish can be modeled as:

$$w(d, y, t) = w_y(y, t) w_d(d) \sin(2\pi(\phi_1(d) - ft)) \tag{4.16}$$

Where $\phi_1(d)$ is the phase of the wake at d. The exact profile of the wake is not important for the present control scheme, so we model the vorticity of the oncoming wake as approximately:

$$w(d, t) \sim \sin(2\pi(\phi_1(d) - ft)) \tag{4.17}$$

For the present case, the phase ϕ_1 of the upstream wake at distance $d = 1$ downstream (the leading edge position of the following fish), was calculated from vorticity plots of the upstream fish swimming alone, and found to be $\phi_1(1) = 0.8867$. This vorticity estimate for the upstream wake is plotted as w in Figure 4-31.

To explore potential strategies for approximating w directly using the pressure measurements (without a physics-based model), we also show in figure 4-31 (a) the pressure measured at a single point left of the nose, (b) the position of the stagnation point over time, and (c) the pressure at a point left of the nose with the self-induced pressure subtracted.

It is immediately obvious that the vorticity $w(d = 1, t)$ cannot be approximated by a single pressure measurement on the nose (figure 4-31a). The pressure signals close to the nose, in fact, actually contain multiple peaks per cycle, oscillate significally over time, and do not have any simple relationship to the actual wake vorticity at $d = 1$.

Does the position of the stagnation point reveal more information about the oncoming wake? While this signal is cleaner than that of a single pressure measurement near the nose, it also does not have a simple relationship to the vortcity $w(d = 1, t)$. It is clear that this signal contains frequency components from both the upstream wake frequency and the swimming frequency of the downstream fish.

This suggests that it may be possible to approximate the oncoming vorticity field better if we subtract the self-induced effect of the fish. P_{exp} is estimated using a potential flow model, and figure 4-31c shows that this signal approximates that of the oncoming vorticity field much better. With the self-induced pressure subtracted, the pressure signal closely matches the frequency of the upstream wake, but contains a small phase difference.

However, we cannot immediately relate the phase difference observed here to the physical wake phase. Perhaps, through conducting a few simulations or experiments, it would be possible to derive an empirical relationship. However, the pressure sensed is not a simple function of the phase of an oncoming vortex street, and the empirical relationship may fail to capture the effect of other variables such as swimming speed,

(a) Pressure left of nose

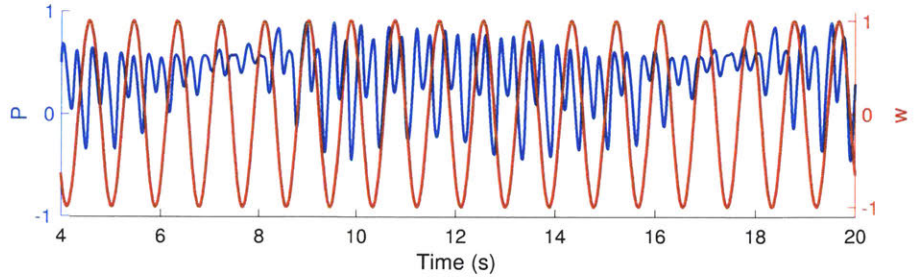

(b) Stagnation point position

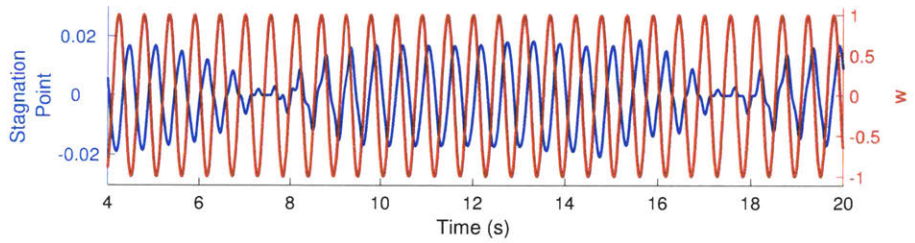

(c) Pressure left of nose (self-induced pressure subtracted)

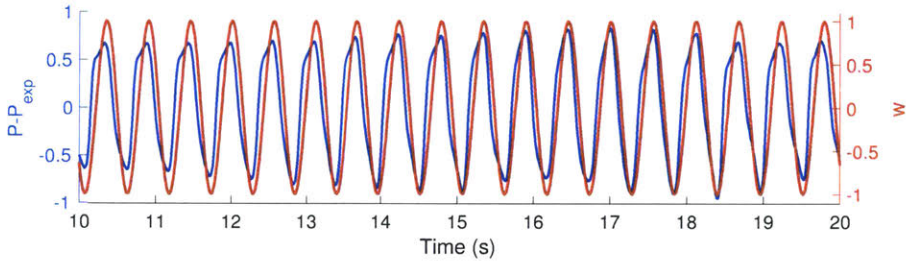

(d) Model estimated wake

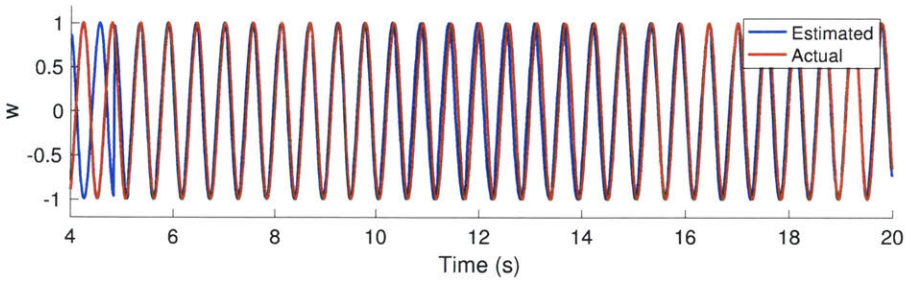

Figure 4-31: (a) the estimated head and tail phase differences and (b) the period-averaged efficiency over time, for a fish which first converges to the desired body undulation phase, and activates the tail control at t=15.

frequency, vortex strength, wake wavelength, and deviation from the wake centerline. If the fish swims at a swimming speed or frequency outside the range of what has been explicitly captured with the empirical dataset, the relationships may no longer hold. The empirical relationships may also fail to capture easily interpretable information while the fish executes control actions. A physics-based model is not subject to this shortcoming.

Simple feedback control laws certainly do work under specific circumstances. For example, Beal [11] used two anemometer probes within the wake upstream from a controlled flapping foil in order to calculate the wake phase which is used in the feedback control law. However, when the feedback sensors are located on the sensing body itself, modeling and "subtracting" the self-induced signal is extremely important.

Figure 4-31 shows the vorticity $w(d = 1, t)$ estimated by the complete model, compared with the actual oncoming vorticity. Although the estimator requires some time to converge at the beginning, it captures the actual vorticity field extremely well after the initial stage. There appears to be a small amount of error around $t = 12$, but this is an artefact. The fish displaces the oncoming vortices slightly, so the actual wake phase at $d = 1$ in a tandem swimming configuration is slightly different from the phase calculated with no downstream swimmer. The model allows the fish to accurately capture the nature of the oncoming wake, regardless of the swimming velocity, frequency, control actions that result in temporary acceleration or deceleration, etc.

4.5.2 Distributed flow sensing for feedforward control

An interesting advantage to a distributed sensing platform is the ability to use sensors within the system as part of a feedforward control system.

A feedforward control term passes information from a source at one point within the environment to a controlled element elsewhere in the environment. Since fish possess lateral line sensors over the entire body, sensors at the head and along the body can potentially capture information about nearby vortices before they reach the tail, which acts as a control surface. Within the current simulation, control actions

are applied slowly, so that the controller converges to the desired vortex-relative phase within 10-20 tail beat periods, which allows the fish to execute timing within relatively regular wakes. However, in less regular wakes where faster control would be desirable, such a feedforward controller would be very valuable in its ability to counteract the time delays inherent to signal processing within the system.

The control system on the tail, within the current system, acts to make minute adjustments to the tail pitch in order to correctly time its motion relative to the approaching induced vortex. As mentioned, the mechanism of of energy savings with respect to this induced vortex is very straightforward - a tail which is held at a higher angle as the vortex approaches can directly enhance thrust generation. The induced vortex is sensed upstream, which allows some time for the tail position to be realized. In the present system, the vortex-relative phase is calculated as the vortices reach the end of the main body, just upstream of the caudal peduncle. However, in theory, the relative phase can be calculated when the induced vortices are further upstream on the body. This would compensate for a greater time delay resulting from sensory processing, as well as for the finite time required to adjust the tail fin to the desired phase/position.

How much of a time delay could be corrected for by using such a feedforward scheme? The induced vortices travel relatively slowly along the length of the body. In the present system, each induced vortex requires nearly 2 full swimming periods to reach the caudal peduncle, from the time of formation, because in general the induced vortices travel much slower than the freestream velocity. In particular, as the induced vortices reach the anterior portion of the body, they have slowed down to 50% of the freestream velocity or less. As a result, the fish can predict where the vortex would be when it reaches the tail nearly 2 tail beat cycles, or about 1 second, before the induced vortex actually reaches the tail. Of course, the motion of the fish and any external disturbances also affect the velocity and position of the induced vortex over time. However, the ability to estimate the position of the induced vortex so early allows the body to begin to implement the appropriate control actions far before the vortex actually reaches the tail.

In the current system, we already take advantage of the distributed nature of the lateral line in some ways. In addition to the ability of a distributed sensory system to provide both spatial and temporal resolution of the pressure field, it also allows for the estimated state of the induced vortex to be refined as the vortex moves over the body. While it can be challenging to characterize a nearby vortex from a single pressure snapshot (for example the pressure sensed as the vortex reaches the peduncle), the state of the induced vortex can be estimated with much lower uncertainty when the UKF has the entire length of the fish (and nearly 2 entire swimming periods) to refine the estimate.

Chapter 5

Concluding Remarks

Animals in nature are experts at exploiting their environments. Salmon are known to be capable of migrating up to 1000 miles upstream without consuming any food after leaving the sea [114]. Such a journey with no refueling would constitute a miraculous feat for a vehicle made by humans. The fish were estimated to be up to 5 times more efficient than engineered vehicles, due to their ability to take advantage of regions of reduced velocity and to extract energy from the turbulent flow. Indeed, numerous subsequent studies have demonstrated that fish do experience substantial energy savings in the presence of altered flows [90]. Research has also demonstrated that fish can swim with $9-20\%$ less energy in schools than when swimming alone [65, 101, 80, 147].

Schooling fish present a paradigm problem in which individual fish are subject to predictable and regular arrays of vortices shed by upstream fish. Research has shown that 1) under predictable circumstances, fish will kinematically adjust to exploit energy from vortex streets, 2) fish have a highly perceptive flow sensing ability, and 3) fish save energy within predictable unsteady flows but generally avoid chaotic flows. Yet, it remains unknown if fish can exert *active* control to exploit the energy of near-field vortices when swimming in a school.

A recent study by Maertens [97] demonstrated that when schooling in a tandem configuration, the downstream fish can save energy even when swimming directly behind another fish and therefore directly within a mean jet-like flow. This result

directly contradicted the hypothesis by early researchers that fish can only save energy when swimming in diamond patterns that allow downstream fish to encounter a mean reduced flow. Obviously, when swimming at a distance directly behind another fish, the only way to save energy would be through capturing the energy of individual vortices, which presents a fascinating problem. It suggests that fish in schools do not only save energy through drafting or passive mechanisms, but that active control may actually be used to harness the energy from individual vortices. How are individual vortices "captured", and are fish actually able to execute the precise control necessary to capture individual vortices?

We studied this problem through studying in detail the hydrodynamic interactions between two fish swimming in tandem, focusing on the sensing ability provided by the lateral line. The lateral line, which is defined in part by a distributed array of sensors over the body that allow for the detection of pressure gradients, is uniquely suited for the detection of flow patterns that vary on a lengthscale shorter than the fish. Although the pressure sensed is a very nonlinear function of the fish motion and surrounding flow, the states of nearby vortices can be precisely decoded from the information contained within the lateral line with a model-based observer. This precise localization of nearby vortices gives rise to the ability of fish to meticulously control their timing in order to extract energy from the upstream wake. We show in simulation that by executing deliberate actions to lock into the frequency of an upstream wake at a desired phase, the downstream fish can improve its swimming efficiency by $10-20\%$. Furthermore, we discovered that fine-tuning of the tail motion can result in even greater energy savings. In this work, we have built onto the concept of vorticity control through showing that for a fish with a distinct tail, subtle control motions can be executed to yield a dramatically increased swimming efficiency of $\eta_{QP} = 90\%$. This demonstrates that vorticity control is a powerful control mechanism that can allow fish to reduce their swimming cost by over 50%, through a small control effort which is informed by the precise and distributed information captured by the lateral line.

Do fish actually sense and actively use vortices when schooling? We may never

know, but the present work demonstrates that in theory, it is certainly possible to, and moreover, the sensing ability that allows them to do so would be an invaluable addition for engineered underwater vehicles.

5.1 Thesis contributions

The contributions of this thesis are divided into 3 main parts: 1) vorticity control in fish schooling, 2) vortex sensing with an undulating body, and 3) active control for wake exploitation. In the following sections, the specific contributions from each of these parts will be discussed in detail and differentiated from similar work in the field.

5.1.1 Vorticity control in fish schooling

In prior work, it has been proposed that fish swim in specific patterns to achieve the greatest energy savings [170]. However, later research found that most fish do not actually swim in regular arrays [118]. The present work corroborates the work by Maertens [97] in showing that although schooling formation is likely important, there exists many positions in which a fish could save energy due to the number and complexity of interactions taking place over the body of the fish. Even when swimming directly within the mean jet flow behind another fish, a downstream fish can still coordinate its motion in order to harness energy from the wake. Fish, which instinctively respond to alterations in the flow surrounding their bodies, are capable of making minute adjustments to take advantage of individual interactions.

Through running a methodical set of simulations for fish swimming at varying body undulation phases, we developed an understanding of the physical hydrodynamic mechanisms which give rise to increased or decreased efficiency along the body of the fish. While prior work has resulted in conclusive heuristics relating the wake topology of a flapping foil to its thrust and efficiency, the current work aims to develop these heuristics on a local level that are observable to the fish. By calculating sectional thrust ratios and partial efficiencies, we identified timing strategies for the

head, body and tail of a fish. At the head, the fish should slalom between oncoming vortices to save energy. Along the body, the fish can save energy by keeping vortices on the upstream slope of its undulating crests (but this timing is fundamentally incompatible with the optimal head timing). At the tail, the fish can save energy by pairing vortices shed at its trailing edge with oppositely signed vortices from upstream. These strategies are consistent across the range of swimming frequencies tested, $f = 1.5$ to $f = 2.7$. We found that timing within all sections contribute about equally to the overall swimming efficiency; good timing compared with bad timing can yield a 50% difference to the thrust ratio within each section and a $5 - 10\%$ difference in the partial efficiency.

For a fish modelled as a NACA0012 airfoil undulating at a frequency of $f = 1.8$ swimming in tandem with another fish at $1L/s$, good timing can result in an energy savings of 15% over solitary swimming ($\eta_{QP} = 60\%, \eta_{QP,solitary} = 51\%$). Even with the least efficient phasing, however, the fish still swims with 3% less energy than required to swim alone ($\eta_{QP} = 53\%$). Due to multiple vortex-body interactions over the body of the fish, some of which are beneficial and some that are detrimental, the potential energy savings is limited and depends on specific parameters such as the swimming frequency.

However, with an additional degree of freedom introduced through modeling the fish with a distinct tail, we observed a much greater potential gain in efficiency. Over the majority of the parameter space spanned by the body undulation phase ϕ and tail pitch phase ϕ_t, the changes in efficiency were were similar to those observed for the continuous fish, ranging from roughly $\eta_{QP} = 50\%$ to 60%. However, for a very narrow range of about 50 degrees, the efficiency was significantly higher ($\eta_{QP} \sim 70\%$). Within this region, fine-tuning of the tail pitch phase resulted in a phenomenal efficiency of $\eta_{QP} = 90\%$. This example demonstrated the ability of fish to profoundly affect their surrounding flow and swimming efficiency through small but precise control motions, and showed that well-executed vorticity control can be a powerful tool. No prior work has explored the benefit of a distinct tail fin in a schooling configuration, or shown that such a dramatically increased efficiency can be achieved through vorticity

control in schooling. This work demonstrated that independent control of the tail pitch is extremely important, supporting the evidence from nature that tuna can exercise powerful and independent control of the caudal fin. While the importance of independent tail control has been demonstrated before for fish swimming in quiescent water, this is the first study to demonstrate that independent tail pitch control is even more important in the presence of external vortices.

A distinctive aspect of the current work is the focus on induced vortices along the body of the fish, which are created at the nose through interaction with upstream vortices. Although the formation of secondary vortices is usually associated with energy loss, in this case we demonstrate that they can be controlled in a very beneficial way. Of course, deliberately generating additional vortices so that they can be used downstream is probably not advantageous. However, if vortices are already generated upstream, such as when a fish encounters a reverse Kármán vortex street or through vortex shedding from upstream fins, the ability to extract energy from them at a downstream point is very advantageous. For the fish with a distinct tail, optimally capturing the induced vortices downstream in a manner that greatly reduces the force oscillations experienced by the rigid tail allows the fish to harness the wake from an upstream fish to swim with less than 50% of the energy required for solitary swimming.

5.1.2 Vortex sensing with an undulating body

We have demonstrated that a fish can execute precise vorticity control to achieve impressive swimming efficiencies. However, is it feasible for a fish to actually execute such precise control? To do so would require the ability to sense the surrounding flow in great detail. Therefore, a large part of this project focuses on characterizing the sensing ability of the fish lateral line for a fish swimming in tandem with another fish.

Since Chapter 2 demonstrated that the efficiency of the downstream swimmer depends specifically on the timing of the fish relative to the vortices in the upstream wake and the induced vortices, the goal within this section has been to characterize in great detail the ability of fish to extract the states of near-field vortices from

the pressure sensed by the lateral line. Although vortices are invisible to the eyes, they are extremely detectable and characterizable flow structures for the lateral line. Yet, as we demonstrated in Chapter 3, this signal is a nonlinear function of the fish motion and the surrounding flow. The nonlinearity makes it difficult, and maybe impossible, to develop a low-order model using statistical methods that consistently relates the states of surrounding vortices to the pressure sensed. An effective model must account for the physics of the system, and in particular the self-induced effect of the fish. We developed a model using potential flow theory, and modeled the fish using a panel method. We demonstrated that by combining physical models and physical heuristics, a fish can interpret the low-bandwidth and relatively sparse signals captured by the lateral line in order to understand the surrounding flow. An unscented Kalman filter was used in conjunction with the potential flow model in order to estimate the position of vortices in the near-field. We showed that this framework can be used to characterize around 10 vortices in the near-field of a fish swimming through a wake, which are all interacting significantly with the fish. This is the first example, to the knowledge of the author, that demonstrates the possibility of localizing so many vortices that are strongly interacting with an undulating body, using sensors on the body.

The strong vortex-body interactions are exactly what gives rise to energy savings, but they also make the estimation problem more challenging. In particular, while some studies in the past have shown that a similar methodology (Bayesian filtering) can be used to estimate the positions of one or two vortices near a flat plate, these studies also conclude that when multiple vortices are so close together that their signals overlap, the estimation problem becomes significantly more challenging, if not impossible [146, 50]. In a school of fish, the vortices are inevitably close together. For fish swimming with a tail-beat frequency of $f = 1.8$ at $1L/s$, there may be 5 or more vortices from the upstream wake that impose a significant effect on the fish at any instant. In addition, the interaction between the fish and the upstream wake results in the generation of new vortices, resulting in 3 or more induced vortices along the body of the fish at any instant.

Indeed, it is generally impossible to simultaneously estimate the positions of so many vortices which are close together and strongly interacting with the fish. However, we have shown that physical information about the system can be used to augment the estimation algorithm to improve its estimation ability and the accuracy of estimated vortex positions. For example, rather than estimating the states of individual vortices within the oncoming vortex street, we can reduce the number of unknown states by treating them as a group of vortices in a specific configuration. A similar idea has been demonstrated in the past; in potential flow, there is a well known equation for an infinite row of vortices. The wavelength, strength, velocity, and distance to a laterally positioned sensing body could theoretically be estimated by a lateral line [125]. However, this model fails when the vortex street is directly ahead of the fish or in any way strongly interacting with the fish, which is critical for energy savings. Of course, the concept of characterizing a group of vortices with a reduced number of states only works if the vortices retain an ordered and predictable pattern. Indeed, real fish only tend to be attracted only to flows with a predictable spatiotemporal component [46, 140, 90].

We showed that vortices from the original wake that become nearly unobservable as they pass the nose of the fish can still be roughly localized through dead-reckoning, and very basic intuition about the wake and the formation of the secondary vortex can be used to prevent the estimator from converging to an inaccurate state estimate (local minimum). Through augmenting the estimation model with physical insights about the system, we developed a robust and accurate vortex estimator, despite the fundamental limitations to observability.

In the study of sensitivity and observability, we demonstrated that the observability of the fish is fundamentally very limited. Researchers in the past have shown that the lateral line is a near-field sensor, usually limited to signals within a single body length of the fish. A blind fish approaching a wall does not react to it until it is within about 10% of its body length [177, 179]. Through studying the observability of vortices near the fish by looking at the system sensitivity, the conditioning number of the local observability matrix, and a new uncertainty metric, we find similar

results. Although a vortex (of roughly the same strength as the vortices shed by the fish during steady swimming) may yield a discernible signal outside of a body length, the uncertainty in its position is high ($0.4L$ given measurement error of $e_p \sim 0.01$). Within about 10% of the body length, a vortex can be localized with relatively high accuracy.

We also perform an optimization of the number, density and layout of lateral line sensors for a 2D fish which has the goal of localizing oncoming vortices. There is relatively little work in the literature regarding the optimal number of sensors within a distributed flow sensing system, and our present work suggests that for localizing upstream vortices with a positional error $e_x < 0.02$, the fish should possess between 10 and 22 sensors at the head (nearly regularly spaced in the longitudinal direction, with about $N = 150$ sensors over the whole body). These results compare very well with real fish, who have an estimated 14 sensors along a 2D plane of the head, and about 94 sensors along a 2D plane of the body.

Finally, we demonstrate that although the self-induced effect of the fish makes interpreting the lateral line signal more complicated - more complicated than sonar, electrosense, vision, etc due to the interaction involved - it is also critical for sensing. We definitively show that the interaction gives rise to additional information about the flow. In this system, while the sign of a vortex cannot be discerned using a single flow snapshot obtained by a flat plate or a ghost body, a curved solid body interacts with the vortex in a way that reveals its sign. Modeling the self-induced effect is important for both sensing and control. The flow cannot be consistently interpreted (under varying swimming conditions) without modeling the self-induced effect, and control is deficient without accounting for the self-induced effect.

5.1.3 Active control for wake exploitation

The existing body of research on flow control for schooling fish is extremely sparse. The dominant focus of the existing work is on formation control rather than control of local hydrodynamic interactions. This is the first study, to the author's knowledge, to develop an active controller which uses feedback from a simulated lateral line to

directly control the interaction between a self-propelled fish and surrounding vortices.

By using the optimal phase differences learned through optimization, and the lateral line for localizing near-field vortices, we demonstrated that a fish can lock in to the frequency of an upstream wake at a desired phase to save a lot of energy. Through fine control of the tail phase, the fish can converge to the optimal efficiency of $\eta_{QP} = 90\%$. This work demonstrated that not only is it theoretically possible to extract energy from an upstream wake through executing a precise swimming motion, but that it is possible for fish to perform this under the realistic conditions of not being able to directly "see" vortices around it and the consequence of continuously altering the flow it is trying to observe and control. Despite large variations in the lateral line signal as the fish adjusts its motion, the physical model developed allows the fish to track the surrounding vortices accurately and consistently. Modeling the self-induced effect is critical for this.

This control approach is distinctly different from approaches reported in the past. These other approaches generally do not incorporate a physical model, instead drawing relationships between the pressure sensed by an artificial lateral line and the flow state using empirical data. In these studies, linear regression tools are usually used to model these relationships for use in feedback control systems. While they have been shown to enable a robotic fish to perform simple tasks such as station holding and recognition of an upstream wake [131], the control is typically executed over a long time (e.g., 300 seconds, which is roughly 600 tail-beat periods). If it is desirable to execute finer control (e.g., responding to a single vortex) or faster control, it becomes important to model the faster (and particularly the self-induced) dynamics. In the present study, our simulated fish could converge to the desired swimming configuration in only 20 seconds (about 36 tail-beat periods). Through tuning the controller, even faster convergence is likely possible, as the convergence is not limited by unmodeled dynamics. Furthermore, empirically-derived controllers would likely fail when tested under conditions that deviate too much from the empirical dataset used to train the controllers. This is not a limitation for model-based controllers, which continue to accurately model the relationship between the flow state and pres-

sure sensed regardless of specific swimming parameters such as swimming speed and tail-beat frequency.

5.2 Limitations of the current methodology

There do exist some limitations to the current methodology. Most importantly, the majority of this study was carried out in simulation. While the estimation scheme was shown to be robust to gaussian white noise (section 3.6.5), it is unclear if this is a good assumption for a real flow environment. Furthermore, in real life, wakes shed by fish are much more irregular. The upstream fish may go through cycles of swimming and gliding, encounter external vortices of its own, and adjust its swimming kinematics, all of which complicate the wake the downstream fish is subject to. In contrast, the system tested in simulation is extremely controlled and predictable. While this allowed us to systematically identify vortex interaction mechanisms and to develop and test a sensing and control scheme, it is a somewhat inadequate model of real flow. With this said, many of the the interaction mechanisms and ideas developed here are still applicable to more complicated flows.

Secondly, while the present model is capable of capturing the pressure sensed by the lateral line despite significant interaction with near-field vortices, there is a limit to the interaction it can capture accurately. It was somewhat surprising that the observer developed presently was capable of tracking vortices even as the fish directly intercepted them. In general, such strong interaction with a nearby vortex would create a significant (and potentially unmodeled) change in the locally measured pressure. As a result, there may exist certain conditions under which the unmodeled interaction is so large that the observer fails to discern the vortex that caused it. If this were discovered to be a real limitation, it would be possible to develop a specific model of the interaction to incorporate into the estimation algorithm.

Finally, research has shown that there can be important differences between 2D and 3D fish swimming [16, 17]. While many of the basic principles carry over from 2D to 3D, the 3D case also contains a more complex wake and certain mechanisms that

do not exist in 2D. Furthermore, in 3D, fish are likely able to sense even more details about the oncoming wake that may improve observability, and it would be interesting to investigate the optimal sensor configuration around the head that allows for this. Since 3D simulations require significantly more computational power and time to conduct, we limited our investigation to 2D. However, there are certainly aspects of the 3D flow that simply cannot be captured in 2D.

5.3 Implications for AUV technology and recommendations for future work

Nearly all biological organisms in the aquatic world possess the ability to sense the flow around them. Fish, despite being relatively simple animals, are ubiquitously equipped with a lateral line that provides the ability to sense the distribution of flow over their entire body. In contrast, engineered vehicles are equipped with vision, sonar, proprioception, and acoustic current profilers, but no ability to characterize the flow directly surrounding them. This effectively makes them (almost) hydrodynamically blind.

The ability to sense the local flow can improve stability as well as observability. Vortices incident on the hull or fins of underwater vehicles can cause substantial and unexpected forces [128]. Waves and recirculating currents within the surf zone create a dangerous environment for ships and submerged vehicles, often resulting in capsizing or broaching [162]. Even ships operating in close proximity to each other or within narrow channels occasionally experience unexpected and overwhelming forces, resulting in collision. Yet, despite these dangers, there is a growing interest in the development of unmanned marine vehicles for applications including ship and structure inspection, port security, and scientific data collection. The ability to sense and characterize the flow immediately surrounding these vehicles would provide the chance to respond to them. For unmanned systems, an artificial lateral line would be inexpensive, small, and low-bandwidth, providing information that would allow for

more robust autonomous operation.

Furthermore, the underwater environment is far from being a quiescent body of water. Particularly in shallow water, streams, and around other animals, objects, and submerged structures, there can exist unsteady currents, large-scale vortex shedding, and sharp flow gradients. Underwater animals have inspired us by demonstrating that rather than being only a challenge to overcome, these unsteady flows can also be exploited for energy savings. Research has already shown that knowledge of large-scale currents can enable path-planning that minimize travel time for an autonomous ocean vehicle [94]. The present works suggests that smaller-scale flow structures could also be used to help an autonomous underwater vehicle (AUV) travel more economically, with the help of a distributed flow sensing system.

The current study has shown that an artificial lateral line has a lot of potential in the abilities it could provide for an AUV. Although it is only a local flow sensor, and the observability is limited to a small distance from the vehicle, a significant amount of useful information can be deciphered from the signals collected within this region. We have shown that the information obtained can be used to perform the complex task of exploiting an upstream wake for energy savings. In the process, we have discovered a few areas that would be very interesting to explore further.

5.3.1 Machine learning for wake-relative interactions

The present work assumes that the optimal wake-relative phase differences $\Delta\phi_h$ and $\Delta\phi_t$ have been learned *a priori*, which was effectively performed by the optimization routine. However, this would be an interesting problem to investigate with machine learning techniques. The actual vortex positions have a much more direct and physical relationship with the swimming efficiency (compared with the pressure measurements of the lateral line). Could a learning technique such as a neural network capture a consistent physical relationship between various swimming configurations and optmal vortex-relative phase differences?

5.3.2 Subtracting the self-induced effect

The present work has shown that modeling the physics of the system, and in particular the self-induced effect of the fish, is very important for both sensing and control. Fish are known to be able to generate a negative image of their self induced flow, which is used in a feedforward loop to cancel out self-generated signals [106, 13]. Pressure is not linear and contributions from various sources cannot simply be superimposed; yet fish demonstrate that simply subtracting the self-induced term may be sufficient for many tasks. It would be interesting to further explore the limits of this. The self induced pressure requires solving only the forward model, and is therefore less computationally costly than solving the full inverse problem (running the observer requires solving the forward problem $2n + 1$ times at every timestep, where n is the number of unknown states). Could a simple algorithm relate the positions of nearby vortices with the pressure, with self-induced term subtracted?

5.3.3 Optimal configuration for 3D sensing

The cranial lateral line on fish, in contrast the the trunk lateral line canal, consists of several branches that cover a three-dimensional space over the head. Despite the remarkable diversity of fish, the morphology of the cranial lateral line canals consists of certain highly conserved patterns [169]. Nature is notoriously practical with regard to the evolution of animals, so there must be a reason for the patterns that we observe. It would be extremely interesting to explore the sensing problem in 3D, to determine if specific patterns of sensors over the head give rise to increased observability.

5.3.4 Interactions between fins

Although the model of a fish with a distinct tail fin considered here includes only one distinct fin, fish in nature have many fins. In particular, the dorsal and anal fins of fish have been proposed to shed vorticity which can interact with the caudal fin for enhanced thrust or efficiency [142, 44, 3]. The shedding of vorticity around the many fins of a fish presents a rich environment for flow control. How much control do fish

have over the interaction of vorticity with downstream fins? It would be interesting to further investigate the existence and/or potential of intentional vortex interactions between fins.

5.3.5 Distributed control algorithms

The lateral line is a distributed sensory organ. While we have shown here that lateral line feedback can be used in a conjunction with a system model to estimate local flow parameters and ultimately change specific swimming parameters, it is possible that control in fish is not executed on a central level but on a distributed level. There is a significant amount of evidence that control may be distributed. Fish are known to be controlled in part by a central pattern generator (CPG), which produces coordinated patterns of rhythmic activity while being modulated by simple control parameters [71].

Researchers have also shown that disrupting the lateral line on fish impairs swimming efficiency [181]. In fact, for swimming fish, Anderson et al. [5] observed that inflected boundary layers would periodically appear, but appeared to be stabilized at later phases of the undulatory cycle. This is fascinating, because it suggests that fish may actively tune their swimming motions in order to swim at the brink of separation, where the friction drag is reduced [5]. This would require local flow sensing, but it would also require local control.

Furthermore, it is well known that fish musculature consists of individual myotomes distributed longitudinally along the body. When Kármán gaiting , fish activate only their anterior muscles, seemingly allowing the posterior part of the body to simply "go with the flow" [88]. The present work has shown that by modifying a global variable such as the undulation phase, efficiency can be improved. However, sometimes it may be desirable to adjust the motion within only a small portion of the body. For example, fine-tuning of only the tail motion in the present work was shown to drastically increase the efficiency. Maybe a new control architecture, such as a CPG, would allow for the exploration of distributed control. While some research has attempted to control fish locomotion using CPGs [33, 86, 183, 111, 72], no work

to the author's knowledge has combined lateral line feedback with CPG control.

Bibliography

[1] Kim Aarestrup, Finn Økland, Michael M Hansen, David Righton, Patrik Gargan, Martin Castonguay, Louis Bernatchez, Paul Howey, Henrik Sparholt, Michael I Pedersen, et al. Oceanic spawning migration of the european eel (anguilla anguilla). *Science*, 325(5948):1660–1660, 2009.

[2] B Ahlborn, Stafford Chapman, R Stafford, and R Harper. Experimental simulation of the thrust phases of fast-start swimming of fish. *Journal of Experimental Biology*, 200(17):2301–2312, 1997.

[3] Imran Akhtar, Rajat Mittal, George V Lauder, and Elliot Drucker. Hydrodynamics of a biologically inspired tandem flapping foil configuration. *Theoretical and Computational Fluid Dynamics*, 21(3):155–170, 2007.

[4] Yu G Aleyev. *Nekton*. Springer Science & Business Media, 2012.

[5] ERIK J. Anderson, WADE R. McGillis, and MARK A. Grosenbaugh. The boundary layer of swimming fish. *Journal of Experimental Biology*, 204(1): 81âĂŞ102, 2001.

[6] J. M. Anderson, K. Streitlien, D. S. Barrett, and M. S. Triantafyllou. Oscillating foils of high propulsive efficiency. *Journal of Fluid Mechanics*, 360:41–72, April 1998.

[7] Jamie M Anderson. Vorticity control for efficient propulsion. Technical report, Massachusetts Institute of Technology, 1996.

[8] Miroslav Balda. FletcherâĂŹs version of the levenberg-maquardt algorithm for nonlinear least-squares, version 1.6, 2013. URL `https://www.mathworks.com/matlabcentral/fileexchange/39564-lmfnlsq2`.

[9] D. S. Barrett, M. S. Triantafyllou, D. K. P. Yue, M. A. Grosenbaugh, and M. J. Wolfgang. Drag reduction in fish-like locomotion. *Journal of Fluid Mechanics*, 392:183–212, 1999.

[10] D. N. Beal, F. S. Hover, M. S. Triantafyllou, J. C. Liao, and G. V. Lauder. Passive propulsion in vortex wakes. *Journal of Fluid Mechanics*, 549:385–402, February 2006.

[11] David N. Beal. *Propulsion through wake synchronization using a flapping foil.* Phd thesis, Massachusetts Institute of Technology, 2003.

[12] J Thomas Beale and Andrew Majda. High order accurate vortex methods with explicit velocity kernels. *Journal of Computational Physics*, 58(2):188–208, 1985.

[13] Curtis C Bell, Victor Han, and Nathaniel B Sawtell. Cerebellum-like structures and their implications for cerebellar function. *Annu. Rev. Neurosci.*, 31:1–24, 2008.

[14] Michel Bergmann and Laurent Cordier. Optimal control of the cylinder wake in the laminar regime by trust-region methods and pod reduced-order models. *Journal of Computational Physics*, 227(16):7813–7840, 2008.

[15] Graham Berry. How to ride a wave. *Engineering and Science*, 25(3):20–21, 1986.

[16] I. Borazjani and F. Sotiropoulos. On the role of form and kinematics on the hydrodynamics of self-propelled body/caudal fin swimming. *J Exp Biol*, 213 (1):89–107, January 2010.

[17] Iman Borazjani and Mohsen Daghooghi. The fish tail motion forms an attached leading edge vortex. In *Proc. R. Soc. B*, volume 280, page 20122071. The Royal Society, 2013.

[18] N Bose and J Lien. Energy absorption from ocean waves: a free ride for cetaceans. *Proceedings of the Royal Society of London B: Biological Sciences*, 240(1299):591–605, 1990.

[19] Neil Bose. Explicit kutta condition for an unsteady two-dimensional constant potential panel method. *AIAA journal*, 32(5):1078–1080, 1994.

[20] Charles Marcus Breder. The locomotion of fishes. *Zoologica*, 4:159–297, 1926.

[21] Ido Bright, Guang Lin, and J Nathan Kutz. Compressive sensing based machine learning strategy for characterizing the flow around a cylinder with limited pressure measurements. *Physics of Fluids*, 25(12):127102, 2013.

[22] John Buck. Synchronous rhythmic flashing of fireflies. ii. *The Quarterly review of biology*, 63(3):265–289, 1988.

[23] Bernd U Budelmann and Horst Bleckmann. A lateral line analogue in cephalopods: water waves generate microphonic potentials in the epidermal head lines ofsepia andlolliguncula. *Journal of Comparative Physiology A: Neuroethology, Sensory, Neural, and Behavioral Physiology*, 164(1):1–5, 1988.

[24] Bernd-Ulrich Budelmann. Hydrodynamic receptor systems in invertebrates. In *The mechanosensory lateral line*, pages 607–631. Springer, 1989.

[25] Erik Burgerhout, Christian Tudorache, Sebastiaan A Brittijn, Arjan P Palstra, Ron P Dirks, and Guido EEJM van den Thillart. Schooling reduces energy consumption in swimming male european eels, anguilla anguilla l. *Journal of experimental marine biology and ecology*, 448:66–71, 2013.

[26] Julie M Butler and Karen P Maruska. The mechanosensory lateral line is used to assess opponents and mediate aggressive behaviors during territorial interactions in an african cichlid fish. *Journal of Experimental Biology*, 218(20): 3284–3294, 2015.

[27] Pinaki Chakraborty, S Balachandar, and Ronald J Adrian. On the relationships between local vortex identification schemes. *Journal of fluid mechanics*, 535: 189–214, 2005.

[28] LD Chambers, O Akanyeti, R Venturelli, J Ježov, J Brown, M Kruusmaa, P Fiorini, and WM Megill. A fish perspective: detecting flow features while moving using an artificial lateral line in steady and unsteady flow. *Journal of The Royal Society Interface*, 11(99):20140467, 2014.

[29] Qigang Chen, Qiang Zhong, Meilan Qi, and Xingkui Wang. Comparison of vortex identification criteria for planar velocity fields in wall turbulence. *Physics of Fluids*, 27(8):085101, 2015.

[30] Kelly Cohen, Stefan Siegel, and Thomas McLaughlin. Feedback control of a cylinder wake low-dimensional model. *AIAA Journal*, 41(7), 2003.

[31] S. Coombs, H. Bleckmann, R.R. Fay, and A.N. Popper. *The Lateral Line System.* Springer Handbook of Auditory Research. Springer New York, 2013. ISBN 9781461488514. URL `https://books.google.com/books?id=2DC5BAAAQBAJ`.

[32] Sheryl Coombs, John Janssen, and Jacqueline F Webb. Diversity of lateral line systems: evolutionary and functional considerations. In *Sensory biology of aquatic animals*, pages 553–593. Springer, 1988.

[33] Alessandro Crespi, Daisy Lachat, Ariane Pasquier, and Auke Jan Ijspeert. Controlling swimming and crawling in a fish robot using a central pattern generator. *Autonomous Robots*, 25(1-2):3–13, 2008.

[34] Jenna M. Crowe-Riddell, Edward P. Snelling, Amy P. Watson, Anton Kyuseop Suh, Julian C. Partridge, and Kate L. Sanders. The evolution of scale sensilla in the transition from land to sea in elapid snakes. *Open Biology*, 6(6), 2016. doi: 10.1098/rsob.160054.

[35] Erik Dahl. Antennal sensory hairs in talitrid amphipods (crustacea). *Acta Zoologica*, 54(3):161–171, 1973.

[36] T Burt De Perera. Fish can encode order in their spatial map. *Proceedings of the Royal Society of London B: Biological Sciences*, 271(1553):2131–2134, 2004.

[37] Guido Dehnhardt, Björn Mauck, and Horst Bleckmann. Seal whiskers detect water movements. *Nature*, 394(6690):235, 1998.

[38] Bradley H Dickerson, Zane N Aldworth, and Thomas L Daniel. Control of moth flight posture is mediated by wing mechanosensory feedback. *Journal of Experimental Biology*, 217(13):2301–2308, 2014.

[39] Michael H Dickinson, Claire T Farley, Robert J Full, MAR Koehl, Rodger Kram, and Steven Lehman. How animals move: an integrative view. *Science*, 288(5463):100–106, 2000.

[40] Sven Dijkgraaf. The functioning and significance of the lateral-line organs. *Biological Reviews*, 38(1):51–105, 1963.

[41] T L Doligalski, C R Smith, and J D A Walker. Vortex interactions with walls. *Annual Review of Fluid Mechanics*, 26(1):573–616, 1994.

[42] Gen-Jin Dong and Xi-Yun Lu. Characteristics of flow over traveling wavy foils in a side-by-side arrangement. *Physics of Fluids*, 19(5):057107–057107–11, May 2007.

[43] E. G. Drucker and G. V. Lauder. Locomotor forces on a swimming fish: three-dimensional vortex wake dynamics quantified using digital particle image velocimetry. *Journal of Experimental Biology*, 202(18):2393–2412, September 1999.

[44] Eliot G Drucker and George V Lauder. Locomotor function of the dorsal fin in teleost fishes: experimental analysis of wake forces in sunfish. *Journal of Experimental Biology*, 204(17):2943–2958, 2001.

[45] Jeff D Eldredge and David Pisani. Passive locomotion of a simple articulated fish-like system in the wake of an obstacle. *Journal of Fluid Mechanics*, 607: 279–288, 2008.

[46] Eva C Enders, Daniel Boisclair, and André G Roy. The effect of turbulence on the cost of swimming for juvenile atlantic salmon (salmo salar). *Canadian Journal of Fisheries and Aquatic Sciences*, 60(9):1149–1160, 2003.

[47] Bard Ermentrout. An adaptive model for synchrony in the firefly pteroptyx malaccae. *Journal of Mathematical Biology*, 29(6):571–585, 1991.

[48] Karine Faucher, Eric Parmentier, Christophe Becco, Nicolas Vandewalle, and Pierre Vandewalle. Fish lateral system is required for accurate control of shoaling behaviour. *Animal Behaviour*, 79(3):679–687, 2010.

[49] Céline Feillet, Peter Krusche, Filippo Tamanini, Roel C Janssens, Mike J Downey, Patrick Martin, Michèle Teboul, Shoko Saito, Francis A Lévi, Till Bretschneider, et al. Phase locking and multiple oscillating attractors for the coupled mammalian clock and cell cycle. *Proceedings of the National Academy of Sciences*, 111(27):9828–9833, 2014.

[50] Vicente I Fernandez. *Performance analysis for lateral-line-inspired sensor arrays.* Phd thesis, Massachusetts Institute of Technology, 2011.

[51] Harry L Fierstine and Vladimir Walters. Studies in locomotion and anatomy of scombroid fishes. *Biological Sciences*, page 4, 1968.

[52] Frank E Fish and Clifford A Hui. Dolphin swimming–a review. *Mammal Review*, 21(4):181–195, 1991.

[53] Frank E. Fish and Clifford A. Hui. Dolphin swimmingâĂŞa review. *Mammal Review*, 21(4):181–195, December 1991.

[54] Thomas Fletcher, John Altringham, Jeffrey Peakall, Paul Wignall, and Robert Dorrell. Hydrodynamics of fossil fishes. In *Proc. R. Soc. B*, volume 281, page 20140703. The Royal Society, 2014.

[55] Pascal Fries. A mechanism for cognitive dynamics: neuronal communication through neuronal coherence. *Trends in cognitive sciences*, 9(10):474–480, 2005.

[56] Mattia Gazzola, Philippe Chatelain, Wim M Van Rees, and Petros Koumoutsakos. Simulations of single and multiple swimmers with non-divergence free deforming geometries. *Journal of Computational Physics*, 230(19):7093–7114, 2011.

[57] Mattia Gazzola, Wim M Van Rees, and Petros Koumoutsakos. C-start: optimal start of larval fish. *Journal of Fluid Mechanics*, 698:5–18, 2012.

[58] Mattia Gazzola, Andrew A Tchieu, Dmitry Alexeev, Alexia de Brauer, and Petros Koumoutsakos. Learning to school in the presence of hydrodynamic interactions. *Journal of Fluid Mechanics*, 789:726–749, 2016.

[59] R. Gopalkrishnan, M. S. Triantafyllou, G. S. Triantafyllou, and D. Barrett. Active vorticity control in a shear flow using a flapping foil. *Journal of Fluid Mechanics*, 274:1–21, September 1994.

[60] WR Graham, J Peraire, and KY Tang. Optimal control of vortex shedding using low-order models. part iâĂŤopen-loop model development. *International Journal for Numerical Methods in Engineering*, 44(7):945–972, 1999.

[61] El S Hassan. Hydrodynamic imaging of the surroundings by the lateral line of the blind cave fish anoptichthys jordani. In *The Mechanosensory Lateral Line*, pages 217–227. Springer, 1989.

[62] El-Sayed Hassan. On the discrimination of spatial intervals by the blind cave fish (anoptichthys jordani). *Journal of Comparative Physiology A: Neuroethology, Sensory, Neural, and Behavioral Physiology*, 159(5):701–710, 1986.

[63] Ck Hemelrijk, Dap Reid, H Hildenbrandt, and Jt Padding. The increased efficiency of fish swimming in a school. *Fish Fish*, pages n/a–n/a, January 2014.

[64] Robert Hermann and Arthur Krener. Nonlinear controllability and observability. *IEEE Transactions on automatic control*, 22(5):728–740, 1977.

[65] J Herskin and JF Steffensen. Energy savings in sea bass swimming in a school: measurements of tail beat frequency and oxygen consumption at different swimming speeds. *Journal of Fish Biology*, 53(2):366–376, 1998.

[66] Dorian Houser, Steve Martin, Mike Phillips, Eric Bauer, Tim Herrin, and Patrick Moore. Signal processing applied to the dolphin-based sonar system. In *OCEANS 2003. Proceedings*, volume 1, pages 297–303. IEEE, 2003.

[67] F. S. Hover, ÃŸ. Haugsdal, and M. S. Triantafyllou. Effect of angle of attack profiles in flapping foil propulsion. *Journal of Fluids and Structures*, 19(1): 37–47, January 2004.

[68] Guan-Chyun Hsieh and James C Hung. Phase-locked loop techniques. a survey. *IEEE Transactions on industrial electronics*, 43(6):609–615, 1996.

[69] Laura M Hudy, Ahmed Naguib, and William M Humphreys. Stochastic estimation of a separated-flow field using wall-pressure-array measurements. *Physics of Fluids*, 19(2):024103, 2007.

[70] WF Humphreys and MN Feinberg. Food of the blind cave fishes of northwestern australia. *Records of the Western Australian Museum*, 17:29–33, 1995.

[71] Auke Jan Ijspeert. Central pattern generators for locomotion control in animals and robots: a review. *Neural networks*, 21(4):642–653, 2008.

[72] Auke Jan Ijspeert and Jérome Kodjabachian. Evolution and development of a central pattern generator for the swimming of a lamprey. *Artificial Life*, 5(3): 247–269, 1999.

[73] Jinhee Jeong and Fazle Hussain. On the identification of a vortex. *Journal of fluid mechanics*, 285:69–94, 1995.

[74] Jaas Ježov, Otar Akanyeti, Lily D Chambers, and Maarja Kruusmaa. Sensing oscillations in unsteady flow for better robotic swimming efficiency. In *Systems, Man, and Cybernetics (SMC), 2012 IEEE International Conference on*, pages 91–96. IEEE, 2012.

[75] Lai-Bing Jia and Xie-Zhen Yin. Passive oscillations of two tandem flexible filaments in a flowing soap film. *Physical review letters*, 100(22):228104, 2008.

[76] Simon J Julier and Jeffrey K Uhlmann. Unscented filtering and nonlinear estimation. *Proceedings of the IEEE*, 92(3):401–422, 2004.

[77] Joseph Katz and Allen Plotkin. *Low-speed aerodynamics*, volume 13. Cambridge university press, 2001.

[78] W Kaufmann. Uber die ausbreitung kreiszlindrischer wirbel in zahen flussigkeiten. *Ing. Arch.*, 31(1):1, 1962.

[79] Scott David Kelly and Parthesh Pujari. Propulsive energy harvesting by a fish-like vehicle in a vortex flow: Computational modeling and control. In *Decision and Control (CDC), 2010 49th IEEE Conference on*, pages 1058–1064. IEEE, 2010.

[80] Shaun S Killen, Stefano Marras, John F Steffensen, and David J McKenzie. Aerobic capacity influences the spatial position of individuals within fish schools. In *Proc. R. Soc. B*, volume 279, pages 357–364. The Royal Society, 2012.

[81] Sohae Kim, Wei-Xi Huang, and Hyung Jin Sung. Constructive and destructive interaction modes between two tandem flexible flags in viscous flow. *Journal of Fluid Mechanics*, 661:511–521, 2010.

[82] Spyrosa Kinnas and Ching Hsin. Boundary element method for the analysis of the unsteady flow around extreme propeller geometries. *AIAA journal*, 30(3): 688–696, 1992.

[83] Adrian Klein and Horst Bleckmann. Determination of object position, vortex shedding frequency and flow velocity using artificial lateral line canals. *Beilstein journal of nanotechnology*, 2:276, 2011.

[84] Manoochehr M Koochesfahani. Vortical patterns in the wake of an oscillating airfoil. *AIAA journal*, 2012.

[85] Arthur J Krener and Kayo Ide. Measures of unobservability. In *Decision and Control, 2009 held jointly with the 2009 28th Chinese Control Conference. CDC/CCC 2009. Proceedings of the 48th IEEE Conference on*, pages 6401–6406. IEEE, 2009.

[86] Daisy Lachat, Alessandro Crespi, and Auke Jan Ijspeert. Boxybot: a swimming and crawling fish robot controlled by a central pattern generator. In *Biomedical Robotics and Biomechatronics, 2006. BioRob 2006. The First IEEE/RAS-EMBS International Conference on*, pages 643–648. IEEE, 2006.

[87] David Lentink, Florian T Muijres, Frits J Donker-Duyvis, and Johan L van Leeuwen. Vortex-wake interactions of a flapping foil that models animal swimming and flight. *Journal of Experimental Biology*, 211(2):267–273, 2008.

[88] J. C. Liao, D. N. Beal, G. V. Lauder, and M. S. Triantafyllou. Fish exploiting vortices decrease muscle activity. *Science*, 302(5650):1566–1569, 2003.

[89] James C Liao. The role of the lateral line and vision on body kinematics and hydrodynamic preference of rainbow trout in turbulent flow. *Journal of Experimental Biology*, 209(20):4077–4090, 2006.

[90] James C Liao. A review of fish swimming mechanics and behaviour in altered flows. *Philosophical Transactions of the Royal Society B: Biological Sciences*, 362(1487):1973 –1993, November 2007.

[91] James C. Liao, David N. Beal, George V. Lauder, and Michael S. Triantafyllou. The Kármán gait: novel body kinematics of rainbow trout swimming in a vortex street. *J Exp Biol*, 206(6):1059–1073, March 2003.

[92] MJ Lighthill. Aquatic animal propulsion of high hydromechanical efficiency. *Journal of Fluid Mechanics*, 44(2):265–301, 1970.

[93] Geng Liu, Yan Ren, Haibo Dong, and George Lauder. Fin-body interaction and its hydrodynamic benefits in fish's steady swimming. In *APS Meeting Abstracts*, 2016.

[94] Tapovan Lolla, Pierre FJ Lermusiaux, Mattheus P Ueckermann, and Patrick J Haley. Time-optimal path planning in dynamic flows using level set equations: theory and schemes. *Ocean Dynamics*, 64(10):1373–1397, 2014.

[95] A. P. Maertens, M. S. Triantafyllou, and D. K. P. Yue. Efficiency of fish propulsion. *Submitted to Bioinspiration and biomimetics*, 2015. Under review.

[96] Audrey P Maertens. *Touch at a distance: underwater object identification using pressure sensors.* Masters thesis, Massachusetts Institute of Technology, 2011.

[97] Audrey P Maertens. *Fish swimming optimization and exploiting multi-body hydrodynamic interactions for underwater navigation.* PhD thesis, Massachusetts Institute of Technology, Dept. of Mechanical Engineering, 2015.

[98] Audrey P. Maertens and Gabriel D. Weymouth. Accurate cartesian-grid simulations of near-body flows at intermediate reynolds numbers. *Computer Methods in Applied Mechanics and Engineering*, 283:106–129, January 2015.

[99] Audrey P Maertens, Amy Gao, and Michael S Triantafyllou. Optimal undulatory swimming for a single fish-like body and for a pair of interacting swimmers. *Journal of Fluid Mechanics*, 813:301–345, 2017.

[100] J. J. Magnuson. Locomotion by scombrid fishes: hydromechanics, morpholog and behavior. *Fish Physiology*, 7:239–313, 1978.

[101] Stefano Marras, Shaun S Killen, Jan Lindström, David J McKenzie, John F Steffensen, and Paolo Domenici. Fish swimming in schools save energy regardless of their spatial position. *Behavioral ecology and sociobiology*, 69(2):219–226, 2015.

[102] James D McCleave and Robert C Kleckner. Selective tidal stream transport in the estuarine migration of glass eels of the american eel (anguilla rostrata). *ICES Journal of Marine Science*, 40(3):262–271, 1982.

[103] William J McCroskey. Unsteady airfoils. *Annual review of fluid mechanics*, 14 (1):285–311, 1982.

[104] Juan Melli and Clarence W Rowley. Models and control of fish-like locomotion. *Experimental Mechanics*, 50(9):1355–1360, 2010.

[105] JC Montgomery, F McDonald, CF Baker, AG Carton, and N Ling. Sensory integration in the hydrodynamic world of rainbow trout. *Proceedings of the Royal Society of London B: Biological Sciences*, 270(Suppl 2):S195–S197, 2003.

[106] John C Montgomery and David Bodznick. An adaptive filter that cancels self-induced noise in the electrosensory and lateral line mechanosensory systems of fish. *Neuroscience letters*, 174(2):145–148, 1994.

[107] John C Montgomery, Sheryl Coombs, and Cindy F Baker. The mechanosensory lateral line system of the hypogean form of astyanax fasciatus. In *The biology of hypogean fishes*, pages 87–96. Springer, 2001.

[108] Ulrike K Müller, Joris Smit, Eize J Stamhuis, and John J Videler. How the body contributes to the wake in undulatory fish swimming. *Journal of Experimental Biology*, 204(16):2751–2762, 2001.

[109] U. MÃijller, BLEVD Heuvel, E. Stamhuis, and J. Videler. Fish foot prints: morphology and energetics of the wake behind a continuously swimming mullet (chelon labrosus risso). *Journal of Experimental Biology*, 200(22):2893–2906, 1997.

[110] Sujit Nair and Eva Kanso. Hydrodynamically coupled rigid bodies. *Journal of Fluid Mechanics*, 592:393–411, 2007.

[111] Xuelei Niu, Jianxin Xu, Qinyuan Ren, and Qingguo Wang. Locomotion learning for an anguilliform robotic fish using central pattern generator approach. *IEEE Transactions on Industrial Electronics*, 61(9):4780–4787, 2014.

[112] Guido Novati, Siddhartha Verma, Dmitry Alexeev, Diego Rossinelli, Wim M van Rees, and Petros Koumoutsakos. Synchronisation through learning for two self-propelled swimmers. *Bioinspiration & Biomimetics*, 12(3):036001, 2017.

[113] University of Wisconsin Center for Limnology, Wisconsin Department of Natural Resources, and University of Wisconsin Sea Grant Institute. Wisconsin fish identification, 2013. URL `http://www.seagrant.wisc.edu/home/Default.aspx?tabid=604`.

[114] Matthew Fontaine Maury Osborne. The hydrodynamical performance of migratory salmon. *Journal of experimental biology*, 38(2):365–390, 1961.

[115] C. W. Oseen. Uber wirbelbewegung in einer reibenden flussigkeit. *Ark. J. Mat. Astrom. Fys.*, 7:14–21, 1912.

[116] Yulin Pan, Xiaoxia Dong, Qiang Zhu, and Dick KP Yue. Boundary-element method for the prediction of performance of flapping foils with leading-edge separation. *Journal of Fluid Mechanics*, 698:446–467, 2012.

[117] Faust R Parker Jr. Reduced metabolic rates in fishes as a result of induced schooling. *Transactions of the American Fisheries Society*, 102(1):125–131, 1973.

[118] B. L. Partridge and T. J. Pitcher. Evidence against a hydrodynamic function for fish schools. *Nature*, 279(5712):418–419, May 1979.

[119] Brian L. Partridge. Lateral line function and the internal dynamics of fish schools. In William N. Tavolga, Arthur N. Popper, and Richard R. Fay, editors, *Hearing and Sound Communication in Fishes*, Proceedings in Life Sciences, pages 515–522. Springer New York, January 1981.

[120] Brian L. Partridge, Tony Pitcher, J. Michael Cullen, and John Wilson. The three-dimensional structure of fish schools. *Behav Ecol Sociobiol*, 6(4):277–288, March 1980.

[121] Robin D Paulos, Marie Trone, II Kuczaj, and A Stan. Play in wild and captive cetaceans. *International Journal of Comparative Psychology*, 23(4), 2010.

[122] Hans M Peters. Anatomie und entwicklungsgeschichte des lateralissystems von tilapia (pisces, cichlidae). *Zeitschrift für Morphologie der Tiere*, 74(2):89–161, 1973.

[123] JMV Rayner. A vortex theory of animal flight. part 1. the vortex wake of a hovering animal. *Journal of Fluid Mechanics*, 91(4):697–730, 1979.

[124] D.A. Read, F.S. Hover, and M.S. Triantafyllou. Forces on oscillating foils for propulsion and maneuvering. *Journal of Fluids and Structures*, 17(1):163–183, jan 2003.

[125] Zheng Ren and Kamran Mohseni. A model of the lateral line of fish for vortex sensing. *Bioinspiration & biomimetics*, 7(3):036016, 2012.

[126] Harley W Reno. The lateral-line system of the silverjaw minnow, ericymba buccata cope. *The Southwestern Naturalist*, pages 347–358, 1971.

[127] Leif Ristroph, James C Liao, and Jun Zhang. Lateral line layout correlates with the differential hydrodynamic pressure on swimming fish. *Physical review letters*, 114(1):018102, 2015.

[128] Donald Rockwell. Vortex-body interactions. *Annual Review of Fluid Mechanics*, 30(1):199–229, 1998.

[129] Clarence W Rowley, Igor Mezić, Shervin Bagheri, Philipp Schlatter, and Dan S Henningson. Spectral analysis of nonlinear flows. *Journal of fluid mechanics*, 641:115–127, 2009.

[130] Michael Sachinis. *The design and testing of a biologically inspired underwater robotic mechanism.* PhD thesis, Massachusetts Institute of Technology, 2000.

[131] Taavi Salumäe and Maarja Kruusmaa. Flow-relative control of an underwater robot. In *Proc. R. Soc. A*, volume 469, page 20120671. The Royal Society, 2013.

[132] Taavi Salumäe, Inaki Ranó, Otar Akanyeti, and Maarja Kruusmaa. Against the flow: A braitenberg controller for a fish robot. In *Robotics and Automation (ICRA), 2012 IEEE International Conference on*, pages 4210–4215. IEEE, 2012.

[133] Bodapati Satyanarayana and Sanford Davis. Experimental studies of unsteady trailing-edge conditions. *AIAA Journal*, 16(2):125–129, 1978.

[134] Teis Schnipper, Anders Andersen, and Tomas Bohr. Vortex wakes of a flapping foil. *Journal of Fluid Mechanics*, 633:411–423, 2009.

[135] Lionel Schouveiler, FS Hover, and MS Triantafyllou. Performance of flapping foil propulsion. *Journal of Fluids and Structures*, 20(7):949–959, 2005.

[136] Michael Sfakiotakis, D.M. Lane, and J.B.C. Davies. Review of fish swimming modes for aquatic locomotion. *IEEE Journal of Oceanic Engineering*, 24(2): 237–252, 1999.

[137] Saurabh Sharma, Sheryl Coombs, Paul Patton, and Theresa Burt de Perera. The function of wall-following behaviors in the mexican blind cavefish and a sighted relative, the mexican tetra (astyanax). *Journal of Comparative Physiology A*, 195(3):225–240, 2009.

[138] Scot W Shuler, R Barry Nehring, and Kurt D Fausch. Diel habitat selection by brown trout in the rio grande river, colorado, after placement of boulder structures. *North American Journal of Fisheries Management*, 14(1):99–111, 1994.

[139] Yusni Ikhwan Siregar. Morphology and growth of lateral line organs of the rainbow trout (oncorhynchus mykiss). *Acta zoologica*, 75(3):213–218, 1994.

[140] David L Smith, Ernest L Brannon, and Mufeed Odeh. Response of juvenile rainbow trout to turbulence produced by prismatoidal shapes. *Transactions of the American Fisheries Society*, 134(3):741–753, 2005.

[141] Steven W Smith et al. The scientist and engineer's guide to digital signal processing. 1997.

[142] EM Standen and George V Lauder. Hydrodynamic function of dorsal and anal fins in brook trout (salvelinus fontinalis). *Journal of Experimental Biology*, 210 (2):325–339, 2007.

[143] Knut Streitlien, George S. Triantafyllou, and Michael S. Triantafyllou. Efficient foil propulsion through vortex control. *AIAA Journal*, 34(11):2315–2319, 1996.

[144] Steven H Strogatz. Spontaneous synchronization in nature. In *Frequency Control Symposium, 1997., Proceedings of the 1997 IEEE International*, pages 2–4. IEEE, 1997.

[145] AM Sutterlin and Susan Waddy. Possible role of the posterior lateral line in obstacle entrainment by brook trout (salvelinus fontinalis). *Journal of the Fisheries Board of Canada*, 32(12):2441–2446, 1975.

[146] Takao Suzuki and Tim Colonius. Inverse-imaging method for detection of a vortex in a channel. *AIAA journal*, 41(9):1743–1826, 2003.

[147] Jon Christian Svendsen, Jakob Skov, M Bildsoe, and John Fleng Steffensen. Intra-school positional preference and reduced tail beat frequency in trailing positions in schooling roach under experimental conditions. *Journal of fish biology*, 62(4):834–846, 2003.

[148] Masashige Taguchi and James C Liao. Rainbow trout consume less oxygen in turbulence: the energetics of swimming behaviors at different speeds. *Journal of Experimental Biology*, 214(9):1428–1436, 2011.

[149] J Tautz and DC Sandeman. The detection of waterborne vibration by sensory hairs on the chelae of the crayfish. *Journal of Experimental Biology*, 88(1): 351–356, 1980.

[150] GK Taylor and ALR Thomas. Animal flight dynamics ii. longitudinal stability in flapping flight. *Journal of theoretical biology*, 214(3):351–370, 2002.

[151] JA Taylor and MN Glauser. Towards practical flow sensing and control via pod and lse based low-dimensional tools. *Journal of fluids engineering*, 126(3): 337–345, 2004.

[152] Ngai-Huat Teng. *The development of a computer code (U2DIIF)–for the numerical solution of unsteady.* PhD thesis, 1987.

[153] T Teyke. Collision with and avoidance of obstacles by blind cave fishanoptichthys jordani (characidae). *Journal of Comparative Physiology A: Neuroethology, Sensory, Neural, and Behavioral Physiology*, 157(6):837–843, 1985.

[154] T Teyke. Flow field, swimming velocity and boundary layer: parameters which affect the stimulus for the lateral line organ in blind fish. *Journal of Comparative Physiology A: Neuroethology, Sensory, Neural, and Behavioral Physiology*, 163 (1):53–61, 1988.

[155] M. S. Triantafyllou, G. S. Triantafyllou, and R. Gopalkrishnan. Wake mechanics for thrust generation in oscillating foils. *Physics of Fluids A: Fluid Dynamics (1989-1993)*, 3(12):2835–2837, December 1991.

[156] Michael S. Triantafyllou and George S. Triantafyllou. An efficient swimming machine. *Scientific American*, 272:64–70, March 1995.

[157] Michael S Triantafyllou, Alexandra H Techet, and Franz S Hover. Review of experimental work in biomimetic foils. *IEEE Journal of Oceanic Engineering*, 29(3):585–594, 2004.

[158] Michael S Triantafyllou, Gabriel D Weymouth, and Jianmin Miao. Biomimetic survival hydrodynamics and flow sensing. *Annual Review of Fluid Mechanics*, 48:1–24, 2016.

[159] MS Triantafyllou, AH Techet, Q Zhu, DN Beal, FS Hover, and DKP Yue. Vorticity control in fish-like propulsion and maneuvering. *Integrative and comparative biology*, 42(5):1026–1031, 2002.

[160] Ismail H Tuncer and Max F Platzer. Thrust generation due to airfoil flapping. *AIAA journal*, 34(2), 1996.

[161] Emad Uddin, Wei-Xi Huang, and Hyung Jin Sung. Interaction modes of multiple flexible flags in a uniform flow. *Journal of Fluid Mechanics*, 729:563–583, 2013.

[162] Naoya Umeda, Masami Hamamoto, Yoshifumi Takaishi, Yutaka Chiba, Akihiko Matsuda, Wataru Sera, Shiro Suzuki, Konstantinos Spyrou, and Kenji Watanabe. Model experiments of ship capsize in astern seas. *Journal of the Society of naval Architects of Japan*, 1995(177):207–217, 1995.

[163] Vincent van Ginneken, Erik Antonissen, Ulrike K Müller, Ronald Booms, Ep Eding, Johan Verreth, and Guido van den Thillart. Eel migration to the sargasso: remarkably high swimming efficiency and low energy costs. *Journal of Experimental Biology*, 208(7):1329–1335, 2005.

[164] Sietse M van Netten. Hydrodynamic detection by cupulae in a lateral line canal: functional relations between physics and physiology. *Biological cybernetics*, 94 (1):67–85, 2006.

[165] Roberto Venturelli, Otar Akanyeti, Francesco Visentin, Jaas Ježov, Lily D Chambers, Gert Toming, Jennifer Brown, Maarja Kruusmaa, William M Megill, and Paolo Fiorini. Hydrodynamic pressure sensing with an artificial lateral line in steady and unsteady flows. *Bioinspiration & biomimetics*, 7(3):036004, 2012.

[166] C Von Campenhausen, I Riess, and R Weissert. Detection of stationary objects by the blind cave fishanoptichthys jordani (characidae). *Journal of comparative physiology*, 143(3):369–374, 1981.

[167] Thomas J Walker. Acoustic synchrony: two mechanisms in the snowy tree cricket. *Science*, 166(3907):891–894, 1969.

[168] Kenji Watanabe, Kazuhiko Anraku, Harold M Monteclaro, and Ricardo P Babaran. Morphological characteristics of lateral line in three species of fish. *Aquaculture Science*, 58(1):25–35, 2010.

[169] Jacqueline F Webb. Gross morphology and evolution of the mechanoreceptive lateral-line system in teleost fishes (part 1 of 2). *Brain, behavior and evolution*, 33(1):34–43, 1989.

[170] D. Weihs. Hydromechanics of fish schooling. *Nature*, 241(5387):290–291, January 1973.

[171] Gabriel D Weymouth and Dick KP Yue. Boundary data immersion method for cartesian-grid simulations of fluid-body interaction problems. *Journal of Computational Physics*, 230(16):6233–6247, 2011.

[172] F.M. White. *Viscous Fluid Flow*. McGraw-Hill Education, 2005. ISBN 9780072402315. URL `https://books.google.com/books?id=ixWqQgAACAAJ`.

[173] S Wieskotten, G Dehnhardt, B Mauck, L Miersch, and W Hanke. Hydrodynamic determination of the moving direction of an artificial fin by a harbour seal (phoca vitulina). *Journal of Experimental Biology*, 213(13):2194–2200, 2010.

[174] TM Williams and WA Friedl. Travel at low energetic cost by swimming and wave-riding bottlenose dolphins. *Nature*, 355(6363):821, 1992.

[175] David Joe Willis. *An unsteady, accelerated, high order panel method with vortex particle wakes*. PhD thesis, Massachusetts Institute of Technology, 2006.

[176] Shane P Windsor and Matthew J McHenry. The influence of viscous hydrodynamics on the fish lateral-line system. *Integrative and comparative biology*, 49 (6):691–701, 2009.

[177] Shane P Windsor, Delfinn Tan, and John C Montgomery. Swimming kinematics and hydrodynamic imaging in the blind mexican cave fish (astyanax fasciatus). *Journal of Experimental Biology*, 211(18):2950–2959, 2008.

[178] Shane P Windsor, Stuart E Norris, Stuart M Cameron, Gordon D Mallinson, and John C Montgomery. The flow fields involved in hydrodynamic imaging by blind mexican cave fish (astyanax fasciatus). part i: open water and heading towards a wall. *Journal of Experimental Biology*, 213(22):3819–3831, 2010.

[179] Shane P Windsor, Stuart E Norris, Stuart M Cameron, Gordon D Mallinson, and John C Montgomery. The flow fields involved in hydrodynamic imaging by blind mexican cave fish (astyanax fasciatus). part ii: gliding parallel to a wall. *Journal of Experimental Biology*, 213(22):3832–3842, 2010.

[180] M. J. Wolfgang, J. M. Anderson, M. A. Grosenbaugh, D. K. Yue, and M. S. Triantafyllou. Near-body flow dynamics in swimming fish. *The Journal of Experimental Biology*, 202(17):2303–2327, September 1999.

[181] Kazutaka Yanase, Neill A Herbert, and John C Montgomery. Disrupted flow sensing impairs hydrodynamic performance and increases the metabolic cost of swimming in the yellowtail kingfish, seriola lalandi. *Journal of Experimental Biology*, 215(22):3944–3954, 2012.

[182] Yingchen Yang, Jack Chen, Jonathan Engel, Saunvit Pandya, Nannan Chen, Craig Tucker, Sheryl Coombs, Douglas L Jones, and Chang Liu. Distant touch hydrodynamic imaging with an artificial lateral line. *Proceedings of the National Academy of Sciences*, 103(50):18891–18895, 2006.

[183] Wei Zhao, Junzhi Yu, Yimin Fang, and Long Wang. Development of multi-mode biomimetic robotic fish based on central pattern generator. In *Intelligent Robots and Systems, 2006 IEEE/RSJ International Conference on*, pages 3891–3896. IEEE, 2006.

[184] Q. Zhu, M. J. Wolfgang, D. K. P. Yue, and M. S. Triantafyllou. Three-dimensional flow structures and vorticity control in fish-like swimming. *Journal of Fluid Mechanics*, 468:1–28, October 2002.

[185] Qiang Zhu and Zhangli Peng. Mode coupling and flow energy harvesting by a flapping foil. *Physics of Fluids*, 21(3):033601, 2009.